UNIVERSIDAD AUTÓNOMA DE NUEVO LEÓN FACULTAD DE CIENCIAS QUÍMICAS

Design of Oxazine, Oxazoline, and Hydroxyacetamide Derivatives to Optimize Zn^{2+} Binding and Selectivity Toward Histone Deacetylase: *In Silico* Studies, Synthesis, Characterization, and Anticancer Evaluation of Hydroxyacetamide Derivatives

BY

ASHLY MOHAN

Como requisito parcial para obtener el Grado de DOCTORADO EN CIENCIAS con Orientación en Farmacia

JUNE 2026

Design of Oxazine, Oxazoline, and Hydroxyacetamide Derivatives to Optimize Zn^{2+} Binding and Selectivity Toward Histone Deacetylase: *In Silico* Studies, Synthesis, Characterization, and Anticancer Evaluation of Hydroxyacetamide Derivatives

Tesis Revision

Dra. María Del Rayo Camacho Corona

Co-advisor

Dr. Eder U. Arredondo Espinoza

Tutorial committee

Dr. Abraham García Zepeda

Tutorial committee

Dr. Eugenio Hernández Fernández

Tutorial committee

Dr. Javier Rivera De la Rosa

Subdirector de Posgrado

Design of Oxazine, Oxazoline, and Hydroxyacetamide Derivatives to Optimize Zn^{2+} Binding and Selectivity Toward Histone Deacetylase: *In Silico* Studies, Synthesis, Characterization, and Anticancer Evaluation of Hydroxyacetamide Derivatives

Thesis approval

Dr. Francisco Guadalupe Avalos Alanís

President

Dr. Eder U. Arredondo Espinoza

Secretary

Dr. Miguel Ángel Reyes González

Vocal

Dra. Karina Vázquez Cisneros

Vocal

Dr. Eugenio Hernández Fernández

Vocal

Dr. Javier Rivera De la Rosa

Subdirector de Posgrado

Design of Oxazine, Oxazoline, and Hydroxyacetamide Derivatives to Optimize Zn^{2+} Binding and Selectivity Toward Histone Deacetylase: *In Silico* Studies, Synthesis, Characterization, and Anticancer Evaluation of Hydroxyacetamide Derivatives

Tesis Directors

Dr. Francisco Guadalupe Avalos Alanís

Director

Dra. María Del Rayo Camacho Corona

Co-Director

Acknowledgment

I would like to express my sincere gratitude to my thesis assessor, Dr. Francisco Guadalupe Avalos Alanís, for his valuable guidance, constructive feedback, and continuous support throughout the course of this research. I am equally grateful to my co-assessor, Dr. María Del Rayo Camacho Corona, for her insightful suggestions and encouragement, which greatly contributed to the improvement of this work.

I extend my heartfelt thanks to Dr. José Luis Viveros, Dr. Rubén Antonio Romo Mancillas and Dr. Eugenio Hernández Fernández for their willingness to teach, share their expertise, and provide the necessary facilities that enabled me to successfully carry out my research. Their academic support and cooperation were instrumental in completing this thesis.

I also wish to acknowledge the members of my tutorial committee for their time, guidance, and helpful recommendations at various stages of my research. Their collective input significantly strengthened the quality of this work.

Finally, I gratefully acknowledge SECIHTI for awarding me the scholarship that financially supported my studies and research. Without this support, the completion of this thesis would not have been possible.

Dedication

This thesis is dedicated to my family, whose unconditional love, patience, and constant encouragement have been the foundation of my academic journey. Their belief in me, moral support, and sacrifices provided the strength and motivation necessary to complete this work. I am deeply grateful for their unwavering support throughout my studies.

TABLE OF CONTENTS

LIST OF TABLES

Table **Page**

LIST OF FIGURES

Figure **Page**

Abbreviations

IARC	International Agency for Research
GLOBOCAN	Global Cancer Observatory
RNAs	Ribonucleic acid
NAD	Nicotinamide adenine dinucleotide
HDACs	Histone deacetylases
HDACi	Histone deacetylase inhibitor
miRNAs	MicroRNAs
HATs	Histone acetyltransferase
ncRNAs	Non-coding RNAs
DNMT inhibitors	DNA methyltransferase inhibitors
TSA	Trichostatin A
LBH589	Panobinostat
SIRT2	Sirtuin 2
SAHA	Vorinostat
PFS	Pogression-free survival
CDK	Cyclin-dependent kinase
lncRNAs	long non-coding RNAs
VPA	Valproic acid

LBH589	Squamous cell carcinoma
ZBG	Zinc binding group
NMEs	New molecular entities
HTS	High-throughput screening
CADD	Computer-aided drug design
NuRD	Nucleosome Remodeling and Deacetylase
CoREST	corepressor for element-1-silencing transcription factor
DNMT inhibitors	DNA methyltransferase inhibitors
p21WAF1/CIP1	Cyclin-Dependent Kinase Interacting Protein 1 / Wild-type p53 Activated Fragment 1
p27KIP1	27-kDa Cyclin-Dependent Kinase Inhibitory Protein 1
p57KIP2	57-kDa Cyclin-Dependent Kinase Inhibitory Protein 2
p21	21-kDa protein
p27	27-kDa protein
p57	57-kDa protein
G1 phase	Gap 1 phase
S phase	Synthesis phase
Rb-gene	Retinoblastoma gene
G2/M transition	Gap 2 / Mitosis phase
TSA	Trichostatin A
AKAP95	A-Kinase Anchoring Protein 95
HA95	Homologous to A-Kinase Anchoring Protein 95
PCAF/GCN5	p300/CBP-Associated Factor / General Control Non-repressed Protein 5

LBH589	Panobinostat.
BubR1	Budding Uninhibited by Benzimidazoles-Related 1.
CDC20	Cell Division Cycle 20
CDH1	Cadherin-1
SirReal2	Sirtuin Rearranging Ligand 2.
NEDD4	Neural Precursor Cell Expressed, Developmentally Downregulated 4
E3	Ubiquitin-Protein Ligase
CDK9	Cyclin-Dependent Kinase 9
PCI-34051	HDAC8-selective inhibitor
PCAF	p300/CBP-Associated Factor
c-FLIP	Cellular FLICE-Inhibitory Protein.
Bcl-2	B-cell lymphoma 2.
Bcl-xL	B-cell lymphoma-extra large
Mcl-1	Myeloid Cell Leukemia-1.
Apaf-1	Apoptotic Protease Activating Factor-1.
AIF	Apoptosis-Inducing Factor
PUMA	p53 Upregulated Modulator of Apoptosis
Bax	Bcl-2–Associated X Protein
Bim	Bcl-2–Interacting Mediator of Cell Death
BMF	Bcl-2–Modifying Factor
Ku70	Ku antigen 70 kDa protein
CBP	CREB-Binding Protein
EZH2	Enhancer of Zeste Homolog 2
CDH1	Cadherin-1
ZEB1	Zinc Finger E-box Binding Homeobox 1

MMPs	Matrix Metalloproteinases
miR-200a	microRNA-200a
TGF-b	Transforming Growth Factor-beta.
QSAR	Quantitative Structure-Activity Relationship
SBDD	Structure-Based Drug Design
VS	Virtual screening
H2L	Hit-to-lead
MD	Molecular Dynamics
TMD	Targeted MD
SMD	Steered MD
MM/GBSA	Mechanics/Generalized Born Surface Area
SBDD	Structure-Based Drug Design
MMPs	Matrix metalloproteinases
CI-994	Tacedinaline
FK228	Romidepsin
PDB	Protein Data Bank
DCC	*N, N*'-Dicyclohexylcarbodiimide
DCM	Dichloromethane
HT29	Colon adenocarcinoma cell line
MCF-7	Breast cancer cell line
PC-3	Prostate cancer cell line
HaCaT	Skin keratinocyte cell line
HCT-15	Colon cancer cell line
Pst	Pseudo triplet
qn	Quintet
***p*TsOH**	*p*-toluenesulfonic acid

$CDCl_3$	Deuterated chloroform
DMSO	Dimethyl sulfoxide
EtOH	Ethanol
Et_3N	Triethylamine
ACN	Acetonitrile
NMM	*N*-methyl morpholine
HBTU	Hexafluorophosphate benzotriazole tetramethyl uronium
DIPEA	*N*, *N*-Diisopropylethylamine
BOC_2O	Di-tert-butyl dicarbonate
Pyr	Pyridine
MeCN	Acetonitrile
iBuOCOCl	Isobutyl Chloroformate
HRMS	High Resolution Mass Spectrometry
MW	Microwave
HOMO	Highest Occupied Molecular Orbitals
LUMO	Lowest Unoccupied Molecular Orbital
M.P	Melting point
SDS	sodium dodecyl sulfate
OD	optical density
PBS	Phosphate-buffered saline
ADMET	Chemical absorption, distribution, metabolism, excretion, and toxicity
^{O}C	Degree Celcious

µg	Microgram
µL	Microliter
µM	Micromolar
h	Hours
min	Minutes
H^{1}NMR	Proton nuclear magnetic resonance
C^{13}NMR	Carbon-13 nuclear magnetic resonance

Abstract

Ashly Mohan

Date of Graduation: - August 2026

Universidad Autónoma de Nuevo León

Facultad de Ciencias Químicas

Title: *Design of Oxazine, Oxazoline, and Hydroxyacetamide Derivatives to Optimize Zn^{2+} Binding and Selectivity Toward Histone Deacetylase: In Silico Studies, Synthesis, Characterization, and Anticancer Evaluation of Hydroxyacetamide Derivatives*

Number of pages: 173 **Doctoral candidate of pharmaceutical science**

Area of study: Pharmacy

Research Objectives and Methodology:

My doctoral research focuses on the design, synthesis, and computational evaluation of novel histone deacetylase (HDAC) inhibitors with potential anticancer activity. The study combines medicinal chemistry with *in silico* approaches to optimize Zn^{2+} binding interactions and improve selectivity toward Histone Deacetylase 6 (HDAC6).

A series of heterocyclic and hydroxyacetamide derivatives were designed to explore structure–activity relationships, focusing on zinc coordination and ligand–protein interactions within the catalytic pocket. Molecular docking and molecular dynamics simulations were performed to analyze binding modes, Zn^{2+} coordination patterns, and interaction stability, providing insights into isoform selectivity and the mechanistic differences between the designed scaffolds.

Contribution and Conclusion:

40 heterocyclic and hydroxyacetamide derivatives were designed and subjected to *in silico* evaluation. Among them, 32 heterocyclic compounds and 8 hydroxyacetamide derivatives were investigated through computational studies. Subsequently, the 8

hydroxyacetamide derivatives were synthesized experimentally and evaluated through crystal violet assays. Their anticancer and cytotoxic activities were assessed against MCF-7, PC-3, HCT-15, and HaCaT cell lines. Unfortunately, the compounds did not exhibit anticancer activity against the tested cell lines. Unlike the reference drug Vorinostat, the hydroxyacetamide derivatives showed no cytotoxic effects against any of the evaluated cell lines.

Dr. Francisco Guadalupe Avalos Alanís

Director

Dra. María Del Rayo Camacho Corona

Co-director

CHAPTER 1

1 Introduction

The fundamental units that make up the human body are cells. Cells divide and expand to produce new cells as the body needs them. Cells normally die as they become too old or damaged. Then, in their place, new cells appear. When genetic variations disrupt this orderly mechanism, cancer develops. Cancer is a disease in which cells in a particular part of the body uncontrollably multiply and propagate. Cancerous cells have the ability to invade and kill healthy tissue, including organs. Cancer is the second most common cause of death in the world. Globally, the cancer burden is increasing, putting enormous physical, emotional, and financial pressure on people, families, societies, and health-care systems, which is a major source of income loss. Many health systems in low- and middle-income countries are inadequate to meet this burden. Many cancer patients around the world do not have timely access to high-quality diagnosis and treatment (*Cancer*, n.d.).

The International Agency for Research on Cancer (IARC) has released its GLOBOCAN 2022 cancer incidence and mortality predictions in 185 countries for 36 types of cancer. Worldwide, an estimated 20.0 million new cancer cases and 10.0 million cancer deaths occurred in 2022 (GLOBOCAN 2022). In Mexico, 207,000 cases of cancer are diagnosed annually, of which 96,000 result in death. In the previous year, 747,784 deaths were reported, with malignant tumors accounting for 13% of all deaths (88,683). According to the percentage distribution by gender, women (51%) are more likely than men (49%) to die as a result of this cause.

Despite the fact that the immune system can recognize and kill tumor cells to counteract the effects of cancer cells, a mechanism known as immune surveillance, the immune system cannot always detect and destroy cancer cells. Since the immune response is not always successful, therapeutic strategies to suppress these cells are needed. Currently, there are various treatments; most treatment plans include surgery, immunotherapy, radiotherapy, hormonal therapy, chemotherapy, laser therapy, photodynamic therapy, cryotherapy, or combinations of them. Chemotherapy targets and kills fast-growing cancer cells. Most cancers, including lung cancer, the leading cause of death, are still treated with chemotherapy. Every year, effective cancer control is delayed, the response becomes more costly, the number of preventable deaths rises,

and economic and human growth are suppressed. Lung, skin, prostate, breast, and liver cancers are the most common forms of cancer. Despite continuous pharmacological improvements in the efficacy of anticancer drugs, there is an urgent need for diverse, new, targeted molecules to resolve the problem of drug resistance and boost the potency or reduce the side effects of currently used drugs (Min & Lee, 2022).

1.1 Classification of Histone Deacetylases (HDACs)

Histone deacetylases (HDACs) are enzymes that remove acetyl groups from lysine residues in proteins. In humans, there are eighteen HDACs, which are divided into two distinct families based on their catalytic mechanisms, which are zinc dependent HDACs (HDAC1-11) and NAD^+-dependent sirtuins (SIRT1-7). The zinc depending HDACs act as metalloenzymes that hydrolyze the amide bond using water as a nucleophile, whereas sirtuins require NAD^+ as a cofactor to catalyze deacetylation. Even though both classes catalyze the same acyllysine cleavage reaction, the term "HDAC" commonly used to the zinc-dependent group. These eighteen human HDACs are further classified into four classes based on sequence homology and cellular localization, Class I includes HDAC1, 2, 3, and 8, Class II is subdivided into IIa (HDAC4, 5, 7, 9) and IIb (HDAC6, 10), Class III consists of the sirtuins (SIRT1-7), and Class IV comprises only HDAC11. While this classification does not completely represent the structural and functional differences among HDAC isoforms. Among the HDACs, HDAC1, HDAC2, HDAC3, and HDAC6 show high enzymatic activity toward simple acetylated lysine substrates. As a result, these enzymes are the most extensively studied HDACs. In contrast, the biological functions and substrate preferences of several other isoforms are still not fully understood.(Seto *et al*., 2014).

1.2 HDACs in Cancer: Mechanisms and Consequences

Epigenetics refers to changes in gene expression without altering the DNA sequence. These changes are controlled by mechanisms such as DNA methylation and histone modifications, which control chromatin structure and determine whether genes are turned on or off. These chromatin markers can be maintained in response to environmental, developmental, and pathological factors (Dawson *et al*., 2012). This regulation is essential for normal cellular function. Even though, its disruption, particularly the silencing of genes that control cell growth and death, is a key feature of many diseases, especially cancer. Unlike genetic mutations, epigenetic changes are reversible, making them attractive targets for therapeutic intervention.

HDACs are important elements of the epigenetic system. They are responsible for removing acetyl groups from histones, which influences chromatin structure and regulates gene expression (Ceccacci *et al*., 2016). Their catalytic activity helps to maintain the balance of acetylation within cells. In recent years, HDACs have emerged as promising therapeutic targets, particularly in the fields of neurodegenerative disorders (Chuang *et al.* 2009), genetic diseases (Consalvi *et al.* 2011), and cancer (Barneda-Zahonero *et al*., 2012) (Glozak *et al*., 2007). Small molecules that regulate enzyme activity, such as HDAC inhibitors (HDACi) and histone acetyl transferase activators, can influence HDAC activity and affect cellular acetylation levels. While their primary role was recognized in histone modification, it is now known that HDACs also catalyze the hydrolysis of acetylated lysine residues on nonhistone proteins (Narita *et al*., 2019), including components of transcription factor complexes (H. P. Chen, Y. T. Zhao, and T. C. Zhao, 2015) (Cao *et al*., 2024).

HDACs participate in many cellular processes, including cell differentiation, angiogenesis, and metabolism (Zhao *et al*., 2020; Sweet *et al*., 2012; Molinari *et al*., 2023). Dysregulation of HDAC activity has been linked to several diseases, such as nervous system disorders (Cao *et al*., 2024) (Shukla *et al*., 2020), (L.Y. Zhang *et al*., 2024), cardiovascular diseases (Yu *et al*., 2023), (Bagchi *et al*., 2019), inflammatory

conditions (Shakespear *et al*., 2011), and cancer (Y. Zhang *et al*., 2025), (G. Li, Tian, *et al*., 2020). Understanding the different roles of HDACs in cells is essential for developing effective pharmacological strategies. These approaches aimed at inhibiting or modulating their activity during the onset and progression of various diseases.

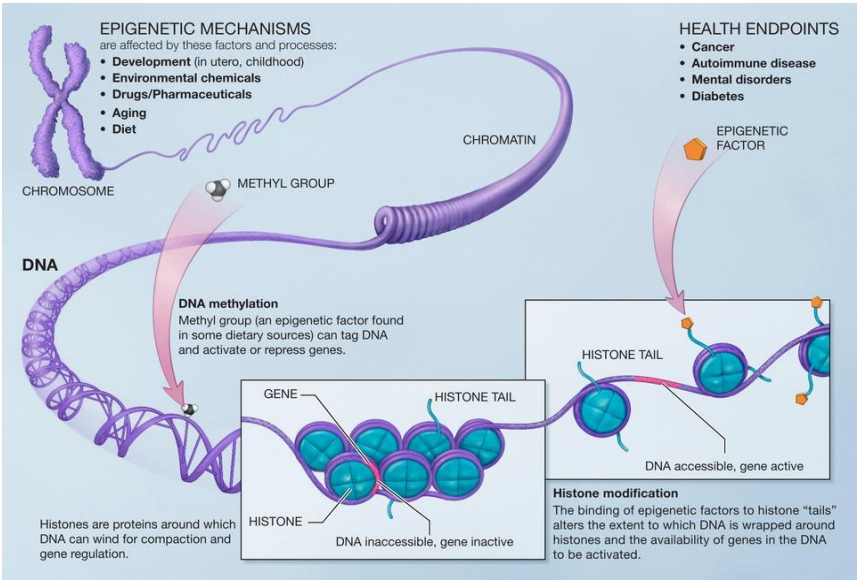

Figure 1.1: Epigenetic Mechanism(https://epi.grants.cancer.gov/epigen/)

The key epigenetic mechanisms (**Figure 1.1**) that control gene expression without modifying the DNA sequence include DNA methylation, histone modification, and non-coding RNAs. DNA methylation involves the addition of methyl groups to cytosine bases, usually at CpG regions. When this occurs in gene promoter regions, it can switch off gene expression. Histone modifications such as acetylation, methylation, and phosphorylation, change the structure of chromatin by changing how tightly DNA is wrapped around histone proteins, thereby influencing the accessibility of genes to the transcription machinery (Aboud *et al*., 2023). Non-coding RNAs, including microRNAs (miRNAs) and long non-coding RNAs (lncRNAs), modulate gene expression at the post transcriptional level by degrading messenger RNA or inhibiting its translation(Ling *et al*., 2013). These mechanisms work together to control gene activity in different cell types and developmental stage. They also respond to environmental and physiological changes (Cavalli & Heard, 2019).

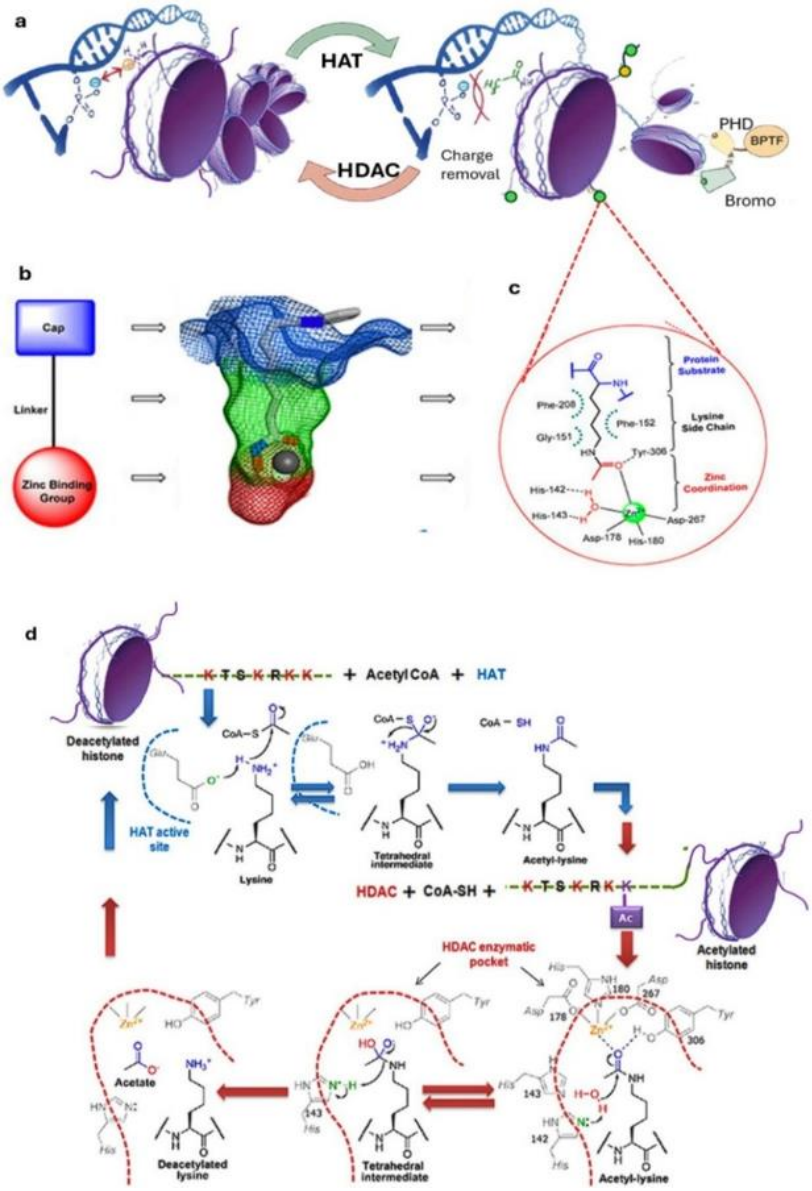

Figure 1.2: (a) Schematic diagram illustrating changes in chromatin structure due to histone deacetylase (HDAC)-catalyzed deacetylation. **(b)** Typical HDAC inhibitor design. **(c)** Representative HDAC-acetyl lysine substrate interactions in an active site. **(d)** Detailed mechanism of the histone acetyltransferase (HAT) and HDAC enzymatic reaction. (*Modified from Sabnam Parbin et al.*)

Histone acetylation is a dominant epigenetic modification that plays a major role in regulating chromatin structure and gene expression. This process (**Figure 1.2**) is

controlled by two opposing enzyme families which are histone acetyltransferases (HATs) and histone deacetylases (HDACs). HAT promotes the addition of acetyl groups to lysine residues on histone tails, which neutralizes their positive charge and reduces the affinity between histones and the negatively charged DNA. This relaxation of chromatin structure results in an open configuration that allows transcriptional machinery to access DNA and activate gene expression. On the other hand, HDACs remove these acetyl groups, leading to chromatin condensation into a closed structure, thereby suppressing gene transcription. The balance between HAT and HDAC activity is essential for normal cellular processes such as cell cycle progression, differentiation, and apoptosis (Peserico *et al*., 2011; X. J. Yang and EHAT Seto, 2007; Gallinari *et al*., 2007). When HDAC activity becomes abnormal, it leads to silencing the tumor suppressor genes. This affects the important functions like cell cycle regulation, apoptosis, and DNA repair, which can contribute to tumorigenesis (Yixuan Li and Edward Seto, 2016) (G. Li, Tian, and Zhu, 2020) (Ropero and Esteller, 2007). Because of this, HDACs are important regulators of cell function and are closely linked to cancer progression.

HDACs can either work alone or as part of large protein complexes such as Sin3, NuRD (Nucleosome Remodeling and Deacetylase), and CoREST (corepressor for element-1-silencing transcription factor) (Asmamaw *et al*., 2024). These complexes are guided to specific genes by transcription factors. Once there, HDACs remove acetyl groups from histones in those gene regions. In cancer, this mechanism becomes dysregulated HDACs are overexpressed, leading to the inappropriate silencing of tumor suppressor genes, including regulation of apoptosis, cell cycle arrest, and DNA repair (Adams *et al*., 2018).

Unlike mutations, epigenetic changes do not alter the DNA sequence and can be reversed. These changes can be influenced by internal signals like aging, cell development, as well as external factors such as diet, stress, toxins, or drugs. This flexibility allows cells to adapt to changing conditions, environments, and developmental signals. (Fardi *et al*., 2018). In cancer, this reversibility is important for treatment. Abnormal epigenetic changes, such as DNA methylation or histone

deacetylation, can sometimes be reversed using drugs called epigenetic therapies. (Castro *et al*., 2023). For example, DNA methyltransferase inhibitors can reactivate silenced genes, while HDAC inhibitors can restore normal gene expression by increasing acetylation levels. These treatments can help "reprogram" cancer cells to behave more normally without changing their DNA. Because of this, epigenetic therapies are considered a promising and potentially less toxic approach for treating cancer.

1.3 HDACs in cancer pathogenesis

In many cancers, HDACs are overexpressed, leading to the silencing of tumor suppressor genes, promotion of cell proliferation, inhibition of apoptosis, and enhanced angiogenesis and metastasis (Ropero & Esteller, 2007).

1.3.1 Cell Cycle Arrest and Cancer Progression

HDACs play an important role in controlling the cell cycle, and loss of HDAC regulation is highly associated with cancer proliferation (Yixuan *et al*., 2016). In healthy cells HDACs regulate gene expression by removing acetyl groups from histones and other proteins. In many cancers, HDACs are over expressed, which leads to uncontrolled cell growth (Liang *et al*., 2023).

A major way HDACs contribute to cancer is by silencing of cell cycle arresting genes including the CDK inhibitors, for example, p21WAF1/CIP1, p27KIP1, and p57KIP2. HDAC1 and HDAC2 bind to the promoter regions of these genes and reduce their expression, which allows cells to continue dividing (Yixuan Li *et.al*, 2016). When HDAC1 or HDAC2 are inhibited, these genes are reactivated and cells stop dividing at the G1 phase (Yamaguchi *et al*., 2010). Similarly, blocking HDAC5 leads to increased p21 and decreased cyclin D1 as well as CDK2/4/6, causing G1 arrest in liver cancer cells (Fan *et al*., 2014). HDACs also affect the transition from G1 to S phase by interfering with the tumor suppressor Rb and E2F proteins. HDAC inhibitors such as Trichostatin A (TSA) can restore Rb activity and cause cell cycle arrest even when Rb

is mutated (Xiao *et al*., 2014). (Tomosugi *et al*., 2012).

HDACs also control later stages of the cell cycle, including the G2/M transition. For example, reducing HDAC1 activity can block cells from completing mitosis and increase cell death (Senese *et al*., 2007). HDAC10 regulates this transition by targeting cyclin A2 through a signaling pathway (Li *et al*., 2015b). HDAC inhibitors such as TSA, SAHA, and valproic acid (VPA) have been found to arrest the cell cycle at the G2/M checkpoint in numerous cancer cells (Juengel *et al*., 2014).

HDAC3 works with mitotic regulators such as Aurora B kinase and is brought to chromatin by AKAP95 and HA95 proteins during mitosis (Li *et al*., 2006). It removes acetyl groups from histone H3, helping chromosomes divide correctly. It also stabilizes cyclin A, a protein required for cell cycle progression from the S phase to mitosis. Inhibition of HDAC3 leads to the hyperacetylation of cyclin A by PCAF/GCN5, which targets cyclin A for degradation and causes cell cycle arrest at S or G2/M phase (Vidal Laliena *et al*., 2013; Bhaskara *et al*., 2008, 2010). Some HDAC inhibitors such as LBH589 cause this arrest by degrading Aurora A and B kinases, particularly in kidney cancer cells (Cha *et al*., 2009). Apart from transcriptional regulation, HDACs also control cell division by non-genetic mechanisms. For example, HDAC2 and HDAC3 modulate the spindle assembly checkpoint (SAC) by deacetylating the checkpoint protein BubR1, which is required for mitosis (Park *et al*., 2017). Sirtuin family members, including SIRT2, play roles in mitosis as well. SIRT2 regulates chromosome separation proteins such as CDC20 and CDH1 and promotes cell movement by deacetylating α-tubulin (Dryden *et al*., 2003; Kim *et al*., 2011; North *et al*., 2003).

HDAC5 has been implicated in upregulating Aurora A kinase by inhibiting the E3 ligase NEDD4, which would otherwise target Aurora A for degradation (Sun *et al*., 2014). Because HDACs affect many parts of the cell cycle, they are important targets for cancer therapy. Combining HDAC inhibitors with other drugs, such as CDK inhibitors, has shown strong effects against cancers like leukemia (Baker *et al*., 2016). Likewise, dual inhibitors such as Roxyl-zhc-84, which inhibit both HDACs and CDKs, potently inhibit cell growth and induce apoptosis in breast and ovarian cancer cells (Huang *et al*., 2018).

HDAC inhibitors also strongly activate tumor suppressor pathways. For example, they increase expression of p21, a CDK inhibitor that blocks cell cycle progression. This happens by increasing histone acetylation at the p21 gene, even when p53 is not functional. (Richon *et al*., 2000; Yoshida *et al*., 1999). In some cases, this involves post translational changes to p53 itself, such as phosphorylation at Thr18 and acetylation at K373/382, which are essential for p21 activation (Wang *et al*., 2012). In liver cancer, the HDAC8 specific inhibitor PCI-34051 has been shown to increase to p21 and cause G2/M arrest (Tian *et al*., 2015). SIRT7 can also indirectly increase p21 by stabilizing p53 (Lu *et al*., 2020). Even in the absence of p21, other inhibitors like p27KIP1 can step in to stop the cell cycle, as seen in lymphoma cells treated with SAHA (Newbold *et al*., 2014). All these findings highlight the potential of HDACs as therapeutic targets because of their involvement in multiple phases of the cell cycle, targeting HDACs can effectively slow down or stop cancer cell proliferation at several key control points.

1.3.1 Apoptosis

HDACs play an important role in regulating apoptosis in many cancer cells by changing the expression level of anti and pro-apoptotic proteins. HDAC inhibitors (HDACi) can induce cell death through both the intrinsic (mitochondria-mediated) and extrinsic (death receptor mediated) apoptotic pathways.

In the extrinsic pathway, HDAC inhibition makes cancer cells more sensitive to TRAIL-induced apoptosis. This occurs through increased expression of death receptors such as DR5 (TRAIL-R2), higher levels of TRAIL and FAS ligand, reduced expression of cytoplasmic FLICE-like inhibitory protein (c-FLIP), and facilitating the assembly of the death-inducing signaling complex (DISC), which results in the activation of caspase-8 (Schuler *et al*., 2010; Riley *et al*., 2013; Zhang and Zhong, 2014). Non-selective HDACi like Vorinostat and Panobinostat can also reduce FLIP expression, further increasing the sensitivity of tumor cells to TRAIL-mediated apoptosis (Bangert *et al*., 2012).

In the intrinsic pathway, HDAC inhibition results in a reduction of anti-apoptotic proteins such as Bcl-2, Bcl-xL, and Mcl-1, while also upregulating pro-apoptotic proteins

such as Bax, Bim, Apaf-1, AIF, PUMA, and BMF (Jung *et al*., 2012; Kim *et al*., 2013; Zhang *et al*., 2006; Kang *et al*., 2014; Feng *et al*., 2013). For example, inhibition of HDAC1 increases the ratio of Bax/Bcl-2, HDAC2 knockdown increases Bax, AIF, and Apaf-1, and suppresses Bcl-2, while inhibition of HDAC3 promote the binding of p53 to the PUMA promoter, resulting in higher PUMA expression (Kim *et al*., 2013; Feng *et al*., 2013). HDAC8, frequently in collaboration with HDAC1, suppresses the transcription of BMF, but its inhibition which using agents such as methylselenopyruvate, results in BMF-mediated apoptosis (Kang *et al*., 2014). HDAC6 also regulates intrinsic apoptosis through the Bax/Ku70 complex. When HDAC6 is inhibited, Ku70 becomes acetylated, releasing Bax and allowing it to initiate mitochondrial apoptosis (Bitler *et al*., 2017).

The role of p53 in HDAC inhibitor-induced apoptosis appears to depend on the cellular context. Some studies suggest that p53 activation is essential, while others show that apoptosis can occur regardless of p53 status (Ellis *et al*., 2009; Bajbouj *et al*., 2012; Sonnemann *et al*., 2014). Overall, HDACi can tip the equilibrium between pro and anti-apoptotic signals, rendering them interesting therapeutic tools for the selective induction of apoptosis in cancer cells.

1.3.1 Metastasis

Epithelial to mesenchymal transition (EMT) is an important process in cancer progression that allows tumor cells to become more invasive and metastatic. One of the main features of EMT is the loss of E-cadherin (CDH1) expression. HDACs contribute to this process by modifying chromatin structure and suppressing gene expression.

Transcriptional repressors such as Snail, ZEB1, and others recruit HDACs to the CDH1 promoter, resulting in the histone H3 and H4 deacetylation and silencing of E-cadherin expression. In prostate cancer cells, Snail forms a complex with HDAC1, and HDAC2 to repress CDH1 expression, thereby promoting EMT, cell invasion, and metastasis (Von Burstin *et al*., 2009). Similar mechanisms have been reported in pancreatic and nasopharyngeal cancers, where Snail/HDAC1/HDAC2 complexes collaborate with

EZH2 to suppress CDH1 transcription (Tong *et al*., 2012). ZEB1 also recruits class I HDACs to the CDH1 promoter in pancreatic cancer cells and contributes to CDH1 silencing through abnormal gene splicing (Aghdassi *et al*., 2012; Liao *et al*., 2013).-

In addition to repressing CDH1, HDACs HDACs also promote metastasis by helping cancer cells invade surrounding tissues. One mechanism involves increasing the expression of matrix metalloproteinases (MMPs), enzymes that degrade the extracellular matrix. In breast cancer cells, overexpression of HDAC1, HDAC6, and HDAC8 increases MMP-9 expression and enhances cellular invasiveness (Li *et.al*, 2016).

1.3.2 Autophagy

Autophagy is a key cellular recycling process that maintains energy balance and removes damaged proteins and organelles, especially under stress conditions (Mizushima *et al*., 2008; Mizushima, 2018). HDACs help regulate autophagy and can either increase or decrease depending on the cell type.

Some HDACs directly support autophagy. For example, HDAC10 supports autophagy flux. When HDAC10 depleted, leads to p62 accumulation, increased LC3-II/I ratio, and heightened sensitivity to cytotoxic agents (Oehme *et al*., 2013). Likewise, SIRT1 promotes autophagy by interacting with autophagy related proteins such as ATG5, ATG7, and ATG8. Loss of SIRT1 results in the accumulation of damaged organelles (Lee *et al*., 2008).

On the other hand, several HDAC inhibitors induce cancer cell death by activating autophagic mechanisms. For example, tenovin-6 is an inhibitor of SIRT1 and SIRT2. It disrupts mitochondrial acetylation, autophagic flux and activates p53. This leads to suppression of the growth of Ewing sarcoma and chronic lymphocytic leukemia cells through the NOTCH signaling pathway. (Lain *et al*., 2008; Ban *et al*., 2014; Yuan *et al*., 2017). SIRT2 also influences autophagy under oxidative stress conditions. Its inhibition causes acetylated FoxO1 to accumulate in the cytoplasm, where it interacts with ATG7 and promotes autophagy (Zhao *et al*., 2010) Several HDAC inhibitors can activate autophagy through major signaling pathways. Valproic acid (VPA) promotes autophagy by suppressing the AKT pathway, whereas SAHA activates autophagy by

inhibiting mTOR signaling (Sun *et al*., 2020; Gammoh *et al*., 2012). Moreover, VPA also impairs DNA repair by promoting autophagic degradation of CtIP, showing the dual nature of autophagy in genome maintenance (Robert *et al*., 2011; Guo and Zhao, 2020)

1.3.3 Angiogenesis

Hypoxia is a common feature in the tumor, where low oxygen levels activate hypoxia-inducible factor 1 alpha (HIF-1α) which is a major protein that promotes the formation of new blood vessels (angiogenesis). The activity and stability of HIF-1α are controlled by several HDACs.

HDAC1 and HDAC4 directly deacetylate HIF-1α at specific residues such as Lys-532. This prevents its ubiquitin-dependent degradation as a result stabilizing the protein(Geng *et al*., 2011; Yoo *et al*., 2006). HDAC5 and HDAC6 promote HIF-1α stability indirectly by deacetylating its helper protein HSP70 and HSP90 (Chen *et al*., 2015; Kong *et al*., 2006). When these HDACs are inhibited, the chaperone proteins become hyperacetylated, which reduces HIF-1α movement into the nucleus and increases its degradation.

HDAC6 has a dual role in angiogenesis. It promotes endothelial movement by deacetylating cortactin, but in some cancers such as hepatocellular carcinoma, it can also reduce blood vessel formation. Taken together, HDACs play complex roles in tumor angiogenesis, making them important potential targets for anti-cancer therapies that aim to block blood vessel growth in tumors (Hubbert *et al*., 2002; Kaluza *et al*., 2011).

1.4 Structural Criteria for HDAC Inhibitor Design

1.4.1 Pharmaceutically accepted structure

Histone deacetylase inhibitors (HDACIs) are important compounds that change gene expression and have potential for treating different diseases. Their basic structure

usually includes three parts, a zinc-binding group (ZBG), a linker, and a cap, which together helps the molecule bind to the target protein. Recent studies suggest an extended pharmacophore model of HDACI (**Figure 1.3**).

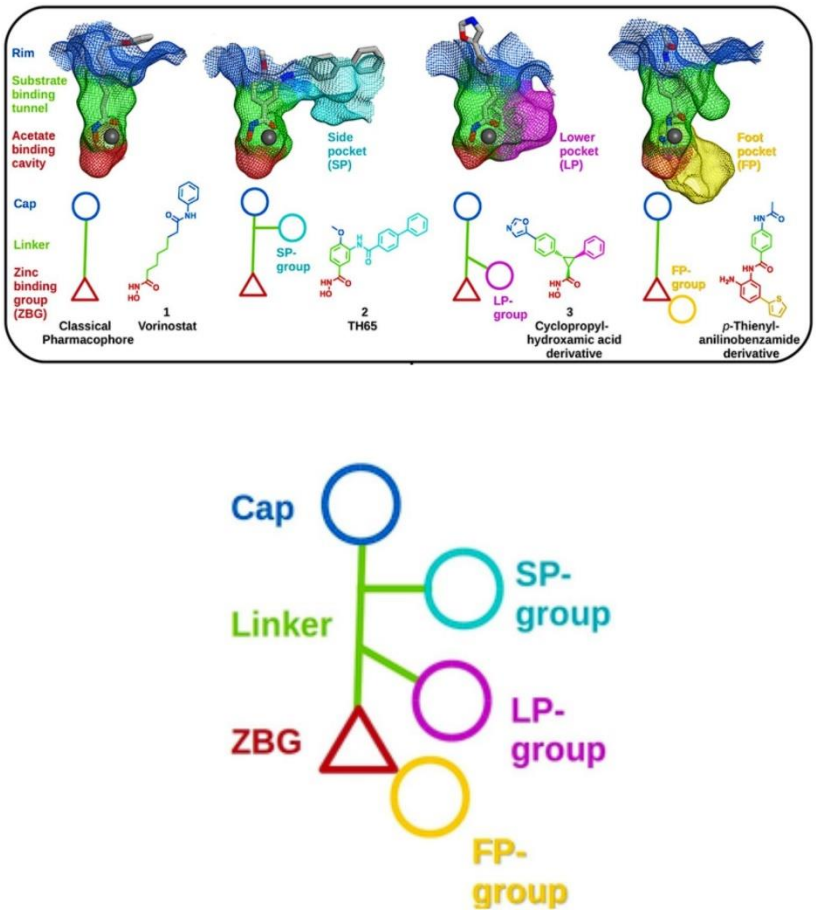

Figure 1.3: Extended pharmacophore model of (HDACi) (Melesina *et al.* 2021).

Catalytic pocket of HDACs, which contains the catalytic zinc ion can be divided into different parts, as shown in **Figure 1.3** The main pocket (A) includes the acetate binding cavity, the substrate binding tunnel, and the rim of the pocket. Additionally, there are sub pockets like the side pocket (B), the lower pocket (C), and the foot pocket (D).
All HDAC crystal structures contain the main pocket, but the sub-pockets may be open or closed depending on the bound ligand and the HDAC isoform. Some HDACs also have an additional pseudo catalytic domain (class IIb HDACs), as well as extra N- or C-terminal regions. For example, HDAC6 contains a unique zinc-finger domain. In

HDAC inhibitor design, the cap and linker regions have been widely studied. However, the ZBG is also very important because it directly interacts with the zinc ion. Hydroxamic acid and benzamide are commonly used by ZBGs, due to their strong ability to bind zinc. However, hydroxamic acid binds zinc very strongly, which can reduce selectivity and also affect other zinc-dependent enzymes, leading to side effects. It also has limitations such as short life and poor bioavailability. Therefore, improving ZBG design, along with optimizing cap and linker regions, is a promising strategy to develop more effective HDAC inhibitors.

1.5 Pan HDACi and Isoform selective HDACi

Histone deacetylase inhibitors (HDACis) are generally classified into pan HDAC inhibitors and isoform selective HDAC inhibitors. Pan HDAC inhibitors, such as Vorinostat and Panobinostat, target multiple HDAC isoforms across different classes (I, II, and IV). Their broad activity can be beneficial in diseases such as cancer, where several HDACs contribute to disease progression (Q. Zhang *et al*., 2019). However, because of their lack of specificity, they leads to higher toxicity and off-target effects.

In contrast, isoform selective HDAC inhibitors, like Ricolinostat (HDAC6 selective) (Vogl *et al*., 2017) and Entinostat (HDAC1/3-selective) (Bae *et al*., 2017), are designed to target specific HDAC isoforms. This provides precise therapeutic approach with reduced side effects. They are useful in diseases where a specific HDAC isoform plays a major role, such as certain cancers and neurological disorders (Gediya *et al*., 2021). Selective HDAC inhibition has several advantages over pan-HDAC inhibition. It targets only disease related HDAC isoforms and avoiding those needed for normal cell function, selective inhibitors reduce off-target effects. As a result, they may cause fewer dose-limiting toxicities, such as fatigue, gastrointestinal problems, and hematological side effects (Bieliauskas and Pflum, 2008).

1.5.1 HDAC6 isoform Selective inhibitors

Inhibition of class I HDACs has been linked to toxic side effects, which limits the use of

broad-spectrum and class I–selective inhibitors outside of cancer treatment due to a limited safety range. However, some studies suggest that class I HDAC inhibitors may also be useful in treating neurodegenerative diseases. In contrast, the toxicity of class II–selective HDAC inhibitors is not well understood because of limited clinical data, which may lead to unclear conclusions. Nevertheless, inhibiting class II HDAC isoforms seems to be less toxic compared to class I isoforms suggesting that selective inhibition may help reduce side effects (Yixuan Li and Edward Seto, 2016).

Structurally, HDAC6 has two catalytic domains and a C-terminal zinc-finger domain that binds ubiquitinated proteins, allowing it to function in several cellular pathways (Ran and Jun Zhou, 2019). Although α- tubulin acetylation is commonly used as a biomarker for HDAC6 inhibition, this does not always directly relate with biological activity (Asthana *et al*., 2013).

HDAC6 is a unique member of the HDAC family because it is mainly found in the cytoplasm and acts on several non-histone proteins such as α-tubulin, HSP90, and cortactin. It plays important roles in protein quality control, cell movement, and immune responses. Because of these functions, HDAC6 has become an important target for treating cancer, neurodegenerative disorders, and inflammatory diseases.

Selective inhibition of HDAC6 can provide therapeutic benefits while reducing the side effects seen with non-selective HDAC inhibitors. Compounds such as Ricolinostat (ACY-1215) and Tubastatin A are designed to specifically target HDAC6 and show anticancer, anti-inflammatory, and neuroprotective effects (Huang *et al*., 2024). Ricolinostat is the first oral HDAC6-selective inhibitor tested in clinical trials, mainly for multiple myeloma and lymphoma. It increases α-tubulin acetylation without significantly affecting histone acetylation, confirming its selectivity (Vogl *et al*., 2017).

Under specific conditions, HDAC6 has been observed in the nucleus, where it coexists with the ligand-dependent corepressor (LCoR) in estrogen responsive MCF-7 cells and suppresses the transactivation of estrogen-responsive reporter genes (Palijan *et al*., 2009), indicating a potential role in epigenetic regulation. Ongoing research continues to study HDAC6 in cancer, autoimmune diseases, and neurodegenerative disorders, both as a single treatment target and in combination with other therapies.

1.6 Types of HDACis

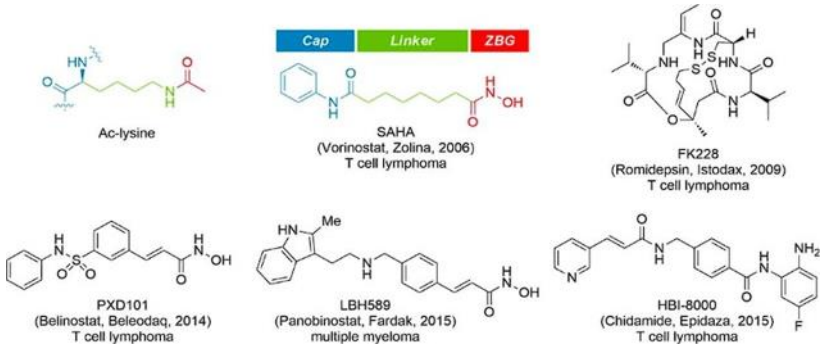

Figure 1.4: FDA approved HDACi (M. A. Choi *et al*., 2019).

HDACis (**Figure 1.4**) are classified based on their chemical structures into several types, including hydroxamic acids, cyclic peptides, benzamides, and short chain fatty acids. Hydroxamic acids, such as suberoylanilide hydroxamic acid (SAHA or Vorinostat), act by chelating the zinc ion at the HDAC active site. They represent one of the most potent HDACi (Marks *et al*., 2001).

Cyclic peptides, such as Romidepsin, derived from natural bacterial products, inhibit HDACs by binding to their active sites in a unique way (Falkenberg *et al*., 2014). Benzamides, such as Entinostat, selectively block class I HDACs and are under clinical trials for various cancers. Short-chain fatty acids like valproic acid are weaker inhibitors, but they are clinically important due to their safety and ability to induce cancer cell differentiation and apoptosis (West *et.al*, 2014). Among these, SAHA (Vorinostat) and Romidepsin are approved by the FDA for treating blood cancers, including cutaneous T-cell lymphoma and peripheral T-cell lymphoma. They show good clinical effectiveness (Falkenberg *et.al*, 2014; Marks *et al*., 2001).

1.6.1 Computational Studies in Drug Synthesis

The drug discovery process is a significant part of modern biomedical research. It aims

to find new therapeutic agents to treat different diseases. Traditional drug discovery takes a long time and costs a lot. It often takes up to 14 years and costs around $800 million USD for a single successful drug (Spedding, 2006). Recent studies show that the cost varies widely. Schlander *et al*., 2021, estimated costs between $161 million USD and $4.54 billion USD, especially high for anticancer drugs. Rennane *et al*., 2022, reported drug costs per day from $113 million USD to over $6 billion USD, narrowing to between $318 million USD and $2.8 billion USD for new molecular entities (NMEs). These reports show that drug development is very costly and highly variable. Even with improvements such as combinatorial chemistry and high-throughput screening (HTS), the number of approved drugs has not increased much. One major problem is that unsuitable compounds are often identified too late, which leads to expensive failures in later stages.

To solve these problems, researchers now use computer-based drug discovery methods. This approach combines *in silico* modelling, chemical synthesis, and biological testing to make the process faster and more efficient (Niazi and Mariam, 2023) (Parasrampuria, *et al*, 2018). *In silico* drug design, also called computer aided drug design (CADD), is an important part of early drug development. It uses computer tools to store, analyze, and simulate chemical and biological data. These tools include chemical databases, compound libraries, and models that predict activity, toxicity, and drug-likeness. Over the years, CADD has grown to include method such as homology modelling, QSAR, virtual screening, and molecular dynamics (MD) simulations. These methods have improved due to advances in cheminformatics, bioinformatics, and structural biology (Van *et al* 2017).

CADD methods are mainly divided into Structure-Based Drug Design (SBDD) and Ligand-Based Drug Design (LBDD). SBDD depends on the three-dimensional structure of the target protein, which is determined using techniques like X-ray crystallography or NMR spectroscopy (Jhoti *et al*., 2007). When the structure is not available, homology modeling is used to predict it. Common methods in SBDD include docking calculations and molecular dynamics (MD) simulations. These methods start by finding potential binding sites or active sites on the target surface. They consider

specific features such as hydrogen donors and acceptors, hydrophobic properties, and size (Ferreira *et al.* 2015). SBDD helps us understand how a molecule's orientation interacts with a biological target. This gives an idea about the important pharmacophoric properties that contribute to therapeutic effects. On the other hand, LBDD uses knowledge about small molecules binding on the target. Normally, researchers combine SBDD and LBDD because they effectively support each other. LBDD methods include techniques such as molecular similarity approaches, quantitative structure-activity relationship (QSAR) methods, and pharmacophore modelling. These techniques come with tasks like virtual screening (VS) to identify similar compounds to a molecule of interest. Then discovering molecules with pharmacological properties, and refining compounds through hit-to-lead (H2L). The use of these various CADD techniques improves drug discovery processes, making them more efficient and effective (Lin *et al* 2022).

Combining these computational methods helps identify promising drug candidates at an early stage and allows for predicting ADME/Tox profiles like absorption, distribution, metabolism, excretion, and toxicity. These evaluations are crucial for eliminating unsuitable compounds early, which reduces the risk of failure in costly preclinical or clinical stages(Kumar *et al*., 2026).

1.6.2 Structure-based drug design (SBDD)

Understanding computer-based drug discovery requires knowing how structure-based drug design (SBDD) and Ligand-Based Drug Design (LBDD) works together. Rather than following only one method, modern drug discovery often combines both methods to improve the chances of finding effective drug candidates. The choice of method can depend on the availability of structural data. Using both SBDD and LBDD together makes the process more efficient (Vázquez *et al*., 2020).

A major part of this process is virtual screening. This technique allows for quick evaluation of large molecular libraries to find compounds that might have biological activity. Virtual screening can use either structure based or ligand-based methods. Ligand based methods, such as molecular similarity screening, compare new compounds to

known active ligands. Pharmacophore mapping is another method that identifies the important chemical features needed for a compound to interact with a target protein. The similarity property principle suggests that structurally similar molecules have similar biological activities. This idea supports many ligand-based screening methods (Gimeno *et al.* 2019).

Molecular docking is another commonly used method that predicts how small molecules bind to proteins. Docking methods simulate the orientation and binding affinity of a ligand in a protein's active or allosteric site (Ferreira *et al.,* 2015). Docking has been used since the early 1980s and is now a major tool in computer-aided drug design. However, traditional rigid docking does not fully consider protein flexibility. To solve this problem, several flexible docking methods have been developed. These methods allow changes in ligand shape and some flexibility in the protein. Ensemble docking uses multiple protein structures from experiments to improve accuracy (Meng *et al.,* 2011). When the binding site is unknown, blind docking techniques are used. The blind docking method looks for possible binding sites on the entire protein surface, such as active pocket (Liu *et al.*, 2019). After identifying these areas, docking simulations help to determine the best binding poses.

Proteins are not fixed structures; they move and change shape during their function. Molecular dynamics (MD) simulations help study these movements and show how proteins and ligands interact over time. These simulations model the physical motions of atoms and molecules based on Newton's laws. MD simulations use physics-based models to track the motion of atoms. Advanced methods such as steered MD (SMD), targeted MD (TMD), and accelerated MD (AMD) help study rare events and longer time scales. One significant result of MD simulations is the binding free energy of a ligand target complex. Binding free energy indicates how thermodynamically favorable interaction is. It is usually calculated using methods like Molecular Mechanics-Generalized Born Surface Area (MM-GBSA). These calculations, which average free energy contributions from MD trajectories. This gives a more realistic estimate of binding strength than docking alone and is widely used for ranking compounds. In summary, using virtual screening, molecular docking, and MD

simulations gives us powerful tools for drug discovery. These methods make target identification and compound optimization more precise. They also reduce experimental cost and time by focusing on the best candidates for further testing.

1.6.3 Ligand-based drug design (LBDD)

LBDD is a computational approach used to identify biologically active compounds by studying known ligands that interact with a specific biological target. It is based on the idea that molecules with similar structures often show similar biological activities, which is known as the similarity property principle.

Unlike SBDD, which needs the 3D structure of target, LBDD can be used when the protein structure is unknown. It uses information from known active compounds to design new molecules with improved selectivity and drug-like properties (Kandakatla and Ramakrishnan, 2014). Common LBDD methods include quantitative structure-activity relationship (QSAR) modelling, pharmacophore modelling, and similarity-based virtual screening. Compared with SBDD, LBDD is faster and more cost-effective when a large amount of ligand data is available but structural information about the target is limited. LBDD plays an important role in the early stages of drug discovery like hit identification, scaffold hopping, and lead optimization. The availability of large public databases such as ChEMBL, PubChem, and BindingDB has increased the usefulness of LBDD by providing access to biological activity data. Furthermore, recent advancements in machine learning and AI have improved the ability of these models. (Lo *et al*., 2018).

Several computational methods are used in this approach. One of the most used techniques is QSAR modelling. It builds the mathematical relationships between molecular properties and biological activity, which allows researchers to predict the activity of new compounds. Modern QSAR methods use machine learning algorithms to improve prediction accuracy (Cherkasov *et al*., 2014). Another important technique is pharmacophore modelling. It identifies the chemical features which is necessary for a molecule to interact with a biological target, such as hydrogen bond donors, hydrogen bond acceptors, hydrophobic regions, and aromatic rings. These pharmacophore

models can then be used to screen large chemical libraries and identify new compounds with similar features (Schuster *et al*., 2006). Similarity searching method compares candidate molecules to known active ligands using 2D or 3D molecular fingerprints and selects compounds with the highest structural similarity. (Willett, 2006). The use of machine learning and AI has improved LBDD. Techniques such as support vector machines, random forests, deep neural networks, and graph-based learning can analyze large datasets and predict biological activity, ADMET properties, and drug-likeness more accurately (Lo *et al*., 2018).

Conventional histone deacetylase (HDAC) inhibitors usually follow a standardized pharmacophore design, that consists of a cap group, a linker, and a zinc binding group (ZBG) that interacts with the catalytic zinc ion within the HDAC active site. While this design has been the cornerstone of many successful HDAC inhibitors, new non-traditional design has also begun to gain attention for their novel inhibitory profiles. In this study, we investigate non-classical HDAC inhibitor scaffolds by focusing on two distinct classes of compounds (1) oxazoline and oxazine derivatives as ZBG and (2) Hydroxyacetamide as a ZBG. Oxazolines and oxazines have previously reported anticancer activity but remain largely unexplored as HDAC zinc-binding motifs. Similarly, hydroxyacetamide derivatives were also investigated because, despite showing promising anticancer activity, their potential role as HDAC-targeting ZBGs has not been thoroughly examined.

These molecules were first analyzed using computational methods to study their possible interaction with the HDAC zinc ion. Selected hydroxyamide derivatives were then synthesized and tested in biological assays to evaluate their inhibitory activity against cancer cells lines. The aim of this work is to find out whether these alternative scaffolds can effectively interact with the HDAC active site and show as a basis for new HDAC-targeted drugs.

Molecular docking, molecular dynamics simulations, and binding free energy analyses were used to evaluate the binding modes, stability, and selectivity of the designed compounds toward HDAC. The synthesized hydroxyacetamide derivatives were characterized using NMR spectroscopy and high-resolution mass spectrometry

(HRMS). Their biological activity was assessed against cancer cell lines using the crystal violet assay. These studies provide insight into the suitability of these alternative zinc-binding motifs for the development of novel HDAC6-targeted inhibitors.

CHAPTER 2

2 Background

This chapter provides an overview of previous studies on histone deacetylases (HDACs), their structural and biological functions, and the development of HDAC inhibitors. It also highlights the importance of *in silico* approaches and synthetic strategies in designing and developing bioactive amide derivatives. In addition, this chapter outlines the rationale for the selection of Histone Deacetylase 6 as the target isoform and the choice of appropriate zinc-binding groups (ZBGs) for the development of novel HDAC inhibitors. Furthermore, the review further identifies research gaps that justify the present study on the design, synthesis, and biological evaluation of potential HDAC inhibitors.

HDACs possess a catalytic site that contains a zinc ion (Zn^{2+}) essential for their deacetylase activity. Inhibitors targeting HDACs typically include a zinc binding group (ZBG) capable of chelating this metal ion, thereby blocking the catalytic function. Conventional ZBGs are designed to mimic the natural interaction of the substrate's acetyl group with the zinc center. The most mostly used conventional ZBGs in HDAC inhibitors include (Zhang *et al*., 2018):

1. Hydroxamic acid (-CONHOH): the most common and potent ZBG, forming a bidentate coordination with Zn^{2+}.
2. Carboxylic acid (-COOH): binds monodentately or bidentately, found in short-chain fatty acid inhibitors like valproic acid.
3. Thiols (-SH): strong Zn^{2+} chelators but less commonly used due to instability and toxicity.

Among these, hydroxamic acid remains the most effective and widely studied ZBG due to its strong zinc affinity and presence in several approved HDAC inhibitors such as Vorinostat (SAHA) and Trichostatin A (TSA). The most common zinc binding groups found in pharmaceutically approved HDAC inhibitors are summarized in **Table 2.1**.

Table 2.1 Pharmaceutically approved and investigational HDAC inhibitors classified by their Zinc Binding Group (ZBG).

No	Compound	ZBG class	HDAC class	IC_{50} (nM/μM)	Reference
1	Vorinostat (SAHA)	Hydroxamic acid	Class I, II	HDAC1= 10nM HDAC3= 20 nM	(Hrzenjak *et al*., 2010)
2	Belinostat (PXD101)	Hydroxamic acid	Pan-HDAC	HDAC1≈ 27nM	(Plumb *et al*., 2003)
3	Panobinostat (LBH589)	Hydroxamic acid	Class I, II, IV	HDAC1≈ 5nM	(Scuto *et al*., 2008)
4	Ricolinostat (ACY-1215)	Hydroxamic acid	HDAC6 selective	HDAC6 = 5 nM HDAC1 = 58 nM	(Santo *et al*., 2012)
5	Entinostat 275)	Benzamide	Class I (HDAC 1,2,3)	HDAC1=0.51μM; HDAC3 = 1.7μM	(Connolly, Rudek, and Piekarz, 2017)
6	Chidamide	Benzamide	HDAC1, 2, 3, 10	0.25–1μM	(Ning *et al*., 2012)
7	Romidepsin (FK228, Istodax®)	Thiol (cyclic disulfide pro drug)	Class I (HDAC1, 2)	HDAC1= 36nM; HDAC2= 47nM	(Sequera *et al*., 2025)
8	Valproic acid, Butyric acid, Phenyl butyrate	Carboxylic acid	Weak pan-HDAC inhibition	0.3–3 mM	(Kusaczuk.*et al*., 2015)

2.1 Hydroxamic acid

Hydroxamic acid (–CONHOH) is broadly used ZBG in HDACIs. It exhibits a strong affinity for the catalytic Zn^{2+} ion in the HDAC active site through a bidentate interaction (**Figure 2.1B**), ensuring high inhibitory potency and broad activity. Because of its strong zinc coordination ability, hydroxamic acid has been employed in several clinically relevant HDAC inhibitors, such as TSA and SAHA. Most current HDAC inhibitors in clinical trials are hydroxamate-based analogs, due to their simple synthesis, good solubility, and stable behavior in laboratory conditions (Shirbhate *et al*., 2025). It can also bind the Zn^{2+} ion in a monodentate manner, as shown in **Figure**

2.1B.

Despite these advantages, hydroxamic acids also have several limitations. They generally lack isoform selectivity and act as pan-inhibitors (Luo *et al*., 2020). Their strong ability to bind metals can also affect other zinc-dependent enzymes such as aminopeptidases, matrix metalloproteinases (MMPs), and carbonic anhydrases, leading to off-target effects. Furthermore, hydroxamic acid, based inhibitors shows poor pharmacokinetic properties, rapid metabolic activity, short plasma half-life, and hydrolytic conversion into the corresponding carboxylic acids, which undergo phase II conjugation metabolism.

Another significant drawback is the possible toxicity, such as genotoxicity and mutagenicity associated with the Lossen rearrangement mechanism (**Figure 2.1A**) (Friedrich *et al*., 2020). The deprotonated hydroxamate intermediate can form reactive isocyanate derivatives that may bind to DNA and cause cellular damage (Shen *et al*., 2015).

To overcome these issues, researchers are exploring modifications in the cap and linker regions or developing alternative zinc-binding groups such as benzamides, hydrazides, thiols, and ketones. These methods aim to improve selectivity, metabolic stability, and safety of HDAC inhibitors (Milazzo *et al*., 2020).

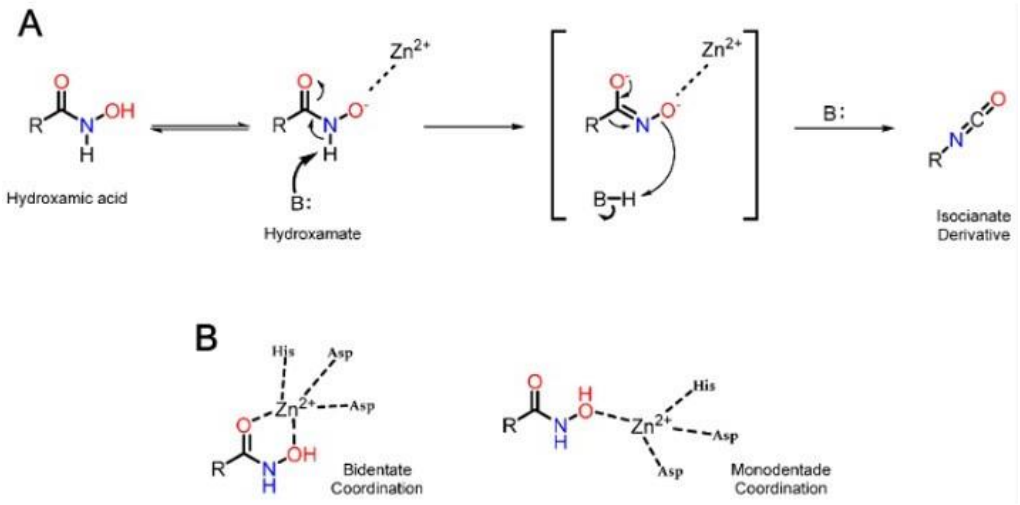

Figure 2.1 (A) Formation of isocyanate derivatives by Lossen rearrangement. **(B)** Form of monodentate and bidentate complexation of hydroxamates with Zn^{2+}. (Pires *et al.*, 2025).

2.2 Benzamide

Benzamide derivatives represent an important class of histone deacetylase inhibitors (HDACIs) characterized by their superior Class I HDAC selectivity compared to hydroxamic acid-based inhibitors. Structurally, benzamide coordinates with the catalytic zinc ion through its amino group, while the carbonyl oxygen maintains a longer distance (greater than 2.5 Å), resulting in weaker metal interaction but enhanced isoform selectivity. This selective binding contributes to reduced off target effects and improved safety profiles (Frühauf *et al.*, 2021). Several benzamide-based HDACIs have demonstrated clinical potential, including Chidamide (Epidaza) (X. Lu *et al.*, 2016) approved by the Chinese Food and Drug Administration (CFDA) for treating relapsed or refractory peripheral T-cell lymphoma along with MS-275 (Entinostat) and MGCD0103 (Mocetinostat) (Boumber *et al.*, 2011), both selective for HDAC1 and HDAC2 and under investigation for hematologic and solid tumors (Banik *et al.*, 2019). Another derivative, CI-994 (Tacedinaline), has shown promising activity in clinical trials. The principal advantage of benzamide derivatives lies in their high isoform selectivity, which minimizes side effects and enables their use as molecular probes to study specific HDAC isoforms involved in disease processes. However, these

compounds also have limitations, including relatively modest therapeutic efficacy, potential in vivo toxicity from the exposed amino group, and the risk of drug resistance due to their narrow target range. Furthermore, their weaker zinc chelation compared to hydroxamates may contribute to reduced potency. Despite these challenges, benzamide-based HDACIs continue to be valuable scaffolds in the development of selective and safer HDAC targeted therapeutics. Ortho-aminoanilides, a benzamide-based class of zinc binding groups, are widely studied in HDAC inhibitor design and show higher selectivity for class I HDACs (1, 2, 3) than hydroxamic acids. Their aromatic ring allows further substitution, and bulky para groups enhance HDAC1/2 selectivity and enable bidentate coordination (**Figure 2.2B**). Two representatives of these inhibitors are entinostat also known as MS-27-275, and tucidinostat (**Figure 2.2A**) (Li *et al.*, 2015).

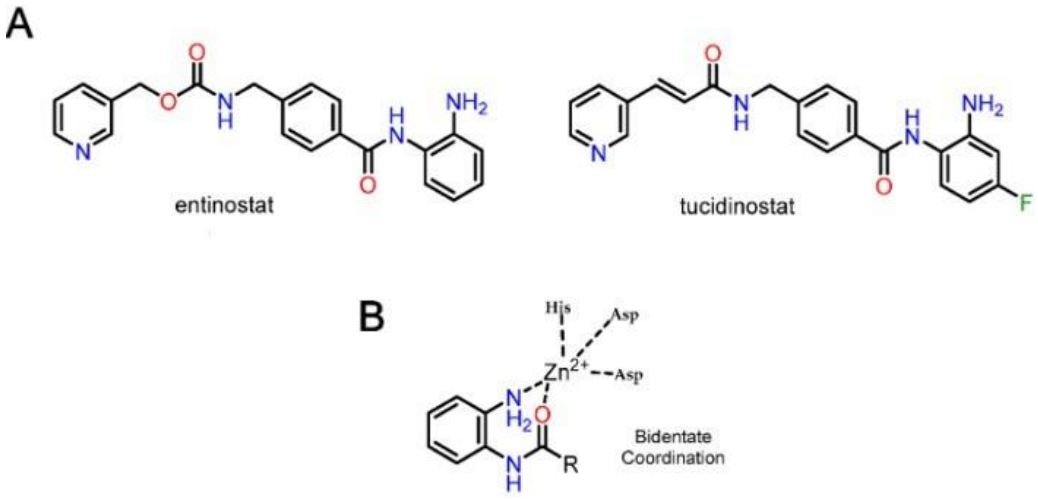

Figure 2.2: (A) Chemical structure of entinostat and tucidinostat. **(B)** Form of bidentate complexation of ortho-aminoanilides with Zn^{2+} (Pires *et al.*, 2025).

2.3 Carboxylic acid

Carboxylic acid derivatives constitute a relatively small class of histone deacetylase inhibitors (HDACIs). Due to their relatively weak zinc ion (Zn^{2+}) binding affinity,

short-chain fatty acids have received less attention than inhibitors containing conventional zinc binding groups such as hydroxamic acids or benzamides. These compounds typically coordinate the catalytic zinc ion in a monodentate manner through carboxylate oxygen (**Figure 2.3B**). Representative short chain fatty acids, including valproic acid, butyric acid (**Figure 2.3A**), and phenylbutyrate, have nonetheless been investigated in clinical trials as histone deacetylase inhibitors. However, these compounds demonstrated relatively low inhibitory potency, with IC_{50} values in the millimolar range, as indicated by *in vitro* enzymatic assays (L. Zhang *et al*., 2018). Despite their weak inhibition profile, the therapeutic and commercial potential of these derivatives continues to be explored, with clinical data suggesting possible applications in tumor treatment.

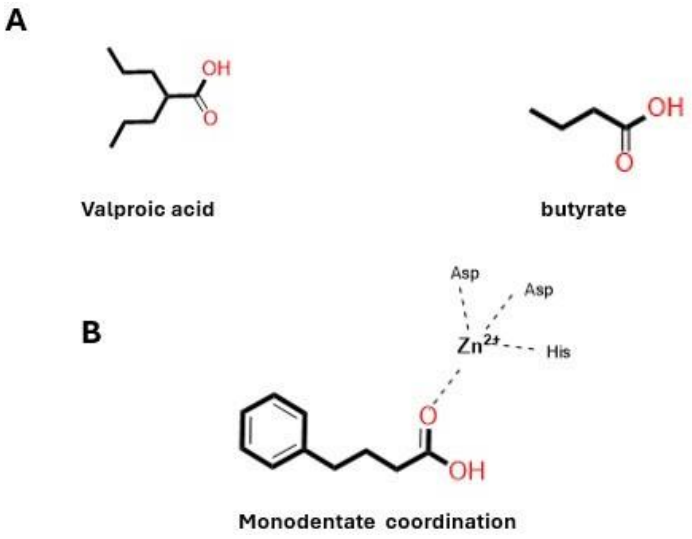

Figure 2.3: (A) Chemical structure of Valproic acid and butyrate (B) Form of monodentate complexation of Benzenebutyric acid with Zn^{2+}.

2.4 Thiols

Thiol (-SH) groups, also known as sulfhydryl groups, represent a strong class of zinc binding moieties widely utilized in metalloprotein-targeted drug design due to their high affinity toward divalent metal ions. A classic example is Captopril, an angiotensin-converting enzyme inhibitor, which demonstrates effective Zn^{2+} chelation through a thiol group (Zheng *et al*., 2022). In the field of histone deacetylase inhibitors

(HDACIs), the first natural compound approved by the U.S. Food and Drug Administration (FDA), FK228 (Romidepsin), incorporates a latent thiol functionality. FK228 is a prodrug that undergoes glutathione-mediated reduction to generate an active thiol form, which subsequently coordinates the catalytic zinc ion within the HDAC active site, leading to potent enzyme inhibition. Inspired by this mechanism, several synthetic thiol-based HDACIs have been developed via structural modification of established scaffolds such as SAHA (Vorinostat) or by de novo molecular design. Despite their promising *in vitro* potency, none of these thiol derivatives have progressed to clinical evaluation to date. Largazole is a marine-derived natural product that's another example of a thiol-containing drug (**Figure 2.4**), demonstrating strong inhibitory activity against class I HDAC isoforms (HDAC1, HDAC2, and HDAC3) at nanomolar IC_{50} levels, while displaying substantially lower potency toward class II isoforms (Hong et.al, 2012).

The thiol group provides strong Zn-S chelation, ensuring robust inhibition; however, these same property limits isoform selectivity, as thiols exhibit minimal differentiation between various HDAC active sites. Consequently, the selectivity of thiol-containing HDACIs must be achieved primarily through structural optimization of the linker and capping regions rather than modification of the ZBG itself. Moreover, thiols can present safety and stability concerns, including off target metal binding to other metalloproteins and oxidation to disulfides, potentially reducing *in vivo* stability and increasing systemic toxicity (Zhang *et al*., 2018). Therefore, while thiol-based ZBGs contribute to strong zinc chelation and potent HDAC inhibition, their lack of isoform selectivity, chemical reactivity, and potential for off target interactions remain significant limitations that have hindered their clinical advancement.

A

Figure 2.4: Chemical structure of Largazole activated form.

The drawbacks of conventional zinc binding groups have encouraged the development of novel chemotypes that offer better selectivity, potency, and pharmacological performance. Although none of the HDACIs with novel ZBG has gained access to clinical trial currently, such investigations guaranteed the rise of new generations of HDACIs with improved pharmacological and pharmacokinetic profiles.

2.4.1 Unusual Zinc Binding Group

Recent studies have highlighted the alkylated hydrazide moiety as a promising new zinc binding group in HDAC inhibitor design (**Figure 2.5**). Several studies have identified hydrazides bearing n-propyl or n-butyl chains as promising scaffolds for HDAC inhibition. For instance, Xiaoyang Li *et al.* reported a series of hydrazide-containing, class I-selective HDAC inhibitors derived from Panobinostat, among which compound one showed exceptional potency, achieving picomolar to low-nanomolar IC_{50} values against HDAC1 and HDAC3 and exhibiting distinct toxicity profiles across cancer cells with different FLT3 and p53 backgrounds. Specifically, one inhibited HDAC1 and HDAC3 with IC_{50} values of 5.17 and 0.95 nM respectively but showed much weaker activity toward HDAC8 (IC_{50} = 1.75 μM) (X. Li *et al.*, 2020). Supporting the therapeutic relevance of this ZBG, Yunfei Wang and co-workers reported a benzoyl hydrazide scaffold exhibiting strong selectivity toward class I HDACs. Their lead compound (two) showed potent inhibition of HDAC1 and HDAC3 with IC_{50} values of 460 and 190 nM, respectively, and inhibited the proliferation of HCT116 colon cancer cells with an IC_{50} of 0.46 μM (Y. Wang *et al.*, 2015). Complementing these findings, Jesse J. McClure and colleagues designed a series of potent and selective class I HDAC inhibitors featuring a hydrazide motif that is resistant to glucuronidation and acts through an allosteric mechanism. Their most active analogue, compound three, exhibited extremely potent inhibition of HDAC3 (IC_{50} = 0.28 nM) and HDAC1 (IC_{50} = 4.69 nM) while maintaining selectivity over HDAC8 (IC_{50} = 1755 nM). In addition, the compound demonstrated antiproliferative activity in acute myeloid leukemia models (IC_{50} = 0.95 μM) along with favourable pharmacokinetic properties (McClure *et al.*, 2016). These results further support hydrazide-based zinc-binding groups as promising alternatives to hydroxamic acids in HDAC inhibitor development.

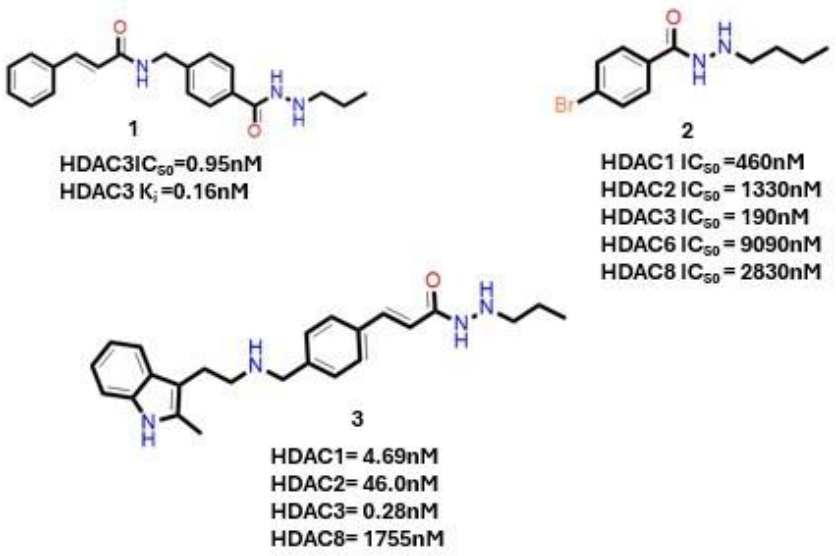

Figure 2.5: Alkyl-hydrazide-based zinc binding group.

A novel addition to non-hydroxamate zinc-binding motifs is the thione-based scaffold (**Figure 2.6)**. An imidazolethione-containing compound (compound four) was identified through an enzyme-based screening strategy and exhibited selective inhibition of HDAC8 ($IC_{50} \approx 500$ nM) over HDAC1 and HDAC3 ($IC_{50} > 10{,}000$ nM). The imidazolethione motif is proposed to coordinate with the catalytic zinc ion and therefore represents a promising zinc-binding group for the development of selective HDAC inhibitors (Hu *et al*., 2003).

Additionally, Vishal Patil and colleagues identified 3-hydroxypyridin-2-thione (3-HPT) (compound five) as a non-hydroxamate zinc-binding group capable of supporting HDAC inhibition. This scaffold inhibited HDAC6 and HDAC8 with IC_{50} values of 681 nM and 367 nM, respectively. Further structural optimization produced several 3-HPT-based HDAC inhibitors, including compound 6, which displayed improved potency toward HDAC6 ($IC_{50} = 306$ nM) while showing weaker activity against HDAC8 ($IC_{50} = 3105$ nM) (Patil *et al*., 2013).

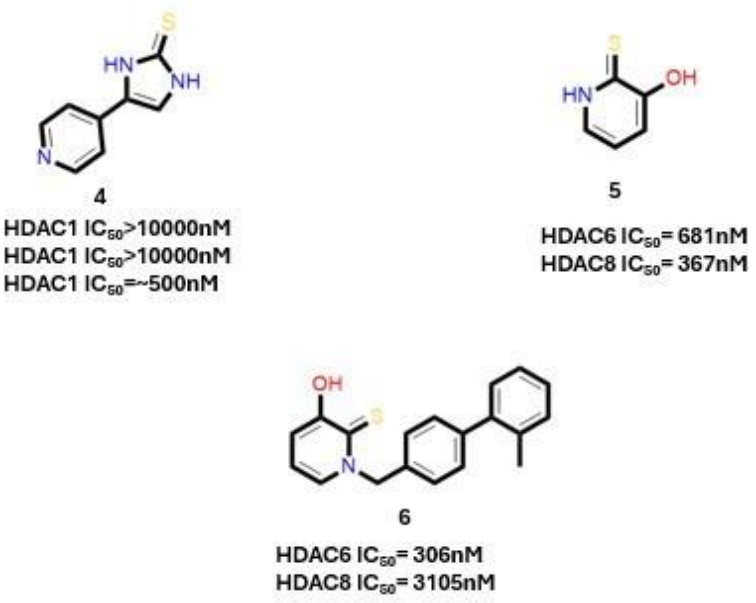

Figure 2.6: Thione-based derivative as a novel zinc binding group.

Likewise, Wu and colleagues developed 2-(oxazol-2-yl) phenol as a novel non-hydroxamate zinc-binding group capable of generating HDAC inhibitors. A series of analogues incorporating this motif were synthesized, several of which showed inhibitory activity toward class I HDACs and class IIb isoforms such as HDAC6 and HDAC10. Among these, compound seven (**Figure 2.7**) demonstrated measurable inhibition at 20 μM, producing 61%, 54%, 62%, and 47% inhibition of HDAC1, HDAC2, HDAC6, and HDAC10, respectively. Furthermore, this compound exhibited moderate antiproliferative activity against the MV-4-11 leukemia cell line with an IC_{50} of 7.5 μM, indicating its cellular activity (Zhou *et al*., 2015).

In a related study, Youxuan Li and Patrick M. Woster introduced a β-hydroxymethyl chalcone derivative (compound 8) as another non-hydroxamate HDAC inhibitor scaffold. This compound showed moderate inhibitory activity against HDAC1 (IC_{50} = 3680 nM) and HDAC2 (IC_{50} = 9190 nM) while displaying very weak inhibition of HDAC3 (IC_{50} > 50,000 nM). These findings further highlight chalcone-derived structures as emerging scaffolds for the development of alternative zinc-binding motifs in HDAC inhibitor design. A reaction mechanism-based pattern was proposed in the binding of the derived inhibitor

to zinc ion by intramolecular cyclisation which was catalysed by the zinc atom. (Jingwei Zhou *et al*., 2015).

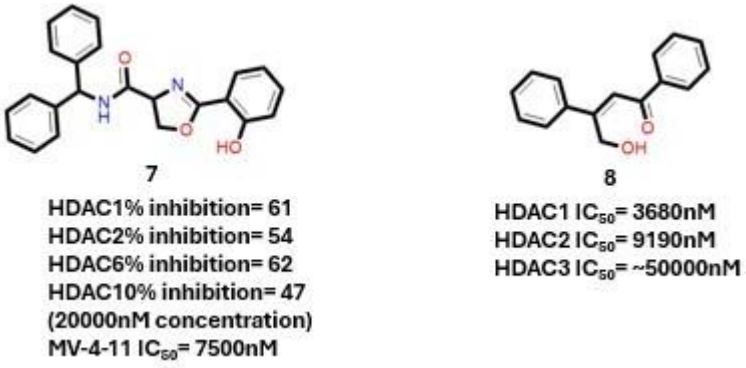

Figure 2.7: Chalcone derivative as a novel zinc binding group.

Kai Chen *et al.* employed the strategy described in the methods section to compute a library of potential bidentate ligands coordinated to a simplified active site model using the M05-2X functional (**Figure 2.8**). Based on earlier reports, the zinc center in HDACs is expected to adopt a five-coordinate geometry. Accordingly, a collection of minimal fragments capable of bidentate coordination through any two O, N, or S atoms positioned at 1-4, 1-5, or 1-6 arrangements were generated. Both neutral and anionic species were evaluated, despite the higher desolvation cost associated with charged ligands.

Within the neutral set, 1f (4-hydroxymethylimidazole) emerged as the most favorable binder, exhibiting an interaction energy of -20.1 kcal/mol substantially stronger than other fragments, the ZBG found in well characterized HDAC inhibitors such as MS275. In 1f, the 3-nitrogen of the imidazole ring provides effective zinc coordination, while the hydroxyl group forms a stabilizing hydrogen bond with a nearby carboxylate residue. Several structurally related fragments, 1h, 2f, 2i, 2h, and 2e display comparable binding energies and all incorporate an amino group. Such amino groups have been used previously as zinc binding motifs in neutral HDAC inhibitors (for example, amino carbonyl fragments observed in PDB structures 3MAX and 3SFF). Besides functioning

as Lewis bases, these amino groups can also form two additional hydrogen bonds with His145 and His146 in the active site. A more complete representation of the enzyme environment is needed to fully capture and evaluate these interactions (K. Chen, Xu, and Wiest, 2013).

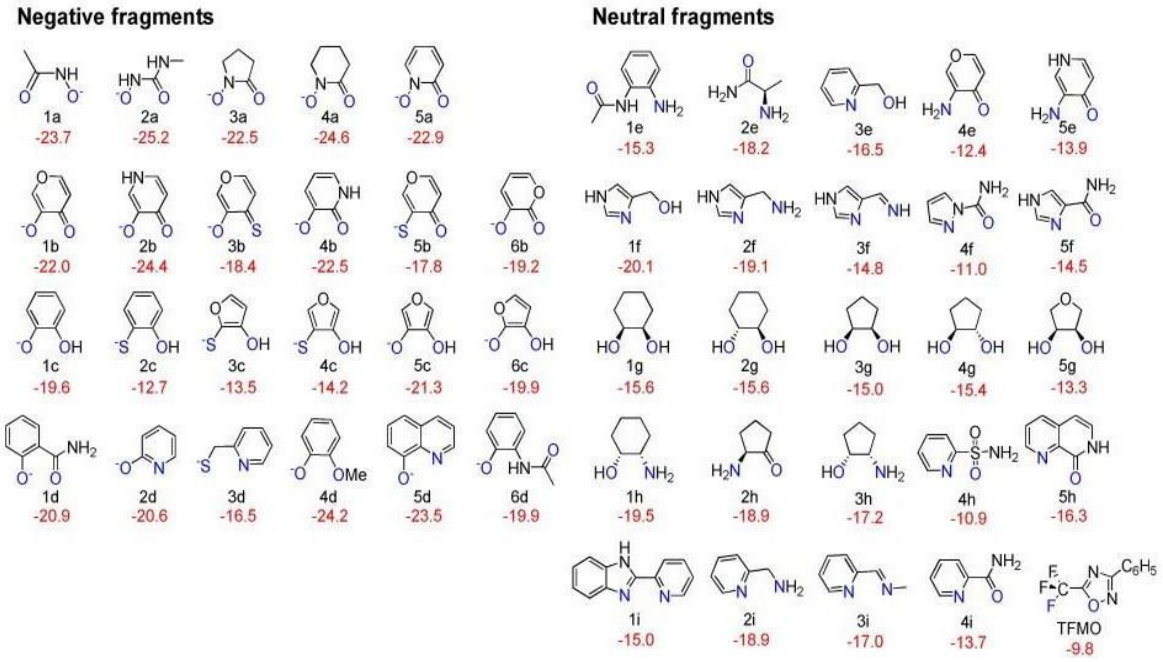

Figure 2.8: Fragment library with the interaction energy with the fixed small model is showed in red, and atoms designed to coordinate with zinc ion in blue.

Baud *et al.* reported that Psammaplin A (compound nine), a marine-derived natural product, acts as a potent HDAC inhibitor with strong preference for HDAC1 **(Figure 2.9)**. To better understand its mechanism of action and epigenetic selectivity, several related analogues were synthesized and tested to identify the structural features responsible for its activity.

Their studies revealed that Psammaplin A acts as a prodrug, becoming active after reduction to its corresponding free thiol form. *In vitro* assays shows that the reduced species exhibits extremely potent inhibition of HDAC1 (IC_{50} = 0.001 μM), it also inhibiting HDAC6 (IC_{50} = 0.36 μM) and to a lesser extent HDAC7 (IC_{50} = 17 μM) and HDAC8 (IC_{50} = 1.3 μM). Importantly, the free thiol group (R^2 = SH) at the sulfur end was essential for both strong activity and selectivity. When this thiol group was masked

as a thioether (R^2 = SMe), the compounds showed little or no inhibition of HDAC1 or HDAC6. Consistent with its strong HDAC1 preference, treatment with compound 9 increased histone H3 acetylation but had only a small effect on tubulin acetylation. This was also linked to increased expression of p21, which is a known marker of Class I HDAC inhibition (Y. Wang *et al*., 2015).

Similarly, Junquan He and colleagues reported two series of compounds containing novel zinc-binding groups (ZBGs) (compound ten). These molecules were designed, synthesized, and evaluated for anti-timor activity across several human cancer cell lines, including A549, HeLa, HepG2, and MCF-7. Among them, compound ten exhibited the most notable cytostatic activity, particularly against HeLa cells, and demonstrated HDAC1 and HDAC6 inhibitory activity with IC_{50} values of 5.30 ± 1.31 µM and 8.90 ± 1.90 µM, respectively. Enzymatic assays using HeLa cell extracts further confirmed the HDAC inhibitory activity of compound 10. Other compounds in the series showed more selective inhibition toward HDAC6, which was also supported by Western blot results (He *et al*., 2020). Additionally, the inhibitory mechanism of compound nine toward HDAC1 and HDAC6 was further explored using computational approaches, providing insights into its binding mode, conformational behavior, and energetic profile within the enzyme active sites.

.

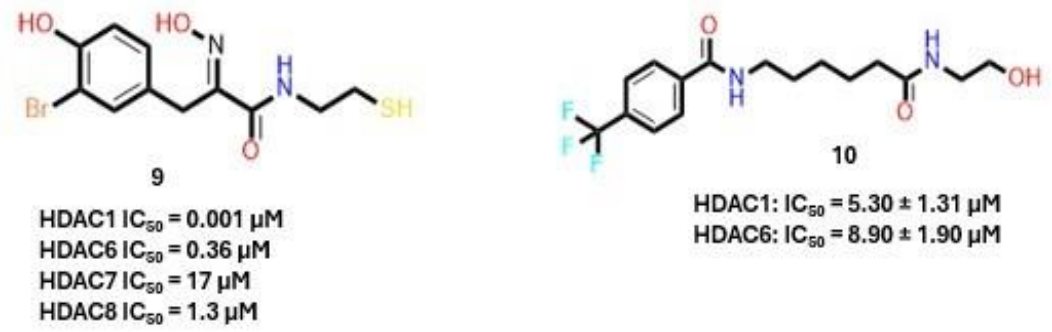

Figure 2.9: Novel zinc binding group.

2.4.2 Heterocyclic Zinc Binding Group

Heterocycles have been investigated as potential zinc binding groups (ZBGs) across multiple enzyme classes, including HDACs, matrix metalloproteinases (MMPs) and LpxC inhibitors, among them, Matthews *et al.* showed that oxazoline rings can serve as efficient cap groups. They provide a rigid and compact structure that helps improve how the molecule fits in the binding site.

On the other hand, oxazolines also work as cap-linker hybrids, facilitating optimal positioning of the ZBG within the catalytic pocket. Based on these findings and the structural similarity between HDACs and bacterial deacetylases, Kline *et al*. developed compound L-162,240. (**Figure 2.10**), which is a potent inhibitor of the deacetylase enzyme LpxC present in Pseudomonas aeruginosa. They showed that oxazoline linkers were the most effective, giving higher activity than oxazine and thioxazoline analogues Cook *et al.* proposed that the oxazoline moiety, in combination with an additional functional group, could act as a zinc binding group by chelating the active site zinc. Later studies confirmed that oxazoline derivatives show notable MMP inhibitory activity. In particular, compound eleven (**Figure 2.10**), which contains a styrene group, showed strong inhibition of MMP-9 with good selectivity over gelatinase B. They further hypothesized that zinc coordination involves both the oxazoline nitrogen and a nearby hydroxyl group in the beta position. Inspiring from these results, the Hanessian group developed related structures (compound twelve) (**Figure 2.10**) and investigated oxazoline as a potential zinc binding group, however, none of their analogues displayed HDAC inhibitory activity. Because there is limited information on oxazoline and oxazine scaffolds in HDAC inhibition, more structure–activity studies are still needed.

To date, only one study has examined hydroxy acetamide as a zinc binding group, and likewise only a single report has evaluated oxazoline as a ZBG, without offering a clear picture of its potential. Interestingly, related scaffolds have shown good activity in other zinc dependent enzymes. Therefore, this lack of research highlights the need for further studies on their possible use as HDAC inhibitors.

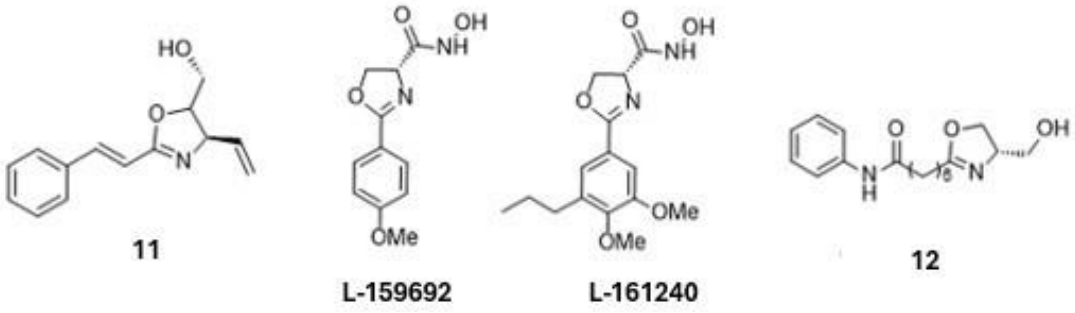

Figure 2.10: Reported structure of two of Merck's deacetylase inhibitors (L-159692, L-161240), compounds 13, and 14 are the compounds having oxazoline as a ZBG which are studied HDAC inhibitor and MMP inhibitors.

The currently FDA-approved HDAC inhibitors show limited selectivity and tend to inhibit multiple zinc-dependent HDAC isoforms (Yang, 2011; Qiao *et al*., 2013). This lack of selectivity may lead to various adverse effects during treatment, including dehydration, thrombocytopenia, anorexia, and cardiac arrhythmia (Chakrabarti *et al*., 2016; Buonvicino *et al*., 2018; Cosenza and Pozzi, 2018; Laino *et al*., 2019). Furthermore, the hydroxamic acid moiety, commonly used as the ZBG, presents several limitations such as poor chemical stability, rapid metabolic degradation, weak affinity toward class IIa HDAC isozymes, and insufficient selectivity. These drawbacks indicate the need to design and develop HDAC inhibitors with alternative zinc-binding groups (ZBGs) (Di Micco *et al*., 2008; Botta *et al*., 2011; Burli *et al*., 2013; Zhao *et al*., 2018; Banerjee *et al*., 2019).

Based on these findings, oxazine and oxazoline are hypothesized to function as potential zinc-binding groups in HDAC inhibitors, as these heterocyclic scaffolds have shown good interactions with Zn^{2+} in other zinc-dependent proteins.

According to the previous studies, hydroxyacetamide derivatives also have shown promising anticancer activity. Hydroxyamic acids, although effective HDAC

inhibitors, can have limitations due to the presence of N-O bond, which makes them reactive and susceptible to hydrolysis and metabolic degradation (Friedrich *et al*., 2020). Therefore, hydroxyacetamide gained attention as an alternative ZBG because they may be providing better stability.

Among the different HDAC isoforms, Histone Deacetylase 6 was selected as the primary target because of its unique structure, cytoplasmic localization, and important role in cancer-related cellular processes. Unlike most HDACs, which are localized in the nucleus, HDAC6 is mainly found in the cytoplasm and deacetylates non-histone substrates. Structurally, HDAC6 is unique because it contains two catalytic deacetylase domains (CD1 and CD2) along with a zinc-finger ubiquitin-binding domain (ZnF-UBP)(Hai & Christianson, 2016), which allows the enzyme to recognize ubiquitinated proteins. One of the CD2 catalytic domain is responsible for removing the acetyl group from lysine 40 (K40) of α-tubulin (Haggarty *et al*., 2003). These structural features make HDAC6 an attractive target for the development of selective inhibitors.

HDAC6 regulates several important cytoplasmic proteins, including α-tubulin, heat shock protein 90 (Hsp90), and cortactin (Hubbert *et al*., 2002). These proteins are involved in microtubule organization, protein folding, cell movement, and cytoskeleton remodeling. Through these substrates, HDAC6 participates in important cellular functions such as cell migration, stress response, and intracellular protein transport (Valenzuela-Fernández *et al*., 2008). Moreover, HDAC6 plays an essential role in the aggresome-autophagy pathway, a cellular quality control mechanism responsible for the removal of misfolded or aggregated proteins (Su *et al*., 2011). In this pathway, HDAC6 binds ubiquitinated misfolded proteins and transports them along microtubules to aggresomes, where they are degraded through autophagy. Since cancer cells rely on this pathway to survive under conditions of proteotoxic stress, inhibition of HDAC6 can disrupt protein homeostasis and suppress tumor growth.

Most currently approved HDAC inhibitors act as pan-HDAC inhibitors, targeting multiple HDAC isoforms simultaneously. Though these agents show anticancer activity, their lack of selectivity leads to side effects. Conversely, selective HDAC6 inhibition has been reported to maintain anticancer effects while reducing toxicity

(Ferreira-Silva *et al*., 2024). Therefore, HDAC6 has emerged as an attractive target for the development of selective HDAC inhibitors with improved pharmacological profiles.

These compounds were examined through an integrated cheminformatics and computational evaluations, including molecular docking, molecular modelling, and free energy analyses. From these results, the most promising candidates were selected for synthesis and biological evaluation.

2.5 Synthesis of Ester

As previously mentioned, the presence of heteroatoms plays a crucial role in HDAC inhibitory activity. The reaction of α-haloesters with aliphatic and aromatic amines is one of the most reported methods because of its synthetic simplicity, proceeding through a bimolecular nucleophilic substitution (S_N2) mechanism, as illustrated by

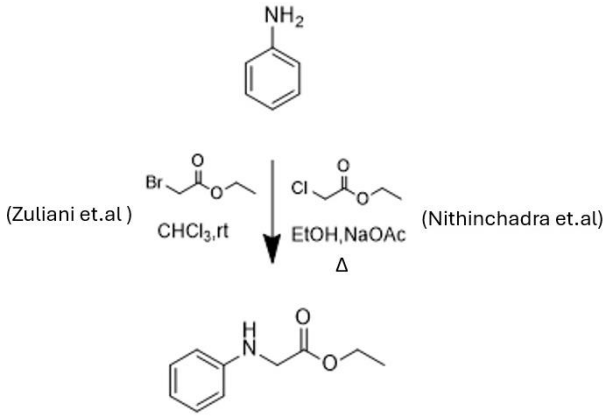

Figure 2.11: Literature background of Preparation of ester.

Nithinchandra *et al.* reported the synthesis of the corresponding ester by refluxing a mixture of substituted aniline, ethyl chloroacetate, and anhydrous sodium acetate in of ethanol using an oil bath for 6 h (**Figure 2.11**) (Nithinchandra *et al*., 2012). Similarly, Zuliani *et al*., reported the synthesis of the ester by slowly introducing ethyl bromoacetate into a stirred chloroform solution of the corresponding primary amine and allowing the reaction to proceed for 2 h (Zuliani *et al*., 2009).

2.6 Synthesis of amide

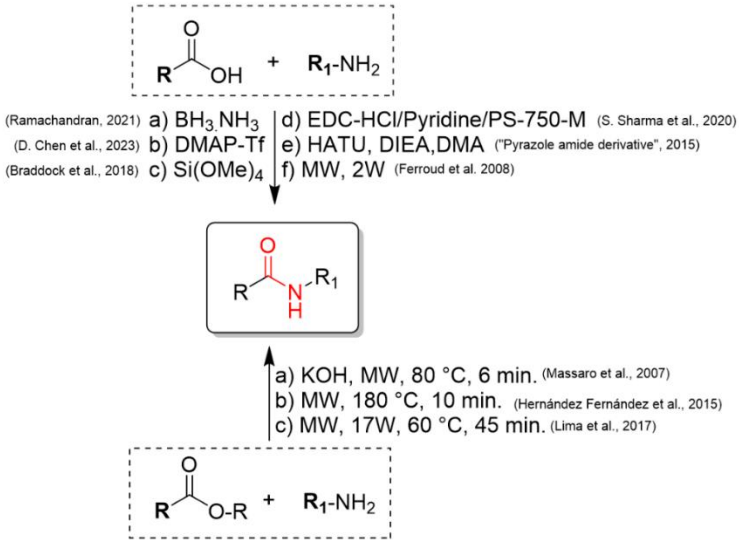

Figure 2.12: Literature background of amidation.

According to prior literature, a wide range of coupling reagents has been explored for amide bond formation. Some important literature reports on amide synthesis are summarized in **Figure 2.12** Ramachandran and co-workers reported that ammonia–borane functions as an effective precatalyst for the direct amidation of both aromatic and aliphatic carboxylic acids, delivering yields of up to 90%. In comparison, Procopio *et al.* employed EDC·HCl as the coupling reagent, obtaining yields in the range of 34-97%. Meanwhile, Chen and colleagues developed a rapid amidation protocol that enabled efficient coupling of amines and acids within 5 minutes. A patent from Teijin Pharma Limited describes a procedure in which a solution of the amine, HATU, and DIEA in DMA is treated with the corresponding carboxylic acid and heated at 60 °C for 2 hours, affording the desired amide in 45% yield. Additionally, Bradook *et al.*, demonstrated that tetramethyl orthosilicate (TMOS, 200-250 mol%) can serve as an efficient reagent for direct amidation, providing the target amides in good to quantitative yields.

The methodologies discussed above present notable limitations, such as the formation of undesirable byproducts or residual waste, the high cost associated with coupling

reagents, and restricted substrate compatibility. To address these challenges, catalytic systems based on boron derivatives, as well as other homogeneous, heterogeneous, and enzymatic catalysts, have been developed as efficient alternatives to conventional amidation strategies (Ojeda-Porras *et al*., 2015). Thus, the thermal amidation of carboxylic acids with amines is a complementary procedure to eliminate some of the reported synthetic challenges. Moreover, microwave assisted protocols provide relatively mild conditions for the direct formation of amides from non-activated carboxylic acids and amines, eliminating the need for both coupling reagents and solvents. Despite its synthetic potential, this reaction method has been neglected for many years principally because of the long reaction times and high temperatures needed (Charville *et al*., 2010).

Clotilde Ferroud and co-workers reported a catalyst free, microwave assisted method for the direct preparation of acetamides from amines, employing carboxylic acids or their derivatives as acetylating agents (Ferroud *et al*., 2008). The transformation was completed within 1-2 hours, affording the desired products in good yields. Similarly, Andria Ojeda *et al*., reported an improved and environmentally sustainable method for the direct amidation of carboxylic acids with amines, employing silica gel as a solid support (Ojeda-Porras *et al*., 2015). This solvent free protocol delivered the corresponding amides in 64-98% yield within 40 minutes, thereby enhancing the eco-friendly nature of the process. Although azeotropic removal of water resulted in only a marginal increase in yield, it substantially shortened the reaction time, contributing to greater overall efficiency. In a related study, Eugenio Hernandez-Fernandez and co-authors developed a base free, microwave assisted strategy for the amidation of non-activated ethyl esters with both achiral and chiral 1,2-amino alcohols. The method delivered the target amides in 30-85% yield within 10 minutes (Hernández-Fernández *et al*., 2015). Likewise, Rafaely N. Lima and colleagues examined amide bond formation using ethyl salicylate as a model substrate in reactions with ten distinct primary amines. Under optimized conditions (heating at 60 °C for 45 minutes), the corresponding amides were obtained in consistently high yields ranging from 77% to 94% (Lima *et al*., 2017).

CHAPTER 3

3 Hypothesis and Objective

3.1 Hypothesis

Newly designed oxazine, oxazoline and hydroxyacetamide derivatives are hypothesized to act as zinc-binding groups capable of interacting with HDAC enzymes based on *in silico* studies. The presence of these zinc-binding group improves optimize Zn^{2+} binding interactions and enhance selectivity toward HDACs. Among them, hydroxyacetamide derivatives exhibit stronger anticancer activity against HCT-15, MCF-7, and PC-3 cancer cell lines, while showing reduced cytotoxicity toward the non-cancerous HaCaT cell line compared with the reference HDAC inhibitor Vorinostat.

3.2 General Objectives

To design and study novel oxazoline, oxazine, and hydroxyacetamide based HDAC inhibitors using *in silico* approaches, including molecular docking, molecular dynamics simulations, MM-GBSA calculations, and PROTOX toxicity prediction. The most promising hydroxyacetamide compounds will then be synthesized and tested for anticancer activity against HCT-15, MCF-7, and PC-3 cancer cell lines, as well as for toxicity in normal HaCaT cells.

3.2.1 Specific Objetives

1. To perform *in silico* screening and molecular docking of oxazoline, oxazine, and hydroxyacetamide derivatives to identify compounds with ideal binding affinity and selective zinc binding properties.
2. To evaluate the *in silico* ADMET properties and toxic activity of the designed compounds to identify potential lead candidates.
3. To select the hydroxyamide derivative with the better *in silico* profile for experimental validation.
4. To synthesize and characterize each of the compounds using the ^{1}H and ^{13}C Nuclear Magnetic Resonance techniques (NMR ^{1}H, ^{13}C), High Resolution Mass

Spectroscopy (HRMS)

5. To evaluate the *in vitro* anticancer activity of the selected hydroxyacetamide derivative against HCT-15, MCF-7, and PC-3 cancer cell lines.
6. To assess the *in vitro* cytotoxicity of the selected compound toward normal cells (HaCaT).
7. To compare the anticancer efficacy and cytotoxicity profile of the selected hydroxyacetamide derivative with the reference drug SAHA.

CHAPTER 4

4 Materials and Method

4.1 Software and Tools

4.1.1 Data collection

The lead compound and its derivatives were drawn using Marvin Sketch and saved as .mol files, which were then converted into .sdf files using Open Babel and make library.

4.1.2 Protein preparation

The top three HDAC isoforms were selected from the total of eleven known isoforms for each compound set, namely the hydroxyamide derivatives and the oxazine and oxazoline derivatives. The structures of HDACs were obtained from the Protein Data Bank {PDB ID: 4LXZ (chain B),4A69 (chain A),1T69 (chain A), 2VQM (chain A), 3C10 (chain A), 5EDU (chain B), 7U59 (chain A)}through the website https:// www.rcsb.org/. To improve the quality of the protein structures, the Protein Preparation Wizard within the Maestro software (Schrödinger Suite 2018-1) was used. This tool fixed specific errors observed during X-ray crystallography, such as missing hydrogen atoms. Bond orders were assigned, and absent hydrogen atoms in the Protein Data Bank (PDB) structure were added. Along with, water molecules were removed, and missing side chains were filled, optimizing hydrogen bonds to prevent steric clashes. The structures were refined using the OPLS4 force field, with a heavy-atom RMSD of 0.3 Å applied during the energy minimization step (C. Lu *et al.*, 2021).

4.1.3 Ligand preparation

The ligands were prepared using LigPrep in Maestro. During this preparation, salts were removed, and hydrogen atoms were added. Various ionization and tautomeric states were generated using the Epik configuration at a pH range of 7 ± 2. OPLS4e force fields were applied, and the states with the lowest penalty were selected for subsequent processes.

4.1.4 Molecular docking

Molecular docking studies were performed using the Schrödinger Maestro software suite (Schrödinger LLC, New York, NY, USA) to evaluate the binding interactions of two series of ligands, namely hydroxy acetamide derivatives and oxazoline and oxazine derivatives, with the prepared protein targets.

Grid Preparation

Receptor grids were generated to define the docking space around the active site. The binding site was identified based on the position of the co-crystallized ligand, and the grid box was centered on the Zn^{2+} ion and its coordinating residues. The grid dimensions were set large enough to encompass the catalytic Zn^{2+} center and the surrounding amino acid residues involved in ligand recognition.

Since the selected proteins contain a catalytically active Zn^{2+} ion, a metal coordination constraint was applied to ensure realistic ligand–metal interactions during docking. The Glide module utilizes the ligand's position and size to calculate default coordinates and dimensions for the grid region. During grid generation, the Van der Waals radius scaling was set to 1.0, softening the potential for nonpolar receptor atoms, and the partial charge cut-off was set to 0.25.

Docking of Oxazoline and Oxazine Derivatives

The Oxazoline and Oxazine derivatives were docked using the prepared receptor grids: HDAC6 (-31.02, 21.89, and 30.09 Å), HDAC3 (-77.3, -12.5, 24.6 Å), and HDAC8 (11.476, -1.396, 20.745 Å), under identical docking conditions. Multiple binding poses were generated for each ligand, and the top ranked conformations were selected based on Glide docking scores and predicted binding free energies. Key molecular interactions, including Zn^{2+}-coordination, hydrogen bonding, and hydrophobic contacts, were analyzed using Pose Viewer and LigPlot+.

Docking of Hydroxyamide Derivatives

The Hydroxyamide derivatives were docked using the prepared receptor grids: HDAC6 (-41.02, 31.09, and 6.09 Å), HDAC2 (-80.3, -22.54, 33.16 Å), and HDAC8

(59.76, -13.96, 34.45 Å). Binding scores were recorded, with special attention to the orientation of heteroatoms in coordinating the Zn^{2+} ion and interacting with surrounding residues. Comparative evaluation was conducted between the amide and oxazole derivatives to highlight differences in binding affinity, binding modes, and interaction profiles.

4.1.5 MM-GBSA calculations

The docking complexes were subjected to MM-GBSA calculations. After docking, the complexes were minimized using the local optimization feature in Prime. The OPLS4 force field was utilized to calculate the binding energy for the receptor-ligand pairs. The binding free energy was calculated using the following equation:

$$\Delta G_{\text{Bind}} = \Delta E_{\text{MM}} + \Delta G_{\text{solv}} + \Delta G_{\text{SA}} \qquad (4.1)$$

The ΔE_{MM} represents the difference in minimized energy between the protein-ligand complexes, while ΔG_{solv} signifies the variation in GBSA solvation energy between the protein-ligand complexes and the combined solvation energies of the individual protein and ligand. ΔG_{SA} indicate surface area energies from both the protein and ligand, along with the difference in surface area energies for the complexes. The minimization of the docked complexes was achieved through the local optimization.

4.1.6 Pharmacokinetic profiles and toxicity in silico

The drug-like properties of the compounds were assessed using the online computational tool SwissADME (http://www.swissadme.ch/). The analysis was based on the Rule of Five (Ro5) criteria, considering parameters such as molecular weight (MW), hydrogen bond acceptor (HBA), hydrogen bond donor (HBD), lipophilicity (Log P), topological polar surface area (tPSA), and aqueous solubility (Log S). The toxicological properties of the compounds were predicted by an online server PROTOX (https://tox.charite.de/protox3/).

4.1.7 Molecular dynamics simulation

The ligand–protein complexes obtained from docking were prepared for molecular dynamics simulations in Maestro. The systems were solvated with TIP4P water molecules within an orthorhombic box extending 10 Å beyond the solute in each dimension. Counterions were automatically added to neutralize the system. Prior to production, the system was equilibrated for 2 ns under standard conditions. A 100 and 500 ns production simulation were then performed using Desmond with the NPT ensemble, maintaining a constant temperature of 310 K and pressure of 1 atm. The trajectories were analyzed to evaluate structural stability and flexibility, including root mean square deviation (RMSD) and root mean square fluctuation (RMSF) of the protein backbone and ligands.

4.2 Synthesis Method

The reagents and solvents used were acquired from Sigma-Aldrich®. Reactions were monitored through thin layer chromatography on Merck® plates (TLC Silica gel 60 F254). The compounds were purified by chromatographic column with SiO_2 of pore size of 60 Å (Sigma-Aldrich) and characterized by Nuclear Magnetic Resonance in a Bruker Ultra shield spectrometer of 400 MHz, High-resolution mass spectra were recorded using a JEOL HRMStation JHRMS-700. Microwave-assisted reactions were conducted under stirring in sealed vessels using a Monowave 300 manufactured by Anton Paar.

4.2.1 Methodology of synthesis compounds

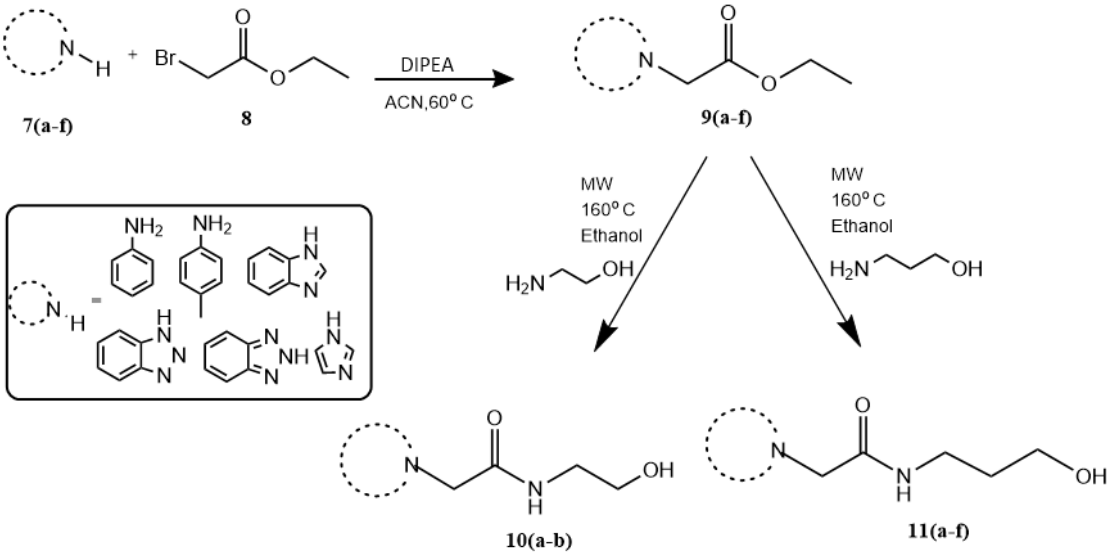

Figure 4.1: Synthesis route for preparation of amide derivatives.

According to the literature, aryl acetate derivatives (**9a–f**) were obtained through a nucleophilic substitution (S_N2) reaction. In this step, a mixture of aryl/heteroaryl amines (**7a–f**), ethyl bromoacetate (**8**), and *N*, *N*-diisopropylethylamine in acetonitrile was refluxed at 50 °C. Subsequently, the resulting Aryl/ Hetroarylglycine ethyl esters

were used in the next reaction with either 2-ethanolamine or 3-Amino-1-propanol in ethanol, in the presence of *p*-toluenesulfonic acid, under microwave reaction to obtain the corresponding hydroxyacetamide derivatives (**10a**–**b**) and (**11a**–**f**). Reaction conditions, including the base, solvent, reaction time, and temperature, varied depending on the substrate, and the details for each compound are summarized in **Table 4.1** and **Table 4.2.**

4.3 General procedure

4.3.1 Synthesis of *N*-aryl and heteroaryl glycine ethyl esters 9a-f

The synthesis of ethyl ester derivatives was carried out using a same procedure. In a round-bottom flask, the corresponding *N*-containing aryl and heteroaryl precursor was dissolved in acetonitrile. To this solution, the DIPEA or K_2CO_3 was added as a base, and the mixture was stirred at room temperature for 10 min. Then, ethyl bromoacetate was added dropwise under continuous stirring. The reaction mixture was then refluxed in a sand bath at the optimized temperature and duration (**Table 4.1**). After completion (monitored by TLC), the mixture was evaporated and purified by column chromatography using the hexane: ethyl acetate (7:3) solvent system or crystallization to yield the corresponding glycine ethyl ester derivatives. The obtained compounds were characterized by ^{1}H NMR and ^{13}C NMR spectroscopy and mass spectrometry.

Table 4.1: Summary of reaction conditions for synthesis of *N*-Aryl/Heteroaryl glycine ethyl esters.

Compound	Equivalence (Precursor: Base: E.B*:)	Solvent	Time	Temp
9a	1:2.06:1	Acetonitrile	2 h	50 °C
9b	1:2.06:1	Acetonitrile	16 h	R.T.
9c	1:2.1:1	Acetonitrile	6 h	140 °C
9d,9e	1:1.1:1	Acetonitrile	5 h	Ultrasonicate (R.T.)
9f	1:2.1:1	Acetonitrile	3 h	80 °C

E.B – Ethyl bromoacetate; R.T. – Room temperature.*

Preparation of ethyl phenylglycinate 9a

Aniline 0.4 g (0.00429 mol, 1 eq) was dissolved in 6 mL of acetonitrile, followed by the addition of *N*,*N*-diisopropylethylamine 1.48 mL (0.00884 mol, 2.06 eq) The mixture was stirred at room temperature for 10 minutes. Subsequently, ethyl bromoacetate (0.478 mL 0.00429 mol, 1 eq) was added dropwise, and the reaction was reflux in sand bath at 50 °C for 2 h.

Preparation of ethyl p-tolylglycinate 9b

Toluidine 0.2 g (0.00186 mol, 1 eq) was dissolved in 3 mL of acetonitrile, and *N*,*N*-diisopropylethylamine 0.482 mL (0.0037 mol, 2.06 eq) was added to the solution. The mixture was stirred at room temperature for 10 minutes. Ethyl bromoacetate 0.478 mL (0.00186 mol, 1 eq) was then added dropwise, and the reaction was stirred at room temperature for 16 h.

Preparation of ethyl 2-(1H-benzo[d]imidazol-1-yl) acetate 9c

1 g (0.0084, 1eq) of benzimidazole was dissolved in 25 mL of acetonitrile, followed by the addition of 2.45 g of K_2CO_3 (0.0177 mol, 2.1 eq). The mixture was stirred for 10 minutes, after which 0.942 mL of ethyl bromoacetate (0.0084 mol, 1 eq) was added. The reaction mixture was then heated at 140 °C, for 6 h.

Preparation of benzotriazolyl ethyl acetate 9d, 9e

In a round bottom flask, benzotriazole (1.0 eq), ethyl bromoacetate (1.1 eq), and potassium carbonate (1.5 eq) were added in a round bottom flask. Acetonitrile (30 mL) was added to dissolve the benzotriazole. Then the reaction mixture was kept under ultrasonicate for ~5h. Afterwards, the reaction mixture was allowed to undergo ultrasonication for about 5 hours. Once the reaction is complete, distilled water (30 mL) was added to the reaction mixture, and the product was extracted thrice with ethyl acetate (30 mL each time). The organic layer was washed with distilled water, dried over anhydrous sodium sulfate, and concentrated. The crude product was purified through column chromatography using hexane and ethyl acetate (8:2) as the solvent

system. Purification revealed the formation of two compounds (9d and 9e). This is because of the tautomeric nature of the benzotriazole whereby the hydrogen atom changes position among the nitrogen atoms in solution.

Preparation of ethyl 2-(1H-imidazol-1-yl) acetate 9f

A solution of the 1 g of imidazole (0.0146 mol, 1 eq) in acetonitrile (10 mL) was treated with 4.26 g K_2CO_3 (0.0308 mol, 2.1 eq) and 1.63 mL of ethyl bromoacetate (0.0146 mol, 1 eq). The reaction mixture was stirred at reflux for 3 h under 80 °C.

4.3.1 Preparation of hydroxy acetamides 10(a-b), 11(a-f)

N-Aryl/heteroaryl glycine ethyl esters (**9a-f**) (1.0 eq) were dissolved in ethanol (10-15 mL) in a 30 mL microwave reaction vessel. 1eq of amino alcohol (3-amino-1-propanol or ethanolamine) and catalytic amount of *p*-toluenesulfonic acid monohydrate were then added. The reaction mixture was heated under microwave irradiation at 140–160 °C for 1-4 h. After the reaction, the solvent was removed under reduced pressure. The resulting crude product was purified by column chromatography using an appropriate solvent system to obtain the desired products.

The purity of the final compounds was confirmed by ^{1}H NMR spectroscopy. The duration of the reaction changes according to the specific *N*-aryl or heteroaryl precursor used **Table 4.2.**

.

Table 4.2: Summary of reaction conditions and results for hydroxyamide derivatives.

Compound	Equivalence (precursor: amine:catalyst)	Solvent	Time	Temp.
10a	1:2.4:0.20	Ethanol	4 h	160 °C
10b	1:2.4:0.20	Ethanol	3 h	140 °C
11a	1:2.4:0.24	Ethanol	3 h	140 °C
11b	1:3:0.24	Ethanol	4 h	160 °C
11c	1:3:0.24	Ethanol	2 h	140 °C
11d	1:3:0.24	Ethanol	45 minutes	140 °C
11e	1:3:0.24	Ethanol	45 minutes	140 °C
11f	1:3:0.24	Ethanol	1 h	140 °C

Preparation of N-(2-hydroxyethyl)-2-(phenylamino) acetamide 10a

A solution containing the ethyl phenyl glycinate 0.50 g (0.00330 mol, 1 eq), ethanolamine 0.479 mL (0.00793 mol, 2.4 eq), and *p*-toluenesulfonic acid monohydrate as a catalyst 0.125g (0.000657 mol, 0.20 eq) in ethanol (10 mL) was prepared in a G30 glass vessel compatible with the Anton Paar 300 monomer microwave system. The mixture was thoroughly mixed and subjected to microwave heating at 140 °C for 4 h. The reaction mixture was purified using a solvent system ethyl acetate followed by ethyl acetate and methanol in a 9:1 ratio, resulting in the formation of compound **10a**.

Preparation of N-(2-hydroxyethyl)-2-(p-tolylamino) acetamide 10b

In a G30 glass, a solution with 0.50 g of ethyl *p*-tolylglycinate (0.00278 mol, 1 eq), 0.375mL of ethanolamine (0.00621 mol, 2.4 eq), and 0.098 g of *p*-toluenesulfonic acid monohydrate as a catalyst (0.000517 mol, 0.20 eq) in ethanol (10 mL) was made. After the mixture was well combined, it was microwave heated for 3 h at 140 °C. Purification of the reaction mixture with ethyl acetate and then ethyl acetate/methanol (9:1) yielded compound **10b**.

Preparation of N-(3-hydroxypropyl)-2-(phenylamino) acetamide 11a

A solution of ethylphenylglycinate 0.50 g (0.00330 mol, 1 eq), propanolamine 0.493 mL, (0.00793 mol, 2.4 eq), and a catalytic amount of *p*-toluenesulfonic acid monohydrate 0.157 g, 0.000826 mol, 0.24 eq) in ethanol (3 mL) was prepared in a G10 glass vessel. The mixture was thoroughly stirred and heated under microwave irradiation at 140 °C for 3 h. Purification was carried out using the same solvent system as described in the previous reaction.

Preparation of N-(3-hydroxypropyl)-2-(p-tolylamino) acetamide 11b

In a G30 glass vessel, 0.5 g of ethyl *p*-tolylglycinate (0.00278 mol, 1 eq), 0.639 mL of propanolamine (0.00836 mol, 2.4 eq), and 0.127 g of catalytic quantity of *p*-toluenesulfonic acid monohydrate (0.000667 mol, 0.24 eq) were dissolved in ethanol (15 mL). It was heated for 4 h at 160 °C using microwave radiation. Purification was carried out using the same solvent system as described in the previous reaction.

Preparation of 2-(1H-benzo[d]imidazol-1-yl)-N-(3-hydroxypropyl) acetamide 11c

This reaction was carried out following the same procedure as described above 0.5 g of ethyl 2-(1H-benzo[d]imidazol-1-yl)acetate (0.0026 mol, 1 eq), 0.603 mL of propanolamine (0.0078 mol, 3 eq), and 0.120 g of catalytic quantity of *p*-toluenesulfonic acid monohydrate (0.00063 mol, 0.24 eq) were dissolved in ethanol (15 mL) in a G30 glass vessel. The mixture was stirred thoroughly and kept in the microwave irradiation at 140 °C for 2 h. The reaction mixture was purified by column chromatography using 1:1 ethyl acetate: methanol as the eluent, affording the product.

Preparation of 2-(1H-benzo[d][1,2,3]triazol-1-yl)-N-(3-hydroxypropyl)acetamide 11d

0.5 g of Ethyl 2-(benzo[d] [1,2,3]triazol-1-yl) acetate (0.0024 mol, 1 eq) 0.559 mL of propanolamine (0.00730 mol, 3 eq) and 0.111 g of catalytic amount of *p*-toluenesulfonic acid monohydrate (0.000584 mol, 0.24 eq) were dissolved in 10 mL of ethanol in a G30 glass vessel. The mixture was stirred and exposed to microwave irradiation at 140 °C for 45 minutes. The resulting mixture was purified by gradient column chromatography using 9:1 ethyl acetate: methanol yielding a white solid

product.

Preparation of 2-(2H-benzo[d][1,2,3]triazol-2-yl)-N-(3-hydroxypropyl)acetamide 11e

0.2 g of 2-(2*H*-benzo[d][1,2,3]triazol-2-yl)acetate (0.00097 mol, 1 eq), 0.305 mL of propanolamine (0.0029 mol, 3 eq) and 0.44 g catalytic amount of *p*-toluenesulfonic acid monohydrate (0.00023 mol, 0.24 eq) in ethanol (3 mL) were irradiated in a G10 vessel at 140 °C for 45 minutes, and the resulting mixture was purified by gradient column chromatography using 9:1 ethyl acetate:methanol yielding product.

Preparation of N-(3-hydroxypropyl)-2-(1H-imidazol-1-yl) acetamide 11f

A solution of 0.4 g of ethyl 2-(1*H*-imidazol-1-yl)acetate (0.0028 mol, 1 eq), 0.654 mL of propanolamine (0.0085 mol, 3 eq), and a catalytic amount of 0.130 g *p*-toluenesulfonic acid monohydrate (0.00068 mol, 0.24 eq) in 15 mL of ethanol was irradiated in a G30 vessel at 140 °C for 1h, and the crude product was purified by washing with cold ethanol and further purification by gradient column chromatography (8:2 ethyl acetate: hexane; 9:1 ethyl acetate: methanol) afforded a fine white powder.

4.4 Biological Evaluation and Cytotoxicity Studies

4.4.1 Cell Seeding

The cell concentration was used to calculate the volume needed to reach the required seeding density. This volume was transferred into a 15 mL conical tube, and additional culture medium was added to make up the final volume. Cells were seeded at a density of 5,000 cells/cm², dispensing 100 µL of the suspension into each well of a 96 well plate. Plates were incubated for 24 h to allow cell attachment prior to treatment.

4.4.2 Crystal Violet Assay

A total of 5×10^3 cells per well were added into 96 well plates containing 200 µL of complete RPMI medium. After a 24 h pre-incubation period, the cells were treated with test compounds (including the reference drug, Vorinostat) at various concentrations (25, 50, 100 and 200 µg/mL) for 48 hours. Control cells were exposed to solvent alone in equal volume that was used to dissolve the compound and were used to normalization. After treatment, the cells were washed with phosphate-buffered saline (PBS) followed by staining with 0.5% crystal violet solution (25 µL) for 30 min. The wells were then rinsed with tap water and air dried. Dye bound to cells was solubilized by adding 200 µL of 1% SDS solution. Plates were then shaken for 5 min prior to measurement of OD at 570 nm using the Cytation 5 Imaging Reader (BioTek Instruments, Inc.). The cytotoxicity activity was quantified in terms of percentage of cell viability in comparison to control, calculated using the formula given below:

$$Viability\ (\%) = \frac{Absorbance\ of\ negative\ control - Blank}{Absorbance\ of\ sample - Blank} \times 100 \qquad (\mathbf{4.2})$$

4.4.3 Handling and Disposal of Waste

The collection and proper disposal of hazardous waste generated by the research project was carried out in accordance with the safety and hygiene regulations of the Facultad de Ciencias Químicas, UANL e Instituto de Química, UNAM, for biological-infectious waste; continuing with the specific containers most used during the project.

Table 4.1: Containers used for waste collection.

Container	Waste
A	Saline solutions, organic and inorganic acids and bases.
B	Inorganic solids.
C	Toxic, flammable substances, amines, and non-halogenated organic solvents.
D	Toxic, flammable substances, amines, and halogenated organic solvents.
E	Highly toxic, carcinogenic organic substances.
G	Combinations of organic solids.
RPBI	Infectious biological hazardous waste.
-	Industrial waste
-	Contaminated glass

CHAPTER 5

5 Results and Discussion

5.1 Computational studies

5.1.1 *In silico* studies in heterocyclic analogs and hydroxy acetamide derivatives

Molecular docking

A library of 32 O, N, S-substituted heterocyclic analogs along with eight hydroxy acetamide derivatives (**Figure 5.3**) were docked to multiple HDAC isoforms using the Schrödinger ligand docking module, employing grid-based ligand docking with energy (GLIDE) in extra precision (XP) mode. Integrated evaluation of docking and ADMET results identified 24 heterocyclic analogues with high binding affinity toward HDAC isoforms. Among these, selected heterocycles were predicted to exhibit particularly good binding score with HDAC3 (4A69) (**Table A2**), HDAC6 (5EDU) (**Table 5.1**), and HDAC8 (1T64) (**Table A2**) compared to the reference compound SAHA, whereas the hydroxy acetamide derivatives demonstrated strong interaction across all isoforms HDAC2 (4LXZ), HDAC3 (4A69), HDAC4 (2VQM), HDAC6 (5EDU), HDAC7 (3C10), HDA10 (7U59) (**Table A3**), according to the docking analysis. Based on these findings, HDAC3, HDAC6, and HDAC8 were selected for further investigation with heterocyclic analogues, whereas HDAC2, HDAC6, and HDAC8 were chosen for studies involving hydroxy acetamide derivatives. During ADMET screening, compounds predicted to have carcinogenicity >70%, mutagenicity >80%, or extensive metabolic susceptibility were excluded, prioritizing the most promising candidates for further study. In the *in silico* analysis, we concentrated on the HDAC6 isoform for both the heterocyclic and hydroxyacetamide series due to their good interaction profile with the analogs. Overall, the integrated computational results identified compounds **4a, 3a, 3b, 10b, 11b**, and **11c** demonstrated strong interactions with the Zn^{2+} catalytic center of HDAC6, exhibiting docking scores between -8.70 and -6.719 kcal/mol (**Table 5.1**).

Table 5.1: Docking score of best compounds in HDAC6.

PROTEIN	COMPOUNDS	DOCKING SCORE (kcal/mol)
HDAC6	**3a**	-6.783
	3b	-6.914
	4a	-6.104
	7a	-6.719
	7b	-6.744
	10b	-8.7
	11b	-7.37
	11c	-7.27
REF(SAHA)		*-7.9*

.

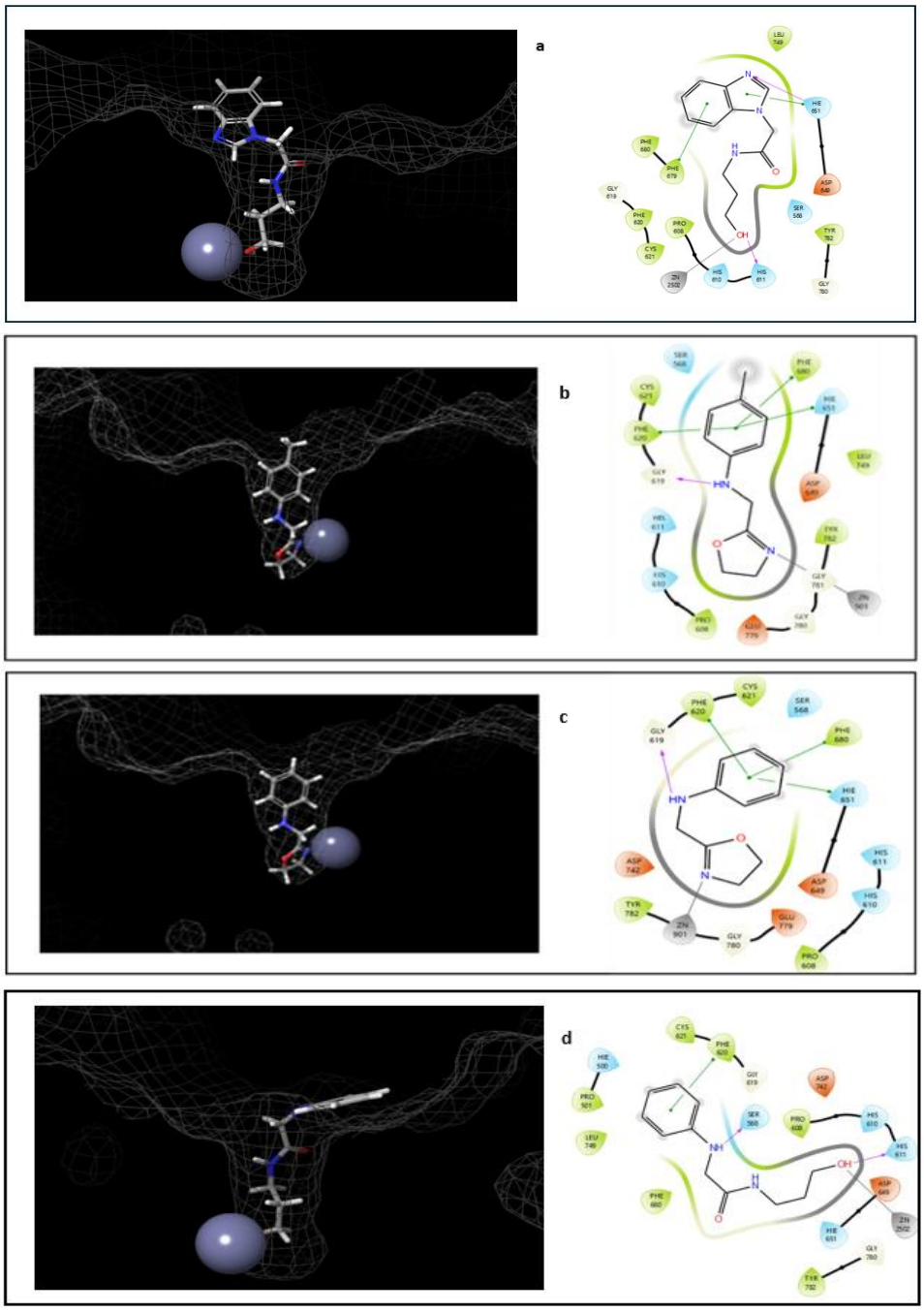

Figure 5.1: 2D and 3D diagram of interaction of compounds inside the HDAC6 pocket. **(a)11c, (b)3b, (d) 3a,** and **(d)10b**.

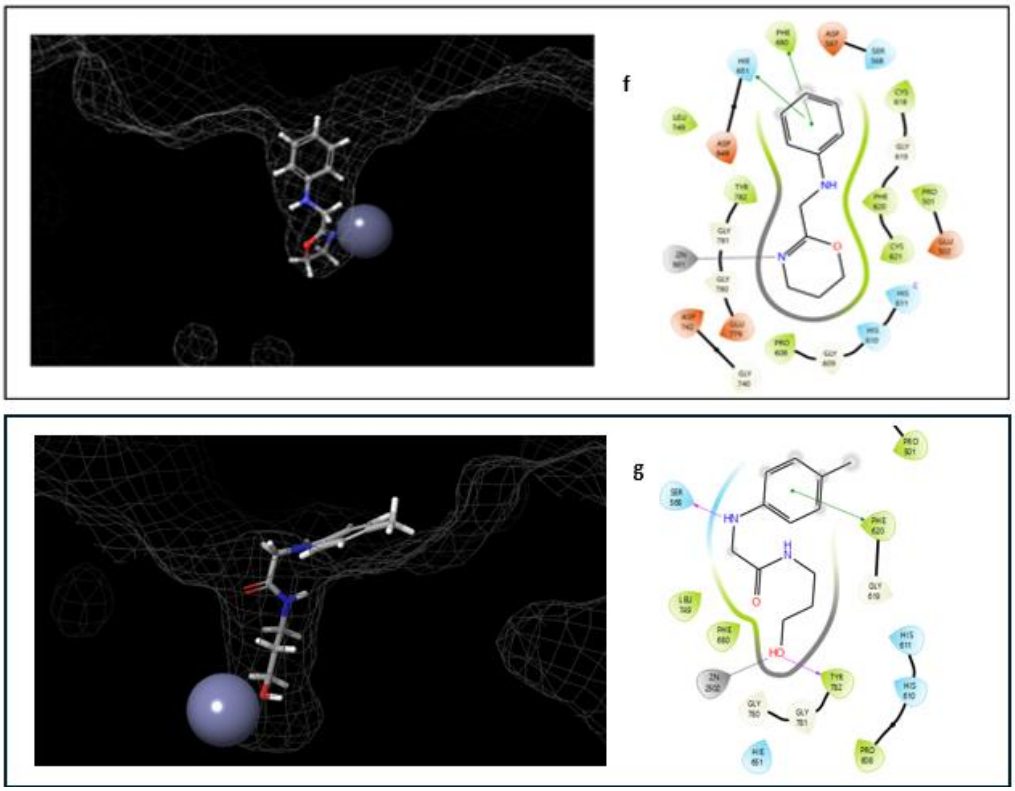

Figure 5.2: 2D and 3D diagram of interaction of compounds inside the HDAC6 pocket. (e) **4a** and (g) **11b**.

For each of the compounds, 10 poses were obtained per target. The binding behavior of all poses was then analyzed. Based on these results, the best poses in terms of binding mode and energy (oxazoline, oxazine and hydroxyacetamide) were selected to perform short MD simulations and post-process the docking results.

Table 5.2: Summary of intermolecular interactions of the top nine molecules with HDAC6.

Ligand	Hydrophobic interaction	H-bond interaction	Metal coordination	Polar interaction	Other interaction
3a	PHE 620, CYS621, PHE680, TYR782, PRO680	GLY619	Zn901	HIS610, HIS611, SER568, HIE651	Negative: ASP649, GLU779, ASP742
3b	CYS621, PHE620, PHE680, LEU749, TYR782,PRO608	GLY619	Zn901	HIE651, SER568, HIS611, HIS610	Pi-Pi stacking: PHE620, PHE680 Negative: GLU779, ASP649 Pi-Pi stacking: PHE680, HIS651, PHE620
4a	CYS618, PHE620, PHE680, LEU749, TYR782, PRO608, PRO501, CYS621		Zn901	HIE651, SER568, HIS611, HIS610	Negative: ASP742, ASP649, ASP567, GLU779, GLU502 Pi-Pi stacking: PHE680, HIS651, PHE620
7a	CYS621, PHE620, PHE680, PHE679, LEU749, TYR782, PRO608	HIE651	Zn901	HIE651, SER568, HIS611, HIS610	Negative: ASP649, GLU779, ASP742 Pi-Pi stacking: PHE680, HIS651
7b	PHE620, PHE680, LEU749, TYR782, PRO608, PHE679, CYS621		Zn901	HIE651, SER568, HIS611, HIS610	Negative: ASP649, ASP779
10b	PHE620, PRO501, TYR782, PHE680, LEU749,	GLY619, HIS610	Zn901	HIE500, SER568, HIS610, HIS611, HIE651	Pi-Pi stacking: PHE680, HIS651 Negative: - ASP742, ASP649, GLU779 Pi-Pi stacking: PHE628
11b	PHE620, PRO501, TYR782, PHE680, LEU749	TYR782, SER568	Zn901	HIE500, SER568, HIS610, HIS611, HIE651	Pi-Pi stacking: PHE628
11c	PHE680, PHE679, PRO608, PHE620, CYS621, LEU749	HIS611, HIE651	Zn901	HIE651, SER568, HIS611, HIS610	Negative: ASP649

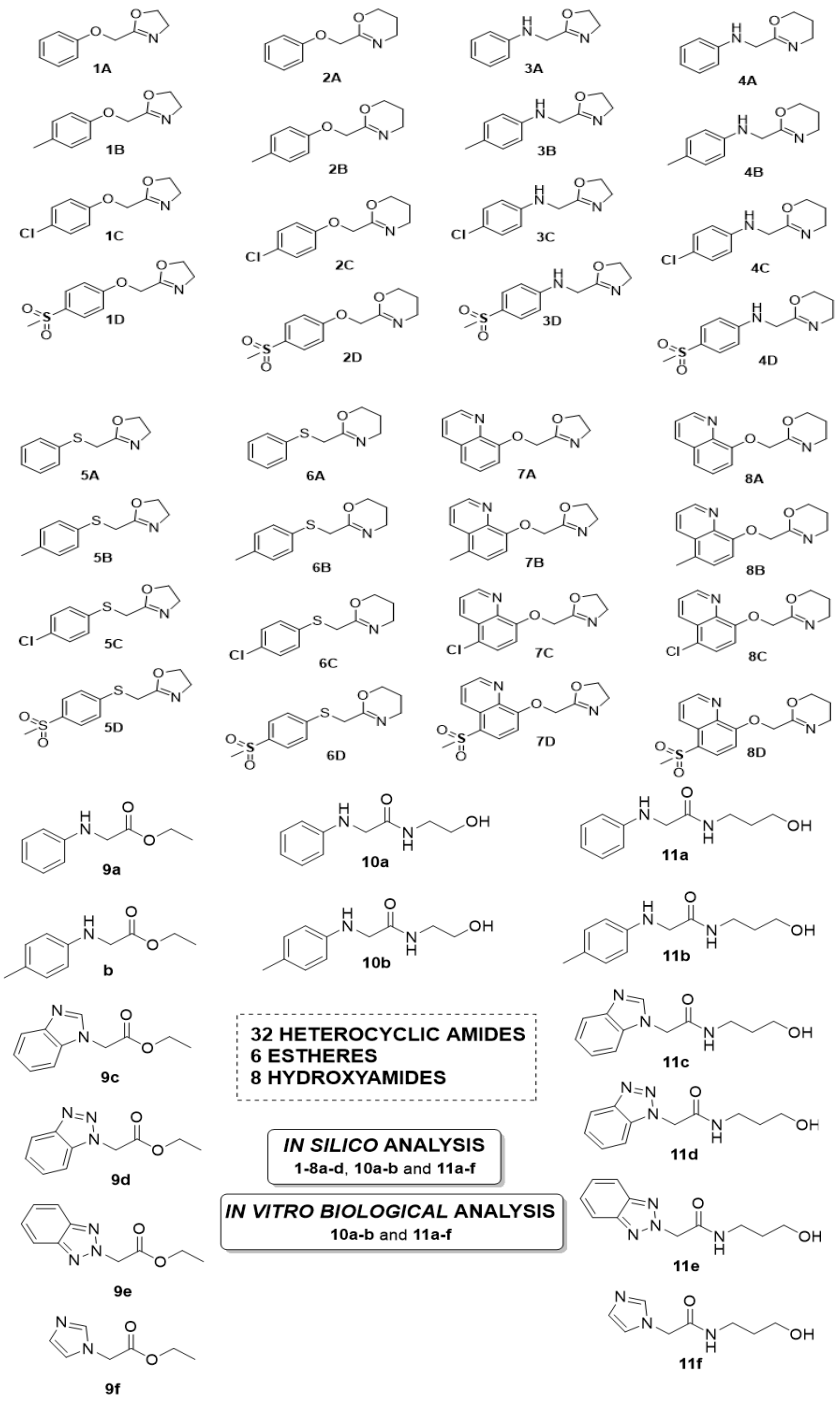

Figure 5.3: Chemical structures of heterocyclic and hydroxyacetamide analogs evaluated via silico modeling studies against HDAC6.

In addition to hydrophobic contacts, the compounds engaged in π-π stacking interactions with PHE620 and PHE680. Polar interactions were observed with HIS610, HIS611,

SER568, and HIE651, while negatively charged residues such as ASP742, ASP649, ASP567, GLU779, and GLU502 participated in electrostatic interactions Hydrogen bonding was specifically noted for compounds **3a, 3b, 7a, 10b, 11b, 11c** (**Figure 5.1**). In **3a** and **3b**, the NH group is located at the α-position relative to the oxazoline group, formed hydrogen bonds with GLY619, concurrently, in **10b** the NH group of amides and also establishes hydrogen bonding with GLY619, while its hydroxyl group additionally interacts with HIS610. For **11b**, SER568 forms a hydrogen bond with NH group of amide and TYR782 interacts with the hydroxyl group. Compound **11c** exhibits a single hydrogen bond interaction between its hydroxyl group and HIS611, whereas **7a** forms a hydrogen bond with HIE651. Important interactions of selected compounds with HDAC6 are mentioned in **Table 5.2** (**Figure 5.1 & 5.2**).

Molecular dynamics

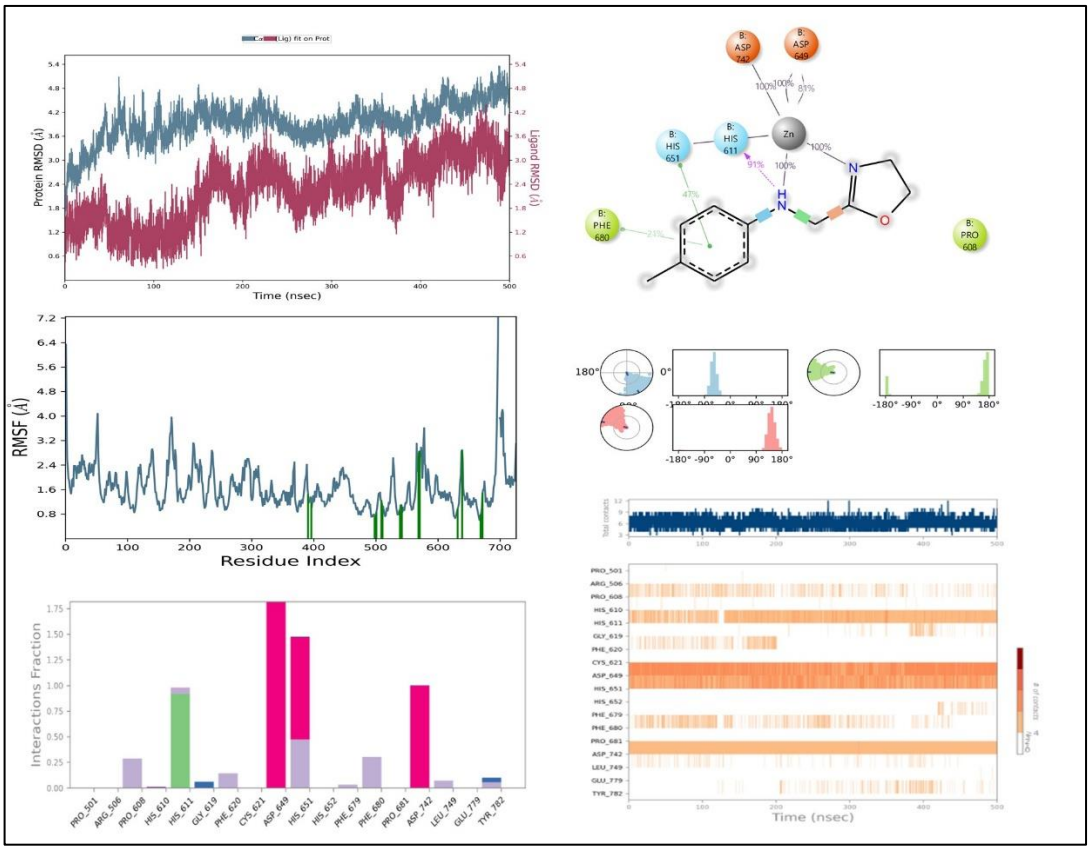

Figure 5.4: RMSD, RMSF, and protein-ligand contact plots of **3b** with protein HDAC6 isoform during MD simulation.

Molecular dynamics (MD) simulations replicate physiological conditions, providing biologically relevant information into protein–ligand interactions. Unlike molecular docking, MD simulations capture the dynamic and flexible nature of these interactions in a fully solvated system. The binding stability of the top six highest scoring molecules was evaluated using 100 and 500 ns molecular dynamics simulation. The analysis focused on root mean square deviation (RMSD), root mean square fluctuation (RMSF), and protein–ligand interactions to assess time dependent stability.

The RMSD plot indicates the MD trajectory of the **3b**-HDAC6 (**Figure 5.4**) complex for 500 ns. The Cα backbone RMSD increased during the initial 120 ns and remained within a defined range thereafter. During the 120–500 ns simulation period, the protein RMSD varied within a narrow range of 1.2 Å. A slight increase toward the final stage of the trajectory may reflect conformational adaptation of flexible protein regions while maintaining overall structural stability. The ligand RMSD exhibited moderate fluctuations during the simulation, indicating conformational changes within the binding pocket. Regardless of these variations, the ligand remained stable in the active site without any dissociation.

RMSF data of the protein show that most residues fluctuate between 1 and 2.5 Å. At the interaction sites, fluctuations were slightly higher (~1.6- 4 Å). The N- and C-terminal regions showed higher peaks above 7.2 Å, which is expected because terminal residues are usually flexible and less structured.

Interaction analysis during the simulation showed that the hydrophobic interaction with Phe680 and the polar interactions with His651 and His611 were maintained throughout the simulation. π-π stacking interactions were observed with Phe680 and His651, occurring during 21% and 47% of the simulation time, respectively. A new persistent hydrogen-bonding interaction was observed between His611 and a nitrogen atom of the ligand, which was maintained in 91% of the simulation frames compared with the XP docking pose. A bidentate interaction was observed between two donor atoms, one from the oxazoline ring and the other corresponding to the nitrogen atom at the α-

position. This suggests stable and sustained interaction within the protein-ligand complex.

The NH group torsions showed narrow angles around ~160–180°, indicating restricted rotation and preference for a single dominant conformation within the binding pocket. The zinc-binding group (orange) remains confined to a narrow range (90° to 180°), showed stable binding geometry. This behavior suggests a stable shape, likely due to strong stabilizing interactions such as metal coordination in the binding site. On the other hand, the cap group showed a wider range of motion (~ -90° to -40°), meaning it is more flexible and exposed to solvent.

Protein-ligand contact analysis revealed persistent interactions between the ligand and several active-site residues throughout the 500 ns simulation. Simultaneously, the same compound formed a monodentate interaction with the zinc ion in HDAC8 through the oxazoline nitrogen atom. (**Figure A1**). The ligand RMSD fluctuated between ~ 2-0-2.5 Å with occasional spikes, indicating higher flexibility in the HDAC8 complex and thus comparatively lower stability than observed for HDAC6. Compared to the previous system, the ligand showed wider torsional angle, indicating greater flexibility during the simulation. Even with this flexibility, the ligand maintained a consistent binding orientation throughout the trajectory.

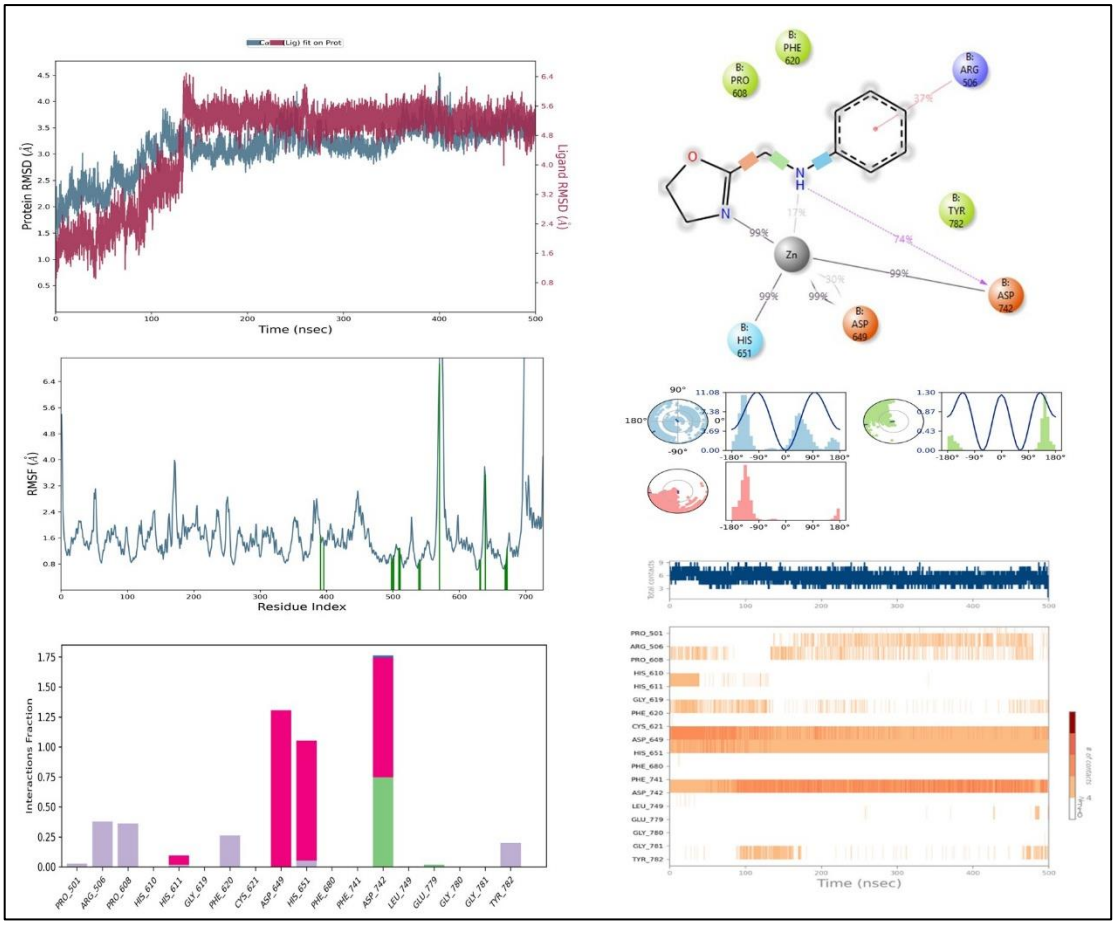

Figure 5.5: RMSD, RMSF, and protein-ligand contact plots of **3a** with protein complex of HDAC6 isoform during MD simulation.

In HDAC6-**3a** complex (**Figure 5.6**) the protein Cα RMSD increased during the initial equilibration phase (~0-120 ns), rising from ~1.5 Å to ~3.0-3.5 Å. At the same time the ligand RMSD increased from ~1.0 Å to ~2.8-3.0 Å, showing structural adaptation and ligand adjustment within the binding pocket. After ~160 ns, both RMSD values become stable, with the protein RMSD fluctuating around ~2.8-3.3 Å and the ligand RMSD around ~3.3-4.1 Å, indicating the formation of a stable complex. Altogether, the RMSD results show that the protein first undergoes equilibration and slight structural changes and then remains stable for the rest of the simulation.

RMSF analysis showed that most residues fluctuated between 1-3 Å, indicating overall stability during the simulation. Higher fluctuations are seen around residues 390-400 (~8 Å) and 450–480 (~4-6 Å), suggesting flexible loop regions during ligand binding.

In the comparison between XP docking and MD-derived interactions revealed that hydrophobic contacts and π-π stacking interactions were maintained, especially with Phe620 and Phe608 residues. While XP docking identified a hydrogen bond between the ligand and Gly619, this interaction was not retained during the MD simulation. Instead, a hydrogen bond between the ligand and Asp742 was observed with an occupancy of 74%. The imine nitrogen within the heterocyclic ring preferentially coordinates to the Zn^{2+} ion, establishing a stable monodentate interaction. However, the α-amino (NH) group of the ligand engages in a competing hydrogen-bond interaction with Asp742, which restricts its ability to approach the metal center. As a result, simultaneous coordination of both donor atoms to Zn^{2+} is disfavored, resulting in a reduced probability of bidentate chelation in this complex relative to the other compound.

The torsional analysis of 3a in the HDAC6 system shows different conformational behaviors across the three dihedral angles. The cap group shows multiple conformations but remains somewhat restricted due to interactions at the solvent-exposed region. The heterocyclic (ZBG) torsion shows a strong preference for extreme angles (around ±180°), indicating restricted rotation and stable positioning. The NH group shows a narrow distribution between 90° and 180°, indicating limited flexibility. Protein–ligand contact analysis shows continuous interactions with major residues such as Phe620, Phe608, Tyr782, Asp742, and Arg506, indicating stable binding in the active site. Compared with compound 3a in HDAC8, the protein-ligand complex achieved stable RMSD values after equilibration; however, the RMSF profile revealed early fluctuations in residues surrounding the interaction region, indicating local conformational flexibility upon ligand binding. In addition, the interaction timeline exhibited relatively weak and intermittent contact patterns, despite the interaction histogram showing recurring residue engagement throughout the simulation. Therefore, no persistent interaction with the catalytic Zn^{2+} ion was detected during the simulation, suggesting that ligand binding was dominated by transient interactions rather than stable persistent contacts. (**Figure A2**). The torsional analysis of 3a in the

HDAC6 system indicates highly dynamic and flexible conformational profile characterized by broad and multimodal angular distributions. The HDAC8-3c complex shows more flexibility, meaning the binding site is less rigid and less specific in how it holds the molecule.

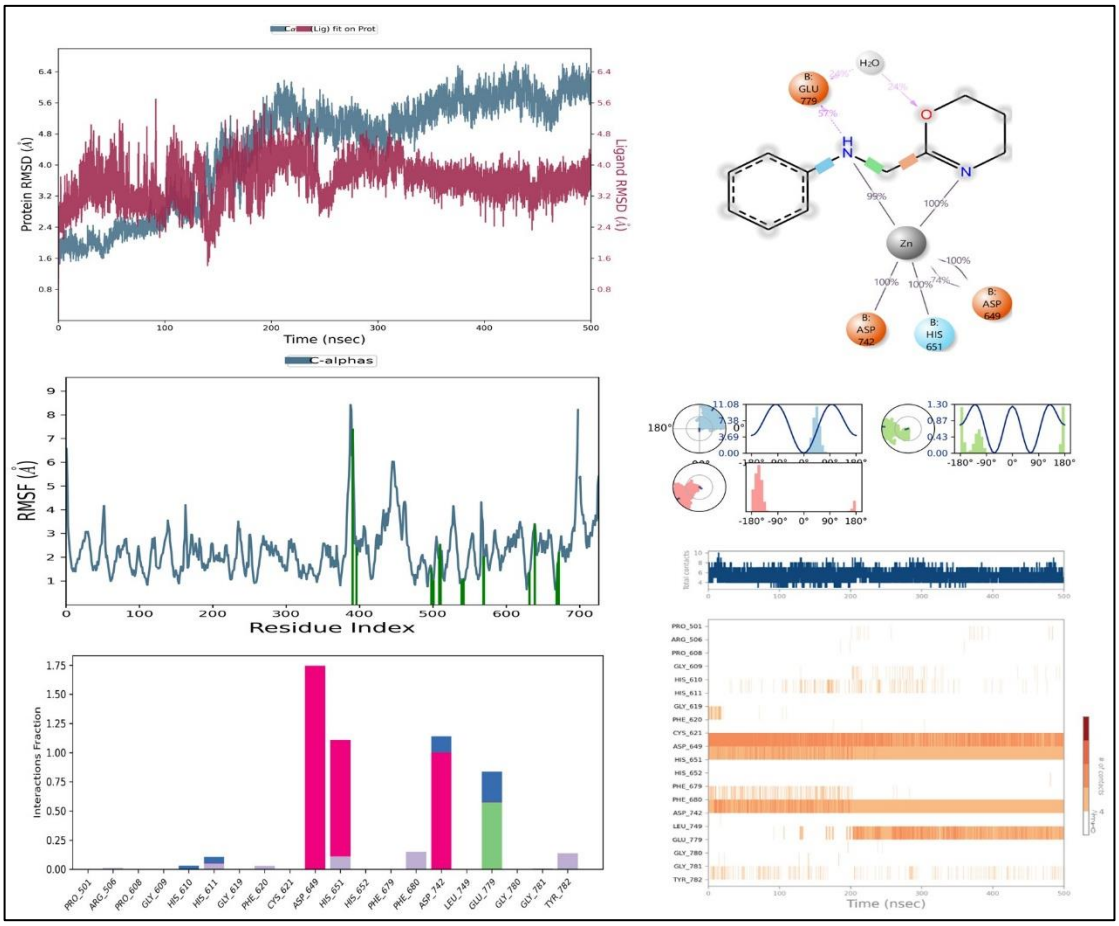

Figure 5.6: RMSD, RMSF, and protein–ligand contact plots of **4a** with protein complex of HDAC6 isoform during MD simulation.

Figure 5.7 depicts the MD analysis of **4a**-HDAC6 complex. The protein RMSD increased during the initial phase of the simulation and reached a stable range after about 150 ns. Between ~120 and 200 ns, the protein backbone RMSD increased to ~4.5-5.5 Å. At the same time, the ligand RMSD decreased to ~1.5–2.0 Å, suggesting that the ligand adopted a more stable position inside the reorganized binding pocket. After this transition (200–500 ns), the protein RMSD stabilized and fluctuated around a new equilibrium, indicating formation of a stable structure.

During the same period, the ligand RMSD remained within ~3.0-4.0 Å, with moderate fluctuations but no dissociation from the binding site. The ligand RMSD, relative to the protein backbone, ~1.6 Å over the same interval, with values mainly within the 2.5-4.0 Å range. RMSF analysis shows that most residues fluctuated below 2.5 Å, with an average of ~2.0 Å, indicating overall protein stability. Higher fluctuations greater than 3.0 Å were mainly seen in terminal and loop regions, reaching up to 8–9 Å, which is typical for flexible protein ends.

Similar to other systems, compound 4a showed bidentate interaction involving the NH group and the nitrogen atom of the oxazine ring. In addition, a water-mediated hydrogen bond was observed between the ligand oxygen atom and the backbone NH of Gly779 through a bridging water molecule. The torsional behavior of 4a in HDAC6 corresponding to the cap group, exhibits high conformational flexibility. While the more restricted behavior observed in zinc binding region. In contrast, compound **4c** in HDAC3 (**Figure A3**) displayed only a monodentate interaction through the NH group and showed no interaction involving the nitrogen atom of the oxazine group. This behavior may be attributed to the interaction of both donor atoms with Gly296, which could restrict coordination with Zn^{2+}.

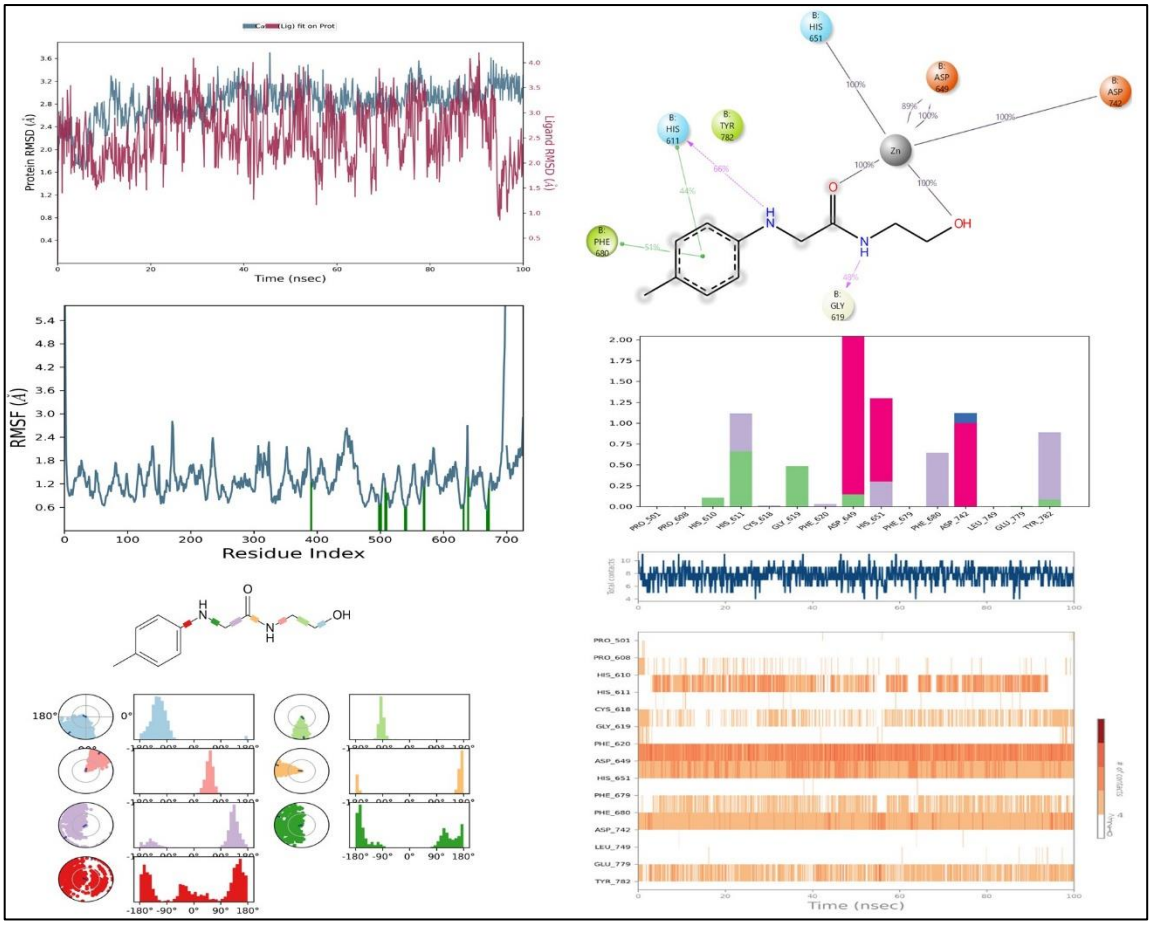

Figure 5.7: RMSD, RMSF, and protein-ligand contact plots of **10b** with protein complex of HDAC6 isoform during MD simulation.

The molecular dynamics results indicate that the **10b**-HDAC6 complex remains stable throughout the 100 ns simulation (**Figure 5.8**). The protein backbone profile shows an initial rise during the equilibration phase followed by relatively stable oscillations between ~2.6 and 3.4 Å, indicating that the protein undergoes conformational relaxation early in the simulation and subsequently maintains a stable structural state, which suggests maintenance of overall structural integrity. The ligand RMSD showed larger fluctuations (~1.0–3.8 Å). However, the ligand remained within the binding pocket, which indicates normal movement is formed without dissociation. RMSF analysis showed that most of the residues remained stable throughout the simulation. Only the terminal and loop regions showed higher fluctuations, whereas the binding-site residues remained stable in the range ~390–680. Interaction analysis showed that

HIS 611, PHE 680 and GLY 619 maintained persistent interaction with the ligand. Overall, these results confirm that the complex maintained a stable binding configuration during the simulation. The HDAC6-1b complex retained key interactions throughout the simulation, including two π-π stacking interactions with PHE680, with 54% occupancy. As well as Hydrogen bond interactions with GLY611 and polar contacts with HIS611 were maintained throughout the simulation, exhibiting occupancy rates of 40% and 44%, respectively. Most importantly, the bidentate interaction involving the hydroxyl and amide carbonyl groups was maintained throughout the simulation with 100% occupancy. Torsional analysis indicated that the zinc-binding region of the ligand maintained restricted conformational space, suggesting preservation of Zn^{2+} coordination geometry throughout the simulation. Although cap group of the ligand (periferal region) exhibited higher flexibility, this did not affect the core binding interactions. Protein-ligand contact analysis further confirmed interactions with key active-site residues such as HIS611, ASP649, and ASP742 in the100 ns trajectory, indicating stable binding within the catalytic pocket

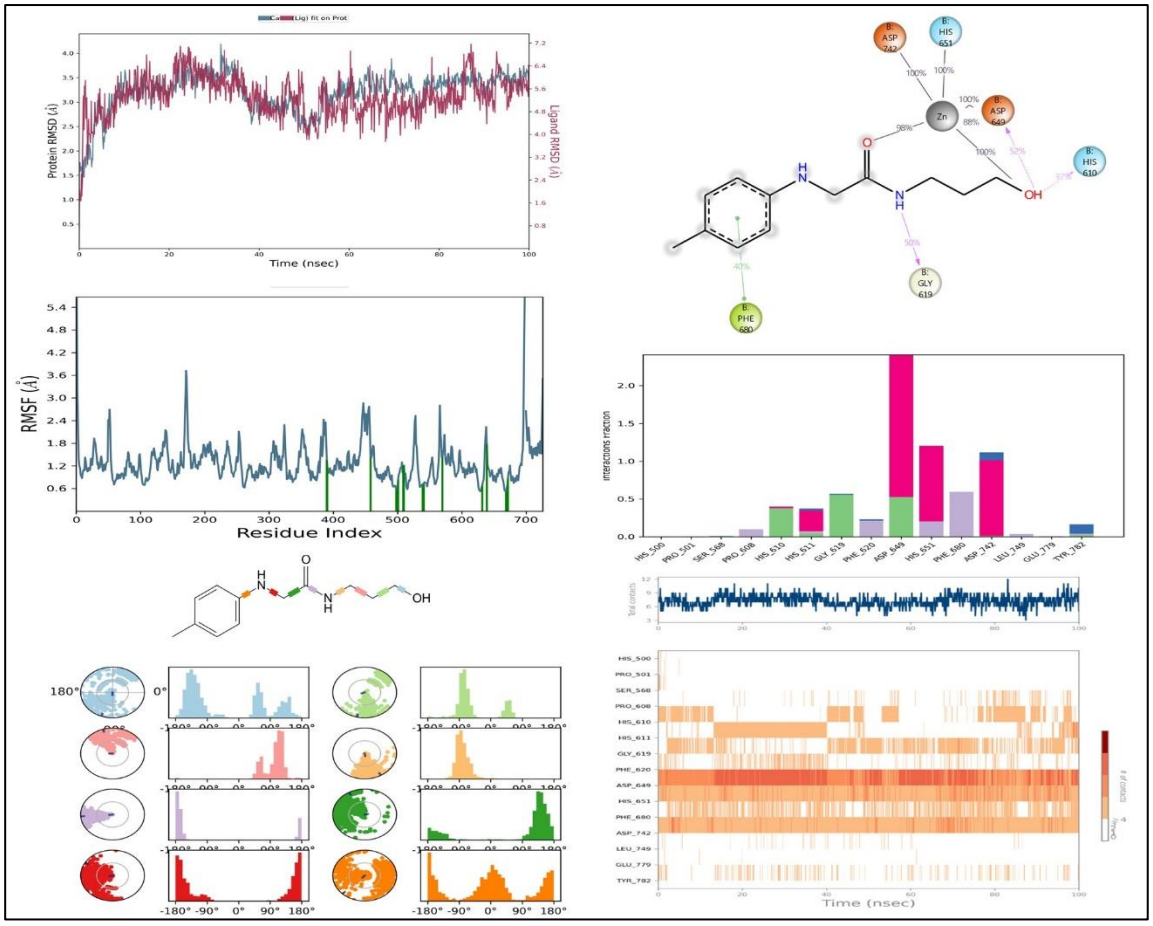

Figure 5.8: RMSD, RMSF, and protein-ligand contact plots of **11b** with protein complex of HDAC6 isoform during MD simulation.

The molecular dynamics results demonstrate that the HDAC6-**11b** complex remains stable over the 100 ns simulation (**Figure 5.9**). The protein backbone RMSD rises during equilibration and then stabilizes within ~3.0-4.0 Å, indicating that the overall structure remained stable. The ligand RMSD showed larger fluctuations (~4.8–6.4 Å). As well as RMSF analysis indicates that most residues fluctuate within ~1.0-1.8 Å. Also, a single pronounced peak exceeding ~5 Å near the terminal region is observed, while binding site residues remain comparatively rigid. Interaction profiling shows that several residues maintain persistent contacts (~0.5-1.2). Overall, these results indicate that the complex remained stable and maintained its binding mode throughout the simulation. In 2D contact summary, the HDAC6-2b complex, π-π interactions with PHE680 were maintained for 47% of the simulation duration. While XP docking

identified a hydrogen bond between the ligand and SER568, this interaction was not retained during the MD simulation. Instead, a hydrogen bond between the ligand and GLY619 was observed with an occupancy of 50%. Furthermore, XP docking identified only one hydrogen bond interaction between the hydroxyl group and TYR782, MD simulation demonstrated a dynamic interaction profile, revealing newly formed hydrogen bonds with ASP649 and HIS610 that were maintained for 52% and 37% of the simulation time, respectively. Zn^{2+} formed stable bidentate interactions with the carbonyl and hydroxyl groups of the compound, with 100% occupancy during the simulation. Torsional analysis of the zinc-binding region revealed moderate flexibility, suggesting dynamic adaptation of the ligand within the catalytic site.

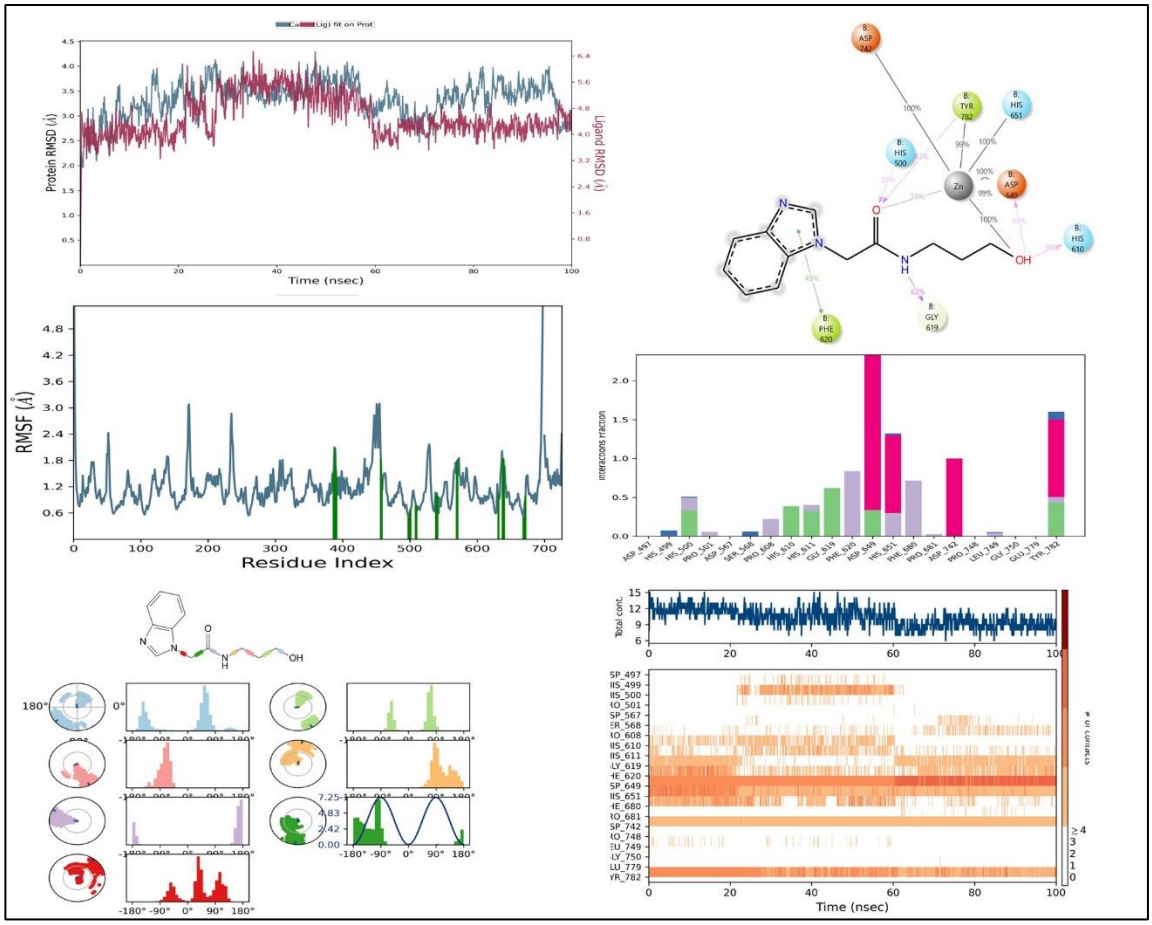

Figure 5.9: RMSD, RMSF, and protein-ligand contact plots of **11c** with protein complex of HDAC6 isoform during MD simulation.

Based on the molecular dynamics study, HDAC6-**11c** complex maintains overall

stability throughout the 100 ns simulation (**Figure 5.10**). The protein backbone RMSD reaches equilibration between ~2.5 and 4.0 Å. This suggests that the structure of the protein was maintained. Whereas, the ligand RMSD shows higher fluctuations, varying from ~ 4.0 to 5.6 Å. This indicates structural flexibility within the binding pocket.

RMSF analysis reveals that majority of residues fluctuate within ~0.8-1.6 Å, with a few regions shows peaks around ~3.0 Å. However, binding site residues remain rigid. Interaction analysis diagram of the protein-ligand complexes showed several residues maintaining steady contacts within the range of ~0.4-1.3. Taken together, these results confirm that the complex reaches an equilibrium and maintains a stable binding mode during the simulation. Comparison between XP docking and MD interactions revealed that hydrophobic contacts and π–π stacking interactions were retained, particularly with PHE620 residue, showing interaction of 45%. Additionally, GLY619 predominantly with 67% of the simulation. ASP649 and HIS610 showed hydrogen bond interactions with the hydroxyl group with occupancies 37% and 30%, respectively. Also, Zn^{2+} bidentate coordination was observed across the simulation period. Protein-ligand complex showed continuous interactions with active-site residues such as HIS651, TYR782, and ASP742 during the simulation. Torsional study indicated moderate fluctuation in certain regions of the ligand, including slight conformational changes near the zinc-binding region. However, the main torsions within the ZBG region remained stable enough to maintain effective coordination.

Interestingly, the hydroxyl moiety (**10a,10b,** and **10c)** forms a continues coordination interaction with Zn^{2+} (100% occupancy), further stabilized by hydrogen bonds with ASP (52-33%) and HIS (37-38%) (**Figure A9**). These interactions support ligand preorganization and enhance metal binding affinity through secondary stabilization. In addition, a hydrogen bond between the NH group of amide and GLY 154 (48-62% occupancy) contributes additional stabilization of the ligand within the pocket. Similarly, heterocyclic moieties of compounds **3b** (80%) and **4a (**42%**)** form hydrogen bonds with HIS611 and a water molecule, respectively.

Based on these findings, compound **10a, 10b** and **4a** showed greater structural stability

and more consistent behavior throughout the molecular dynamic simulation relative to the other evaluated compounds. The hydrogen bonding interaction with the amide NH group plays a major role in stabilization of the ligand within the active site. Even though this interaction does not directly coordinate with the Zn^{2+} center, it contributes to maintaining a good ligand conformation by restricting molecular flexibility, thereby supporting stable metal coordination and enhancing binding stability. As well as hydrogen bond formed by heterocycle moiety also important which also helped maintain the ligand orientation within the active site and supported its interaction with the Zn^{2+} ion.

In silico complexation studies of HDAC6, HDAC3, HDAC2 and HDAC8

Analysis of Zn-ligand distances by donor atom showed different interaction patterns in HDAC6, HDAC3, and HDAC8. The Zn-N (ring nitrogen) distances were short across all isoforms, ranging from ~2.03-2.17 Å in HDAC6 (¡Error! No se encuentra el origen de la referencia.), 2.20-2.47 Å in HDAC8, and 2.16-2.22 Å in HDAC3 (¡Error! No se encuentra el origen de la referencia.**)**, This indicates that the ring nitrogen stays close to the catalytic zinc ion in all systems. Similar coordination distances have been reported for classical zinc binding groups, including hydroxamic acids (Porter *et al*., 2017, 2018) α-amino amide moiety (Xu *et al*., 2022a), and thiols (Watson *et al*., 2023) underscoring the suitability of these scaffolds for effective Zn^{2+} chelation within the HDAC6 active site. On the other hand, Zn-X (Heteroatom) distances showed isoform dependence. In HDAC6, In HDAC6, these distances range from ~2.20–3.51 Å, showing direct coordination and supporting a bidentate binding mode. (**Figure 5.11**). But, in HDAC8 and HDAC3, Zn-X the distances are longer, exceeding 3.8 Å and reaching up to 4.66 Å, indicating that there is no direct coordination and only monodentate binding occurs. (**Figure A7** and **A8**). Zn-O (ring oxygen) distances are large in all systems (HDAC6: ~4.16-4.45 Å; HDAC8: ~4.43-5.01 Å; HDAC3: ~4.62-4.88 Å), showing that this atom does not participate in binding.

A similar trend was observed for the hydroxyacetamide moiety. In HDAC6, compounds 10b, 11b, and 11c show short Zn–OH distances (1.97-2.02 Å) and Zn–C=O distances of 1.80-2.07 Å, indicative of strong bidentate coordination In HDAC2

and HDAC8, Zn–OH distances remain similar (1.92–2.09 Å), but Zn–carbonyl distances are much longer (5.50–6.02 Å) (**Table A6)**, As a result carbonyl group does not participate in binding and only monodentate interaction is possible. The distance between the zinc ion (Zn^{2+}) and the coordinating atom of the ligand is an important parameter for evaluating metal-ligand interactions in HDAC inhibition. In this study, some of the designed compound exhibited a Zn^{2+} coordination distance of 1.80-1.99 Å, which is slightly shorter than that observed for the reference inhibitor Vorinostat (2.01 Å).

Table 5.3: Interatomic Distances of Selected Heterocyclic derivatives Complex with HDAC6, (X=N, O, S).

Class	Compound	Distance Zn-N (Ring) (Å)	Distance Zn-X (Å)	Distance Zn-O (Ring) (Å)
Oxazoline	**3a**	2.08	2.18	4.1
	3b	2.03	2.11	4.11
	7a	2.15	3.51	4.34
	7b	2.11	3.29	4.29
	4a	2.17	2.20	4.22
Oxazine				
	Compound	**Distance Zn-(C=O) (Å)**	**Distance Zn-OH (Å)**	
	10b	1.99	2.00	-
	11b	1.80	1.97	-
	11c	2.07	2.02	-
Reference	***b8*** *(Porter et al., 2017)*	*2.01*	*2.00*	-

The strong interaction of the compounds with HDAC6 is mainly due to their good fit within the binding pocket and their ability to adopt an optimal orientation relative to the zinc ion. That is mainly due to the distance between zinc and doner atom. The comparatively shorter ligand-Zn^{2+} distances observed for hydroxyacetamide analogs may be due to the flexible nature of the amino alcohol group, which can better adjust to the ideal coordination geometry compared to more rigid heterocyclic systems.

According to Xu *et al*., the catalytic domain 2 (CD2) of HDAC6 contains a shallow

hydrophobic pocket approximately 11 Å in length and 3.14 Å in diameter (Xu *et al*., 2022). This feature supports binding of compact but bulky aromatic groups and contributes to HDAC6 selectivity. In line with this, Porter *et al.* reported that compounds bearing bulky substituents on both sides tend to show monodentate Zn^{2+} coordination, whereas ligands with only one or no bulky substituent preferentially form bidentate interactions, which affect binding strength and selectivity (Porter *et al*., 2018).

In the case of heterocyclic analogs, these findings shows that effective Zn^{2+} coordination requires proper ligand geometry and sufficient conformational flexibility. This behavior appears to be isoform dependent. The NH group in the linker forms a hydrogen bond that stabilizes the structure and controls flexibility, helping the ligand maintain the correct orientation for binding. In hydroxyacetamide systems, hydrogen bonding with GLY619 controls the flexibility of the amino alcohol group, keeping it at a suitable distance from the Zn^{2+} ion and limiting its movement. Hydrogen bonds near the zinc center are known to influence ligand shape and stability in HDACs, as shown in crystal structures of HDAC6 inhibitor complexes, where such interactions help stabilize the ligand inside the binding pocket (Porter *et al*., 2017b).

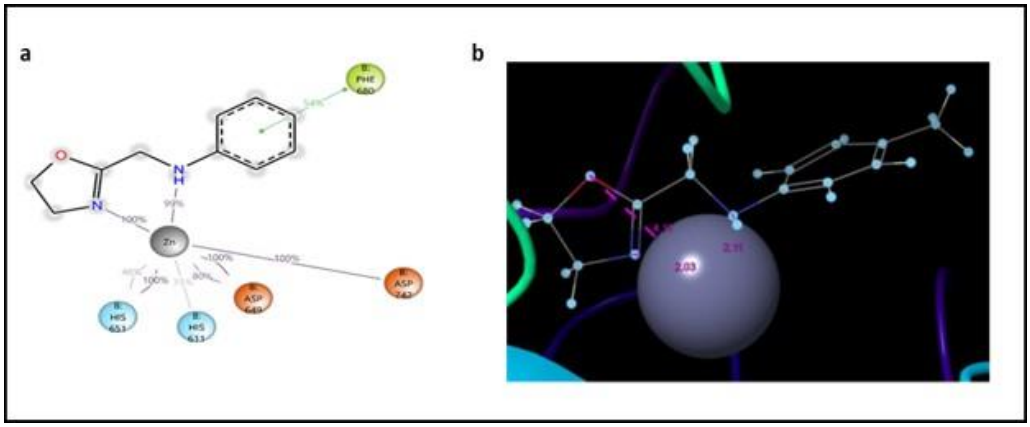

Figure 5.10: Key Zn^{2+} coordination distances observed in the HDAC6-**3a** complex during molecular dynamics simulation, showing bidentate interaction via ring nitrogen (2.17 Å) and α-nitrogen (2.24 Å).

Pharmacokinetic profiles and toxicity in silico

The *in silico* ADMET and drug-likeness was performed on eight selected

hydroxyacetamide compounds as well as three heterocyclic compounds. The result showed that these compounds have generally good pharmacokinetic and physicochemical properties. supporting their suitability as orally active drug candidates (**Table A9**). Among these, seven compounds selected from both classes showed good pharmacokinetic profiles (**Table A7**).

The molecular weights of the compounds ranged from 176.22 to 233.27 g/mol, which is below the recommended limit of 500 Da for oral drugs. The number of hydrogen bond acceptors (2–5) and donors (2–3) was within Lipinski's recommended range. Additionally, the topological polar surface area (TPSA) values, ranging from 61.36 to 80.04 $Å^2$, suggest good intestinal absorption and membrane permeability. The lipophilicity profiles, with consensus LogP values ranging from 0.73 to 1.99, indicate low to moderate lipophilicity, which helps maintain a good balance between membrane permeability and water solubility. Similarly, the AliLogS values (-2.2 to -1.54) and corresponding solubility classifications demonstrate that all compounds possess excellent aqueous solubility.

Pharmacokinetic predictions showed as all compounds exhibited high gastrointestinal absorption and none were predicted to act as P-glycoprotein (P-gp) substrates, lower risk of reduced bioavailability due to efflux transport. Only compounds 3a, 3b, and 4a were predicted to cross the blood-brain barrier (BBB), while the remaining compounds were not expected to enter the central nervous system. Moreover, most compounds showed no inhibitory activity toward major cytochrome P450 isoenzymes, indicating a low risk of metabolism-related drug–drug interactions. Only compounds **3a**, **3b**, and **4a** were predicted to inhibit CYP1A2, while none inhibited CYP2C9 or CYP3A4. Drug-likeness analysis showed that all compounds satisfied the Lipinski, Ghose, Veber, Egan, and Muegge filters without any violations. Along with no PAINS or Brenk alerts, suggesting the absence of problematic structural features that could cause toxicity or false biological activity. Although each compound showed one minor lead-likeness violation, these deviations were small and are unlikely to affect their overall drug development potential.

Among the analysed compounds, compounds **10b**, **11a**, **11c**, and **11d** exhibited the

most balanced ADME profiles. These compounds included moderate lipophilicity, with consensus Log P values ranging from 0.40 to 0.97, showing balance between aqueous solubility and membrane permeability. Taken together, the ADMET results suggest that these compounds possess good physicochemical, pharmacokinetic, and drug-like properties, supporting their use as lead compounds for further molecular docking and molecular dynamics studies.

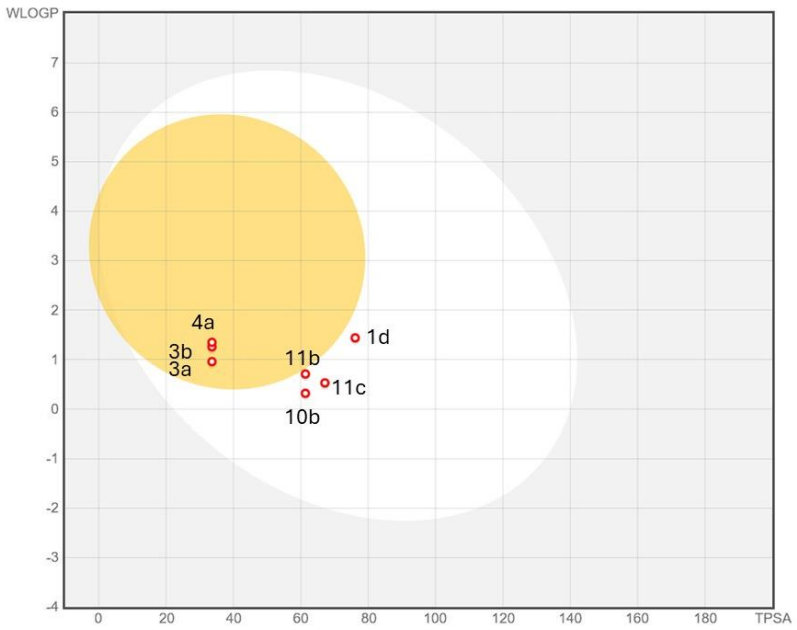

Figure 5.11: BOILED-Egg plot showing the HIA and BBB prediction of the six selected compounds.

To further evaluate the pharmacokinetic profiles of the designed compounds, a BOILED-Egg model was used (**Figure 5.12**). The resulting plot predicts that compounds **3a**, **3b**, and **4a** fall within the yolk region, indicating a high probability of crossing the BBB and potential central nervous system activity. Compounds **10b**, and **11c** are positioned within the white region but outside the yolk, indicating good predicted gastrointestinal absorption but a low probability of BBB permeation. While the compound **11b** was positioned at the boundary of the yellow yolk region, indicating possible but limited BBB penetration. The red markers in the plot represent compounds predicted to be non-substrates of P-gp. This is favorable because such compounds are

less likely to be pumped out of cells, which may improve their intracellular concentration and biological activity. Considering these findings, the BOILED-Egg analysis suggests that most compounds possess physicochemical properties compatible with oral bioavailability, while only a **3a**, **3b**, and **4a** demonstrates characteristics suitable for CNS penetration.

However, toxicity predictions using the PROTOX platform showed that the compounds generally have acceptable safety profiles, although some may have potential risks of neurotoxicity, respiratory toxicity, and nephrotoxicity (**Table 5.4**). Among the derivatives 11d and 11e showed important safety risks, including predicted neurotoxicity, nephrotoxicity, respiratory toxicity, and carcinogenicity. The alkyl-substituted analogues 10a and 10b also showed cardiotoxic and mutagenic risks. In contrast, 11c and 11f exhibited comparatively safer toxicity profiles, Based on the combined ADMET and toxicity predictions, compounds **4a** and **11c** were identified as the better candidates for further HDAC inhibitory and biological evaluation.

Table 5.4: Toxicity prediction of seven selected compounds.

Toxic Prediction	3a	3b	4a	10b	11b	11c
Hepatotoxicity	Inactive (0.88)	Inactive (0.88)	Inactive (0.86)	Inactive (0.9)	Inactive (0.9)	Inactive (0.88)
Neurotoxicity	Active (0.68)	Active (0.67)	Active (0.66)	Active (0.55)	Active (0.54)	Active (0.78)
Nephrotoxicity	Active (0.66)	Active (0.67)	Active (0.64)	Active (0.59)	Active (0.58)	Active (0.58)
Carcinogenicity	Inactive (0.54)	Inactive (0.53)	Inactive (0.56)	Inactive (0.66)	Inactive (0.65)	Inactive (0.68)
Respiratory toxicity	Active (0.79)	Active (0.77)	Active (0.79)	Active (0.73)	Active (0.73)	Active (0.83)
Immunotoxicity	Inactive (0.98)	Inactive (0.99)	Inactive (0.98)	Inactive (0.99)	Inactive (0.99)	Inactive (0.99)
Cytotoxicity	Inactive (0.72)	Inactive (0.71)	Inactive (0.69)	Inactive (0.64)	Inactive (0.64)	Inactive (0.85)
Mutagenicity	Inactive (0.57)	Inactive (0.58)	Inactive (0.58)	Active (0.51)	Inactive (0.5)	Inactive (0.6)
Cardiotoxicity	Inactive (0.67)	Inactive (0.67)	Inactive (0.69)	Active (0.67)	Active (0.65)	Inactive (0.68)

BBB-barrier	Active (0.89)	Active (0.88)	Active (0.90)	Active (0.61)	Active (0.58)	Active (0.71)

Free energy

MMGBSA calculations were used to estimate binding free energies of the ligand-protein complexes. Unlike molecular docking, this method considers solvation effects and molecular mechanics, providing a more accurate evaluation of ligand binding. Therefore, MM/GBSA complements docking studies by helping to confirm binding stability and improve the reliability of *in silico* drug screening and lead optimization.

The different interaction profiles with HDAC6, HDAC8, and HDAC3 are supported by the free energy analysis, which reveals a marked variation in the MM-GBSA binding energy values. The total binding free energy for 16 selected compounds interacting with three HDAC isoforms was calculated by considering several energy contributions, including coulombic, covalent, hydrogen bonding, lipophilic, π-π stacking, solvent generalized bonding (SolvGB) and Van der Waals energies.

The analysis was performed using snapshots obtained from 500 ns molecular dynamics simulations. To ensure a fair comparison among the three HDAC isoforms, the crystal structure of HDAC8 (PDB: 1T69) was used as the reference structure and aligned with HDAC3 and HDAC6, structures rather than generating initial binding poses through redocking of vorinostat. The calculated binding free energies (ΔG_bind) and their energy components are summarized in Table 3.

For HDAC6, compounds **3a**, **3c**, **4c**, **7a**, and **7c** (**Table 5.4**) showed much stronger binding than the reference inhibitor SAHA (Vorinostat). Their binding free energies ranged from −133.89 to −142.07 kcal/mol, while SAHA showed a value of −10.39 kcal/mol. Among these compounds, 4c showed the strongest binding (−142.07 kcal/mol), followed by **3c** (−138.62 kcal/mol) and **3a** (−138.43

kcal/mol). Electrostatic interactions contributed strongly to binding, with Coulombic energy values ranging from −240.85 to −301.94 kcal/mol, which were much stronger than that of SAHA (−74.11 kcal/mol). The order of binding affinity was **7c** > **4c** > **3c** > **3a** > **7a** > SAHA. Van der Waals interactions also played an important role, particularly for compound **3c**, which showed the largest contribution. Lipophilic interactions were goood, especially for compounds **4c** and **3c**. Hydrogen-bonding interactions were also stronger than those observed for SAHA, with compound **7c** showing the highest contribution. These favorable interactions were partially offset by positive solvation penalties (259.19 to 317.99 kcal/mol), where **7c** showed the highest desolvation cost.

In HDAC8, the compounds showed weaker binding than in HDAC6, with binding free energies ranging from −28.50 to −33.43 kcal/mol, compared with −4.39 kcal/mol for SAHA. Electrostatic and hydrogen-bonding contributions were relatively small. Binding was mainly supported by van der Waals and lipophilic interactions, together with lower solvation penalties than those observed for SAHA

For HDAC3, the calculated binding free energies ranged from −37.34 to −42.83 kcal/mol, which were better than that of SAHA (−11.46 kcal/mol). Van der Waals and lipophilic interactions were the main contributors to binding, while hydrogen-bonding contributions remained relatively small. Solvation energy penalties were also lower than those observed for SAHA.

Taken together, the MM/GBSA results show that the designed compounds bind most strongly to HDAC6, followed by HDAC3 and HDAC8. Compounds **3a**, **3c**, and **4c** showed the most attractive binding energies in HDAC6, suggesting stronger and more stable protein–ligand interactions than the reference inhibitor SAHA.

Table 5.5: MM-GBSA of top score compounds in each HDAC6, HDAC8 and HDAC3

COMPOUND	dG_Bind	dG_Coulomb	dG_Hbond	dG_Lipo	dG_Solv_GB	_dG_vdW
HDAC6(5EDU)						
4c	-142.0746	-289.0770	-6.7134	-40.7859	309.4786	-119.3713
3a	-138.4250	-278.3699	-6.5183	-40.1753	296.0438	-116.3622
3c	-138.6218	-282.1277	-6.6117	-40.2330	302.2530	-120.6738
7c	-135.0693	-301.9380	-7.4406	-38.7621	317.9885	-116.2923
7a	-133.8864	-240.8481	-6.8503	-38.8785	259.1942	-115.2676
SAHA	-10.3943	-74.1058	-0.5317	-14.1078	105.0380	-26.6464
HDAC8(1T64)						
6a	-33.9599	-10.2093	-0.0997	-11.0369	21.4018	-34.3836
7b	-28.5093	0.7977	-0.2143	-6.9801	9.6865	-32.5991
3c	-33.4367	-15.7623	-0.2921	-11.1338	19.5272	-28.6647
3a	-33.1014	-11.6571	-0.7814	-10.0323	22.5209	-32.9554
8c	-29.6492	-8.1845	-0.0529	-9.1050	18.1693	-30.2593
SAHA	-4.3986	-47.0896	-1.3275	-10.4610	83.6777	-30.6535
HDAC3(4A69)						
4c	-37.3445	-10.7956	-0.6042	-13.5428	23.8797	-34.6842
7c	-38.7100	-5.8209	-0.1951	-15.8110	22.2015	-36.5358
3b	-42.8300	-1.9802	-0.7376	-11.3097	9.7375	-36.9058
SAHA	-11.4676	-30.0778	-1.2065	-17.7449	85.2099	-50.1839

*dG_bind, binding free energy; dG_coulombic energy; dG_Hbond, hydrogen bond energy; dG_Lipo, lipophilic energy; dG_solv, solvation energy; dG_vdw, van der Waals energy.

5.2 Experimental studies

As mentioned previously, this work involved the design of heterocyclic molecules (oxazolines and oxazines) and hydroxy acetamides as potential novel HDAC inhibitors for cancer applications, using docking and molecular dynamics studies. Heterocycles **3a**, and **3b**, as well as eight hydroxy acetamides (**10a-b** and **11a-f**), show the highest

binding energies specifically for HDAC6. Based on these results and their synthetic accessibility, MM-GBSA analysis was performed on the three heterocycles (which are difficult to synthesize) to confirm the *in-silico* results obtained and to propose these molecules as potential HDAC inhibitors for further synthesis. The eight hydroxyacetamides were synthesized, characterized, and evaluated *in vitro* against three cancer cell lines and their cytotoxicity against a normal cell line. These results are presented and discussed below.

5.2.1 Synthetic Scheme

The synthesis of hydroxy acetamides **10a-b** and **11a-f** was performed following the synthetic route described in the methodology section (**Figure 4.1**) First, *N*-substituted esters **9a-f** were prepared from ethyl bromoacetate and anilines (**a** and **b**), imidazole (**f**), benzimidazole (**c**), and benzotriazole (**d** and **e**), the following results were obtained. The esters were synthesized by reacting ethyl bromoacetate and aniline using DIPEA as base (**Figure 5.13**).

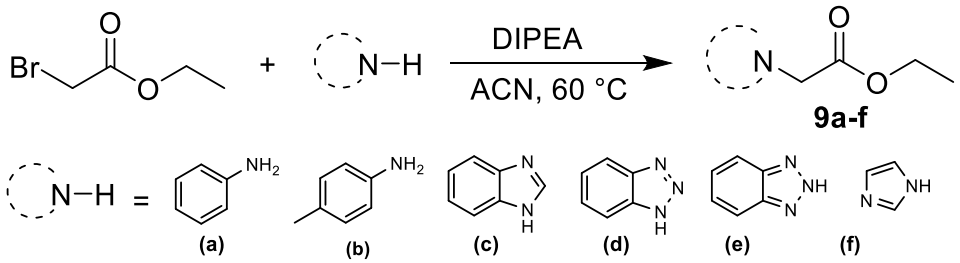

Figure 5.12: synthetic route of ester derivatives.

In order to obtain pure ester intermediates with high yield, various reaction conditions were investigated, including different solvents, temperatures, and catalysts (**Table 5.6**)

Table 5.5: Conditions for the synthesis of ester **9a** and **9b**.

Entry	Solvent	Temperature	Base	Time	Method	Yield (%)
1	Acetonitrile	60 °C	Et_3N	1:45 h	Sonication	85%
2	Acetonitrile	140 °C	Et_3N	5 min	Microwave	86%
3	Acetonitrile	50 °C	DIPEA	3 h	Heating	99%

As can be seen in **Table 5.6**, the three reaction conditions explored for anilines **a** and **b** showed very good yields, greater than 85%. However, the use of DIPEA as a base and acetonitrile as a solvent gives almost quantitative yield of the product.

The TLC of compound **9b** is shown below (**Figure 5.14**). The formation of the ester was confirmed by the appearance of a new TLC spot below ethyl bromoacetate and above the *N*-aryl/heteroaryl precursor when it runs in a 7:3 hexane-ethyl acetate solvent system. The results are summarized in **Table 5.7**.

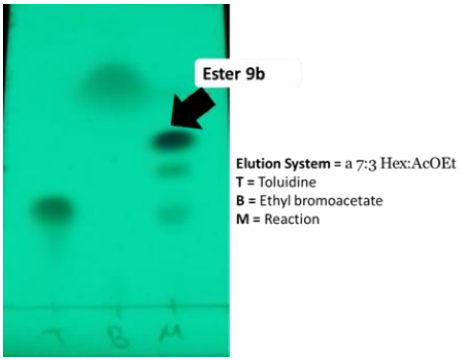

Figure 5.13: TLC of reaction of **9b**

Table 5.6: Physicochemical properties of synthesized ester derivatives.

Compound	Physical appearance	Colour	Yield (%)	M.P. (°C)
9a	Crystalline solid	Yellow	99	54-55
9b	Crystalline solid	Light-yellow	78	55-57
9c	Solid	Yellow	83	68-70
9d	Solid	White	88	83-84
9e	Fine powder	White	89	122-124
9f	Oil	Yellow	72	N.D.

As shown in **Table 5.7**, all the obtained esters, except **9f**, were isolated as solid compounds with yields greater than 70%. Compound **9a** (derived from aniline) was obtained in nearly quantitative yield. It can be observed that the variations in yield are related to the purification technique. The ^{1}H, ^{13}C NMR spectra and HRMS of esters **9a** and **9f** are described below as examples. The spectra of the remaining esters can be found in the Annexes section.

Ethyl phenylglycinate 9a

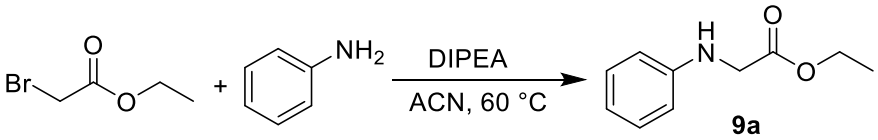

Figure 5.14: Synthesis of ester **9a**.

The most important **^{1}H NMR** signals for ester **9a** are described below (**Figure 5.16**). At a chemical shift of 7.19 ppm, two overlapping signals of the doublet of doublet type are observed, corresponding to aromatic protons labeled 1 and 3, with coupling constants of 7.5, and 7.3 Hz, and integrating for two hydrogens. A triplet of triplet signal at 6.76 ppm is assigned to aromatic proton number 2, which has coupling constants of 7.35, and 1.1 Hz, for 1H. At a shift of 6.61 ppm, two overlapping signals

of the doublet of triplet are again observed, corresponding to aromatic protons of 4 and 6, with coupling constants of 7.65, and 1.2 Hz, and integrating for two hydrogens. The signal at 4.28 ppm is a broad singlet that represents the proton of the NH and integrates for 1H. 4.23 ppm a quadruple signal is observed corresponding to the methylene of the ester, with a coupling constant of 7.0 Hz and integrates for 2H. A doublet at 3.89 ppm (J = 5.05Hz,2H) was assigned to the protons of the CH_2 adjacent to the amine group. At a shift of 1.29 ppm a triplet is detected corresponding to the methyl group of the ester, with a coupling constant of 7.35 Hz and integrates for 3H.

^{1}H NMR (500 MHz, *$CDCl_3$*): δ 7.19 (dd, J = 7.5, 7.3 Hz, 2H, **$H_{Ar\ 3\ and\ 1}$**), 6.76, (tt, 1H, J = 7.35,1.1Hz, **$H_{Ar\ 2}$**), 6.61 (dt, J = 7.65, 1.2 Hz, 2H, **$H_{Ar\ 4,6}$**), 4.28 (bs, 1H, **NH**), 4.23 (q, J = 7.0 Hz, 2H, O**CH_2**), 3.89 (d, J = 5.05 Hz, 1H, NH-**CH_2**), 1.29 (t, J = 7.35 Hz, 3H, **CH_3**CH_2O)

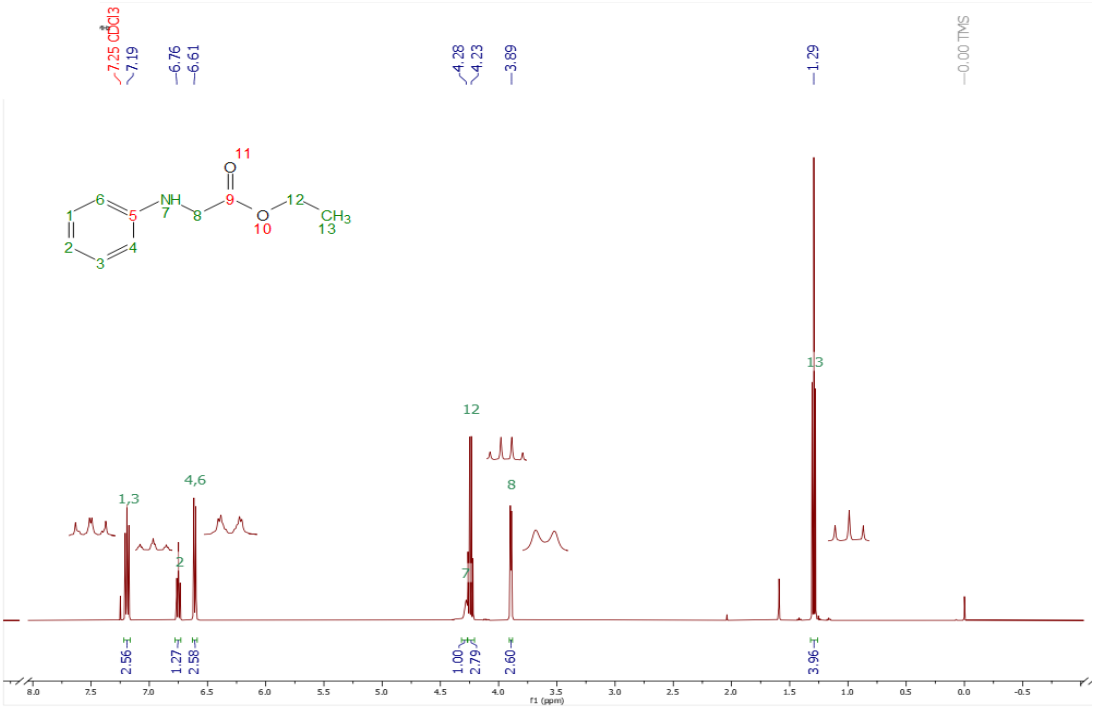

Figure 5.15: ^{1}H NMR spectrum of **9a**.

^{13}C NMR spectrum (176 MHz, *DMSO-d_6*) showed the following signs: δ 171.31 (**C=O**), 147.27 (**C_{Ar5}**-N), 129.54 (**$C_{Ar1,3}$**), 118.42 (**C_{Ar2}**), 113.24 (**$C_{Ar4,6}$**), 61.54 (NH_2-

CH$_2$), 46.10 (O-**CH**$_2$), 14.42 (CH$_2$**CH**$_3$).

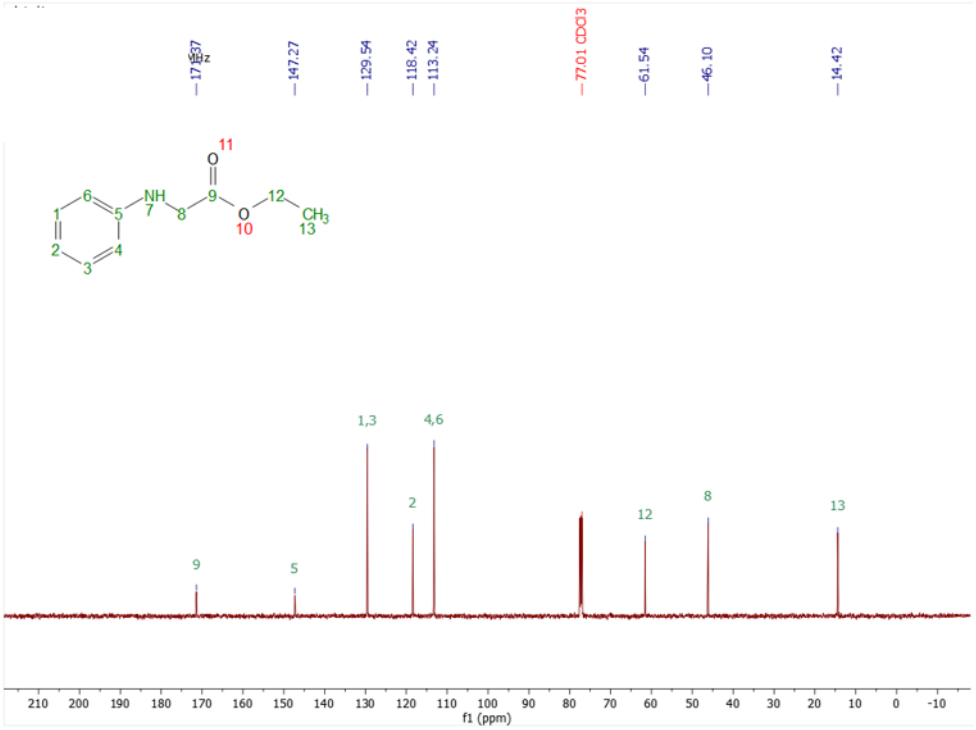

Figure 5.16: ^{13}C NMR spectrum of **9a**.

High Resolution Mass Spectrometry (HRMS) (ESI$^+$): *m/z* calculated for $C_{10}H_{13}NO_2$ 179.0946; found180.1015 for compound **9a**.

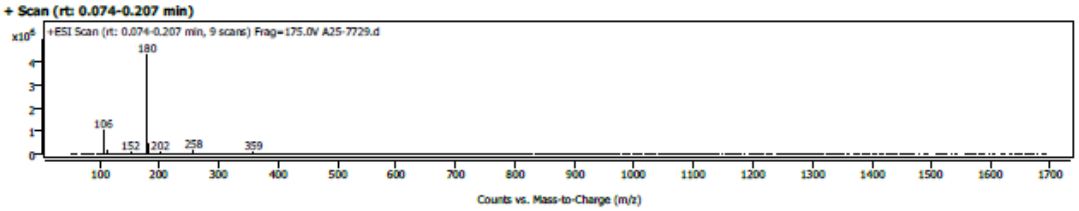

Figure 5.17: HRMS of **9a**.

Ethyl 2-(1H-imidazol-1-yl) acetate 9f

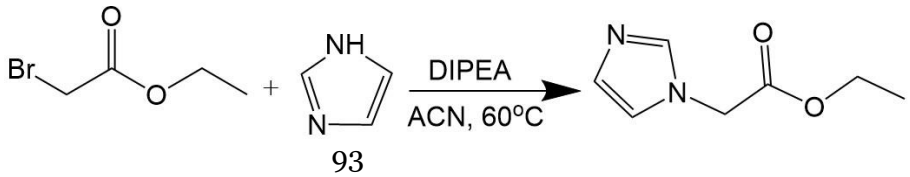

93

Figure 5.18: Synthesis of ester **9f**.

The **^{1}H NMR** signals for ester **9f** are described in **Figure 5.20**. At a chemical shift of 7.52 ppm, a singlet signal is seen to one of the protons of the imidazole group (N=**CH**N), integrating for 1H. A pseudo triplet signal at 7.01 ppm with coupling constants of 1.24 Hz assigned to another of the imidazole protons (N-**CH**-CH) is identified, integrating for 1H, At a shift of 6.98 ppm, another pseudo triplet signal is observed, having coupling constants of 1.36 Hz, which is assigned to the third hydrogen of the imidazole (N**CH**=CH), integrating for 1H. Protons of the methylene group adjacent to the carbonyl of the ester give rise to singlet at 4.73ppm, for 2H. A quartet signal at 4.23 ppm with a coupling constant of 7.16 Hz is observed, for the methylene group of the ester, integrating for 2H. Lastly, at 1.26 ppm, a triplet is noted, consistent with the presence of the methyl group of the ester, with a coupling constant of 7.36Hz and integral for 3H.

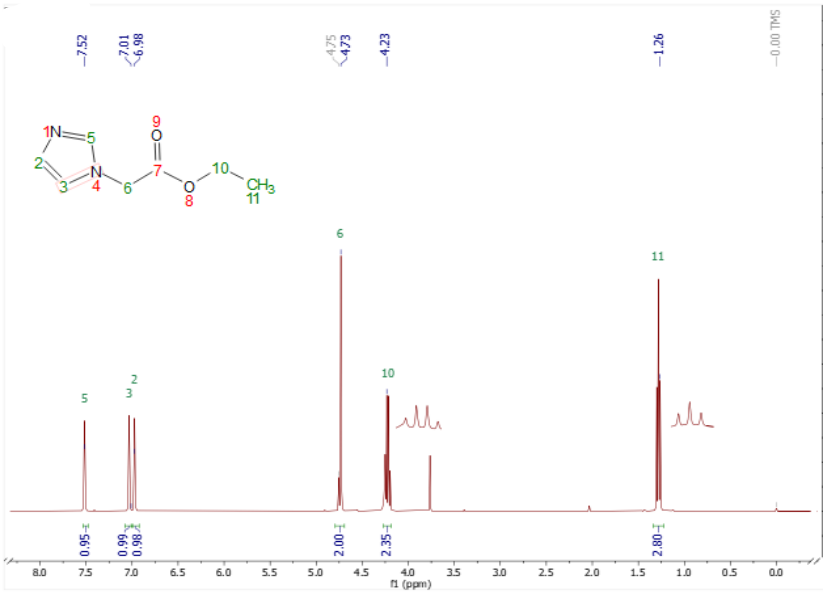

Figure 5.19: ^{1}H NMR spectrum of **9f**.

^{1}H-NMR (400 MHz, *CDCl*$_3$): δ 7.52 (s, 1H, N=**CH**N), 7.01 (pst, J = 1.24 Hz, 1H, N-**CH**-CH), 6.98 (pst, J = 1.36 Hz, 1H, N**CH**=CH), 4.73 (s, 2H, **CH$_2$**C=O), 4.23 (q, J = 7.16 Hz, 2H, O**CH$_2$**), 1.26 (t, 7.36Hz, 3H, **CH$_3$**CH$_2$O).

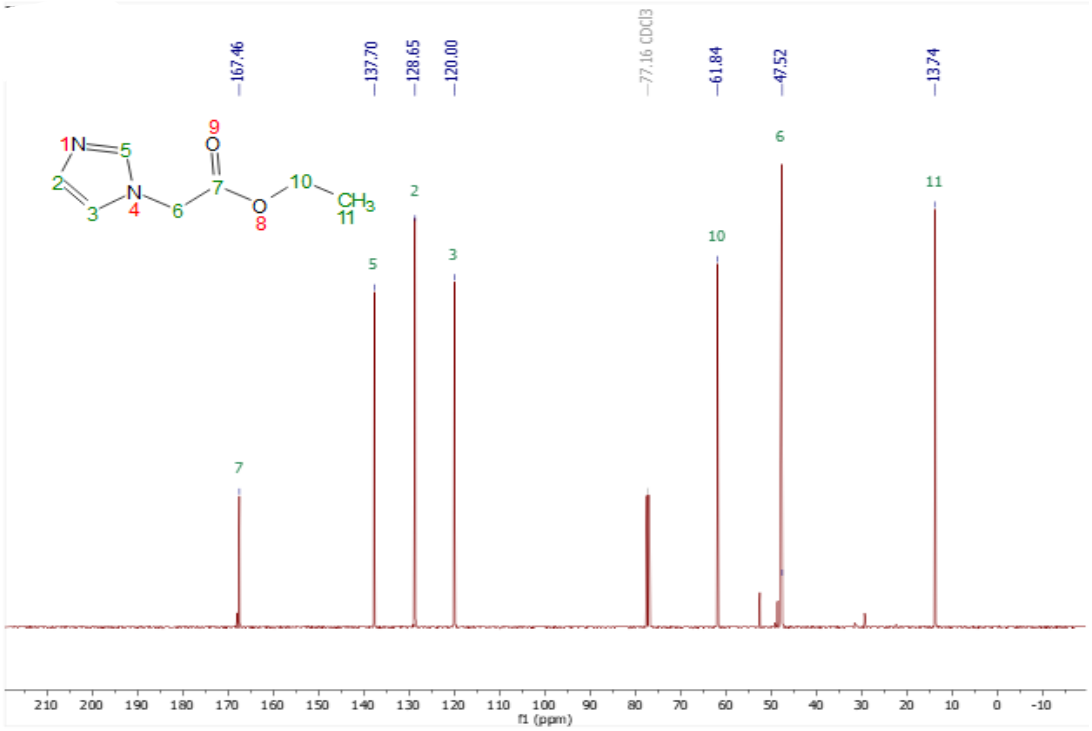

Figure 5.20: 13C NMR spectrum of **9f**.

^{13}C NMR spectrum (176 MHz, *DMSO-d_6*): δ 167.44 (**C=O**), 137.70 (**C_{Ar5}**-N), 128.65 (N=**C**-N), 120.00 (N-**CH**=C), 61.84 (O=C-**CH2**), 47.52 (O-**CH_2**), 13.71 (CH2**CH_3**).

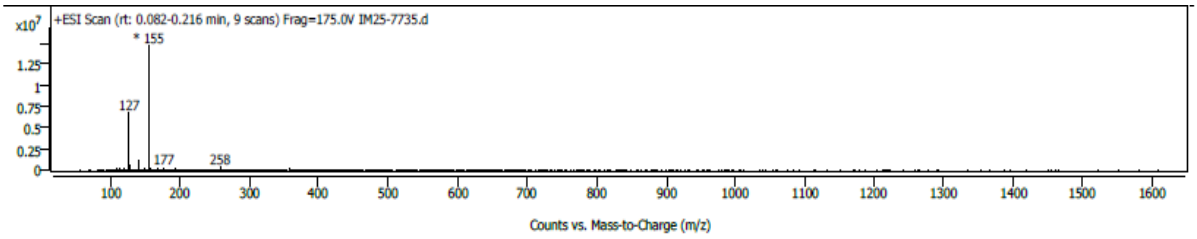

Figure 5.22: HRMS of **9f**.

HRMS (ESI$^+$): *m/z* calculated for $C_7H_{10}N_2O_2$ 154.0742; found 155.0812 for compound **9f**.

With the *N*-substituted esters, the coupling reaction of these esters with ethanolamine (**10**) or propanolamine (**11**) was carried out to form the corresponding

hydroxyacetamides **10a-b** and **11a-f**. Two routes for obtaining *N*-substituted hydroxyacetamides were tested using aniline derivatives as a reference (**Table 5.8**): (a) transforming the ester into its carboxylic acid by basic hydrolysis with NaOH for subsequent coupling with amino alcohols (ethanolamine and propanolamine) under different coupling agents (iBuOCOCl, HBTU, $(Boc)_2O$, and DCC). Condition (b) was to test the same reaction starting from the original ester using coupling agent such as iBuOCOCl or ethyl chloroformate under reflux and microwave conditions (**Figure 5.23**).

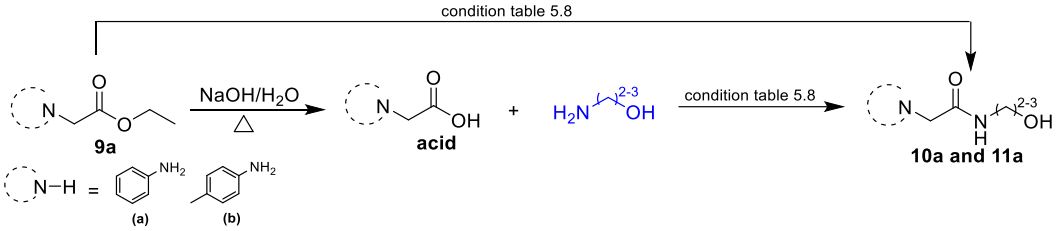

Figure 5.21: Synthetic reaction of hydroxyacetamides derivatives.

Table 5.7: Conditions for the synthesis of hydroxy acetamide **10a** and **11a**.

Acid derivative						
Entry	**Solvent**	**Base /catalyst**	**Coupling reagent**	**Conditions**	**Time**	**Yield (%)**
1	DCM (dry)	NMM	iBuOCOCl	0 °C (only 15 min), Stirring, R.T.	18 h	No reaction
2	DCM (dry)	DIPEA	HBTU	0 °C (only 20 min), Stirring, R.T.	43 h	No reaction
3	DCM (dry)	DMAP, Et_3N	DCC	0 °C (only 15 min), Stirring, R.T.	48 h	No reaction
4	DCM (dry)	DIPEA	HBTU	0 °C (only 15 min), Stirring, R.T.	48 h	No reaction
5	DCM (dry)	DMAP, Et_3N	DCC	0 °C (only 15 min), Stirring, R.T.	24 h	No reaction
6	DCM (dry)	DMAP, Pyr	BOC_2O	0 °C (only 15 min), Stirring 0 °C	8 days	No reaction
Ester derivative						
1	MeCN	Triethylamine	iBuOCOCl	Reflux	24 h	No reaction
2	MeCN	*p*-TsOH	-	Microwave (140-180 °C)	½ h- 4 h	Reaction

As shown in the table, all the reaction conditions tested for coupling from the

carboxylic acid and the amino alcohol failed, as it was not possible to detect the appearance of new spots when monitoring the reaction by TLC; only the raw materials were observed.

The main reason for the unsuccessful amide bond formation is that, despite the carboxylic acids are activated, they immediately undergo acid-base interactions with the amine, which lead to the formation of an insoluble salt (observed as precipitation). As a result, salt formation predominates over the amide coupling reaction, thereby suppressing amide bond formation.

The failure of the coupling reaction between the carboxylic acid and the amino alcohol under conventional conditions can be explained by the formation of a stable orbital, through a combination of frontier molecular orbital analysis, acid-base stabilization of salts, and reaction coordinate studies. Frontier molecular orbital analysis shows that the amine's HOMO orbital (0.240554 Ha, 6.55 eV) and the acid's LUMO orbital (0.002130 Ha, 0.058 eV) are separated by a large energy gap (∼ 0.238 Ha, ≈ 149.6 kcal/mol), indicating nucleophilic reactivity caused by weak orbitals.

Structural optimization of the acid-amine system reveals the spontaneous formation of a tightly bound acid-base complex, characterized by partial proton transfer. This is supported by a short N-H distance (∼ 1.10 Å), a long O-H distance (∼ 1.28 Å), and polarization of the nitrogen atom (N charge ≈ -0.33) (Gilli et.al, 2009). These features indicate that the amine lone pair participates in strong hydrogen bonding and is not freely available for nucleophilic attack. The calculated salt stabilization energy (ΔEsalt ≈ -14.2 kcal/mol) further confirms that the formation of this associated state is thermodynamically favored over productive bond formation. As a result, the system remains trapped in a stable, non-reactive form, preventing amide bond formation under normal conditions. Complete ionization to a separate ammonium carboxylate salt is not observed. Still, the interaction is still strong enough to reduce nucleophilicity and prevent amidation under normal conditions.

Reaction coordinate (C–N bond) scans further support this conclusion. For the acid–amine system, a shallow energy minimum is observed at a long C–N distance (~3.4 Å), corresponding hydrogen-bonded complex between the acid and amine. As the C–

N distance is decreased, the energy increases sharply (above 80 kcal/mol), indicating strong steric/electrostatic repulsion and an unfavorable pathway toward covalent bond formation. (**Figure 5.24**).

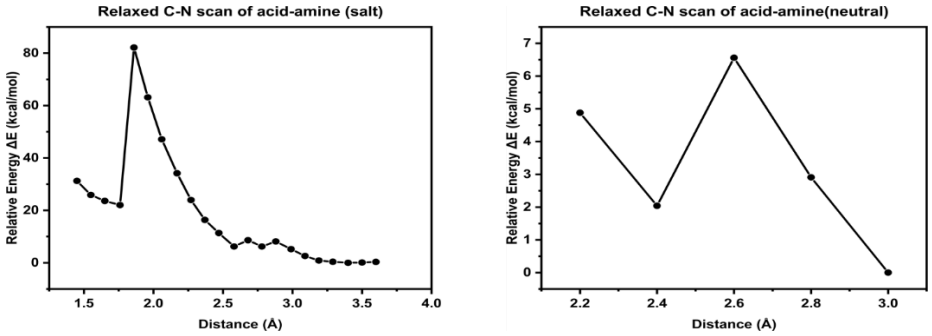

Figure 5.22: Relaxed C–N scan of acid-amine (Salt) and neutral.

In contrast, the ester-amine system does not form a strong acid-base complex. Its C-N scan shows only mild stabilization at intermediate distances (ΔE ≈ -4.4 kcal/mol at 2.8 Å), suggesting that bond formation is more accessible. Even though, a large HOMO-LUMO gap in the ester-amine system makes the reaction unfavorable, the system does not get trapped in a strong acid-base complex. Therefore, when external energy is supplied, the reaction can still occur. (**Figure 5.25**).

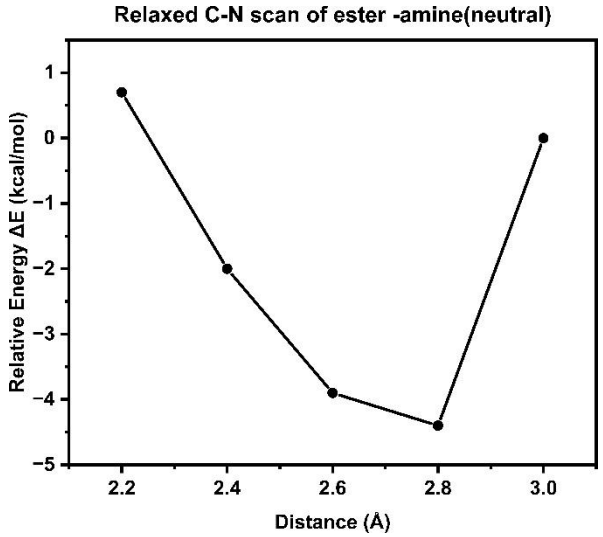

Figure 5.23: Relaxed C–N scan of ester-amine.

Therefore, the coupling reaction was conducted using microwaves as an activation

method in the presence of esters **9a-f**, ethanolamine or propanolamine and *p*-toluene sulfonic acid (*p*TsOH) as a catalyst. The hydroxyacetamides **10a-b** and **11a-f** obtained with yields greater than 70% (**Figure 5.26**).

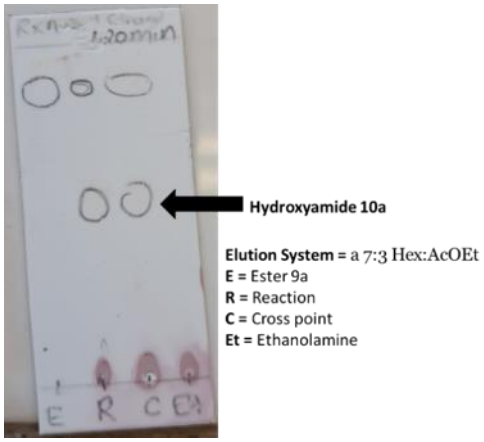

Figure 5.24: TLC of the **10a** coupling reaction by microwaves.

Hence, microwave irradiation in a single vessel was established as the standard condition for amide synthesis (**Figure 5.27**). The physical properties of the synthesized hydroxyamide derivatives are summarized in **Table 5.9**.

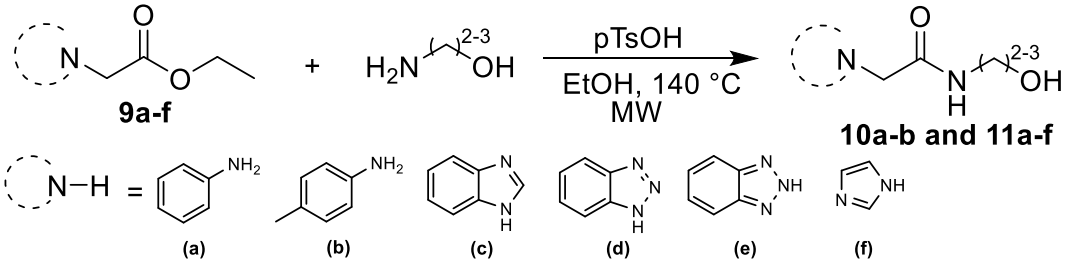

Figure 5:25: Synthetic reaction of hydroxyacetamides derivatives.

Table 5.8: Physicochemical properties of synthesized hydroxyacetamide derivatives.

Compound	Physical appearance	Color	Yield (%)	M.p. (°C)
10a	Crystalline solid	White	91	69-70
10b	Crystalline solid	Yellow	77	69-71
11a	Crystalline solid	Yellowish brown	84	68-70

11b	Viscous liquid	Yellow	88	N. D
11c	Fine powder	White	89	208-210
11d	Fine powder	White	82	125-127
11e	Feather-like solid	White	88	152-154
11f	Fine powder	White	79	98-100

Overall, these results show that the dominant acid-amine association are the main reasons for amidation failure under conventional conditions.

Even though, with the support of coupling agents and microwave energy, the eight hydroxyamides were obtained, with good yields, greater than 77%.

The ^{1}H, ^{13}C NMR spectra and HRMS of hydroxyacetamides **10a, 10b** and **9f** are described below as examples. The spectra of the remaining hydroxyacetamides can be found in the Annexes section.

N-(2-hydroxyethyl)-2-(phenylamino) acetamide 10a

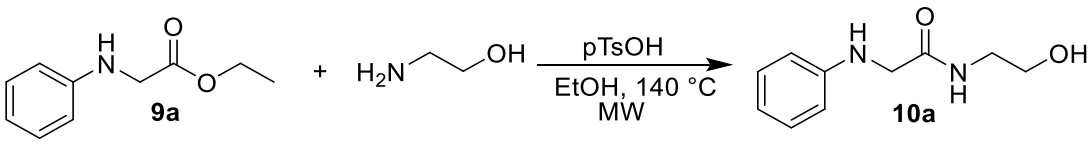

Figure 5.26: Synthetic reaction of hydroxyamide **10a.**

Figure 5.29 shows the **^{1}H NMR** signals for hydroxyacetamide **10a**. At a chemical shift of 7.22 ppm, two merged doublet of doublet signals are observed, and are assigned to aromatic protons labeled 4 and 6, with coupling constants of 7.35 and 7.3 Hz, which is integrate for two hydrogens. A broad singlet has appeared corresponding to the amide NH proton at 7.20 ppm, integrating for 1H. Aromatic proton 2 gives a triplet of triplet signal at 6.82 ppm, with coupling constants of 7.3 and 1.1 Hz, integrating for 1H. At 6.63 ppm, two overlapping signals of the doublet of doublet are again detected, corresponding to the aromatic protons named as 1 and 3, with coupling constants of 7.68 and 1.05 Hz, and integrating for two hydrogens. A pseudo triplet signal at 4.35 ppm with coupling constant 5.04 Hz is found that corresponds to the proton of the NH group of aniline and integrating for 1H. A doublet is seen at 3.80 ppm (J = 5 Hz,2H),

was assigned to the hydrogens of the methylene group adjacent to the NH group. At 3.66 ppm, a triplet signal is detected with a coupling constant of 4.9 Hz assigned to the protons of the methylene group adjacent to the hydroxyl group, integrating for 2H. A quartet signal was detected at 3.44 ppm, with coupling constants 5.65 Hz, which is assigned to the methylene group attached to the NH group and integrating for 2H. At last, broad singlet is found at 3.07ppm integrating for 1H is assigned to OH group

^{1}H-NMR (400 MHz, *CDCl*$_3$) δ 7.22 (dd, J = 7.35, 7.3 Hz, 2H, **H$_{Ar\ 1,3}$**), 7.20 (bs, 1H, **NH**C=O) 6.82 (tt, J = 7.3, 1.1 Hz, 1H, **H$_{Ar\ 2}$**), 6.63 (dd, J = 7.68, 1.05 Hz, 2H, **H$_{Ar\ 4,6}$**), 4.35 (pst, J = 5.04 Hz, 1H, **NH**-CH$_2$), 3.80 (d, J = 5.0 Hz, 2H, NH**CH$_2$**), 3.66 (t, J = 4.9 Hz, 2H, OH-**CH$_2$**), 3.44 (q, J = 5.65 Hz, 2H, **CH$_2$**NH), 3.07 (brs, 1H, **OH**).

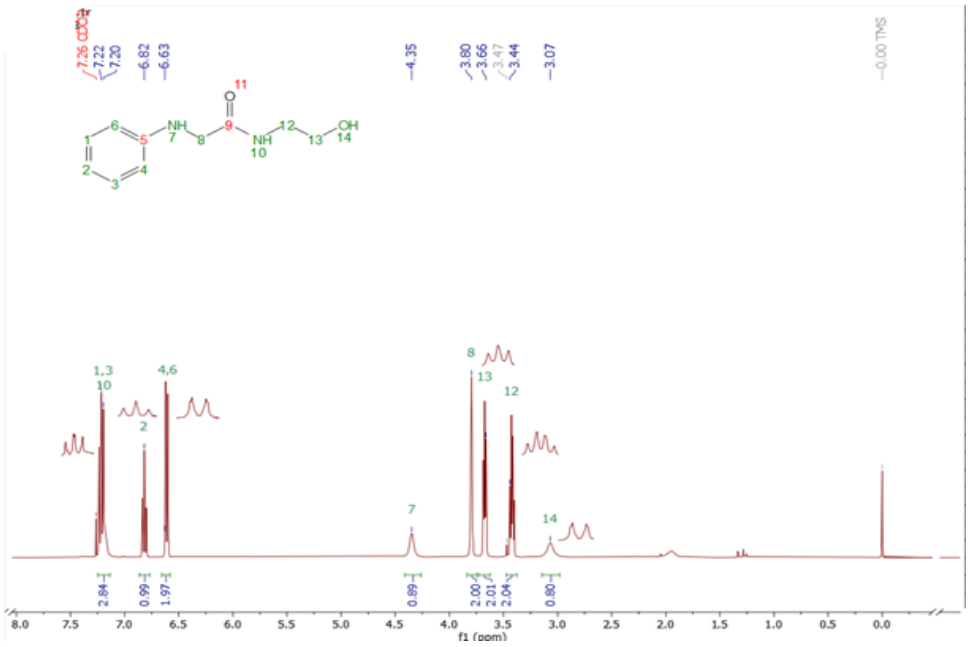

Figure 5.27: ^{1}H NMR spectrum of **10a**.

^{13}C NMR (176 MHz, DMSO-d$_6$): δ 172.02 (**C=O**), 147.09 (**C$_{Ar5}$**-N), 129.51 (**C$_{Ar1,3}$**), 119.20 (**C$_{Ar2}$**), 113.19 (**C$_{Ar4,6}$**), 62.19 (OH-**CH$_2$**), 48.77 (NH-**CH$_2$**), 42.67 (CH$_2$**NHC=O**).

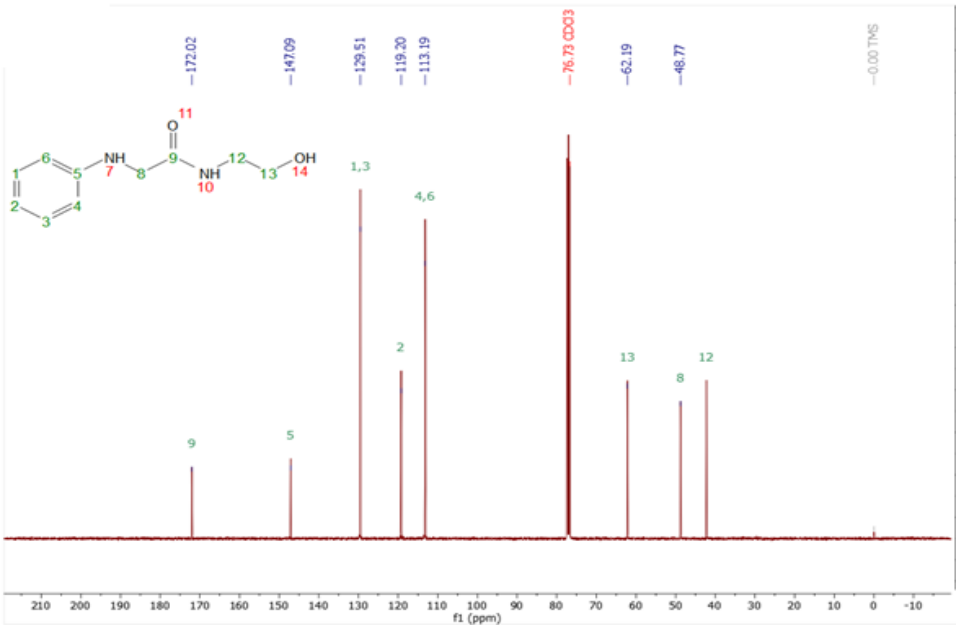

Figure 5.28: ^{13}C NMR spectrum of **10a**.

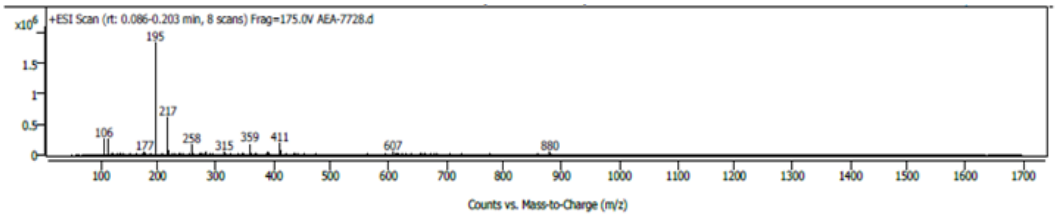

Figure 5.29: HRMS of **10a**.

HRMS (ESI+): *m/z* calculated for $C_{10}H_{14}N_2O_2$ 194.1055; found 195.1119 for compound **10a**.

N-(2-hydroxyethyl)-2-(p-tolylamino) acetamide 10b

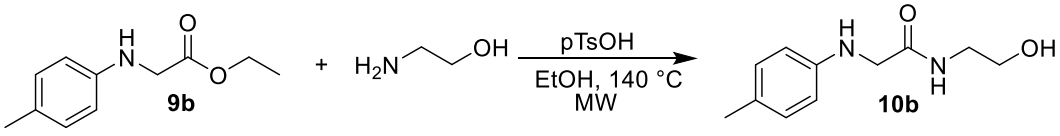

Figure 5.30: Synthetic reaction of hydroxyamide **10b**.

The **^{1}H NMR** characterization of hydroxyacetamide **10b** is shown in Figure **5.33**. The amide group's NH protons exhibit a pseudo triplet signal with a coupling constant of 6.6Hz that

integrates for one hydrogen at a chemical shift of 7.23 ppm. A doublet signal corresponding to aromatic protons 1 and 3, integrating for two hydrogens, is detected at 7.01 ppm. Another doublet corresponding to aromatic protons 4 and 6, integrating for 2H, is found at 6.52 ppm. A broad singlet signal corresponding to the proton of the aniline's NH group, integrating for 1H and is detected at 4.21 ppm. The methyl group near to the NH group is identified by a singlet signal at 3.77 ppm, which integrates for 1H. The methylene group next to the hydroxyl group is assigned to a triplet signal at 3.69 ppm, which integrates for 2H and has a coupling constant of 6.6 Hz. A quartet signal with coupling constants of 6.6 Hz is detected at a shift of 3.41 ppm, it integrates for 2H, which corresponds to the methylene group connected to the NH. At 3.03 ppm broad signal represents the OH group. Lastly, a singlet signal corresponding to the methyl group in the para position to the phenyl ring is detected at 2.25 ppm, integrating for 3H.

^{1}H-NMR (500 MHz, *CDCl*$_3$): δ 7.23 (pst, *J* = 6.6 Hz 1H, **NH**), 7.01 (d, *J* =10.25, 2H, **H$_{Ar\ 1,3}$**), 6.52 (d, *J*=10.05, 2H, **H$_{Ar\ 4,6}$**), 4.21 (brs, 1H, **NH**Ph) 3.77 (s, 2H, **CH$_2$**-NH), 3.69 (t, *J*=6.6 Hz, 2H, **CH$_2$**OH), 3.41 (q, *J*=6.6 Hz, 2H, NH-**CH$_2$**), 3.03 (brs, 1H, **OH**) 2.25 (s, 3H, **CH$_3$**Ph).

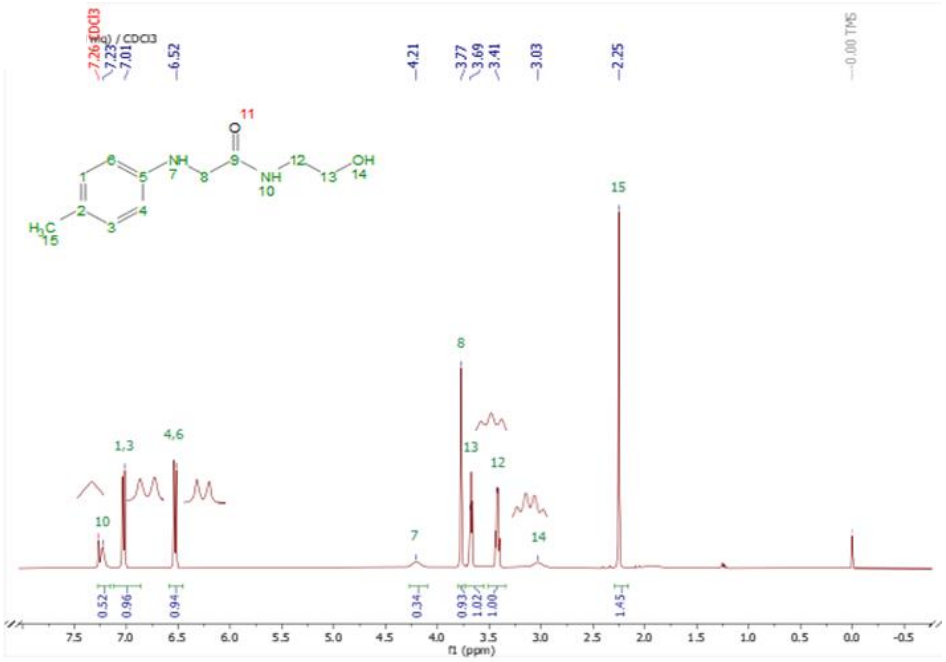

Figure 5.31: ^{1}H NMR spectrum of **10b.**

^{13}C NMR (176 MHz, DMSO-d6): δ 172.26 (**C**=O), 144.78 (Ar_5), 129.98 (**Ar**$_{1,3}$), 128.56 (**Ar**$_2$), 113,26 (**Ar**$_{4,6}$), 62.29 (**CH$_2$**-OH), 49.11 (CH2-C=O), 42.25 (**CH$_2$**NH), 20.39 (CH_3Ph).

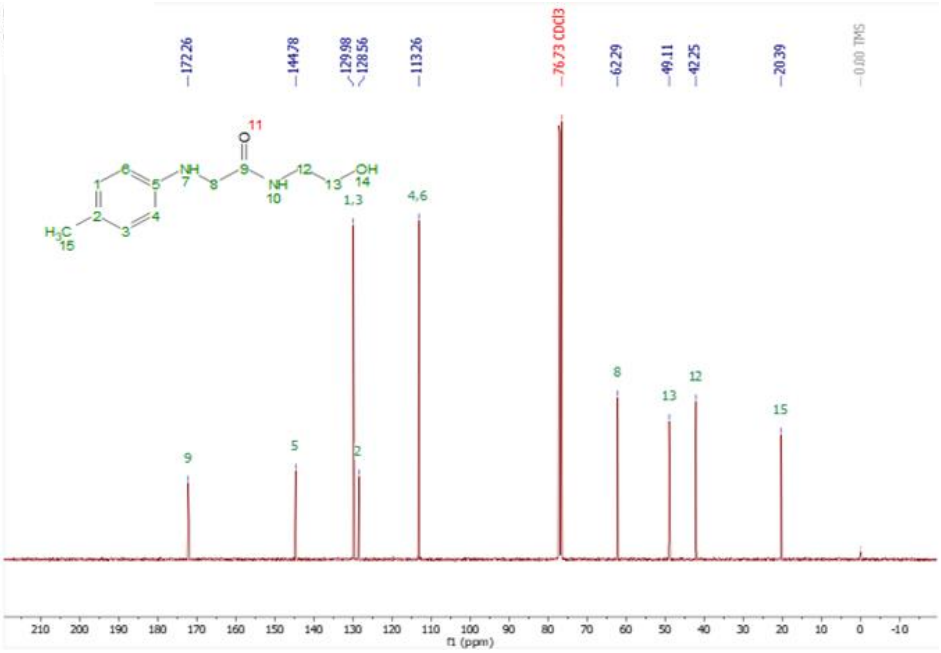

Figure 5.32: ^{13}C NMR of **10b.**

HRMS (ESI$^+$): *m/z* calculated for $C_{11}H_{16}N_2O_2$ 208.1212; found 208.0600 for compound **10b**.

Figure 5.33: HRMS of **10b**.

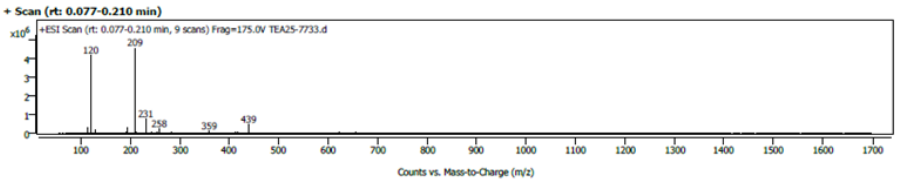

N-(3-hydroxypropyl)-2-(1H-imidazol-1-yl) acetamide 11f

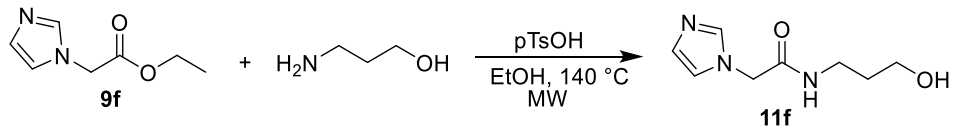

Figure 5.34: Synthetic reaction of hydroxyamide **11f**.

The **^{1}H NMR** data of hydroxyacetamide **11f** are present below (**Figure 5.37**). At a chemical shift of 8.11 ppm, a pseudo triplet signal with a coupling constant of 5.08 Hz is seen, corresponding to the amide proton (**NH**C=O) integrating for 1H. At 7.56 ppm, a pseudo triplet signal assigned to one of the protons of the imidazole ring (N=**CH**-N) is observed integrating for 1H with 1.24 Hz coupling constant. Another pseudo triplet at a shift of 7.07 ppm with coupling constant 1.36Hz is detected corresponding to a second proton of the imidazole ring (N-**CH**=CH) and integrating for 1H. Aromatic proton named as 2 (**CH**=CH-NCH$_2$) give rise to pseudo triplet signal signal at 6.87 ppm with coupling constant 1.2 Hz, integrating for 1H. At 4.62 ppm, a singlet corresponding to the hydrogens of the alpha methylene to the carbonyl is found, integrating for 2H. At 3.41 ppm, a triplet is observed with coupling constants of 6.36, corresponding to the methylene group adjacent to the hydroxyl group, integrating for 2H. A singlet is observed at 3.39 ppm corresponding to OH group. A quartet at 3.15 ppm, is detected with coupling constants of 5.8Hz, assigned to the methylene group adjacent to the amide NH group, integrating for 2H. At the end, a quintet at 1.56 ppm, is seen with coupling constants of 8.3 Hz, corresponding to the methylene group adjacent to the two methylene groups of the propanolamine portion, integrating for 2H. **^{1}HNMR** (500 MHz, *CDCl*$_3$): δ 8.11 (pst, *J* = 5.08 Hz, 1H, **NH**C=O), 7.56 (pst, *J* = 1.24 Hz 1H, N=**CH**-N) 7.07 (pst, *J* = 1.36 Hz 1H, N-**CH**=CH), 6.87 (pst, *J* = 1.2 Hz, 1H, **CH**=CH-NCH$_2$), 4.62 (s, 2H, **CH$_2$**-C=O), 3.41(t, *J* = 6.36 Hz, 2H **CH$_2$**OH), 3.39(brs, 1H, OH), 3.15 (q, *J* = 5.8 Hz, 2H, **CH$_2$**NH), 1.56 (qn, *J* = 8.3 Hz, 2H, CH$_2$-**CH$_2$**-CH$_2$).

Figure 5.35: ^{1}H NMR of **11f.**

^{13}C NMR (176 MHz, DMSO-d6): δ 166.76 (**C**=O), 137.77 (N=**CH**-N), 128.01 (N-**CH**=CH), 120.47 (C=**CH**-N-CH2), 58.38 (**CH_2**OH), 48.74 (**CH_2**C=O), 36.04 (**CH_2**-NH), 32.22 (CH_2-**CH_2**-CH_2).

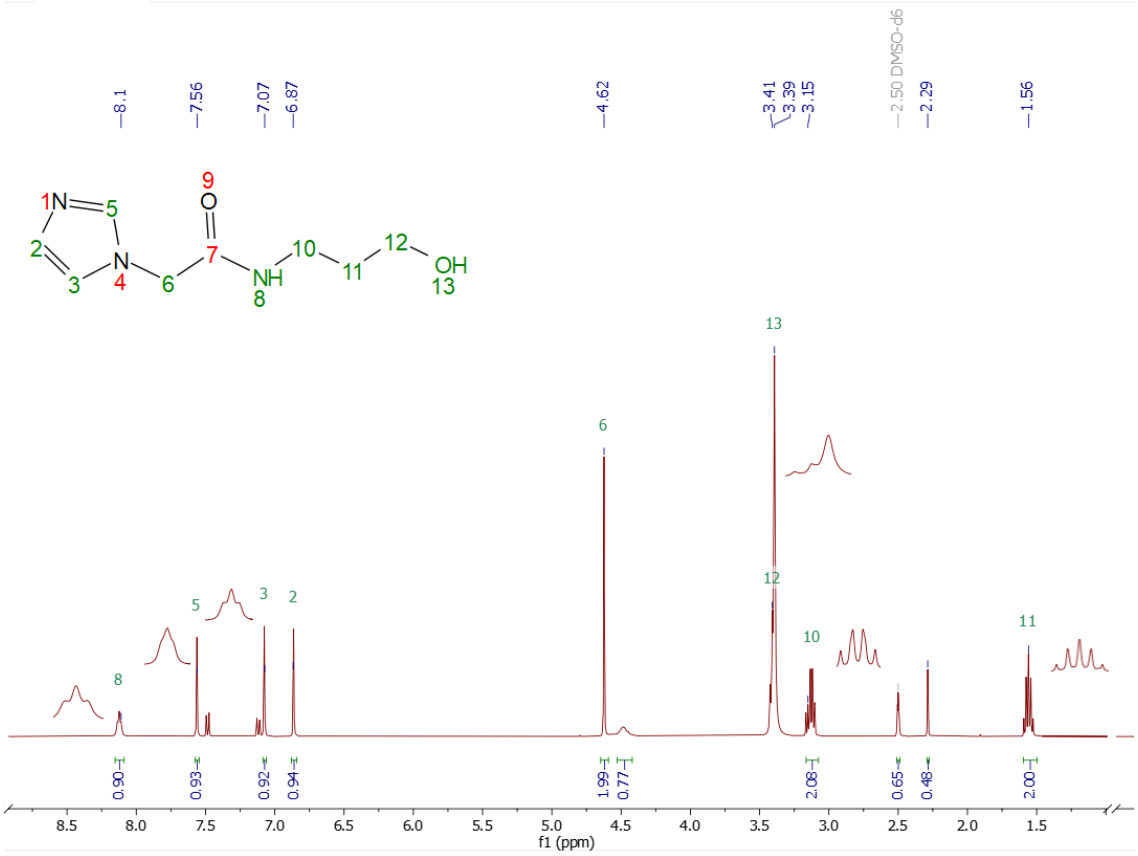

Figure 5.36: ^{13}C NMR of **11f.**

HRMS (ESI^{+}): *m/z* calculated for $C_8H_{13}N_3O_2$ 183.1008 ; found 184.1081 for compound **11f**.

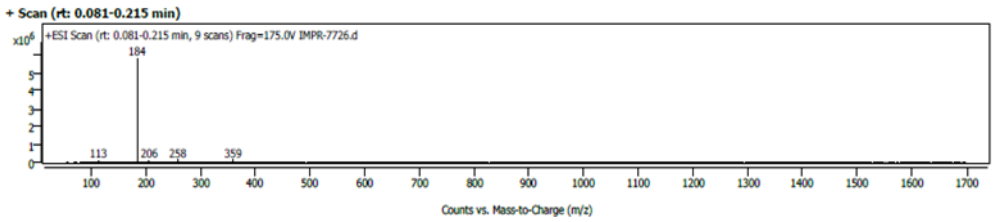

Figure 5.37: HRMS of **11f.**

5.2.2 Crystal violet Assay

The percentage of cell viability of eight amides was determined in three human cancer cell lines (PC-3, MCF-7, and HCT-15) and one normal human cell line (HaCaT) using the crystal violet assay at various concentrations (25, 50, 100, and 200 μM) (**Table 5.10-5.13**) after 48 h of treatment. Results are presented as the mean of triplicate samples and are representative of three independent experiments. DMSO was used as the control.

Table 5.9:MCF-7 (% Viability).

Compound	25 μM	50 μM	100 μM	200 μM
10a	87.00 ± 3.86	88.49 ± 2.44	82.69 ± 5.39	75.35 ± 4.96
10b	108.27 ± 4.56	100.90 ± 8.88	82.80 ± 6.70	80.89 ± 3.44
11a	102.03 ± 10.48	82.89 ± 7.28	83.23 ± 2.51	78.54 ± 7.55
11b	106.55 ± 7.75	88.83 ± 9.49	84.59 ± 2.72	80.77 ± 5.41
11c	93.36 ± 6.14	79.97 ± 5.18	84.02 ± 8.89	80.65 ± 3.95
11d	111.22 ± 2.54	99.20 ± 10.22	80.73 ± 2.08	83.38 ± 6.07
11e	112.84 ± 5.96	80.44 ± 4.00	88.81 ± 5.13	65.25 ± 1.67
11f	98.59 ± 3.95	89.00 ± 8.62	78.32 ± 3.85	76.52 ± 2.54
Vorinostat	**IC_{50} =** 4.62±1.74 μg/mL			

Table 5.10: HCT-15 (% Viability)

Compound	25 μM	50 μM	100 μM	200 μM
10a	111.01±5.81	101.79±6.82	96.68±4.65	86.76±4.65
10b	115.29±10.58	108.90±8.63	110.53±3.62	103.58±7.81
11a	109.49±5.15	94.46±7.87	92.98±6.88	90.61±5.12
11b	108.26±1.98	97.44±8.91	100.76±4.06	87.24±5.06

11c	108.73±8.27	100.51±8.09	98.45±3.29	94.86±3.59
11d	113.88±6.43	106.22±1.36	98.03±8.03	94.43±8.84
11e	96.84±2.61	109.89±6.13	104.09±3.26	89.51±5.81
11f	106.06±2.93	106.47±8.12	98.00±6.75	91.24±5.61
Vorinostat	**IC_{50} =** 3.37±0.67 µg/mL			

Table 5.11: PC-3 (% Viability).

Compound	25 µM	50 µM	100 µM	200 µM
10a	98.32±4.75	99.09±8.59	85.83±6.01	81.15±8.74
10b	91.76±5.16	92.44±8.12	90.27±3.60	92.34±4.47
11a	105.66±7.48	100.05±4.84	92.51±9.12	76.81±10.43
11b	101.68±8.86	91.99±5.46	85.42±8.71	76.48±6.95
11c	109.22±2.83	96.10±9.48	94.27±3.79	89.60±9.93
11d	95.78±4.57	96.05±10.14	79.86±1.94	70.97±6.46
11e	100.84±2.25	77.47±8.42	77.13±1.12	67.76±6.50
11f	105.52±4.56	98.35±5.85	89.33±7.05	78.18±5.21
Vorinostat	**IC_{50} =** 7.47±1.32 µg/mL			

Table 5.12: HaCaT (% Viability).

Compound	25 µM	50 µM	100 µM	200 µM
10a	109.69±4.83	108.70±3.34	100.32±7.00	94.84±6.41
10b	111.77±8.11	104.68±2.50	102.09±7.35	101.34±4.65
11a	106.52±4.24	106.86±4.21	92.96±9.56	50.21±8.82
11b	110.65±7.88	99.69±2.14	97.44±2.36	95.98±7.82
11c	114.79±6.92	109.36±5.11	98.90±2.97	94.86±5.31
11d	110.58±3.04	116.80±2.59	101.31±7.47	85.29±5.50
11e	107.63±5.59	101.94±6.17	102.31±9.26	82.87±8.71

11f	117.62±0.60	102.82±3.11	92.08±9.33	88.28±5.83
Vorinostat	**IC_{50} =** 15.89±1.20 µg/mL			

The present study investigated the cytotoxic and antiproliferative effects of synthesized hydroxamic acid derivatives. These effects were evaluated using the Crystal Violet assay in three cancer cell lines (PC-3, HCT-15, and MCF-7) and one normal cell line (HaCaT). The results at concentrations from 25 to 200 µM showed no reduction in cell growth. In all cases, cell viability remained between 70–90%, and in some cases exceeded 100%. This shows the limited sensitivity of assay for detecting moderate growth inhibition. From the results the compounds did not show measurable cytotoxic activity within the tested conditions. Previous reported study by He *et al* showed the compounds which having hydroxyacetamide zinc binding group have poor inhibitory activities against the cancerous cell lines. In which they observed most of the compound showed mild activity but the compounds with bulky substituents in the cap group showed good inhibitory activities toward Hela and A549. Among them, compounds a9 and b8 were the most active, especially against HeLa cells. Importantly, these compounds showed low toxicity toward normal cells(He *et al*., 2020). None of the compounds were effective against MCF-7 cancer cells. Similarly, other reported amid compounds with bulky groups near the ZBG also did not inhibit MCF-7 cells but did show activity against Hela (Avalos Alanís, 2011).

Whereas the positive control Vorinostat showed clear dose-dependent cytotoxicity with low micromolar IC_{50} values, which is confirming that the assay was working

properly. Therefore, the lack of activity in the test compounds may indicate either weak biological activity or effects below the detection limit of this assay.

This method mainly measures the number of attached viable cells and does not distinguish between reductions in proliferation, early apoptotic events, or changes in cell cycle progression. Some compounds may affect cancer cells through non-lethal mechanisms such as cytostatic, differentiation inducing, or signaling modulatory effects, which may not lead to enough loss of cell biomass to be detected (Forgie *et al*., 2024; Winkler *et al*., 2014). Also, many anticancer mechanisms including epigenetic modulation, kinase inhibition, reactive oxygen species signaling, and cytoskeletal interference can produce delayed cellular responses requiring longer incubation times or different experimental conditions (Hassell, 2019). HDAC inhibition usually causes slow cellular effects because it works by changing gene expression rather than directly killing cells. It first increases histone acetylation quickly, but the effects on gene activity, cell cycle arrest, and cell death happen later over time.

The compounds are hydroxyacetamides derivatives containing both hydroxyl and amide functional groups, which are highly polar and capable of extensive hydrogen bonding. These groups increase water solubility but reduce lipophilicity. The LogP values (–0.42 to 1.33) suggest high solubility but limited ability to pass through cell membranes. Since lipophilicity is strongly associated with passive membrane permeation, limited cellular uptake may occur, resulting in insufficient intracellular concentrations and consequently weak biological activity in the proliferation assay (Liu *et al.*,2011).

Computational studies showed that the compounds interact strongly with the target protein. Docking studies showed that all compounds had good interactions with the HDAC isoforms. Molecular dynamics simulations in HDAC6 isoform reveal compounds **10b** and **11c** maintain stable interactions. These findings suggest that the lack of cytotoxicity may be related to limited cellular uptake rather than poor target binding.

In summary, the Crystal Violet assay shows that these hydroxyacetamide derivatives do not produce notable cytotoxic effects under the tested experimental conditions.

However, the limitations of the assay, together with the physicochemical properties of the compounds and the supportive computational results, suggest that these molecules should not be ruled out at this stage. Therefore, these compounds should be further studied using sensitive proliferation assays, expanded dosing strategies, and mechanistic studies to accurately determine their anticancer potential.

CHAPTER 7

6 Conclusions

1. Molecular docking and dynamics were carried out on 32 N, O, S-phenyl-substituted oxazoline and oxazine heterocycles with HDAC3, 6, and 8, as well as on eight *N*-substituted hydroxy acetamides with HDAC2, **3**, **4**, **6**, **7**, **8**, and **10**. Compounds **3a**, **3b**, **4a** (heterocycles), **10a**, and **11b** (hydroxy acetamides) showed highest binding energies with HDAC6.
2. In HDAC6, bidentate interactions occurred between the zinc ion, the aniline nitrogen, and the nitrogen group of the heterocycle. For the hydroxyacetamides, bidentate interactions occurred between the carbonyl of amide and the hydroxyl group.
3. The hydroxyacetamide derivatives showed comparable interaction energies across all HDAC isoforms, whether from the ethanolamine (**10**) or propanolamine (**11**) series. By contrast, the heterocyclic compounds showed a clear isoform-dependent variation, particularly with HDAC6, where bidentate coordination is observed. With other HDAC, only monodentate interactions are observed. This difference is mainly due to the smaller number of rotatable bonds within the heterocyclic scaffolds, which imposes conformational constraints and consequently limits optimal chemical complementarity within the active site.
4. Considering the *in-silico* results, two β-hydroxy acetamides and six γ-*N*-substituted hydroxy acetamides were synthesized by three reaction steps, achieving yields ranging from 77 to 91%, using microwaves method and *p*-toluenesulfonic acid as a coupling agent. The synthesis of amide was unsuccessful using conventional methods. However, microwave irradiation efficiently promoted amide bond formation by overcoming the immediate formation of acid-amine salt intermediate.
5. Each of the eight synthesized hydroxy acetamides were characterized by ^{1}H, ^{13}C NMR and HRMS, thus demonstrating their structural identity.
6. Based on the *in-vitro* results, no relevant activity was observed for the hydroxyacetamides at the four concentrations (25, 50, 100, and 200 µg/mL),

across all tested cancer cell lines. Cell viability remained above 50.21%. In contrast, Vorinostat, which exhibits quite low IC_{50} values between 3 and 8 µM/mL.

7. The lack of activity shown by the hydroxyacetamides evaluated *in vitro* may be due to their high polarity (LogP -0.3), which hinders their cellular uptake.
8. Vorinostat shows no difference in its cytotoxic effect between cancerous and normal cell lines, with IC_{50} values between 3 and 8 µM/mL and 15.89 µM/mL, respectively.

CHAPTER 8

7 Perspectives

1. Synthesis of oxazolines **3a**, **4a** and **3b** using the following synthesis route. Based on the *in silico* results, these compounds show strong activity as selective inhibitors of HDACs, specifically HDAC6. They also present new zinc-binding groups that have not been reported previously.

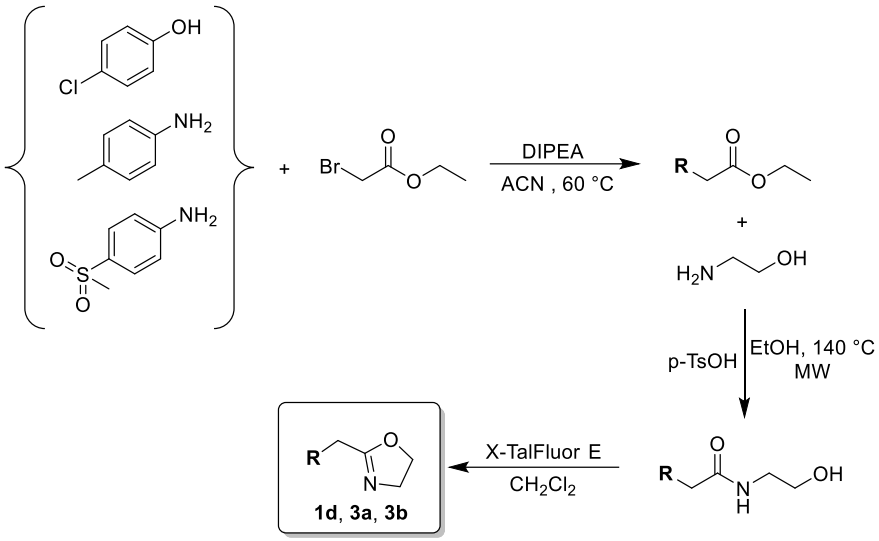

2. Evaluation of the *in vitro* anticancer and cytotoxic activity of compounds **3a**, **3b** and **4a**. Also perform enzymatic analysis with multiple HDAC isoforms, specifically with HDAC6 to confirm the selective inhibition, as well as the relationship with the anticancer activity.
3. Evaluate the antiproliferative effect of hydroxy acetamides **10a-b** and **11a-f** to find out the possible cytostatic effect.
4. Evaluate the inhibitory activity of HDACs to confirm the *in silico* results and determine the lack of anticancer and cytotoxic effects is related to weak enzyme inhibition.

CHAPTER 8

8 Annex

Table A1: Docking score of the Heterocyclic compounds in HDAC6

Compound	Docking score	Glide energy
3d	-7.062	-32.884
3b	-6.914	-39.365
3a	-6.783	-40.203
4a	-6.104	-23.542
7b	-6.744	-30.366
7a	-6.719	-30.224
3c	-6.974	-26.168
7d	-6.776	-31.335
5b	-6.721	-30.892
7c	-6.667	-28.614
4d	-6.667	-30.406
8d	-6.627	-28.37
5c	-6.618	-30.423
5a	-6.568	-29.34
4b	-6.533	-29.927
6a	-6.449	-29.787
4c	-6.433	-26.302
8a	-6.427	-30.898
6b	-6.409	-25.979
6c	-6.398	-24.244
2a	-6.366	-28.108
5d	-6.352	-28.361
8b	-6.31	-27.55
6d	-6.306	-23.857
8c	-6.276	-27.691
1c	-6.185	-23.993
1a	-6.174	-24.956
1d	-6.154	-27.611
2d	-6.11	-34.976
2c	-6.068	-23.266
2b	-6.031	-24.944
1b	-6.009	-24.648

Table A2: Docking Profiles of Hydroxy acetamide across HDAC3 and HDAC8.

PROTEIN	COMPOUNDS	DOCKING SCORE kcal/mol)	GLIDE ENERGY (kcal/mol)
HDAC8	**3b**	-7.013	-26.017
	3a	-6.902	-20.308
	7d	-6.36	-29.393
	8d	-6.104	-21.208
	2d	-5.046	-24.308
	6b	-4.823	-25.544
	SAHA	*-6.902*	*-20.3079*
HDAC3	**4a**	-8.189	-18.792
	3d	-7.879	-30.821
	1d	-6.681	-27.25
	5a	-6.449	-28.746
	5c	-6.107	-23.175
	4c	-6.738	-26.969
	SAHA	*-5.98*	*-25.295*

Table A3: Docking Profiles of Hydroxyacetamide across HDAC2, HDAC3, HDAC4, HDAC6, HDAC7, HDAC8, and HDAC10.

ISOFORM PDB ID	HDAC2 (4LXZ)	HDAC3 (4A69)	HDAC8 (1T69)	HDAC4 (2VQM)	HDAC7 (3C10)	HDAC6 (5EDU)	HDAC10 (7U59)
10a	-8.78	-8.26	-8.26	-7.51	-7.25	-8.22	-8.84
10b	-9.27	-8.27	-8.63	-7.72	-6.68	-8.7	-9.6
11a	-9.17	-7.02	-9.48	-8.34	-6.61	-7.02	-8.7
11b	-9.11	-6.61	-9.13	-8.36	-6.55	-7.37	-6.76
11c	-6.55	-6.65	-7.29	-7.28	-6.27	-7.27	-6.44
11d	-8.55	-6.7	-8.48	-6.84	-5.9	-7.35	-6.47
11e	-6.57	-6.51	-8.17	-7.3	-6.19	-7.02	-7.62
11f	-6.27	-6.19	-7.99	-6.63	-6.2	-6.68	-6.09

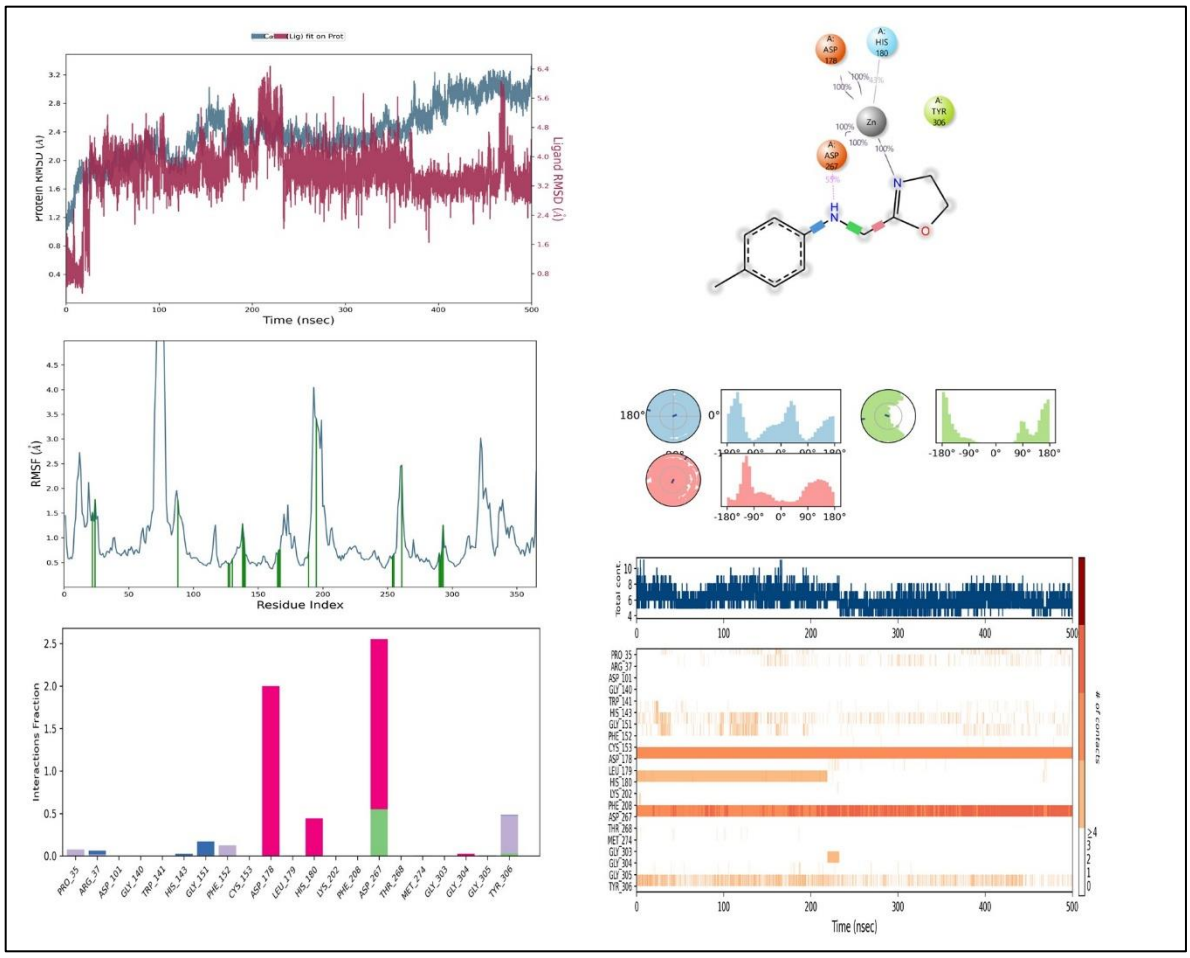

Figure A1: RMSD, RMSF, and protein-ligand contact plots of **3b** with protein complex of HDAC8 isoform during MD simulation.

Figure A1 shows the MD analysis of **3b**-HDAC8 complex which exhibited the protein RMSD increased during the initial phase of the simulation and reached a stable range after ~200 ns. Between ~200 and 230 ns, the protein backbone RMSD increased noticeably from ~ 1.2 Å. After 400 ns, the protein backbone RMSD increased to ~2.4-3.2 Å, suggesting a major structural change. The RMSF results showed that most residues remained stable throughout the simulation, with only a few regions having higher flexibility. Some fluctuations near the binding site residues may be related to changes in the protein structure after ligand binding. The torsional analysis at ZBG showed a varied

angle distribution. Interaction analysis revealed that ASP267 maintained hydrogen-bond interactions with the NH group throughout the simulation, supporting stable ligand binding

Figure A2: RMSD, RMSF, and protein-ligand contact plots of **3a** with protein complex of HDAC8 isoform during MD simulation.

The RMSD profile of **3a** in HDAC8 (**Figure A2**) showed an initial structural transition during the early stage of the simulation, particularly between 90–150 ns. After the change, both the protein and ligand RMSD values stabilized and fluctuated within the narrow range (~1.8–2.4 Å), with an overall variation of ~0.6 Å. This reveals that complex has reached equilibrium in a new conformational state. The RMSF analysis showed that most

protein residues remained stable during the simulation, with fluctuations below 1.0 Å. Residues around ~70–80 and ~190–200 exhibited higher fluctuations, reveals that localized flexibility. Some interaction-related residues also showed moderate mobility. The broader torsional angle distribution in the ZBG indicates ligand flexibility, which is consistent with the interaction analysis showing transient interactions.

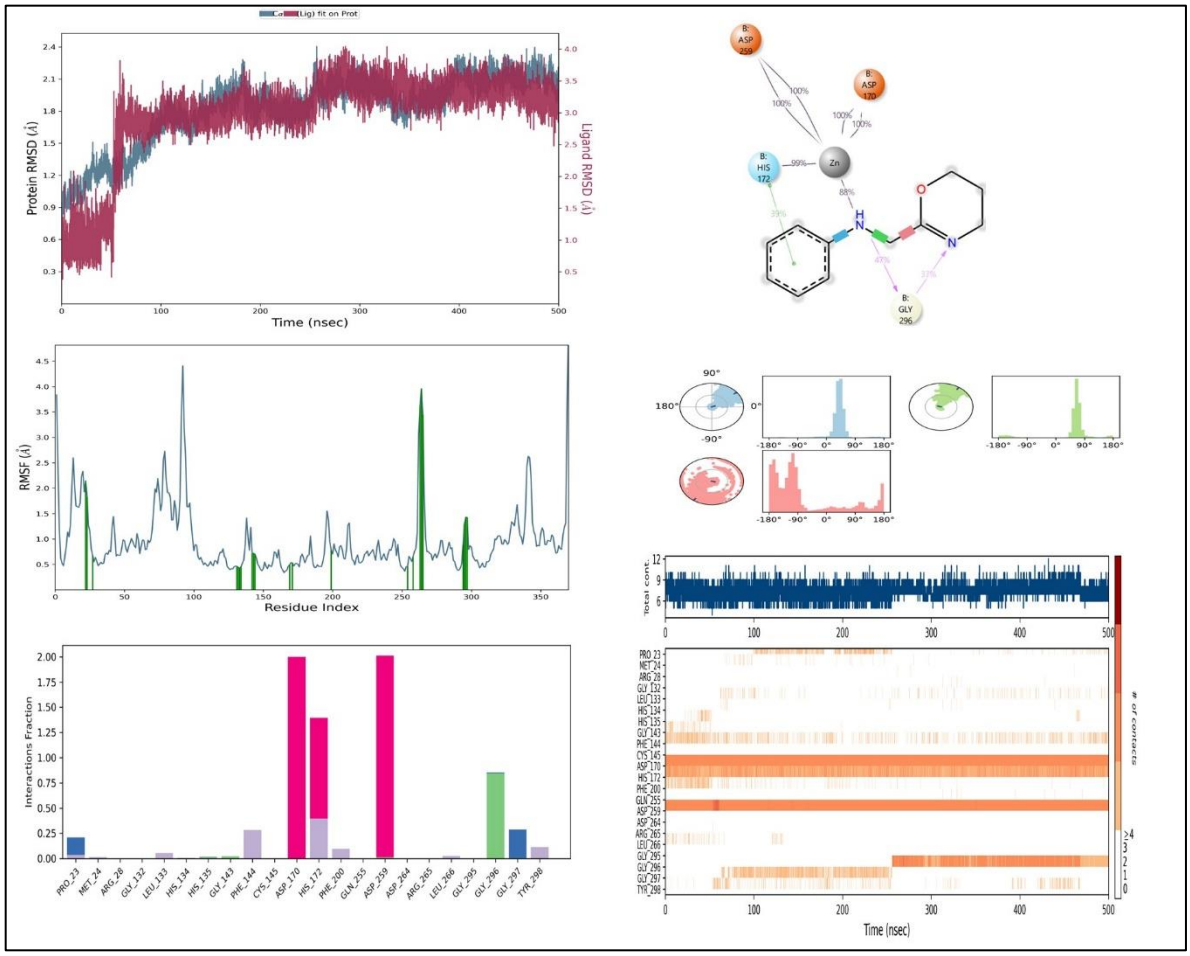

Figure A3: RMSD, RMSF, and protein-ligand contact plots of **4a** with protein complex of HDAC3 isoform during MD simulation.

As shown in the **Figure A3**, the RMSD plot of **4a**-HDAC3 shows initial equilibration within the first 10–15 ns, thereafter a gradual increase and small fluctuations throughout the remainder of the simulation. This behavior suggests conformational adaptation rather than instability. The system stabilizes in a slightly different structural state toward the end

of the trajectory. The ligand RMSD shows initial equilibration within the first ~20 ns, followed by minor fluctuations at later time (~26–48 ns). These deviations remain within a narrow range (~0.8–1.0 Å). The interaction histogram shows Strong interactions are seen for residues such as PHE144, ASP170, HIS172, PHE144, PRO209, and PHE200 throughout the simulation. The torsion profile analysis reveals that the key interacting torsion which is with the part of zinc binding group remains highly restricted, with most conformations centered around 180°, indicating a stable trans conformation throughout the simulation.

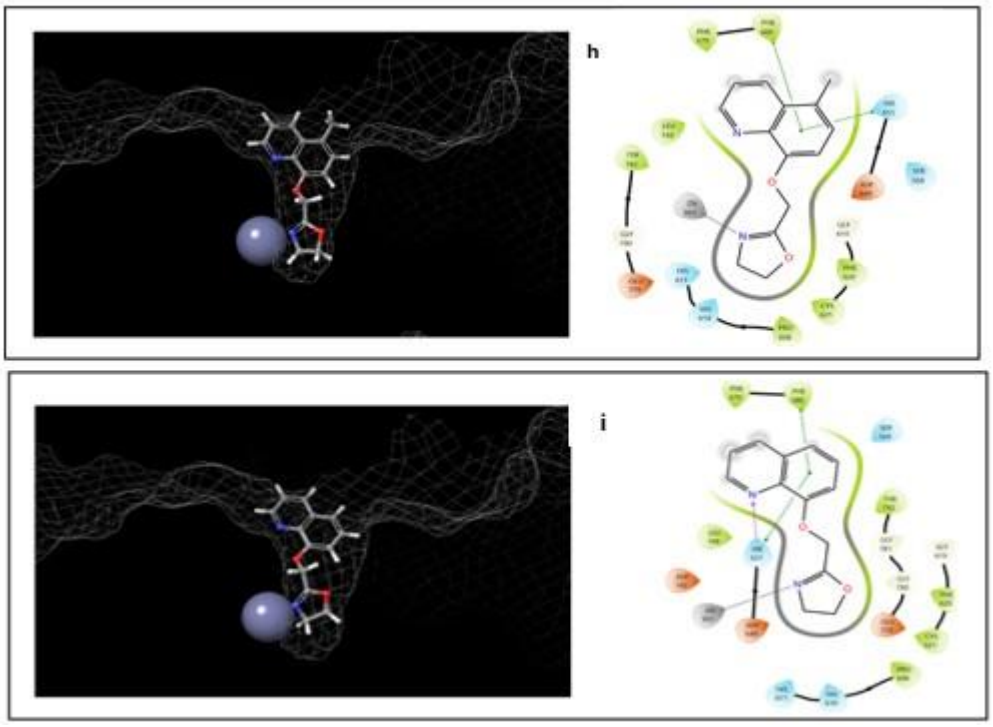

Figure A4: 2D and 3D diagram of interaction of compounds inside the HDAC6 pocket. (h) **7b,** (i) **7a**.

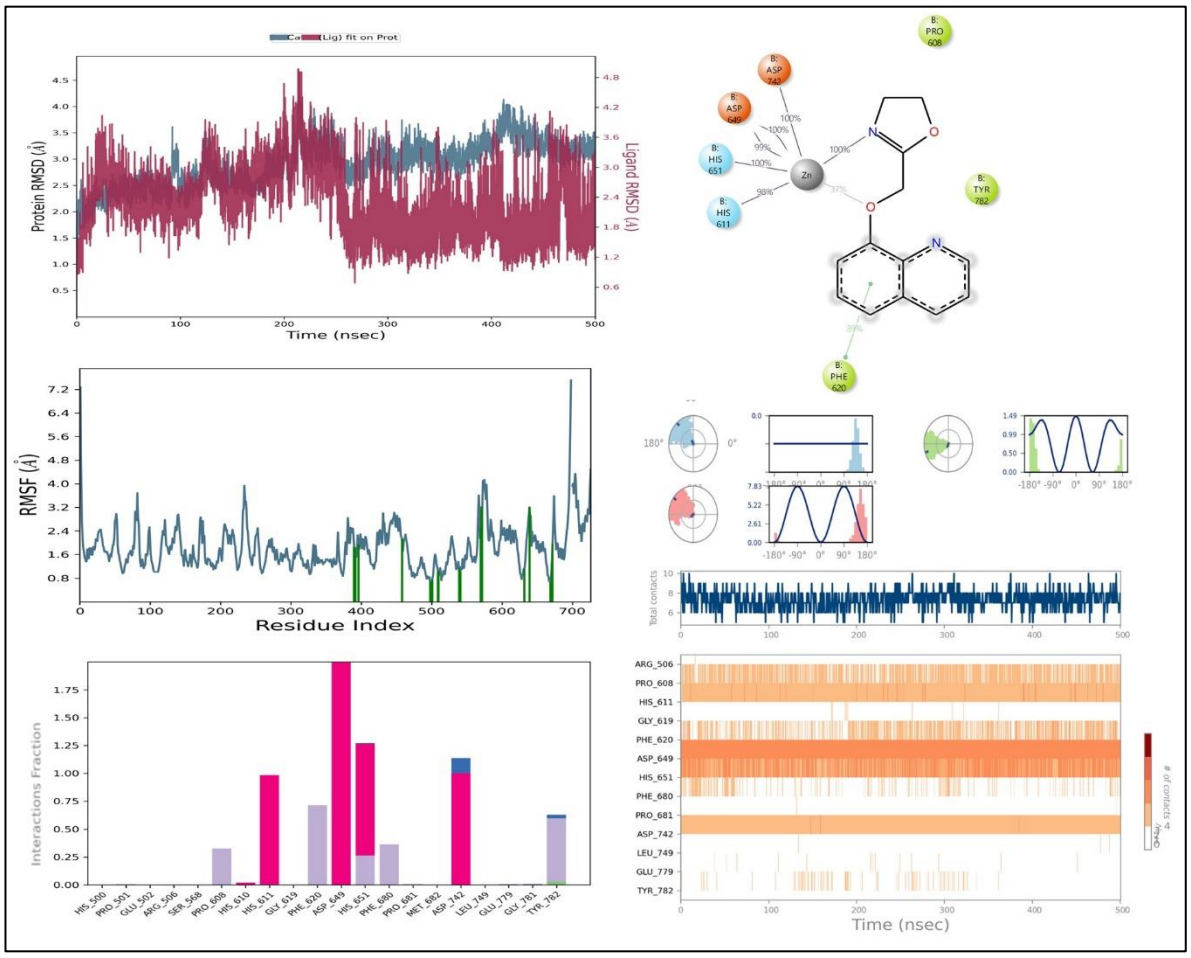

Figure A5: RMSD, RMSF, and protein–ligand contact plots of **7a** with protein complex of HDAC6 isoform during MD simulation.

The ligand RMSD of **7a**-HDAC6 (**Figure A5**) calculated with respect to the protein binding site showed stabilization after equilibration, with fluctuations ~2.0 Å. Between ~150 and ~230 ns, a marked increase in ligand RMSD is observed, reaching values of ~4.0–4.5 Å, showing of reorientation within the binding pocket. After this period, the ligand RMSD decreases and stabilizes around ~1.2–1.8 Å, shows adoption of a more stable binding pose. Most residues indicate RMSF values below 2.0 Å, with an average RMSF of around 1.5 Å. Higher fluctuations greater than 2.5 Å were localized in terminal regions. The residues within the binding site remained below 2.0 Å. Protein-ligand interaction analysis revealed that PHE620 and PRO608 shows hydrophobic interactions.

Throughout the simulation, the torsional angle distributions mainly confined to different regions, suggesting that the ligand maintained preferred conformations with limited flexibility. The **7a**–HDAC6 complex demonstrated a stable bidentate interaction through the oxazoline NH group with 100% occupancy, whereas the oxygen atom at the α-position participated less frequently, showing 37% occupancy.

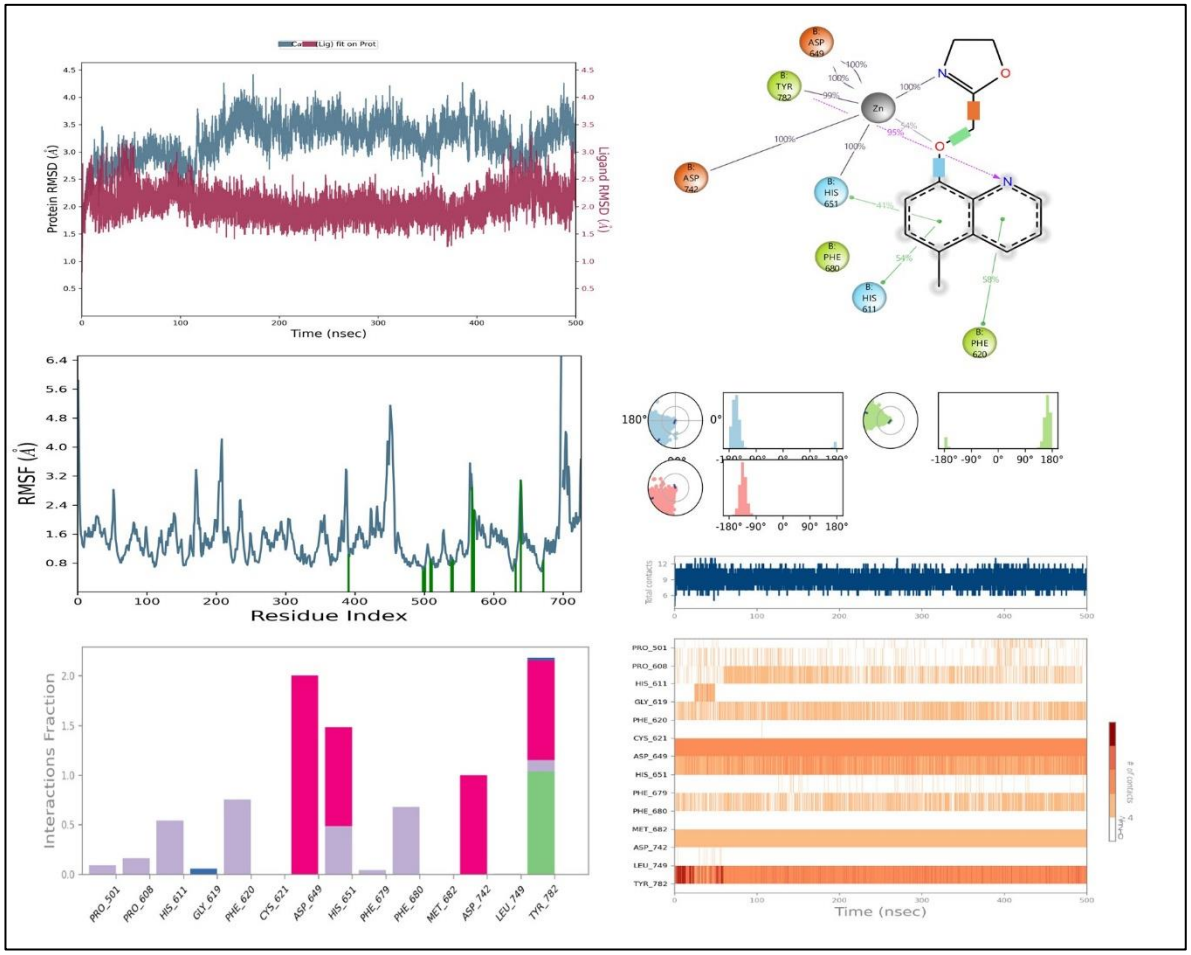

Figure A6: RMSD, RMSF, and protein-ligand contact plots of **7b** with protein complex of HDAC6 isoform during MD simulation.

The MD analysis of the **7b**–HDAC6 complex during 500 ns simulation is showed in **Figure A6**. After equilibration at ~40–60 ns, the protein backbone RMSD reached a stable state, with deviations of ~1Å throughout the simulation. The ligand showed low

deviations, with RMSD values between 1.5 and 2.5 Å. The RMSD results reveal that the protein maintained its stable structure and allowed only limited flexibility. Therefore, the ligand is firmly associated with the binding pocket throughout the simulation. The torsional angles were concentrated to specific regions in the diagram, indicating that the ligand attain dominant conformations with comparatively low flexibility. Compound **7b** maintained π–π stacking interactions with PHE620 were preserved 58% of the simulation time. Polar interactions with HIS651 and HIS611 were also seen with 41% and 54% occupancy. The interaction profile shows that HIS651 maintained hydrophobic and ionic interactions throughout the simulation. Even though compounds **7a** and **7b** exhibited consistent bidentate coordination with the HDAC6 protein, they showed lower oxygen interaction occupancy compared to the other compounds, which displayed occupancies of 37% and 54%, respectively.

Table A4: Interatomic Distances, Bond Angles, and Dihedral Angles of Selected Compounds in Complex with HDAC3 and HDAC8 (X=N, O, S).

Class	Compound	Distance Zn-N(Ring) (Å)	Distance Zn-X (Å)	Distance Zn-O (Ring) (Å)	Angle (degree)	Dihedral Angle (degree)
HDAC 8	**3a**	2.24	4.59	4.17	113	164
	3b	2.47	4.65	4.71	116	169.3
	6b	2.23	4.64	4.54	108	107.1
	8a	2.22	4.98	4.57	119	167.5
	7d	2.2	5.18	4.46	114	152
HDAC 3	**4a**	2.22	4.21	4.5	116.1	176
	8c	2.22	4.21	4.5	116.1	176
	3d	2.16	4.22	4.4	121.9	172

Table A5: Interatomic Distances of Selected Hydroxyacetamide derivative Complex with HDAC6.

Class	Hydroxyacetamide	Distance Zn-OH (Å)	Distance Zn-(C=O) (Å)
HDAC8	**10b**	1.97	5.69
	11b	1.92	2.15
	11c	2.05	5.81
HDAC2	**10b**	2.06	2.08
	11b	2.09	5.50
	11c	2.03	6.02

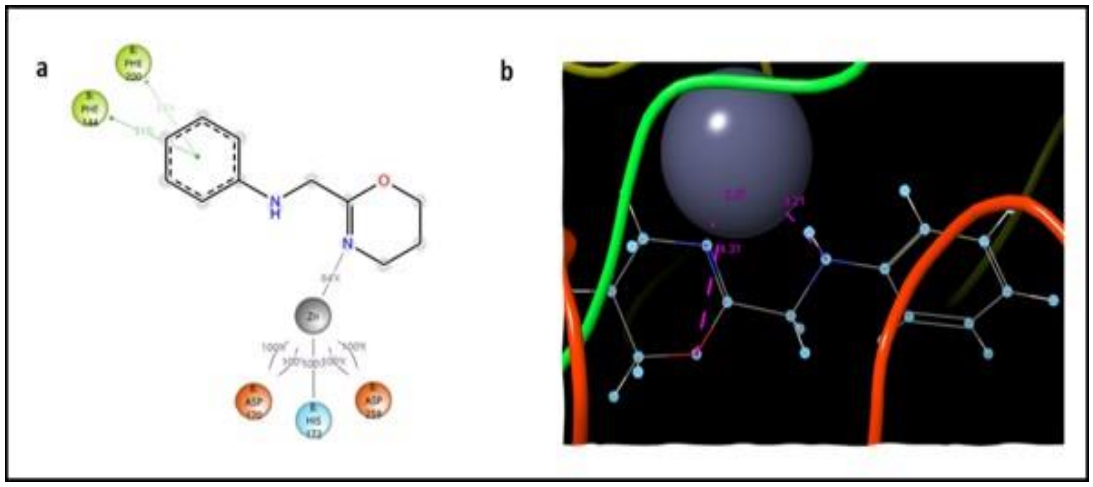

Figure A7: Key Zn^{2+} coordination distances observed in the HDAC3-**4a** complex during molecular dynamics simulation, showing bidentate interaction via ring nitrogen (2.22 Å) and α-nitrogen (4.21 Å).

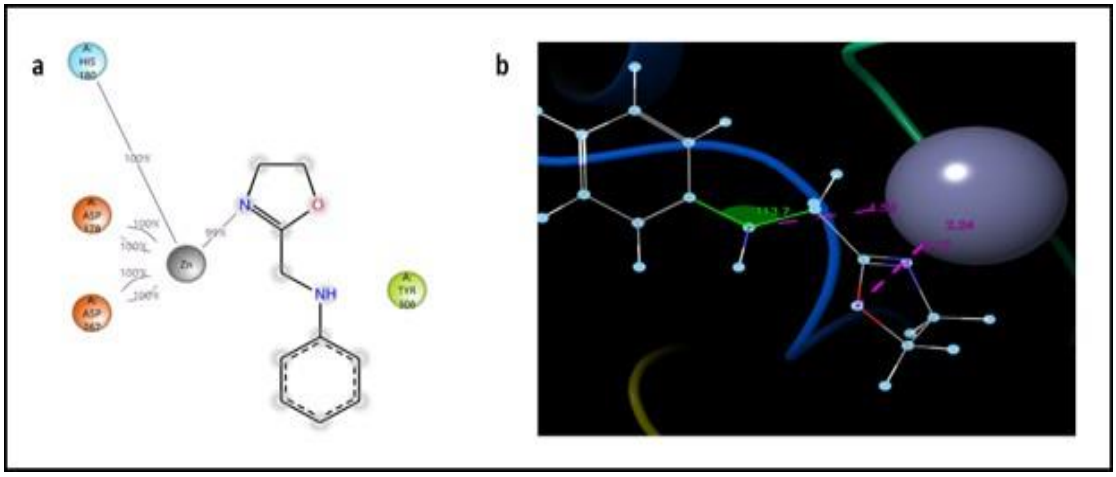

Figure A8: Key Zn^{2+} coordination distances observed in the HDAC8-**3a** complex during molecular dynamics simulation, showing bidentate interaction via ring nitrogen (2.24 Å) and a-nitrogen (4.59 Å).

Table A6: ADME properties of selected compounds (**10b, 11b, 11c, 3a, 4a, 3b, 1b**).

	3a	3b	4a	10b	11b	11c
MW	176.22	190.24	190.24	208.26	222.28	233.27
H-bond acceptors	2	2	2	2	2	3
H-bond donors	1	1	1	3	3	2
TPSA				61.36	61.36	67.15
iLOGP	2.16	2.29	2.29	1.67	1.92	1.35
XLOGP3	1.51	1.87	1.87	0.93	1.29	0.56
Consensus Log P	1.68	1.99	1.96	0.97	1.3	0.73
Ali Log S	-1.82	-2.2	-2.2	-1.8	-2.18	-1.54
Ali Class	Very soluble	Soluble	Soluble	Very soluble	Soluble	Very soluble
GI absorption	High	High	High	High	High	High
BBB permeant	Yes	Yes	Yes	No	No	No
Pgp substrate	No	No	No	No	No	No
CYP1A2 inhibitor	Yes	Yes	Yes	No	No	No
CYP2C19 inhibitor	No	No	No	No	No	No
CYP2C9 inhibitor	No	No	No	No	No	No
CYP2D6 inhibitor	No	No	No	No	No	No
CYP3A4 inhibitor	No	No	No	No	No	No
log Kp (cm/s)	-6.3	-6.13	-6.13	-6.91	-6.74	-7.33
Lipinski violations	0	0	0	0	0	0
Ghose violations	0	0	0	0	0	0
Veber violations	0	0	0	0	0	0
Egan violations	0	0	0	0	0	0
Muegge violations	0	0	0	0	0	0
Bioavailability Score	0.55	0.55	0.55	0.55	0.55	0.55
PAINS alerts	0	0	0	0	0	0
Brenk alerts	0	0	0	0	0	0
Leadlikeness violations	1	1	1	1	1	1
Synthetic Accessibility	2.87	2.79	2.87	1.53	1.62	2.01

Table A7: ADME properties of Hydroxyacetamide compounds.

SMILE	OCCNC(=O)CNc1ccccc1	OCCNC(=O)CNc1ccc(cc1)C	OCCCNC(=O)CNc1ccccc1	OCCCNC(=O)CNc1ccc(cc1)C	OCCCNC(=O)Cn1cnc2c1cccc2	OCCCNC(=O)Cn1nnc2c1cccc2	OCCCNC(=O)Cn1nc2c(n1)cccc2	OCCCNC(=O)Cn1cncc1
	10a	**10b**	**11a**	**11b**	**11c**	**11d**	**11e**	**11f**
MW	194.23	208.26	208.26	222.28	233.27	234.25	234.25	183.21
H-bond acceptors	2	2	2	2	3	4	4	3
H-bond donors	3	3	3	3	2	2	2	2
TPSA	61.36	61.36	61.36	61.36	67.15	80.04	80.04	67.15
iLOGP	1.39	1.67	1.57	1.92	1.35	1.34	1.52	0.83
XLOGP3	0.57	0.93	0.92	1.29	0.56	-0.03	1.06	-0.87
Consensus Log P	0.62	0.97	0.93	1.3	0.73	0.4	0.5	-0.42
Ali Log S	-1.43	-1.8	-1.79	-2.18	-1.54	-1.2	-2.33	-0.06
Ali Class	Very soluble	Very soluble	Very soluble	Soluble	Very soluble	Very soluble	Soluble	Very soluble
GI absorption	High	High	High	High	High	High	High	High
BBB permeant	No	No	No	No	No	No	No	No
Pgp substrate	No	No	No	No	No	No	No	No
CYP1A2 inhibitor	No	No	No	No	No	No	No	No
CYP2C19 inhibitor	No	No	No	No	No	No	No	No
CYP2C9 inhibitor	No	No	No	No	No	No	No	No

CYP2 D6 inhibitor	No	No	No	No	No	No	No	No
CYP3 A4 inhibitor	No	No	No	No	No	No	No	No
log Kp (cm/s)	-7.08	-6.91	-6.92	-6.74	-7.33	-7.75	-6.98	-8.04
Lipinski violations	0	0	0	0	0	0	0	0
Ghose violations	0	0	0	0	0	0	0	1
Veber violations	0	0	0	0	0	0	0	0
Egan violations	0	0	0	0	0	0	0	0
Muegge violations	1	0	0	0	0	0	0	1
Bioavailability Score	0.55	0.55	0.55	0.55	0.55	0.55	0.55	0.55
PAINS alerts	0	0	0	0	0	0	0	0
Brenk alerts	0	0	0	0	0	0	0	0
Leadlikeness violations	1	1	1	1	1	1	1	1
Synthetic Accessibility	1.5	1.53	1.58	1.62	2.01	2.37	2.02	1.85

Table A8: ADME properties of Heterocyclic compounds.

SMILES		c1ccc(cc1)NCC1=NCCO1	Cc1ccc(cc1)NCC1=NCCO1	c1ccc(cc1)NCC1=NCCCO1	C1CN=C(O1)COc1cccc2c1nccc2	Cc1ccnc2c1cccc2OCC1=NCCO1
Compounds		**3a**	**3b**	**4a**	**7a**	**7b**
Physicochemical properties	MW	176.22	190.24	190.24	228.25	242.27
	H-bond acceptors	2	2	2	4	4
	H-bond donors	1	1	1	0	0
Lipophilicity & Water Solubility	iLOGP	2.16	2.29	2.29	2.32	2.34
	XLOGP3	1.51	1.87	1.87	1.62	2.13
	Consensus Log P	1.68	1.99	1.96	2.04	2.36
	Ali Log S	-1.82	-2.2	-2.2	-2.15	-2.68
	Ali Class	Very soluble	Soluble	Soluble	Soluble	Soluble
Pharmacokinetics	GI absorption	High	High	High	High	High
	BBB permeant	Yes	Yes	Yes	Yes	Yes
	Pgp substrate	No	No	No	No	No
	CYP1A2 inhibitor	Yes	Yes	Yes	Yes	Yes
	CYP2C19 inhibitor	No	No	No	No	Yes
	CYP2C9 inhibitor	No	No	No	No	No
	CYP2D6 inhibitor	No	No	No	No	Yes
	CYP3A4 inhibitor	No	No	No	No	No
Drug likeness	log Kp (cm/s)	-6.3	-6.13	-6.13	-6.54	-6.27
	Lipinski violations	0	0	0	0	0

	Ghose violations	0	0	0	0	0
	Veber violations	0	0	0	0	0
	Egan violations	0	0	0	0	0
	Muegge violations	1	1	1	0	0
	Bioavailability Score	0.55	0.55	0.55	0.55	0.55
Medicinal chemistry	PAINS alerts	0	0	0	0	0
	Brenk alerts	0	0	0	0	0
	Lead likeness #violations	1	1	1	1	1
	Synthetic Accessibility	2.87	2.79	2.87	2.97	2.92

Table A9: MM-GBSA of top score compounds in each HDAC3, HDAC6 and HDAC8.

COMPOUND	MINIMUM ENERGY (kcal/mol)	MEAN ENERGY (kcal/mol)
HDAC6 (5EDU)		
4c	-167.7821	-142.0745
7a	-148.5953	-133.8864
7b	-151.1089	-135.0693
SAHA ***(Bahena et al., 2017)***	*-83.16*	
HDAC8 (1T64)		
3a	-43.2887	-33.10135
3c	-49.8763	-33.4366
6a	-58.0195	-33.9598
7b	-65.199	-43.2327
8c	-49.6508	-29.6495
SAHA ***(Bahena et al., 2017)***	*-78.67*	
HDAC3 (4A69)		
3b	-55.4402	-42.8299
4c	-47.7377	-37.3444
8d	-53.1784	-47.3527
SAHA ***(Kumbhar et al., 2022)***	*−25.4*	

Table A10: In silico toxicity prediction profile of heterocyclic compounds.

Toxic Prediction	7a	7b
Hepatotoxicity	Inactive (0.80)	Inactive (0.80)
Neurotoxicity	Active (0.64)	Active (0.64)
Nephrotoxicity	Active (0.73)	Active (0.72)
Carcinogenicity	Active (0.50)	Inactive (0.50)
Respiratory toxicity	Active (0.78)	Active (0.77)
Immunotoxicity	Inactive (0.75)	Inactive (0.53)
Cytotoxicity	Inactive (0.68)	Inactive (0.68)
Mutagenicity	Inactive (0.58)	Inactive (0.57)
Cardiotoxicity	Inactive (0.62)	Inactive (0.62)

BBB-barrier	Active (0.85)	Active (0.86)

8.1 *In silico* studies in amide compounds

8.1.1 Molecular docking

A library of eight hydroxyacetamide derivatives (Figure 1) was docked into multiple HDAC isoforms using the Schrödinger Glide docking module in extra precision (XP) mode. The receptor grid was generated based on the position of the co-crystallized ligand and centered on the catalytic Zn^{2+} ion to accurately define the active site for docking. According to the docking analysis, hydroxyacetamide derivatives demonstrated strong interaction across all isoforms HDAC2 (4LXZ), HDAC3 (4A69), HDAC4 (2VQM), HDAC6 (5EDU), HDAC7 (3C10), HDA10 (7U59) (Table 1) within the range of -5.9 and -9.48 kcal/mol. For subsequent studies, HDAC6 was selected as the primary focus because of its significant role within the HDAC family.

8.1.2 Molecular dynamics

Protein does not have a fixed structure because of rapid conformational changes in the presence of solvent. Movement in protein backbone causes changes of □-helix, B-sheet and loop conformation as protein domains during folding and unfolding process, which in turn affect enzyme–inhibitor stability and interactions at the active site. Molecular dynamics simulation then aims to evaluate this change. In order to assess the flexibility and stability of the protein HDACs-Ligands complexes, molecular dynamics simulations for 100 ns were carried out using the desmond software. Following the docking studies, eight selected compounds were subjected to molecular dynamics simulations with each protein. During the molecular dynamics analysis of these compounds in HDAC6, some ligands exhibited bidentate interactions with the zinc ion (Figure 5), whereas others formed monodentate interactions.

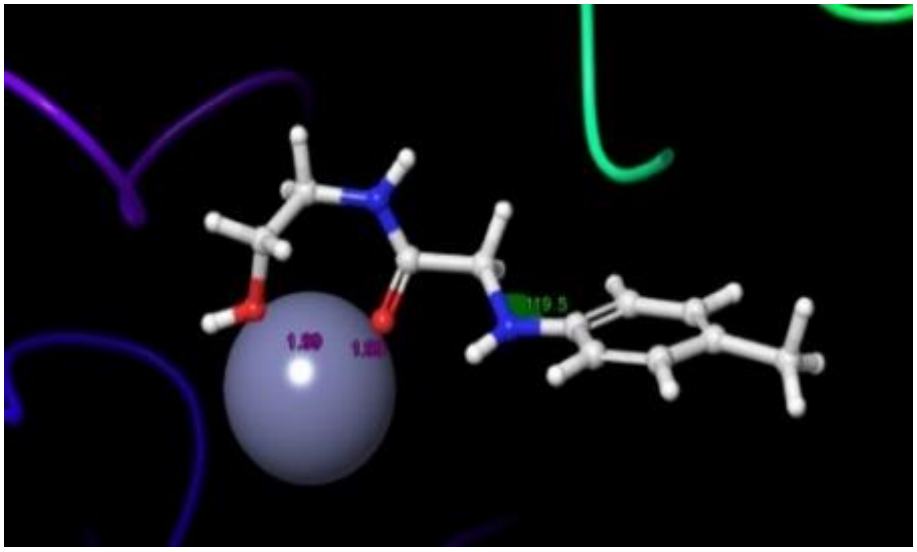

Figure A9: Molecular docking **11a** in HDAC8

8.2 Comparative study of selected three compounds in HDAC2, HDAC6 and HDAC6

To compare the interactions of the selected compounds within the different HDAC classes, HDAC2 and HDAC8 were used as Class I reference isoforms, while HDAC6 was selected as a Class IIb isoform.

8.2.1 HDAC6

The Cα RMSD graph of HDAC6 indicated general stability of the system throughout the simulation **Figure A10(a).** Complexes **2b** and **2c** showed initial fluctuations ~1 Å during the first 40 ns and 60 ns, respectively, after which they maintained stable phase for the rest of the simulation. All three complexes revealed stable RMSD (Root means square deviation) during the later phase of the trajectory.

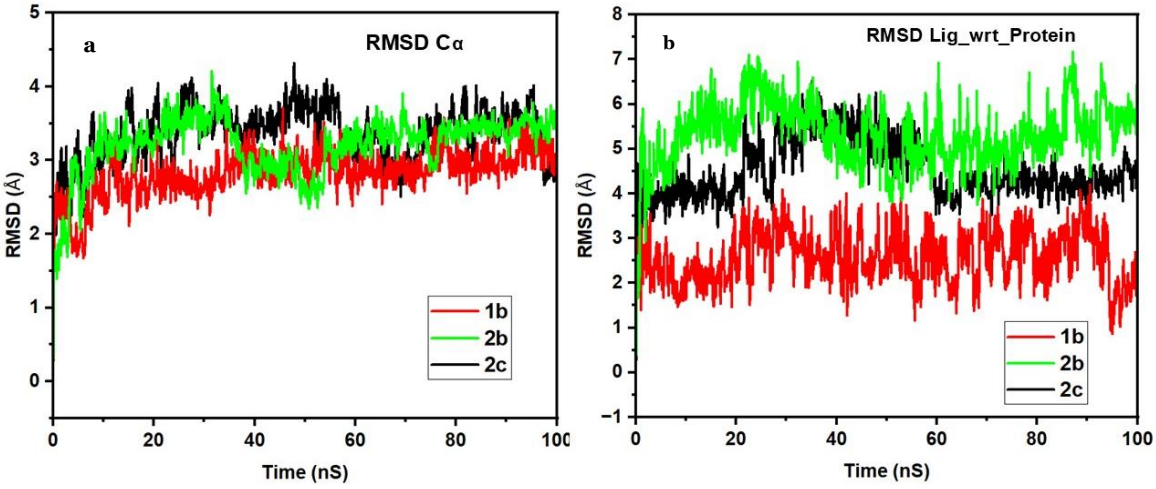

Figure A10: **(a)** Comparative RMSD profile plots of Cα atoms of HDAC6 with **1b, 2b** and **2c**. **(b)** Comparative RMSD profile plots of ligand with respect protein of HDAC6 with **1b, 2b** and **2c.**

Figure A10(b) represents the RMSD profiles of ligand with respect to protein in HDAC6 and its complexes with ligands **1b**, **2b**, and **2c** exhibited noticeable fluctuations during the early stages of the simulation. Specifically, HDAC6 and its complexes with ligands **2c** and **2b** showed clear changes within the first 40 ns, followed by a significant decrease in both complexes. While ligand **1b** showed pronounced conformational deviations during the initial 20 ns, after which its RMSD stabilized and plateaued beyond 40 ns. Beyond 60 ns, all systems displayed stable RMSD values, indicating that structural equilibrium had been achieved.

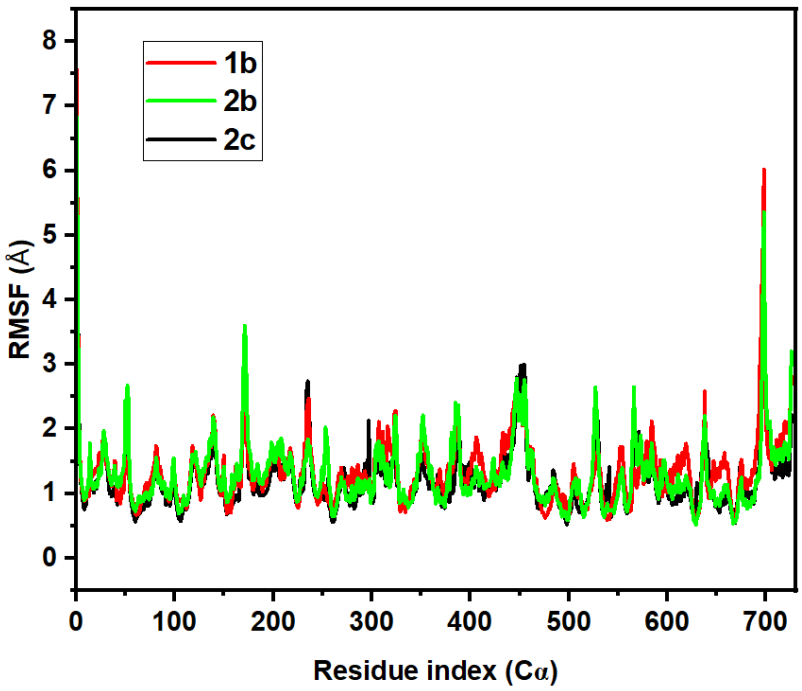

Figure A11: Comparative RMSF profile plots of Cα atoms of HDAC6 with **1b**, **2b** and **2c**.

The RMSF analysis revealed that the protein maintained an overall stable conformation during the simulation, with most residues exhibiting low fluctuations within the range of 1-2.5 Å (**Figure A11).** Moderate variations observed in certain loop regions indicate localized flexibility. Among the tested compounds, **1b**, **2b**, and **2c** induced noticeable fluctuations around residue 80, while **2b** and **2c** showed additional peaks near residue 250. All three complexes exhibited a prominent peak around residue 450. The highest fluctuations were detected at the N- and C-terminal regions, exceeding 2.5 Å, which is typical for these solvent-exposed. Overall, the RMSF profiles confirm that the protein backbone remained stable in all complexes, with only expected flexibility in loop and terminal regions.

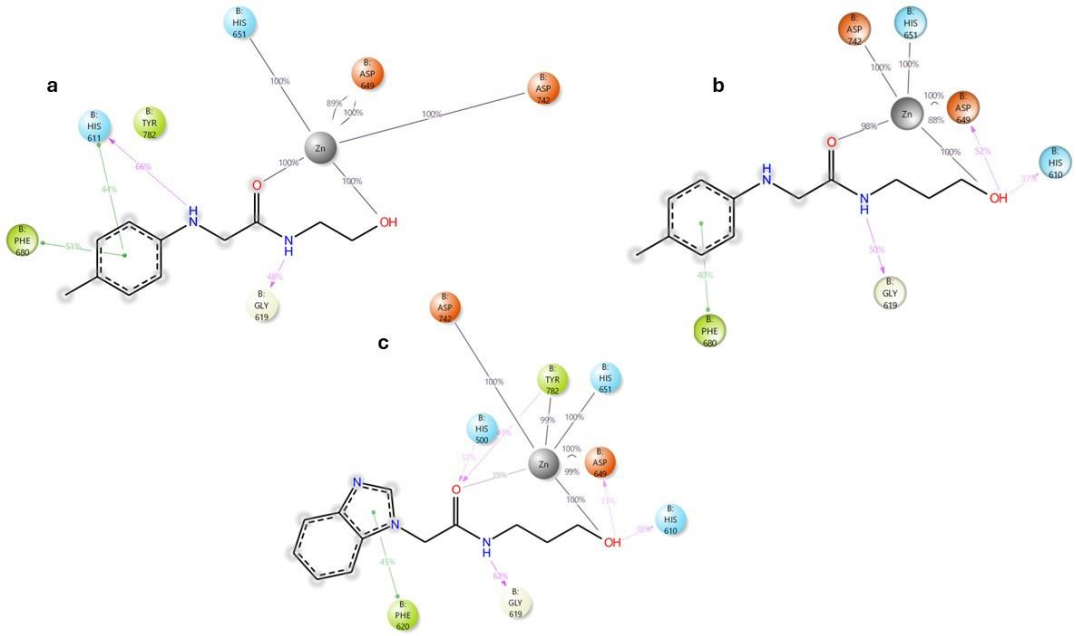

Figure A12: 2D summary of interaction analysis results of HDAC6-ligand complexes; HDAC6-**1b**, HDAC6-**2b** and HDAC6-**2c**.

Ligand interaction diagram of HDAC2 with compounds **1b, 2b**, and **2c** (**Figure A12**) showed bidentate interaction in the binding site. The zinc ion coordinated with both the hydroxyl and carbonyl groups of the ligands. In the case of the other ligands, monodentate binding occurred within HDAC6. Furthermore, the alpha amino group of all compounds formed a hydrogen bond with the residue Gly154. The hydroxyl groups in ligands 2b and 2c also formed hydrogen bonds with the residue His410.

8.2.2 HDAC8

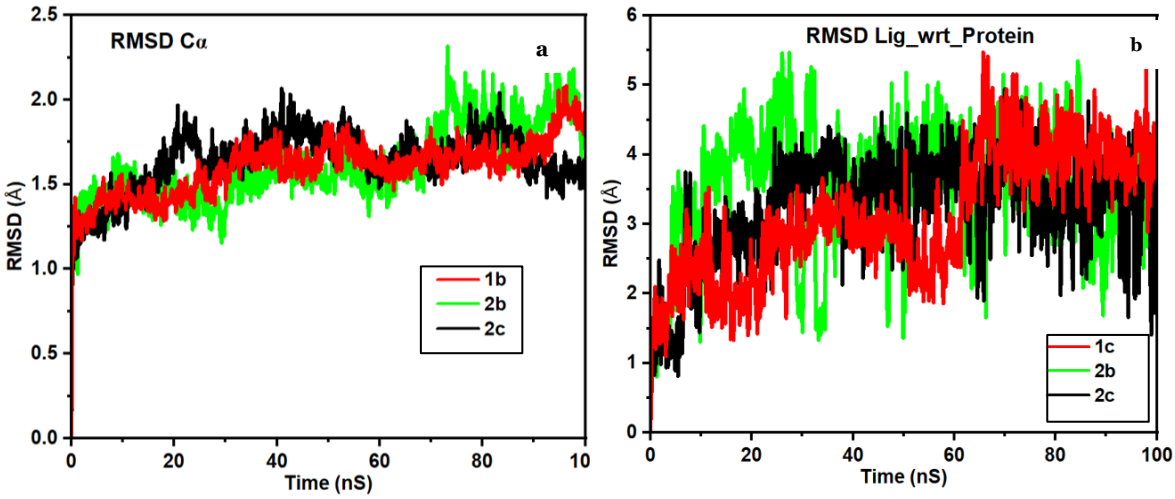

Figure A13: **(a)**Comparative RMSD profile plots of Cα atoms of HDAC8 with **1b, 2b** and **2c**. **(b)** Comparative RMSD profile plots of ligand with respect protein of HDAC6 with **1b, 2b** and **2c**

RMSD of the protein backbone was analyzed to assess structural stability of the complexes during the 100 ns molecular dynamics simulation. As shown in **Figure A13(a)**, all complexes exhibited an increase in RMSD within the first 10 ns, as the system reached equilibrium and protein relaxes structurally upon ligand binding. After 20 ns, the RMSD became stable, indicating that all systems reached a steady state.

The RMSD Lig_wrt_Protein profiles (**Figure A13(b)**) indicated that compounds **1c** and **2c** experienced gradual increases in RMSD during the initial stages of the simulation, reaching stable values by approximately 30 ns. Compound **2b** maintained RMSD values of around 2.5 Å before reaching a steady state phase. For compound **2c**, an early stage rise in RMSD was observed during the first 10 ns, followed by a clear peak around 20 ns. A subsequent conformational change occurred at ~60 ns, after which the RMSD stabilized, indicating a new equilibrium binding mode within the active site

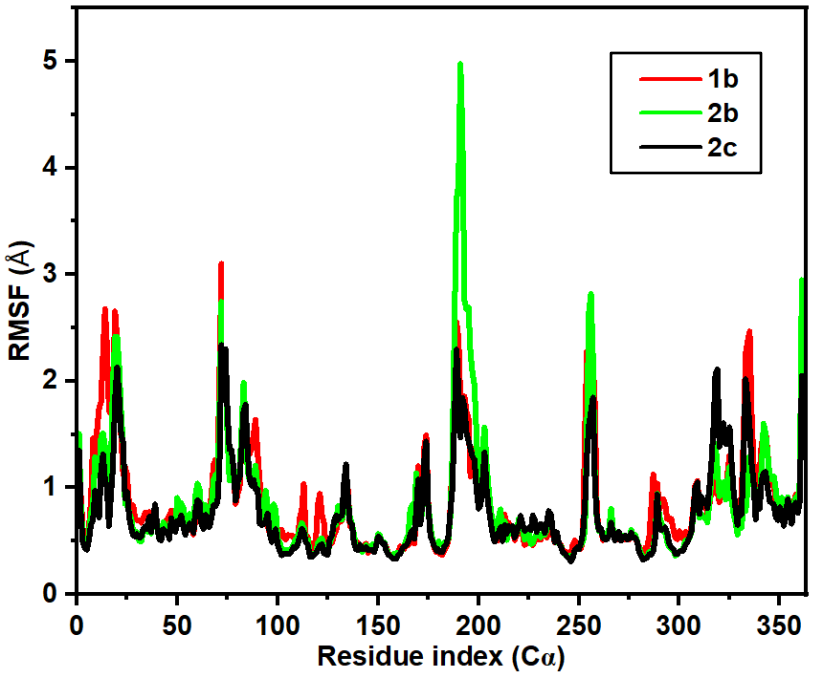

Figure A14: Comparative RMSF profile plots of Cα atoms of HDAC8 with **1b, 2b** and **2c**.

Root Mean Square Fluctuation (RMSF) analysis was performed to evaluate the residue level flexibility of the protein backbone in the presence of different ligands (**1b**, **2b**, and **2c**) throughout the 100 ns molecular dynamics simulation (**Figure A14**). Among the analyzed complexes with HDAC8, Ligand **1b** and **2b** maintained the lowest and most stable RMSD fluctuations (1.0-2.0 Å), suggesting minimal structural perturbation and greater conformational stability of the protein backbone. while exhibiting slightly higher deviations (>4Å), indicating localized flexibility or weaker stabilizing interactions. Overall, the reduced atomic fluctuations in **1b** and **2c** complexes suggest that these ligands provide greater conformational stability to the protein compared to **2b**, consistent with their potentially stronger binding affinities and favorable interaction profiles observed in docking and MD analyses.

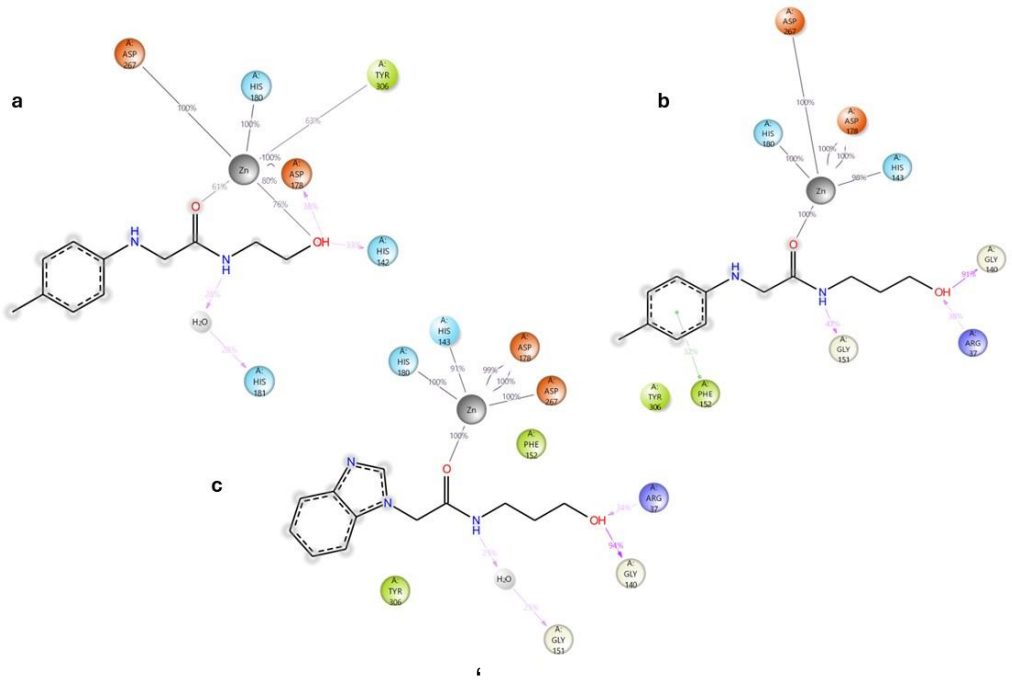

Figure A15: 2D summary of interaction analysis results of HDAC8-ligand complexes; HDAC8-**1b**, HDAC8-**2b**, HDAC8-**2c**.

Compound **1b** exhibited bidentate coordination within the HDAC8 active site, with the catalytic Zn^{2+} ion interacting simultaneously with both the hydroxyl and carbonyl oxygen atoms of the ligand. In contrast, compounds **2b** and **2c** displayed monodentate coordination through the carbonyl group. Furthermore, compounds **1b** and **2c** formed water-mediated hydrogen-bonding interactions with His181 and Gly151, respectively, via their amide NH groups, whereas compound **2b** established a direct hydrogen bond with Gly151 (**Figure A15**).

8.2.3 HDAC2

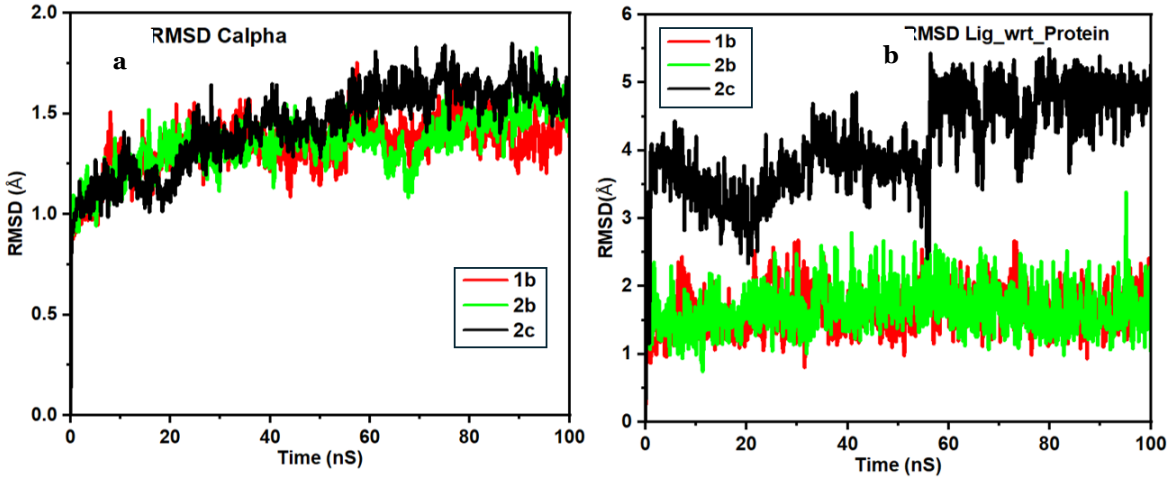

Figure A16: **(a)** Comparative RMSD profile plots of Cα atoms of HDAC2 with **1b, 2b** and **2c**. **(b)** Comparative RMSD profile plots of ligand with respect protein of HDAC6 with **1b, 2b** and **2c.**

All four complexes of HDAC2 with the compounds (**1b**, **2b**, and **2c**) (**Figure A16(a)**) show a rise in RMSD during the first 10-15 ns, which indicates the expected initial structural relaxation phase of the protein-ligand systems. After this early fluctuation, the RMSD values gradually stabilized within the range of 1.2-1.7 Å throughout the remaining simulation up to 100 ns. All systems maintain RMSD values below 2.0 Å, indicating good structural stability.

The ligand RMSD profiles relative to the protein backbone revealed distinct binding behaviors among the three complexes (**Figure A16(b)**). Compounds **1b** and **2b** maintained low RMSD values throughout the simulation, fluctuating primarily between 1 and 2.5 Å, indicating stable binding poses within the HDAC6 active site. Although **2b** exhibited slightly greater fluctuations than **1b**, both ligands remained stable in the binding pocket. In contrast, compound **2c** displayed higher RMSD values, ranging from ~3 to 5.5 Å. Conformational changes were observed around 55-60 ns, after which the RMSD stabilized at a higher level. These results suggest that

2c showed major reorientation within the binding pocket and adopted an alternative binding mode, whereas **1b** and **2b** retained their initial binding conformations throughout the simulation.

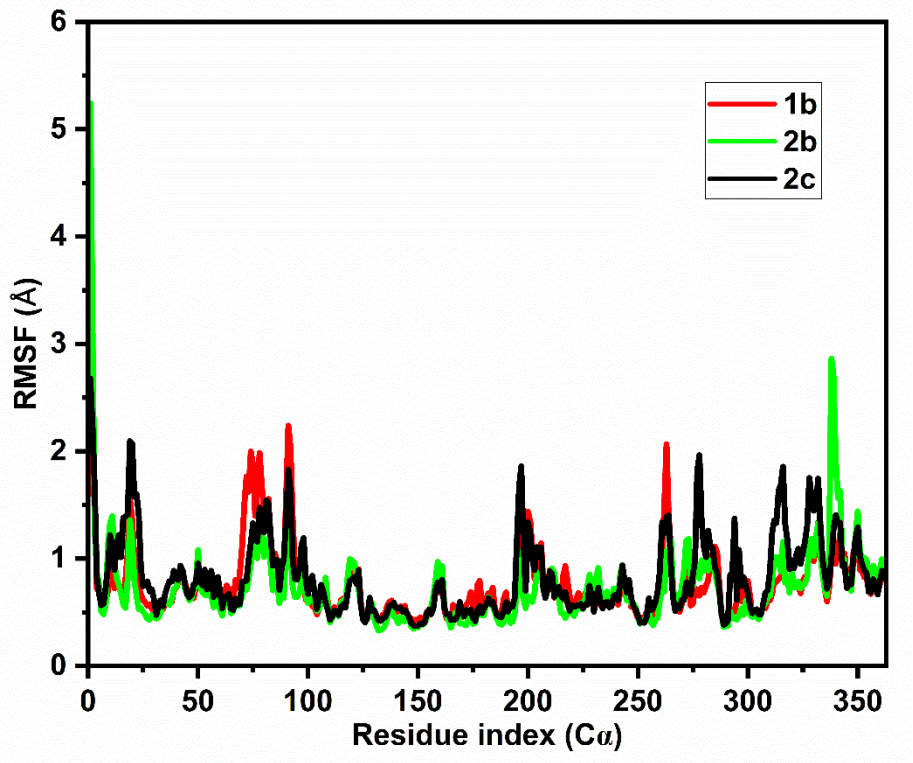

Figure A17: Comparative RMSD profile plots of Cα atoms of HDAC2 with **1b, 2b** and **2c.**

As shown in the figure, the residues remained largely stationary in all complexes over the 350 ns molecular dynamics simulations. **Figure A17** further shows that all four complexes exhibited comparable RMSF profiles, with most residues fluctuating below 2 Å, indicating overall structural stability. Among the tested ligands, **1b** exhibited slight peaks of 1-2 Å at residues 50-80 and around residue 260.while **2b** showed a pronounced peak near residue 350. A minor peak observed at residue 225 for **2c** suggests localized flexibility, possibly due to ligand induced conformational adjustments. Overall, all the compound's fluctuations within the indicate favorable conformational stability.

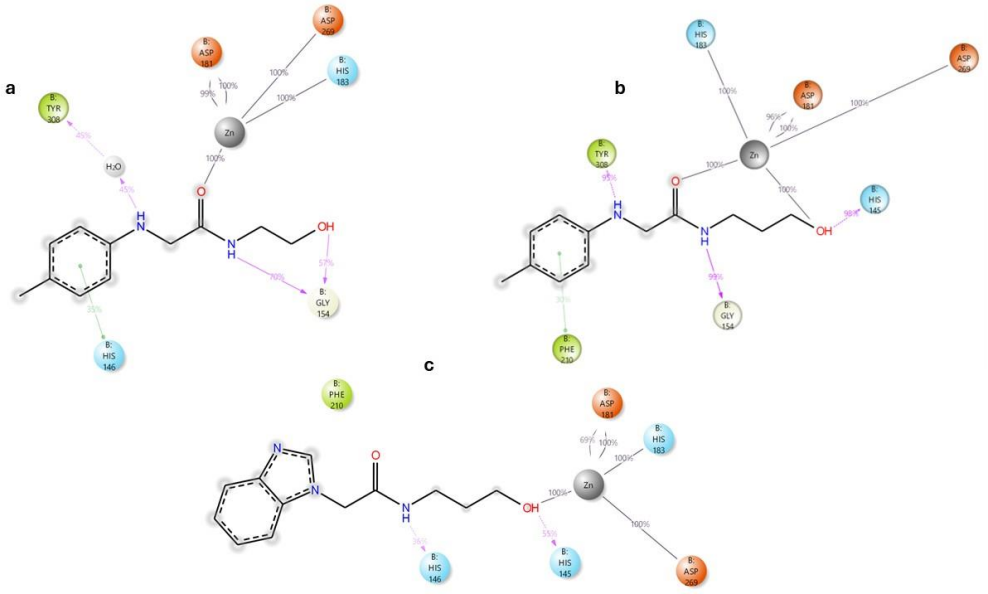

Figure A18: 2D summary of interaction analysis results of HDAC2-ligand complexes; HDAC2-**1b**, HDAC2-**2b** and HDAC2-**2c.**

In the HDAC2 active site, compound **2b** exhibited bidentate coordination with the catalytic Zn^{2+} ion through both the hydroxyl and carbonyl groups. In contrast, compounds **1b** and **2c** displayed monodentate coordination via the carbonyl and hydroxyl groups, respectively (**Figure A18**). Additionally, the α-amino group of all ligands formed hydrogen-bonding interactions with Gly154 and His146. The α-amino groups of compounds **1b** and **2b** established additional interactions with Tyr308 through both water-mediated and direct hydrogen bonds. Furthermore, the hydroxyl groups of all ligands, except **1b**, participated in hydrogen-bonding interactions with His145.

Table A11: *In silico* toxicity prediction profile of synthesized compounds.

TOXICITY	10a	11a	11d	11e	11f
Hepatotoxicity	Inactive(0.92)	Inactive(0.91)	Inactive(0.55)	Inactive(0.55)	Inactive(0.88)
Neurotoxicity	Active(0.62)	Active(0.62)	Active(0.74)	Active(0.74)	Active(0.64)
Nephrotoxicity	Active(0.53)	Active(0.53)	Active(0.63)	Active(0.63)	Active(0.59)
Respiratory toxicity	Active(0.72)	Active(0.72)	Active(0.82)	Active(0.82)	Active(0.68)
Cardiotoxicity	Active(0.52)	Active(0.5)	Inactive(0.7)	Inactive(0.7)	Inactive(0.63)
Carcinogenicity	Inactive(0.63)	Inactive(0.63)	Active(0.55)	Active(0.55)	Inactive(0.61)
Immunotoxicity	Inactive(0.97)	Inactive(0.98)	Inactive(0.97)	Inactive(0.98)	Inactive(0.99)
Mutagenicity	Active(0.54)	Active(0.52)	Active(0.62)	Active(0.62)	Inactive(0.61)
Cytotoxicity	Inactive(0.61)	Inactive(0.62)	Inactive(0.73)	Inactive(0.73)	Inactive(0.84)
BBB-barrier	Active(0.65)	Active(0.62)	Active(0.72)	Active(0.72)	Active(0.69)
Ecotoxicity	Inactive(0.54)	Inactive(0.54)	Inactive(0.56)	Inactive(0.56)	Inactive(0.63)

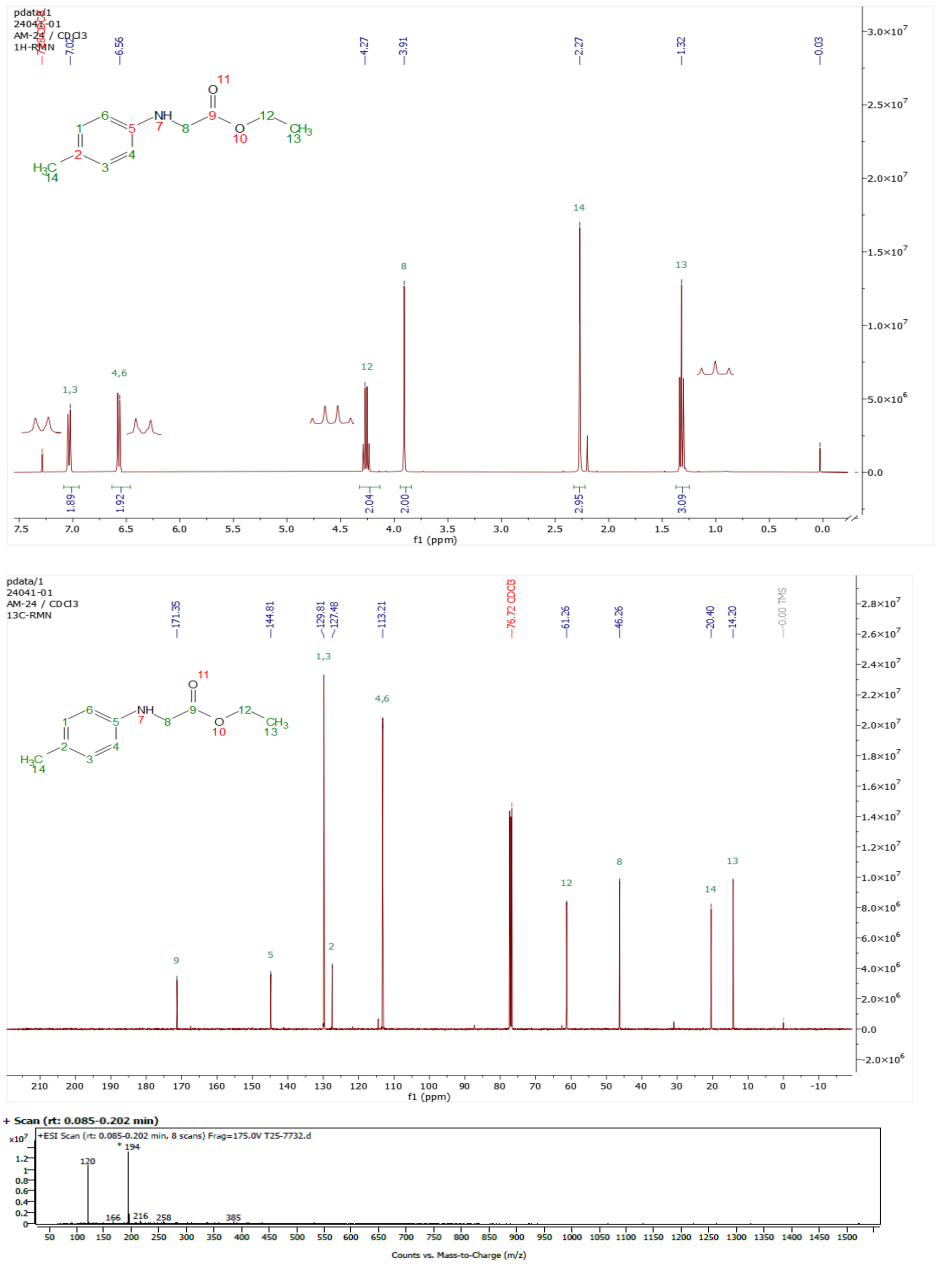

Figure A19: ^{1}H NMR, ^{13}C NMR, and Mass spectra of compound **9b**.

^{1}H NMR (400 MHz, *CDCl*$_3$): δ 7.02, (d, 2H, J = 8.4 Hz, **H**$_{Ar\,1,3}$), 6.57 (d, J = 8.4 Hz, 2H, **H**$_{Ar\,4,6}$), 4.26 (c, 2H, J = 7.0 Hz, **OCH**$_2$), 3.91 (s, 2H, O=C**CH**$_2$), 2.27 (s, 3H, **CH**$_3$Ph), 1.32 (t, J = 7.0 Hz, 3H, **CH**$_3$CH$_2$O). **^{13}C NMR** (176 MHz, *DMSO-d*$_6$): δ 171.36 (**C=O**), 144.82 (**C**$_{Ar5}$), 129.82 (**C**$_{Ar1,3}$), 127.49 (**C**$_{Ar2}$), 113.22 (**C**$_{Ar4,6}$), 61.27 (CH$_3$-**CH**$_2$-O), 46.27 (NH-**CH**$_2$), 20.41 (**CH**$_3$-Ph), 14.21 (O-CH$_2$**CH**$_3$). **HMRS (ESI+) [M+H]$^+$** *m/z* calculated for $C_{11}H_{15}NO_2$ 193.1103; found **194.1173**.

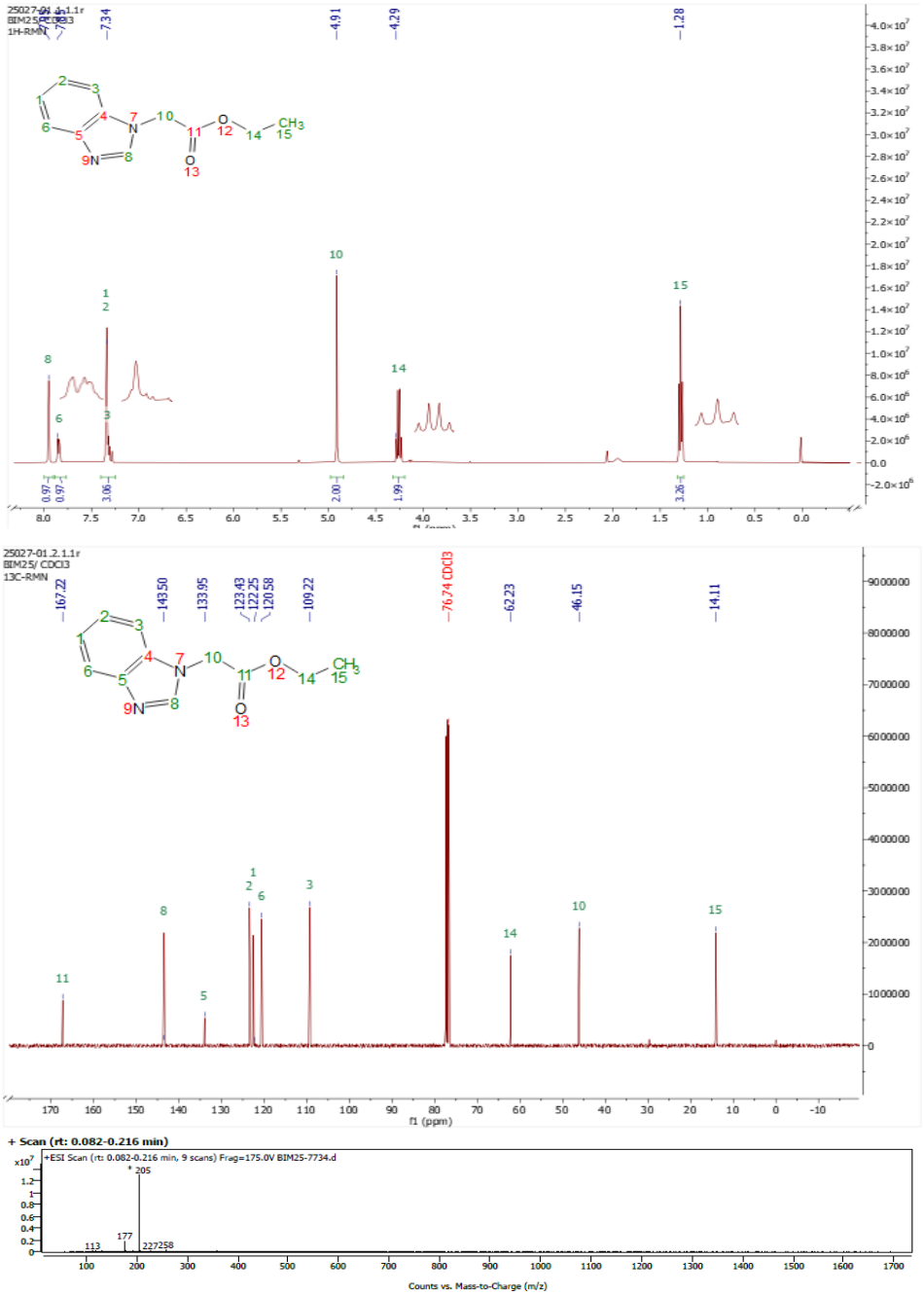

^{1}H NMR (400 MHz, *CDCl*$_3$): δ 7.95, (s, 1H, **H$_{Ar8}$**), 7.84 (m, 1H**, H$_{Ar6}$**), 7.27-7.35 (m, 3H, **H$_{Ar1,2,3}$**) 4.91 (s, 2H, O=C**CH$_2$**), 4.25 (q, *J* = 7.2, 2H, O**CH$_2$**-CH$_3$), 1.28 (t, *J* = 7.2 Hz, 3H, **CH$_3$**CH$_2$O). **^{13}C NMR** (176 MHz, *DMSO-d*$_6$): δ 167.22 (**C=O**), 143.50 (N-**C**-N), 133.95 (**C$_{Ar4,5}$**), 123.43 (**C$_{Ar2}$**), 122.25 (**C$_{Ar1}$**), 120.58 (**C$_{Ar6}$**), 109.22 (**C$_{Ar3}$**), 62.23 (CH$_3$-**CH$_2$**-O), 46.15 (NH-**CH$_2$**), 14.11 (O-CH$_2$**CH$_3$**). **HMRS (ESI+) [M+H]$^+$** *m/z* calculated for $C_{11}H_{12}N_2O_2$ 204.0899; found 205.0967

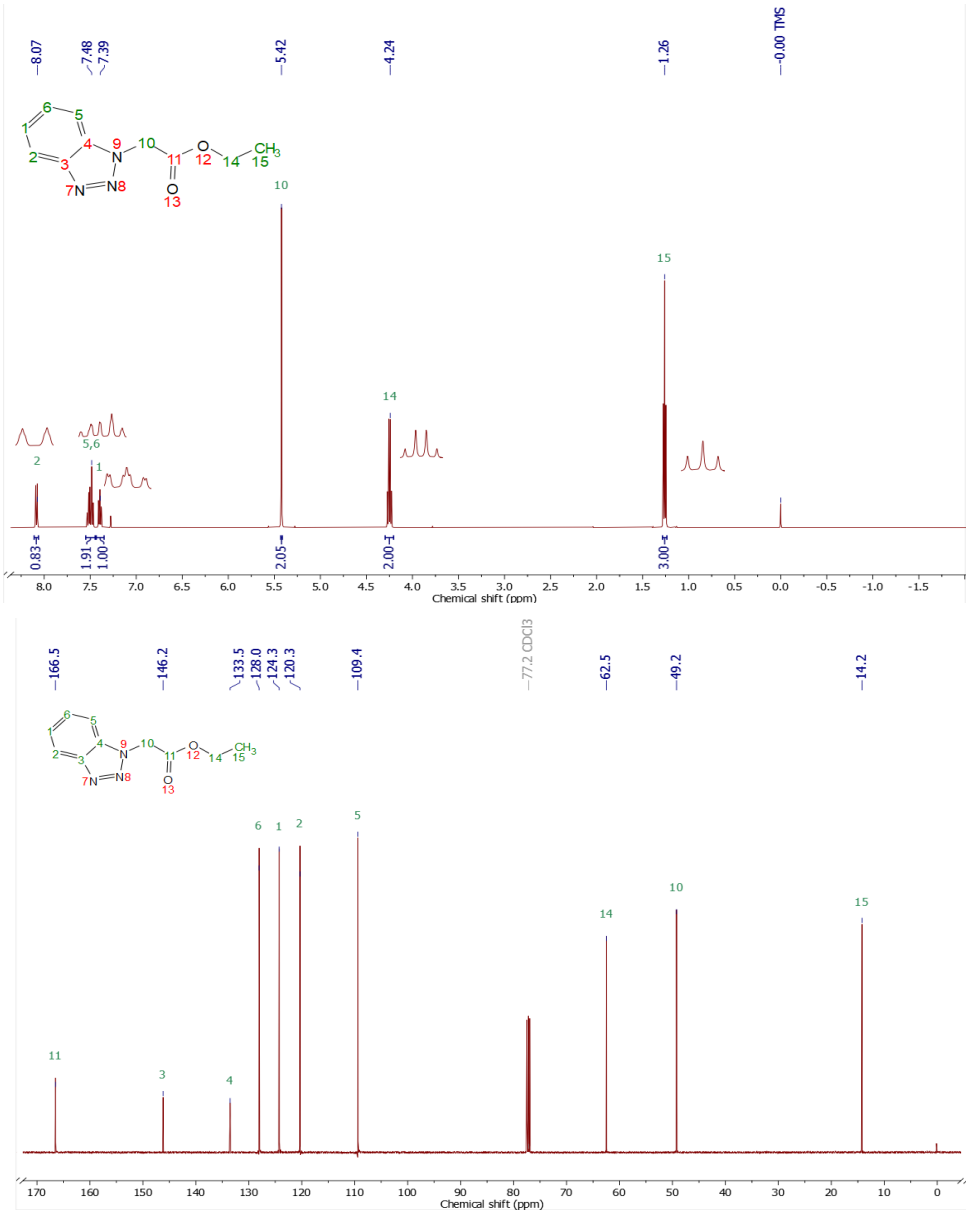

Figure A21: ^{1}H NMR, ^{13}C NMR, Mass spectrum of compound **9d.**

^{1}H NMR (500 MHz, $CDCl_3$): δ 8.07 (td, *J* = 8.44, 1.0 Hz, 1H, **$H_{Ar\,2}$**), 7.49 (m, 2H, **$H_{Ar\,5,\,6}$**), 7.7 (td, *J* = 8.20, 1.50 Hz 2H, **H_{Ar1}**), 5.42 (s, 2H, **CH_2**-C=O), 4.24 (q, *J* = 7.2 Hz, 2H, **CH_2**-CH_3), 1.26 (t, *J* = 7.05 Hz, 3H, CH_2-**CH_3**). **^{13}C NMR** (126 MHz, $CDCl_3$): δ 166.5 (**C=O**), 146.2 (**C_{Ar3}**) 133.5 (**C_{Ar4}**), 128.0 (**C_{Ar6}**), 124.3 (**C_{Ar1}**), 120.3 (**C_{Ar2}**), 109.4 (**C_{Ar5}**), 62.5, (**CH_2**-CH_3) 49.2 (**CH_2**- C=O), 14.2 (CH_2-**CH_3**) . HRMS (ESI+): $C_{10}H_{11}N_3O_2$ *m/z* calculated for 206.0930, found *m/z* **206.0922.**

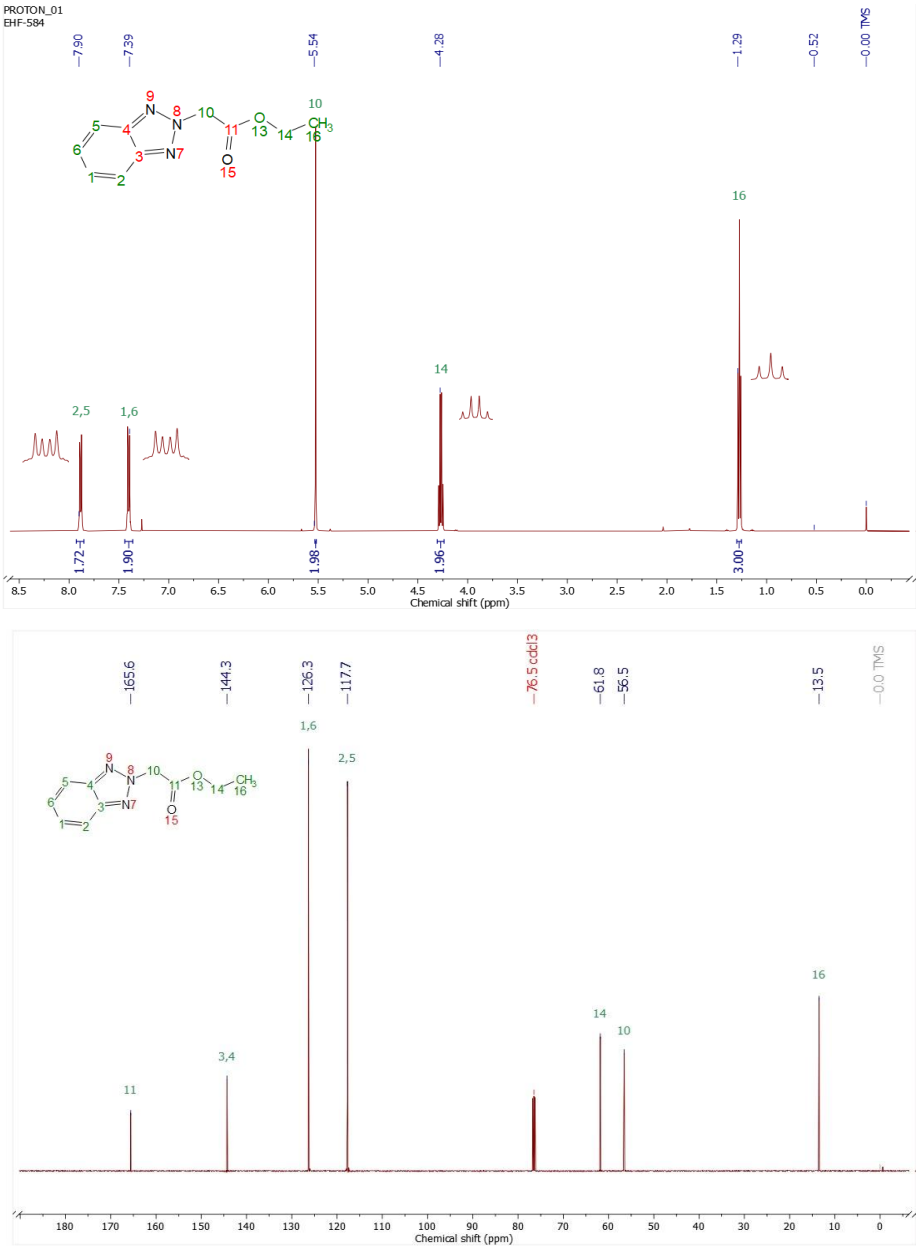

Figure A22: ^{1}H NMR, ^{13}C NMR, Mass spectrum of compound **9e.**

^{1}H NMR (500 MHz, $CDCl_3$): δ 7.90 (dd, *J* = 9.65, 2.9 Hz, 2H, **$H_{Ar2,5}$**), 7.39 (dd, *J* = 9.65, 2.8 Hz, 2H, **$H_{Ar1,6}$**), 5.54 (s, 2H, **CH_2-** C=O) 4.26 (q, *J* = 7.25 Hz, 2H, **CH_2**-CH_3), 1.27 (t, *J* = 7.25 Hz, 3H, CH_2-**CH_3**). **^{13}C NMR** (126 MHz, $CDCl_3$): δ 165.7 (**C=O**), 144.3 (**$C_{Ar3,4}$**), 126.3 (**$C_{Ar1,6}$**), 117.7 (**$C_{Ar2,5}$**), 61.8 (**CH_2**-CH_3), 56.5 (**CH_2**-C=O), 13.5 (CH_2-**CH_3**). **HRMS (ESI+)**: $C_{10}H_{11}N_3O_2$ *m/z* calculated for 206.0930, found *m/z* **206.0921**.

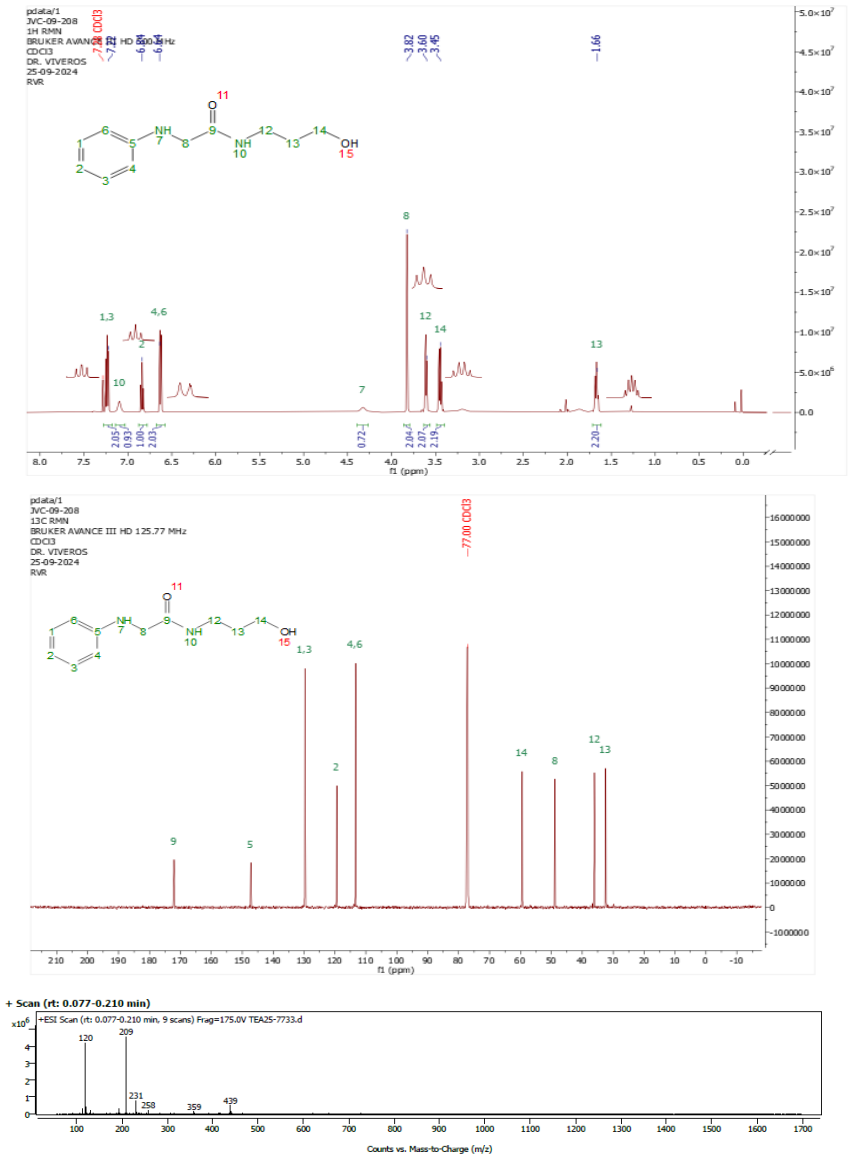

Figure A23: ^{1}H NMR, ^{13}C NMR, Mass spectrum of compound **11a.**

^{1}H NMR (500 MHz, *CDCl*$_3$): δ 7.23, (dd, J = 8.5, 8.7, 2H, **H$_{Ar3,1}$**), 7.09 (bs, 1H**, NH**-C=O), 6.83 (tt, J = 7.3, 1.05, 1H, **H$_{Ar2}$**), 6.62 (dd, J = 7.65, 1.05, 2H, **H$_{Ar4,6}$**), 4.31 (bs, 1H, **NH**-CH$_2$), 3.82 (s, 2H, NH-**CH$_2$**), 3.61 (t, *J* = 5.7 Hz, 2H, HOCH$_2$-CH$_2$-**CH$_2$**-), 3.45 (q, *J* = 6.4 Hz, 2H, HO**CH$_2$**-CH$_2$-CH$_2$-), 1.67 (qn, *J* = 6.0 Hz, 2H, -CH$_2$**CH$_2$**CH$_2$OH). **^{13}C NMR** (176 MHz, *DMSO-d*$_6$): δ 162.07 (**C=O**), 147.24 (**C$_{Ar5}$**), 129.73 (**C$_{Ar1,3}$**), 119.44 (**C$_{Ar2}$**), 113.36 (**C$_{Ar4,6}$**), 59.42 (-CH$_2$-CH$_2$-**CH$_2$**-OH), 48.87 (NH-**CH$_2$**), 36.11 (-**CH$_2$**-CH$_2$-CH$_2$OH), 32.48(-CH$_2$-**CH$_2$**-CH$_2$OH). **HMRS (ESI+)[M+H]$^+$** *m/z* calculated for $C_{11}H_{16}N_2O_2$ 208.1212; found **209.1292**.

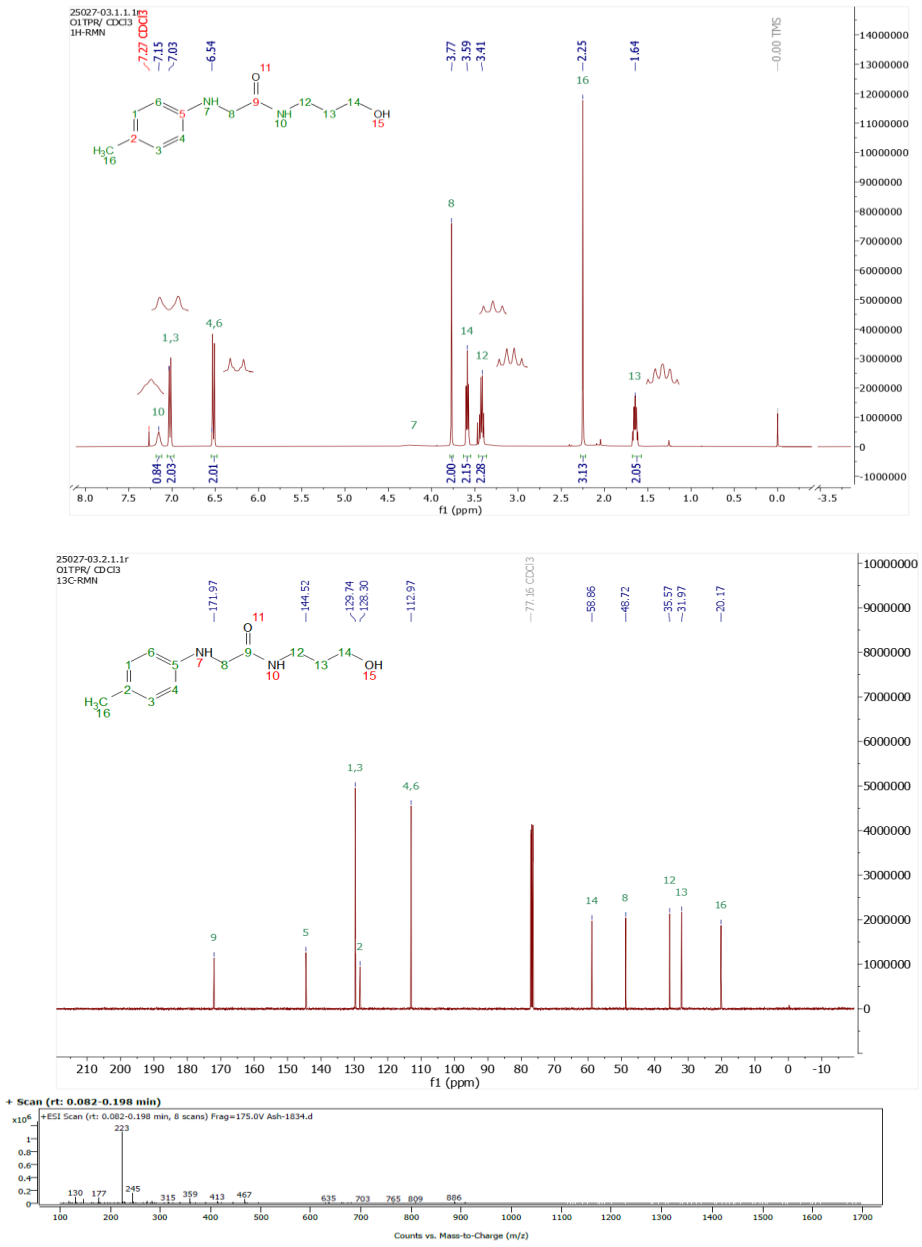

Figure A24: 1H NMR, 13C NMR, Mass spectrum of compound **11b.**

^{1}H-NMR (400 MHz, *CDCl*$_3$): δ 7.17 (pst, *J* = 6.48 Hz 1H, **NH**), 7.01 (d, *J* = 8.32 Hz, 2H, **H**$_{\mathbf{Ar\,1,3}}$), 6.52 (d, *J* = 8.56 Hz, 2H, **H**$_{\mathbf{Ar\,4,6}}$), 4.22 (brs, 1H, **NH**Ph), 3.77 (s, 1H, **NH**Ph), 3.67 (t, *J* = 5.64 Hz, 2H, **CH$_2$**OH), 3.41 (q, *J* =6.08 Hz, 2H, NH-**CH$_2$**), 2.25 (s, 3H, **CH$_3$**Ph) 1.66 (qn, , *J* = 6.08 Hz 2H, CH_2-**CH_2**-CH_2)). **^{13}C NMR** (176 MHz, *DMSO-d*$_6$): δ 171.97 (**C=O**), 144.52 (**C$_{Ar5}$**), 129.74 (**C$_{Ar1,3}$**), 129.98 (**C$_{Ar2}$**), 112.97 (**C$_{Ar4,6}$**), 58.87 (-CH_2-CH_2-**CH_2**-OH), 48.72 (NH-**CH_2**), 35.57 (-**CH_2**-CH_2-CH_2OH), 31.97 (-CH_2-**CH_2**-CH_2OH), 20.17 (-**CH_3**-Ph). **HMRS (ESI+)[M+H]$^+$** *m/z* calculated for $C_{11}H_{16}N_2O_2$ 222.29; found **223.1425.**

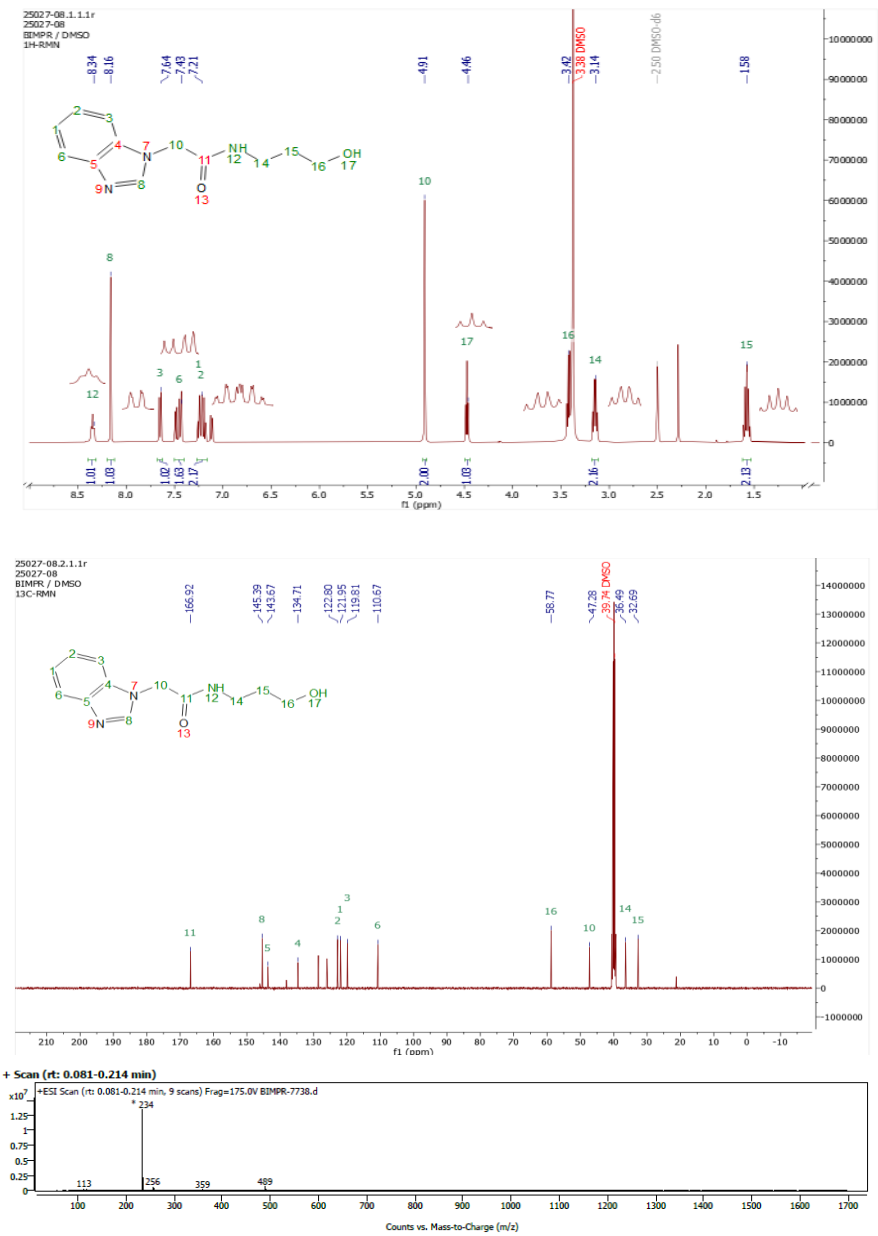

Figure A25: ^{1}H NMR, ^{13}C NMR, Mass spectrum of compound **11c.**

^{1}H NMR (500 MHz, *CDCl*$_3$): δ 8.34 (t, 7.0 Hz, 1H, **NH**-C=O), 8.16 (s, 1H, N-**CH**-N), 7.64 (dd, J = 7.4 , 1.55 Hz, 1H, **H$_{Ar3}$**), 7.44 (dd, 7.55, 1.6, Hz, 1H, **H$_{Ar6}$**), 7.21 (m, 2H, **H$_{Ar1,2}$**), 4.91 (s, 2H, **CH$_2$**-C=O), 4.47 (t, 6.3 Hz, 1H, **OH**), 3.42 (q, J=6.4 Hz, 2H, OH-**CH$_2$**-) 3.14 (q, J= 6.85 Hz, 2H, NH-**CH$_2$**-), 1.57 (qn, J = 8.2 Hz, 2H, HOCH$_2$-**CH$_2$**-CH$_2$-). **^{13}C NMR** (176 MHz, *DMSO-d*$_6$): δ 166.92 (**C=O**), 145.39 (**C$_{Ar8}$**), 143. 67 (**C$_{Ar5}$**), 134. 71 (**C$_{Ar4}$**), 122.80 (**C$_{Ar2}$**), 121.95 (**C$_{Ar1}$**), 119.81 (**C$_{Ar3}$**), 110.67 (**C$_{Ar6}$**), 58.67 (OH-**CH$_2$**-), 47.28 (O=C-**CH$_2$**-), 36.49 (NH-**CH$_2$**-), 32.69 (-CH$_2$-**CH$_2$**-CH$_2$OH). **HMRS (ESI+)[M+H]$^+$** *m/z* calculated for $C_{12}H_{15}N_3O_2$ 233.1164; found **234.1234.**

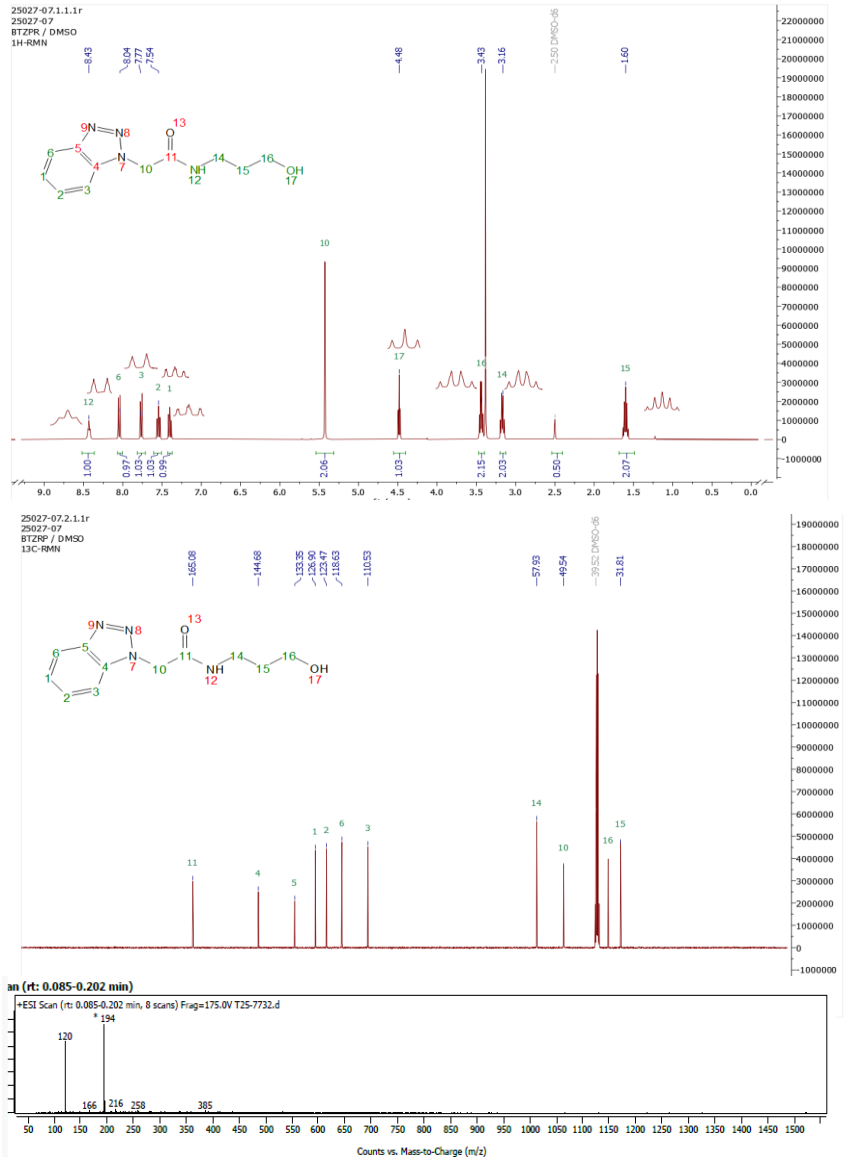

Figure A26: ^{1}H NMR, ^{13}C NMR, Mass spectrum of compound **11d**

^{1}H NMR (500 MHz, *CDCl*$_3$): δ 8.43 (brt, 6.85 Hz, 1H, **NH**-C=O), 8.04 (dt, J =8.1, 1.15 Hz, 1H, **HAr$_6$**), 7.76 (dt, J = 8.0 , 1.15, Hz 1H, **H$_{Ar3}$**), 7.54 (td, J =7.5, 1.1, Hz, 1H, **H$_{Ar2}$**), 7.40 (td, J = 7.50, 1.15 Hz, 1H, **H$_{Ar1}$**), 5.42 (s, 2H, **CH$_2$**-C=O), 4.43 (t, J = 6.35 Hz, 1H, **OH**), 3.43 (q, 6.7 Hz, 2H, -**CH$_2$**CH$_2$CH$_2$-OH), 3.16 (q, J=7.2 Hz, 2H, OH-**CH$_2$**-CH$_2$-CH$_2$-), 1.59 (qn, J = 8.55 Hz, 2H, HOCH$_2$-**CH$_2$**-CH$_2$-). **^{13}C NMR** (176 MHz, *DMSO-d*$_6$): δ 165.06 (**C=O**), 144.68 (**C$_{Ar4}$**), 133.32 (**C$_{Ar5}$**), 126.60 (**C$_{Ar1}$**), 123.47 (**C$_{Ar2}$**), 118.63 (**C$_{Ar6}$**), 110.53 (**C$_{Ar3}$**), 57.93 (OH-**CH$_2$**-CH$_2$CH$_2$-), 35.70 (OH-CH$_2$-CH$_2$**CH$_2$**-), 31.81 (-CH$_2$-**CH$_2$**-CH$_2$OH). **HMRS (ESI+)[M+H]$^+$** *m/z* calculated for $C_{11}H_{14}N_4O_2$ 234.1117; found **235.1180**

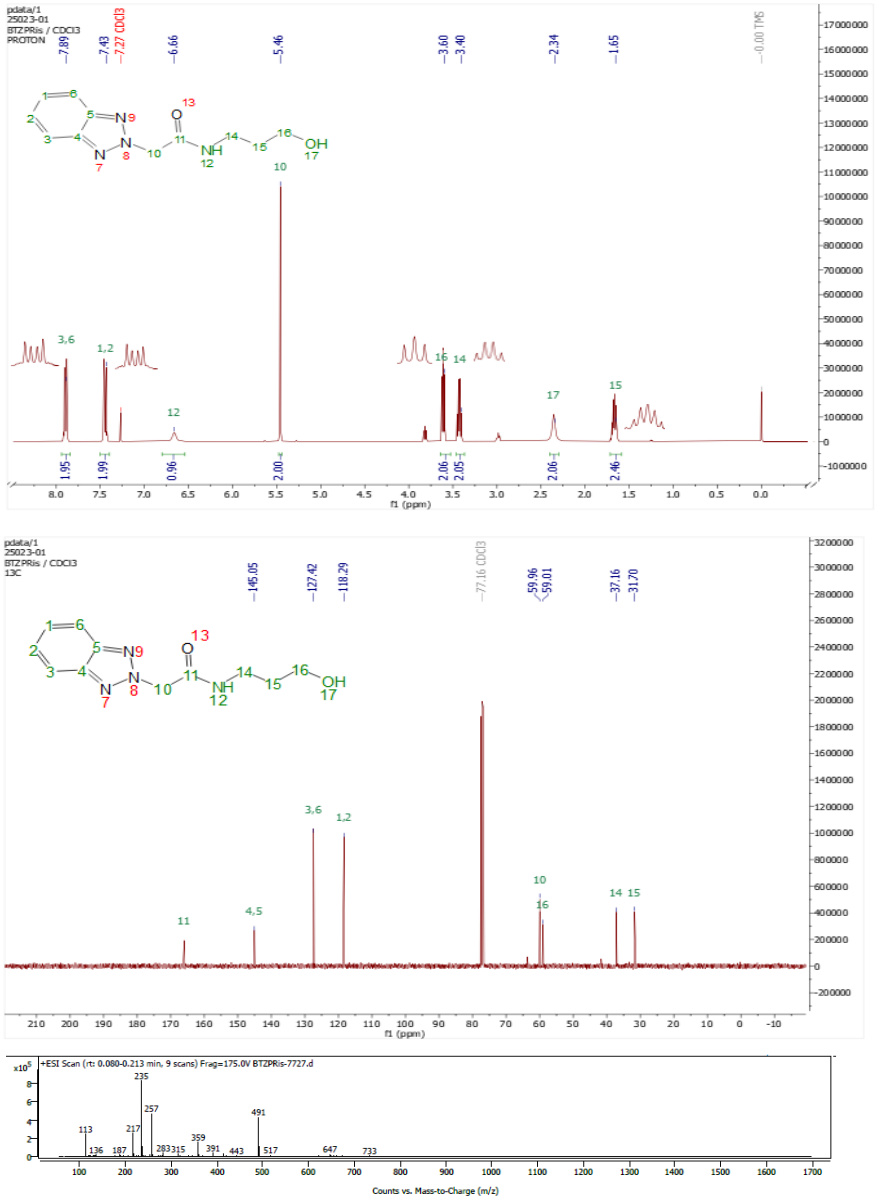

Figure A27: ^{1}H NMR, ^{13}C NMR, Mass spectrum of compound **11e**

^{1}H NMR (500 MHz, *CDCl*$_3$): δ 7.89 (dd, J = 8.2, 8.25 Hz, 2H, **H$_{Ar3,6}$**), 7.44 (dd, *J* =8.25, 8.25 Hz, 2H, **HAr$_{1,2}$**), 6.65 (brs, 1H, **NH**), 5.46 (s, 2H, **CH$_2$**-C=O), 3.60 (t, *J* = 7.0 Hz, 2H, OHCH$_2$CH$_2$**CH$_2$**-), 3.42 (q, 7.5 Hz, 2H, -CH$_2$CH$_2$**CH$_2$**-OH), 2.35 (brs, 1H, **OH**), 1.66 (qn, *J* = 7.5 Hz, 2H, HOCH$_2$-**CH$_2$**-CH$_2$-). **^{13}C NMR** (176 MHz, *DMSO-d*$_6$): δ 165.82 (**C=O**), 145.06 (**C$_{Ar4,5}$**), 127.42 (**C$_{Ar3,6}$**), 118.29 (**C$_{Ar1,2}$**), 59.96 (OH-**CH$_2$**-CH$_2$CH$_2$-), 59.01(**CH$_2$**-C=O), 37.16 (OH-CH$_2$-CH$_2$**CH$_2$**-), 31.70 (-CH$_2$-**CH$_2$**-CH$_2$OH). **HMRS (ESI+)[M+H]$^+$** *m/z* calculated for $C_{11}H_{14}N_4O_2$ 234.1117; found **235.1192**.

8.3 Pharmacokinetic profiles and toxicity of Heterocyclic compounds

ADME properties, predicted using SwissADME, indicate that the selected compounds could act as promising HDAC6 inhibitors (**Table A9**). All compounds follow the acceptable ranges for molecular weight, hydrogen bond donors, and hydrogen bond acceptors. The LogP values from 1.68 (3a) to 2.36 (7a), indicating moderate lipophilicity that supports good oral absorption. All compounds showed good predicted oral bioavailability and the ability to cross the blood–brain barrier (BBB). CYP inhibition analysis predicted that all compounds inhibit CYP1A2, while none showed inhibition of CYP2C9 or CYP3A4, indicating a low risk of major drug–drug interactions. Compound **7a** was also predicted to inhibit CYP2C19 and CYP2D6. Skin permeability values ranged from -7.33 to -6.13 cm/s, with compound **3a** showing the highest permeability.

The BOILED-Egg model (**Figure A28**) shows that all six molecules (**4a, 3a, 3b, 7a**, and **7b**) are positioned within the white region, meaning a high probability of passive gastrointestinal absorption (HIA+). Some compounds such as, molecules **3a, 3b**, **4c**, and possibly **7a** and **7b** fall within the yellow region, suggesting potential to penetrate the BBB+. These results show that most compounds have favorable oral bioavailability, and show potential for central nervous system (CNS) activity.

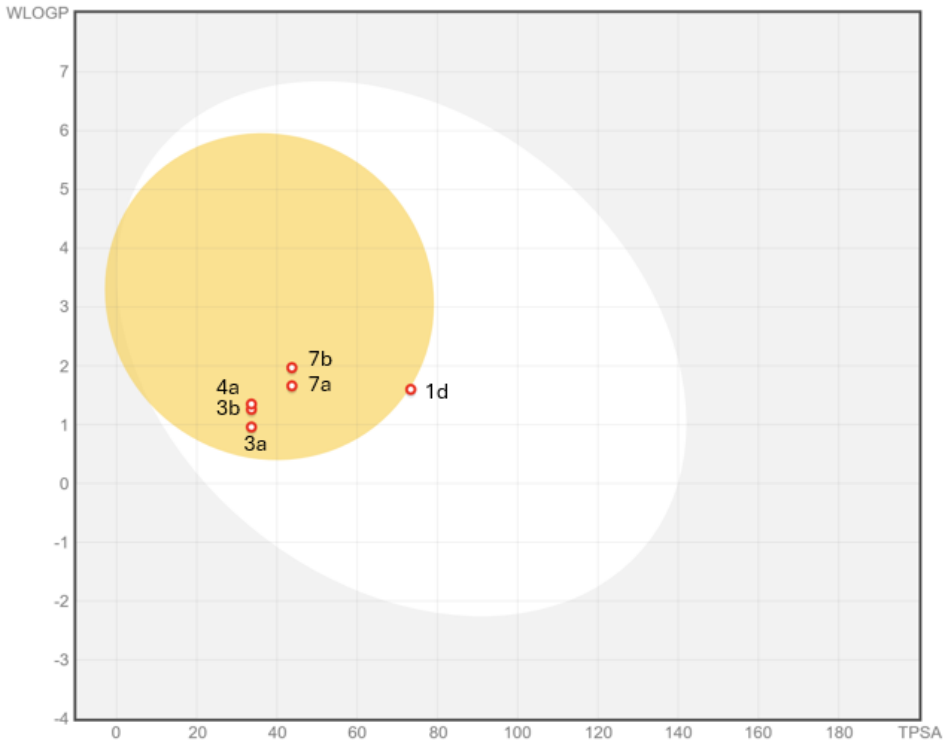

Figure A28: BOILED-Egg plot showing the HIA and BBB prediction of the heterocyclic compounds.

Toxicity predictions using the PROTOX platform show that, an acceptable safety profile, the compounds may cause the risks of neurotoxicity, respiratory toxicity, and nephrotoxicity. The presence of neurotoxicity indicates that, eventhough some compounds may cross the blood-brain barrier, they may not be good candidates for CNS-targeted therapies (**Table A12** and **Table 5.4**). Compound 7b is the least preferred, as it is predicted to be active for neurotoxicity, nephrotoxicity, and respiratory toxicity. It also shows immunotoxicity (0.53) and weaker predictions against carcinogenicity (0.50), which may further limit its therapeutic applicability.

8.4 Pharmacokinetic profiles and toxicity of Hydroxyacetamides

The results from ADMET predictions on eight selected compounds (**Table A8**) showed good pharmacokinetic and physicochemical properties supporting for synthesizing orally effective drugs. The molecular weights from 183.21 to 234.25 g/mol, which is below the 500 Da limit, suggesting an appropriate molecular weight suitable for oral administration. Hydrogen bond acceptors (3-4) and donors (2-3) were within Lipinski's criteria, while TPSA values (61.36-80.04 $Å^2$) suggested appropriate polarity for intestinal absorption and membrane permeability.

The lipophilicity analysis showed consensus Log P values between -0.42 and 1.33, indicating low to moderate lipophilicity favorable for balancing solubility and membrane diffusion. Correspondingly, Ali Logs values (-2.33 to -0.06) classified all molecules as soluble to very soluble, supporting good gastrointestinal absorption. Pharmacokinetic predictions indicated high gastrointestinal absorption, absence of blood–brain barrier (BBB) penetration, and no P-glycoprotein (P-gp) substrate activity, suggesting reduced efflux and improved bioavailability. In addition, none of the compounds inhibited major cytochrome P450 isoenzymes, implying a low risk of drug–drug interactions. Skin permeability values (log Kp -8.04 to -6.74 cm/s) were consistent with poor skin penetration but sufficient oral permeability. All molecules satisfied Lipinski, Ghose, Veber, Egan, and Muegge drug-likeness filters, with a bioavailability score of 0.55 and no PAINS or Brenk alerts, indicating the absence of problematic functional groups. Although a single lead-likeness violation was observed in some compounds, the deviations were minor and did not significantly affect their drug-like properties.

Among the analysed compounds, compounds **10b, 11a, 11c,** and **11d** exhibited the most balanced ADME profiles. These compounds included moderate lipophilicity, with consensus Log P values ranging from 0.40 to 0.97, showing balance between aqueous solubility and membrane permeability. Their predicted solubility was also promising, with Log S values between -1.20 and -1.80. Compounds 2c and 2d showed

slightly better aqueous solubility than compounds **10b** and **11a**, while compounds 10b and **11a** displayed lower molecular weights and reduced TPSA values, which may come up with improved membrane permeability. Therefore, these four compounds showed a good balance between solubility, permeability, and drug-like properties. Compound **2b** also showed strong ADME characteristics, major drug-likeness rules and high gastrointestinal absorption. Even though, its comparatively lower solubility made it slightly less appropriate than compounds **10b, 11a, 11c,** and **11d.** Likewise, compound **11e** displayed acceptable physicochemical and pharmacokinetic properties but showed the lowest predicted solubility among the compounds meanwhile**11e** doesn't show drug-likeness violations which may limit its oral availability. Although compound **10a** demonstrated good solubility and absorption properties, the presence of a Muegge violation slightly reduced its overall drug-likeness. On the other hand, compound **11f** showed the highest aqueous solubility, however, it's very low lipophilicity together with Ghose and Muegge violations indicated a less favourable physicochemical profile. Overall, compounds **10b, 11a, 11c,** and **11d** emerged as the most promising candidates due to their balanced combination of molecular weight, lipophilicity, polarity, solubility, and drug-likeness, making them suitable candidates for further biological evaluation.

The BOILED-Egg (**Figure A29**) model predicted that most compounds lie within the white region, indicating high gastrointestinal absorption. Only **11b** was located near the boundary of the yolk region, suggesting borderline BBB permeability. Most compounds were predicted as non-P-gp substrates, which may enhance intracellular exposure

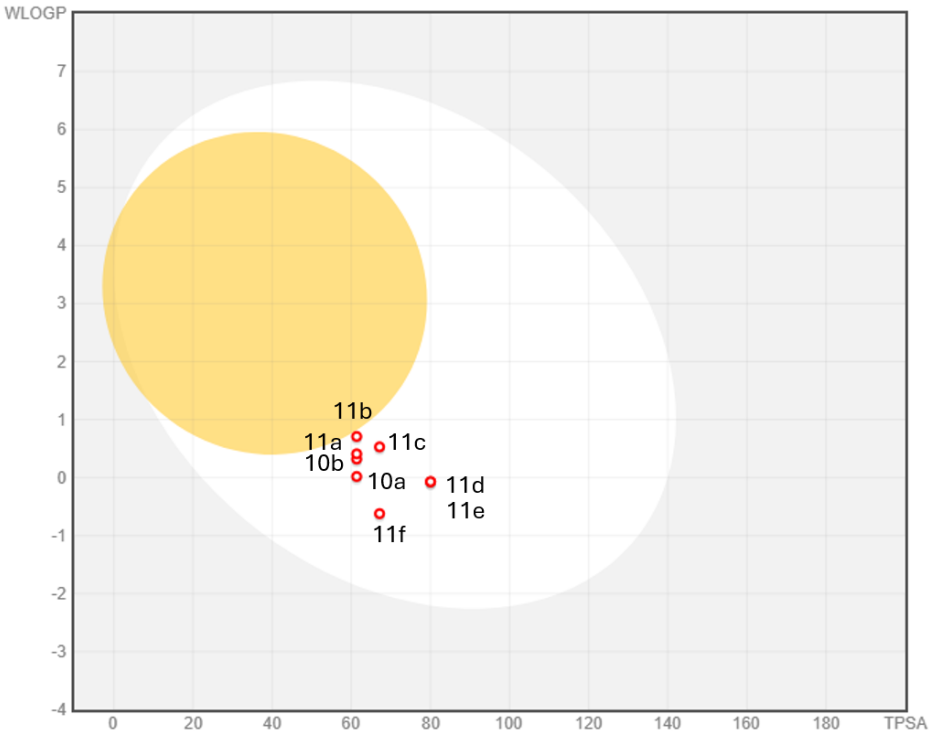

Figure A29: BOILED-Egg plot showing the HIA and BBB prediction of hydroxyacetamide compounds.

A comparative *in silico* toxicity evaluation was performed in all synthesized compounds including **10a, 10b, 11a, 11b, 11c, 11d, 11e**, and **11f** (Table 6). Among the derivatives **11d** and **11e** showed important safety risks, including predicted neurotoxicity, nephrotoxicity, respiratory toxicity, and carcinogenicity. The alkyl-substituted analogues **10a** and **10b** also showed cardiotoxic and mutagenic risks. In contrast, **11c** and **11f** exhibited comparatively safer toxicity profiles. Among them, **11f** showed the lowest predicted toxicity probabilities, identifying it as the most promising lead candidate for further HDAC inhibitory and biological evaluation.

Bibliography

*Adams, Grace E, Aditya Chandru, and Shaun M Cowley (2018). "Co-repressor, co-activator and general transcription factor: the many faces of the Sin3 histone deacetylase (HDAC) complex". In: *Biochemical Journal* 475.24, pp. 3921– 3932.

*Aboud, N. M. Al, Tupper, C., & Jialal, I. (2023). Genetics, Epigenetic Mechanism. StatPearls. https://www.ncbi.nlm.nih.gov/books/NBK532999/

*Asmamaw, Moges Dessale *et al*. (2024). "Histone deacetylase complexes: Structure, regulation and function". In: *Biochimica et Biophysica Acta (BBA)-Reviews on Cancer* 1879.5, pp. 189150.

*Asthana, Jayant *et al*. (2013). "Inhibition of HDAC6 deacetylase activity increases its binding with microtubules and suppresses microtubule dynamic instability in MCF-7 cells". In: *Journal of Biological Chemistry* 288.31, pp. 22516-22526.

*Avalos Alanís, F. G. (2011). Síntesis y caracterización de oxazolinas y amidas quirales a,B-insaturadas: evaluación del efecto citotóxico in vitro.

*Bae, Han-Sol *et al*. (2017). "An HDAC inhibitor, Entinostat/MS-275, partially prevents delayed cranial suture closure in heterozygous Runx2 null mice". In: *Journal of Bone and Mineral Research* 32.5, pp. 951-961.

*Bagchi, Rushita A and Kate L Weeks (2019). "Histone deacetylases in cardiovascular and metabolic diseases". In: *Journal of Molecular and Cellular Cardiology* 130, pp. 151-159.

*Banik, Debarati, Sara Moufarrij, and Alejandro Villagra (May 2019). "Immunoepigenetics Combination Therapies: An Overview of the Role of HDACs in Cancer Immunotherapy". In: *International Journal of Molecular Sciences 2019, Vol. 20, Page 2241* 20.9, pp. 2241. ISSN: 1422-0067. DOI: 10.3390/IJMS20092241.

*Barneda-Zahonero, Bruna and Maribel Parra (2012). "Histone deacetylases and cancer".In: *Molecular oncology* 6.6, pp. 579-589.

*Bahena, L., Cervantes, C., Soto-Arredondo, K. J., Martínez-Alfaro, M., Zarco, N., García-Revilla, M. A., Alcaraz-Contreras, Y., Tirado, L. P., Vázquez, M. A., & Robles, J. (2017). In silico, Synthesis and Biological Investigations of Pyrrolo[3,4-C]Pyrrole Hydroxamic Acid Derivatives as Potential Anticancer Agents. Journal of the Mexican Chemical Society, 61(4), 297–308. https://doi.org/10.29356/JMCS.V61I4.460

*Bieliauskas, Anton V and Mary Kay H Pflum (2008). "Isoform-selective histone deacetylase inhibitors". In: *Chemical Society Reviews* 37.7, pp. 1402-1413.

*Blander, Gil and Leonard Guarente (2004). "The Sir2 family of protein deacetylases".
In: *Annual review of biochemistry* 73.1, pp. 417-435.

*Boumber, Yanis, Anas Younes, and Guillermo Garcia-Manero (June 2011). "Mocetinostat (MGCD0103): a review of an isotype-specific histone deacetylase in- hibitor". In: *Expert opinion on investigational drugs* 20.6, p. 823. ISSN: 13543784. DOI: 10.1517/13543784.2011.577737.

*Braddock, D. Christopher *et al*. (Feb. 2018). "Tetramethyl Orthosilicate (TMOS) as a Reagent for Direct Amidation of Carboxylic Acids". In: *Organic Letters* 20.4, pp. 950–953. ISSN: 15237052. DOI: 10.1021 / ACS . ORGLETT . 7B03841.

*Buonvicino D et.al, Effects of Class II-Selective Histone Deacetylase Inhibitor on Neuromuscular Function and Disease Progression in SOD1-ALS Mice. Neuroscience. 2018 May 21;379:228-238. doi: 10.1016/j.neuroscience.2018.03.022. Epub 2018 Mar 26. PMID: 29588251.

*Cao, Dan-Feng *et al*. (2024). "Unveiling the role of histone deacetylases in neurological diseases: focus on epilepsy". In: *Biomarker Research* 12.1, pp. 142.

*Castro-Muñoz, Leonardo Josué *et al*. (2023). "Modulating epigenetic modifications for cancer therapy". In: *Oncology reports* 49.3, pp. 59.

*Cancer. (n.d.). Retrieved 21 June 2026, from https://www.who.int/news-room/fact-sheets/detail/cancer?utm_source=chatgpt.com

*Cavalli, G., & Heard, E. (2019). Advances in epigenetics link genetics to the environment and disease. Nature, 571(7766), 489–499. https://doi.org/10.1038/S41586-019-1411-0

*Ceccacci, Elena and Saverio Minucci (2016). "Inhibition of histone deacetylases in cancer therapy: lessons from leukaemia". In: *British journal of cancer* 114.6, pp. 605-611.

*Chakrabarti A, Melesina J, Kolbinger FR, Oehme I, Senger J, Witt O, Sippl W, Jung M. Targeting histone deacetylase 8 as a therapeutic approach to cancer and neurodegenerative diseases. Future Med Chem. 2016 Sep;8(13):1609-34. doi: 10.4155/fmc-2016-0117. Epub 2016 Aug 30. PMID: 27572818.

*Charville, H., Jackson, D., Hodges, G., & Whiting, A. (2010). The thermal and boron-catalysed direct amide formation reactions: mechanistically understudied yet important processes. Chemical Communications, 46(11), 1813–1823. https://doi.org/10.1039/b923093a

*Chen, Du *et al*. (June 2023). "Triflylpyridinium as Coupling Reagent for Rapid Amide and Ester Synthesis". In: *Organic Letters* 25.24, pp. 4571-4575. ISSN: 15237052. DOI: 10.1021/ACS.ORGLETT.3C01598.

*Chen, Hong Ping, Yu Tina Zhao, and Ting C Zhao (2015). "Histone deacetylases and mechanisms of regulation of gene expression". In: *Critical Reviews™ in Oncogenesis* 20. pp.1-2.

*Chen, Kai, Liping Xu, and Olaf Wiest (May 2013). "Computational Exploration of Zinc Binding Groups for HDAC Inhibition". In: *The Journal of organic chemistry* 78.10, pp. 5051. ISSN: 00223263. DOI: 10.1021/JO400406G.

*Chen, S., Yin, C., Lao, T., Liang, D., He, D., Wang, C., & Sang, N. (2015). AMPK-HDAC5 pathway facilitates nuclear accumulation of HIF-1α and functional activation of HIF-1 by deacetylating Hsp70 in the cytosol. Cell Cycle, 14(15), 2520. https://doi.org/10.1080/15384101.2015.1055426

*Choi, Myeong A. *et al*. (Sept. 2019). "Design, synthesis and biological evaluation of a series of CNS penetrant HDAC inhibitors structurally derived from amyloid-*β* probes". In: *Scientific Reports 2019 9:1* 9.1, pp. 13187–. ISSN: 2045- 2322. DOI: 10.1038/s41598-019-49784-9.

*Chuang, De-Maw *et al*. (2009). "Multiple roles of HDAC inhibition in neurodegenerative conditions". In: *Trends in neurosciences* 32.11, pp. 591-601.

*Connolly, Roisin M., Michelle A. Rudek, and Richard Piekarz (June 2017). "Entinostat: a promising treatment option for patients with advanced breast cancer". In: *Future Oncology* 13.13, p. 1137. ISSN: 17448301. DOI: 10.2217/FON-2016-0526.

*Consalvi, Silvia *et al*. (2011). "Histone deacetylase inhibitors in the treatment of muscular dystrophies: epigenetic drugs for genetic diseases". In: *Molecular medicine* 17.5-6, pp. 457-465.

*Cosenza M, Pozzi S. The Therapeutic Strategy of HDAC6 Inhibitors in Lymphoproliferative Disease. Int J Mol Sci. 2018 Aug 9;19(8):2337. doi: 10.3390/ijms19082337. PMID: 30096875; PMCID: PMC6121661.

*Dawson, Mark A and Tony Kouzarides (2012). "Cancer epigenetics: from mechanism to therapy". In: *cell* 150.1, pp. 12–27.

*Fardi, Masoumeh, Saeed Solali, and Majid Farshdousti Hagh (2018). "Epigenetic mechanisms as a new approach in cancer treatment: An updated review". In: *Genes & diseases* 5.4, pp. 304-311.

*Ferreira, Leonardo G. *et al*. (July 2015). "Molecular Docking and Structure-Based Drug Design Strategies". In: *Molecules* 20.7, pp. 13384. ISSN: 14203049. DOI: 10.3390 / MOLECULES200713384.

*Ferreira-Silva, G. Á., Rodrigues, D. A., Pressete, C. G., Caixeta, E. S., Gamero, A. M. C., Miyazawa, M., Hanemann, J. A. C., Fraga, C. A. M., Aissa, A. F., & Ionta, M. (2024). Selective inhibition of HDAC6 by N-acylhydrazone derivative reduces the proliferation and induces senescence in carcinoma hepatocellular cells. Toxicology in Vitro, 99, 105884. https://doi.org/10.1016/J.TIV.2024.105884.

*Ferroud, C., Godart, M., Ung, S., Borderies, H., & Guy, A. (2008). Microwaves-assisted solvent-free synthesis of N-acetamides by amidation or aminolysis. Tetrahedron Letters, 49(18), 3004–3008. https://doi.org/10.1016/J.TETLET.2008.02.170

*Ferroud, Clotilde *et al*. (Apr. 2008). "Microwaves-assisted solvent-free synthesis of N-acetamides by amidation or aminolysis". In: *Tetrahedron Letters* 49.18, pp. 3004–3008. ISSN: 0040-4039. DOI: 10.1016/J.TETLET.2008.02.170.

*Forgie, B. N., Prakash, R., Goyeneche, A. A., & Telleria, C. M. (2024). Vitality, viability, long-term clonogenic survival, cytotoxicity, cytostasis and lethality: what do they mean when testing new investigational oncology drugs? Discover. Oncology, 15(1), 5. https://doi.org/10.1007/S12672-023-00857-2

*Friedrich, Annabelle *et al*. (July 2020). "In Vitro Assessment of the Genotoxic Hazard of Novel Hydroxamic Acid- and Benzamide-Type Histone Deacetylase In- hibitors (HDACi)". In: *International Journal of Molecular Sciences 2020*, 21.13, pp. 4747. ISSN: 1422-0067. DOI: 10.3390/IJMS21134747.

*Friedrich, A., Assmann, A. S., Schumacher, L., Stuijvenberg, J. V., Kassack, M. U., Schulz, W. A., Roos, W. P., Hansen, F. K., Pflieger, M., Kurz, T., & Fritz, G. (2020). In Vitro Assessment of the Genotoxic Hazard of Novel Hydroxamic Acid- and Benzamide-Type Histone Deacetylase Inhibitors (HDACi). International Journal of Molecular Sciences, 21(13), 1–21. https://doi.org/10.3390/IJMS21134747

*Frühauf, Anton and Franz Josef Meyer-Almes (Sept. 2021). "Non-Hydroxamate Zinc-Binding Groups as Warheads for Histone Deacetylases". In: *Molecules* 26.17, p. 5151. ISSN: 14203049. DOI: 10.3390 / MOLECULES26175151.

*Gallinari, Paola *et al*. (2007). "HDACs, histone deacetylation and gene transcription: from molecular biology to cancer therapeutics". In: *Cell research* 17.3, pp. 195-211.

*Gediya, Piyush *et al*. (2021). "Histone deacetylase 2: A potential therapeutic target for cancer and neurodegenerative disorders". In: *European Journal of Medicinal Chemistry* 216, pp. 113332.

*Geng, H., Harvey, C. T., Pittsenbarger, J., Liu, Q., Beer, T. M., Xue, C., & Qian, D. Z. (2011). HDAC4 Protein Regulates HIF1α Protein Lysine Acetylation and Cancer Cell Response to Hypoxia. The Journal of Biological Chemistry, 286(44), 38095. https://doi.org/10.1074/JBC.M111.257055.

*Gilli, G., & Gilli, P. (2009). The Nature of the Hydrogen Bond: Outline of a Comprehensive Hydrogen Bond Theory. The Nature of the Hydrogen Bond: Outline of a Comprehensive Hydrogen Bond Theory, 9780199558964, 1–336. https://doi.org/10.1093/acprof:oso/9780199558964.001.0001

*Gimeno, Aleix *et al*. (Mar. 2019). "The Light and Dark Sides of Virtual Screening: What Is There to Know?" In: *International Journal of Molecular Sciences* 20.6, E1375–E1375. ISSN: 1422-0067. DOI: 10.3390/IJMS20061375.

*Glozak, MA and E Seto (2007). "Histone deacetylases and cancer". In: *Oncogene* 26.37, pp. 5420-5432.

*Haggarty, S. J., Koeller, K. M., Wong, J. C., Grozinger, C. M., & Schreiber, S. L. (2003). Domain-selective small-molecule inhibitor of histone deacetylase 6 (HDAC6)-mediated tubulin deacetylation. Proceedings of the National Academy of Sciences of the United States of America, 100(8), 4389–4394. https://doi.org/10.1073/PNAS.0430973100

*Hai, Y., & Christianson, D. W. (2016). Histone deacetylase 6 structure and molecular basis of catalysis and inhibition. Nature Chemical Biology, 12(9), 741–747. https://doi.org/10.1038/NCHEMBIO.2134

*He, Junquan *et al*. (Apr. 2020). "Synthesis and Biological Evaluation of HDAC Inhibitors with a Novel Zinc Binding Group". In: *Frontiers in Chemistry* 8, pp. 512565. ISSN: 22962646. DOI: 10.3389/FCHEM.2020.00256/BIBTEX.

*Hassell, K. N. (2019). Histone Deacetylases and their Inhibitors in Cancer Epigenetics. Diseases (Basel, Switzerland), 7(4), 57. https://doi.org/10.3390/DISEASES7040057

*He, J., Wang, S., Liu, X., Lin, R., Deng, F., Jia, Z., Zhang, C., Li, Z., Zhu, H., Tang, L., Yang, P., He, D., Jia, Q., & Zhang, Y. (2020). Synthesis and Biological Evaluation of HDAC Inhibitors With a Novel Zinc Binding Group. Frontiers in Chemistry, 8, 512565. https://doi.org/10.3389/FCHEM.2020.00256/BIBTEX

*Hernández-Fernández, E., Sánchez-Lara, P. P., Ordóñez, M., Ramírez-Marroquín, O. A., Avalos-Alanís, F. G., López-Cortina, S., Jiménez-Pérez, V. M., & Ibarra-Rivera, T. R. (2015). Synthesis of β-hydroxyacetamides from unactivated ethyl acetates under base-free conditions and microwave irradiation. Tetrahedron: Asymmetry, 26(1), 73–78. https://doi.org/10.1016/J.TETASY.2014.11.015

*Hong, J., & Luesch, H. (2012). Largazole: From Discovery to Broad-Spectrum Therapy. Natural Product Reports, 29(4), 449. https://doi.org/10.1039/c2np00066k

*Hrzenjak, Andelko *et al*. (Mar. 2010). "Histone deacetylase inhibitor vorinostat suppresses the growth of uterine sarcomas *in vitro* and *in vivo*". In: *Molecular cancer* 9. ISSN: 1476-4598. DOI: 10.1186/1476-4598-9-49.

*Hu, Erding *et al*. (Nov. 2003). "Identification of Novel Isoform-Selective Inhibitors within Class I Histone Deacetylases". In: *The Journal of Pharmacology and Experimental Therapeutics* 307.2, pp. 720-728. ISSN: 0022-3565. DOI: 10.1124/JPET.103.055541.

*Huang, Ziqian *et al*. (Sept. 2024). "Small molecules targeting HDAC6 for cancer treatment: Current progress and novel strategies". In: *Biomedicine & Pharmacotherapy* 178, pp. 117218. ISSN: 0753-3322. DOI: 10.1016/J.BIOPHA.2024.117218.

*Hubbert, C., Guardiola, A., Shao, R., Kawaguchi, Y., Ito, A., Nixon, A., Yoshida, M., Wang, X. F., & Yao, T. P. (2002). HDAC6 is a microtubule-associated deacetylase. Nature, 417(6887), 455–458. https://doi.org/10.1038/417455A

*Kaluza, D., Kroll, J., Gesierich, S., Yao, T. P., Boon, R. A., Hergenreider, E., Tjwa, M., Rössig, L., Seto, E., Augustin, H. G., Zeiher, A. M., Dimmeler, S., & Urbich, C. (2011). Class IIb HDAC6 regulates endothelial cell migration and angiogenesis by deacetylation of cortactin. The EMBO Journal, 30(20), 4142. https://doi.org/10.1038/EMBOJ.2011.298

*Kandakatla, Naresh and Geetha Ramakrishnan (2014). "Ligand Based Pharmacophore Modeling and Virtual Screening Studies to Design Novel HDAC2 Inhibitors". In: *Advances in Bioinformatics* 2014, pp. 812148. ISSN: 16878035. DOI: 10.1155/2014/812148.

*Kong, X., Lin, Z., Liang, D., Fath, D., Sang, N., & Caro, J. (2006). Histone Deacetylase Inhibitors Induce VHL and Ubiquitin-Independent Proteasomal Degradation of Hypoxia-Inducible Factor 1α. Molecular and Cellular Biology, 26(6), 2019. https://doi.org/10.1128/MCB.26.6.2019-2028.2006

*Kumar, A., Yadav, M., Ray, P. K., Mishra, R., Upadhyay, A., Tripathi, S. M., & Mishra, S. (2026). In Silico ADMET Profiling: Evolution from Traditional Models to Deep Learning Techniques. Current Topics in Medicinal Chemistry, 26. https://doi.org/10.2174/0115680266439252260329214559

*Kumbhar, N., Nimal, S., Barale, S., Kamble, S., Bavi, R., Sonawane, K., & Gacche, R. (2022). Identification of novel leads as potent inhibitors of HDAC3 using ligand-based pharmacophore modeling and MD simulation. Scientific Reports, 12(1). https://doi.org/10.1038/S41598-022-05698-7;SUBJMETA

*Kusaczuk, Magdalena *et al*. (Jan. 2015). "Phenylbutyrate-a pan-HDAC inhibitor -suppresses proliferation of glioblastoma LN-229 cell line". In: *Tumour Biology* 37.1, pp. 931.ISSN: 14230380. DOI: 10.1007/S13277-015-3781-8.

*Li, Guo, Yuan Tian, and Wei-Guo Zhu (2020). "The roles of histone deacetylasesand their inhibitors in cancer therapy". In: *Frontiers in cell and developmental biology* 8, pp. 576946.

*Li, Xiaoyang *et al*. (May 2020). "Design of hydrazide-bearing HDACIs based on panobinostat and their p53 and FLT3-ITD dependency in anti-leukemia activ- ity". In: *Journal of medicinal chemistry* 63.10, p. 5501. ISSN: 15204804. DOI: 10 .1021 / ACS.JMEDCHEM.0C00442.
*Li, Y., & Woster, P. M. (2015). Discovery of a new class of histone deacetylase inhibitors with a novel zinc binding group. MedChemComm, 6(4), 613–618. https://doi.org/10.1039/c4md00401a
*Li, Yixuan and Edward Seto (2016). "HDACs and HDAC inhibitors in cancer development and therapy". In: *Cold Spring Harbor perspectives in medicine* 6.10, a026831.
*Li, Youxuan and Patrick M. Woster (Apr. 2015). "Discovery of a new class of histone deacetylase inhibitors with a novel zinc binding group". In: *Med. Chem.Comm.* 6.4, pp. 613-618. ISSN: 2040-2511. DOI: 10 .1039 / C4MD00401A.
*Liang, Tao *et al*. (June 2023). "Targeting histone deacetylases for cancer therapy: Trends and challenges". In: *Acta Pharmaceutica Sinica B* 13.6, pp. 2425–2463. ISSN: 2211-3835. DOI: 10.1016/J.APSB.2023.02.007.
*Lima, Rafaely N. *et al*. (2017). "Fast synthesis of amides from ethyl salicylate under microwave radiation in a solvent-free system". In: *RSC Advances* 7.89, pp. 56566–56574. ISSN: 20462069. DOI: 10.1039/C7RA11434F.
*Lima, R. N., Silva, V. R., De Santos, L., Bezerra, D. P., Soares, M. B. P., & Porto, A. L. M. (2017). Fast synthesis of amides from ethyl salicylate under microwave radiation in a solvent-free system. RSC Advances, 7(89), 56566–56574. https://doi.org/10.1039/C7RA11434F
*Lin, Yipeng (Dec. 2022). "Review of Modern Computer-aided Drug Design Methods". In: *International Journal of Biology and Life Sciences* 1.1, pp. 47-50. DOI: 10.54097/IJBLS.V1I1.3230.
*Ling, H., Fabbri, M., & Calin, G. A. (2013). MicroRNAs and other non-coding RNAs as targets for anticancer drug development. Nature Reviews. Drug Discovery, 12(11), 847. https://doi.org/10.1038/NRD4140
*Liu X, Testa B, Fahr A. Lipophilicity and its relationship with passive drug permeation. Pharm Res. 2011 May;28(5):962-77. doi: 10.1007/s11095-010-0303-7. Epub 2010 Oct 30. PMID: 21052797.
*Liu, Yang *et al*. (July 2019). "CB-Dock: a web server for cavity detection-guided protein–ligand blind docking". In: *Acta Pharmacologica Sinica 2019 41:1* 41.1, pp. 138-144. ISSN: 1745-7254. DOI: 10.1038 / s41401 - 019 - 0228 - 6.
*Lu, Chao *et al*. (July 2021). "OPLS4: Improving force field accuracy on challenging regimes of chemical space". In: *Journal of Chemical Theory and Computation* 17.7, pp. 4291–4300. ISSN: 15499626. DOI: 10.1021 / ACS . JCTC . 1C00302.
*Lu, Xianping *et al*. (2016). "Development of chidamide for peripheral T-cell lymphoma, the first orphan drug approved in China". In: *Intractable & Rare Dis- eases Research* 5.3, pp. 185-191. ISSN: 2186-3644. DOI: 10.5582 / IRDR.2016.01024.
* Luis Bahena *et al*. (2017)" In silico, Synthesis and Biological Investigations of Pyrrolo[3,4-C]Pyrrole Hydroxamic Acid Derivatives as Potential Anticancer

Agents" Vol. 61 No. 4 (2017), DOI: https://doi.org/10.29356/jmcs.v61i4.460.
*Luo, Yuxiang and Huilin Li (Nov. 2020). "Structure-Based Inhibitor Discovery of Class I Histone Deacetylases (HDACs)". In: *International journal of molecular sciences* 21.22, pp. 1-25. ISSN: 1422-0067. DOI: 10.3390/IJMS21228828.
*Massaro, Assunta *et al*. (Oct. 2007). "Microwave-Assisted Transformation of Esters into Hydroxamic Acids". In: *Synthesis* 2007.20, pp. 3201–3204. ISSN: 0039-7881. DOI: 10.1055 / S - 2007 - 990803.
*McClure, Jesse J. *et al*. (Nov. 2016). "Development of Allosteric Hydrazide-Containing Class I Histone Deacetylase Inhibitors for Use in Acute Myeloid Leukemia". In: *Journal of medicinal chemistry* 59.21, pp. 9942–9959. ISSN: 1520-4804. DOI: 10.1021/ACS.JMEDCHEM.6B01385.
*McDonel, Patrick, Ita Costello, and Brian Hendrich (2009). "Keeping things quiet: roles of NuRD and Sin3 co-repressor complexes during mammalian development". In: *The international journal of biochemistry & cell biology* 41.1, pp. 108-116.
*Melesina, Jelena *et al*. (May 2021). "Strategies To Design Selective Histone Deacetylase Inhibitors". In: *ChemMedChem* 16.9, pp. 1336–1359. ISSN: 18607187.
DOI: 10.1002/CMDC.202000934
*Meng, Xuan-Yu *et al*. (Nov. 2011). "Molecular Docking: A powerful approach for structure-based drug discovery". In: *Current computer-aided drug design* 7.2, p. 146. ISSN: 15734099. DOI: 10.2174 / 157340911795677602.
*Min, H. Y., & Lee, H. Y. (2022). Molecular targeted therapy for anticancer treatment. Experimental & Molecular Medicine, 54(10), 1670–1694. https://doi.org/10.1038/S12276-022-00864-3
*Mohy El Dine, Tharwat *et al*. (May 2015). "Catalytic chemical amide synthesis at room temperature: one more step toward peptide synthesis". In: *The Journal of organic chemistry* 80.9, pp. 4532–4544. ISSN: 1520-6904. DOI: 10.1021/ ACS.JOC.5B00378.
*Molinari, Susanna *et al*. (2023). "Histone deacetylase functions and therapeutic implications for adult skeletal muscle metabolism". In: *Frontiers in Molecular Biosciences* 10, pp. 1130183.
*Narita, Takeo, Brian T Weinert, and Chunaram Choudhary (2019). "Functions and mechanisms of non-histone protein acetylation". In: *Nature reviews Molecular cell biology* 20.3, pp. 156-174.
* Navanath Kumbhar *et al* (2022) "Identification of novel leads as potent inhibitors of HDAC3 using ligand-based pharmacophore modeling and MD simulation. *Sci Rep* **12**, 1712 (2022). https://doi.org/10.1038/s41598-022-05698-7
*Niazi, Sarfaraz K. and Zamara Mariam (Jan. 2023). "Computer-Aided Drug Design and Drug Discovery: A Prospective Analysis". In: *Pharmaceuticals* 17.1, pp. 22. ISSN: 14248247. DOI: 10 .3390 / PH17010022.
*Ning, Zhi Qiang *et al*. (Apr. 2012). "Chidamide (CS055/HBI-8000): a new histone deacetylase inhibitor of the benzamide class with antitumor activity and the ability to enhance immune cell-mediated tumor cell cytotoxicity". In: *Cancer chemotherapy and pharmacology* 69.4, pp. 901–909. ISSN: 1432-0843. DOI:

10.1007/S00280- 011- 1766- X.

*Nithinchandra, Kalluraya, B., Aamir, S., & Shabaraya, A. R. (2012). Regioselective reaction: Synthesis, characterization and pharmacological activity of some new Mannich and Schiff bases containing sydnone. European Journal of Medicinal Chemistry, 54, 597–604. https://doi.org/10.1016/j.ejmech.2012.06.011

*Ojeda-Porras, Andrea, Alejandra Hernández-Santana, and Diego Gamba-Sánchez (May 2015). "Direct amidation of carboxylic acids with amines under microwave irradiation using silica gel as a solid support". In: *Green Chemistry* 17.5, pp. 3157-3163. ISSN: 1463-9270. DOI: 10.1039/C5GC00189G.

*Palijan, Ana *et al*. (2009). "Function of histone deacetylase 6 as a cofactor of nuclear receptor coregulator LCoR". In: *Journal of Biological Chemistry* 284.44, pp. 30264-30274.

*Parasrampuria, Dolly A., Leslie Z. Benet, and Amarnath Sharma (May 2018). "Why Drugs Fail in Late Stages of Development: Case Study Analyses from the Last Decade and Recommendations". In: *AAPS Journal* 20.3. ISSN: 15507416. DOI: 10.1208/S12248-018-0204-Y.

*Patil, Vishal *et al*. (May 2013). "3-Hydroxypyridin-2-thione as novel zinc binding group for selective histone deacetylase inhibition". In: *Journal of medicinal chemistry* 56.9, pp. 3492–3506. ISSN: 1520-4804. DOI: 10.1021/JM301769U.

*Peserico, Alessia and Cristiano Simone (2011). "Physical and functional HAT/HDAC interplay regulates protein acetylation balance". In: *Biomed Research Interna- tional* 2011.1, pp. 371832.

*Pires, Gustavo Salgado *et al*. (Apr. 2025). "Drug Discovery for Histone Deacetylase Inhibition: Past, Present and Future of Zinc-Binding Groups". In: *Pharmaceuticals 2025, Vol. 18, Page 577* 18.4, p. 577. ISSN: 1424-8247. DOI: 10.3390 / PH18040577.

*Plumb, JA *et al*. (2003). "Pharmacodynamic response and inhibition of growth of human tumor xenografts by the novel histone deacetylase inhibitor". Proc Natl Acad Sci U S A.2017 Dec 19;114(51):13459-13464. doi: 10.1073/pnas.1718823114. Epub 2017 Dec 4. PMID: 29203661 PMCID: PMC5754815

*Porter, N. J., Mahendran, A., Breslow, R., & Christianson, D. W. (2017). Unusual zinc-binding mode of HDAC6-selective hydroxamate inhibitors. Proceedings of the National Academy of Sciences of the United States of America, 114(51), 13459–13464. https://doi.org/10.1073/PNAS.1718823114/SUPPL_FILE/PNAS.201718823SI.PDF

* Nicholas J Porter. (2017). "Unusual zinc-binding mode of HDAC6-selective hydroxamate inhibitors". Mol Cancer Ther. 2003 Aug;2(8):721-8

*Ramachandran, P. Veeraraghavan and Henry J. Hamann (Apr. 2021). "Ammonia-borane as a Catalyst for the Direct Amidation of Carboxylic Acids". In: *Organic Letters* 23.8, pp. 2938-2942. ISSN: 15237052. DOI: 10.1021/ACS.ORGLETT.1C00591.

*Ran, Jie and Jun Zhou (2019). "Targeted inhibition of histone deacetylase 6 in inflammatory diseases". In: *Thoracic Cancer* 10.3, pp. 405-412.

*Ropero, Santiago and Manel Esteller (2007). “The role of histone deacetylases (HDACs) in human cancer”. In: *Molecular oncology* 1.1, pp. 19-25.
*Santo, Loredana *et al*. (Mar. 2012). “Preclinical activity, pharmacodynamic, and pharmacokinetic properties of a selective HDAC6 inhibitor, ACY-1215, in combination with bortezomib in multiple myeloma”. In: *Blood* 119.11, pp. 2579-2589. ISSN: 1528-0020. DOI: 10.1182/BLOOD-2011-10-387365.
*Seto, E., & Yoshida, M. (2014). Erasers of Histone Acetylation: The Histone Deacetylase Enzymes. Cold Spring Harbor Perspectives in Biology, 6(4), a018713. https://doi.org/10.1101/cshperspect.a018713
*Scuto, Anna *et al*. (May 2008). “The novel histone deacetylase inhibitor, LBH589, induces expression of DNA damage response genes and apoptosis in Ph- acute lymphoblastic leukemia cells”. In: *Blood* 111.10, pp. 5093–5100. ISSN: 1528-0020. DOI: 10.1182/BLOOD-2007-10-117762.
*Sequera, Celia *et al*. (Aug. 2025). “The HDAC inhibitor romidepsin renders liver cancer vulnerable to RTK targeting and immunologically active”. In: *Nature Communications 2025 16:1* 16.1, pp. 7919. ISSN: 2041-1723. DOI: 10.1038/s41467-025-62934-0.
*Shakespear, Melanie R *et al*. (2011). “Histone deacetylases as regulators of inflammation and immunity”. In: *Trends in immunology* 32.7, pp. 335-343.
*Sharma, Sudripet *et al*. (Aug. 2020). “Fast Amide Couplings in Water: Extraction, Column Chromatography, and Crystallization Not Required”. In: *Organic letters* 22.15, pp. 5737–5740. ISSN: 1523-7052. DOI: 10.1021/ACS.ORGLETT.0C01676.
*Shen, Sida and Alan P. Kozikowski (Jan. 2015). “Why Hydroxamates May Not Be the Best Histone Deacetylase Inhibitors-What Some May Have Forgotten or Would Rather Forget?” In: *ChemMedChem* 11.1, p. 15. ISSN: 18607187. DOI: 10.1002/CMDC.201500486.
*Shirbhate, Ekta *et al*. (Nov. 2025). “Patent landscape in hydroxamic acid-based HDAC inhibitors (2020–2024): structure-activity relationships and mechanistic insights”. In: *Expert Opinion on Therapeutic Patents*. ISSN: 1354-3776. DOI: 10.1080/13543776.2025.2591483.
*Shukla, Surabhi and Babu L Tekwani (2020). “Histone deacetylases inhibitors in neurodegenerative diseases, neuroprotection and neuronal differentiation”. In: *Frontiers in pharmacology* 11, pp. 537.
*Spedding, Michael (2006). “New directions for drug discovery”. In: *Dialogues in Clinical Neuroscience* 8.3, p. 295. ISSN: 12948322. DOI: 10.31887/DCNS.2006.8.3/MSPEDDING.
*Sung, Hyuna *et al*. (2021). “Global cancer statistics 2020: GLOBOCAN estimates of incidence and mortality worldwide for 36 cancers in 185 countries”. In: *CA: a cancer journal for clinicians* 71.3, pp. 209-249.
*Su, M., Shi, J. J., Yang, Y. P., Li, J., Zhang, Y. L., Chen, J., Hu, L. F., & Liu, C. F. (2011). HDAC6 regulates aggresome-autophagy degradation pathway of α-synuclein in response to MPP+-induced stress. Journal of Neurochemistry, 117(1), 112–120. https://doi.org/10.1111/J.1471-4159.2011.07180.X
*Sweet, Matthew J *et al*. (2012). “HDAC inhibitors: modulating leukocyte

differentiation, survival, proliferation and inflammation". In: *Immunology and cell biology* 90.1, pp. 14-22.

*Van Montfort, Rob L.M. and Paul Workman (Nov. 2017). "Structure-based drug design: aiming for a perfect fit". In: *Essays in Biochemistry* 61.5, p. 431. ISSN: 00711365. DOI: 10.1042/EBC20170052.

*Vasilev, Boris and Mariyana Atanasova (Jan. 2025). "A (Comprehensive) Review of the Application of Quantitative Structure-Activity Relationship (QSAR) in the Prediction of New Compounds with Anti-Breast Cancer Activity". In: *Applied Sciences 2025, Vol. 15, Page 1206* 15.3, p. 1206. ISSN: 2076-3417. DOI: 10.3390/APP15031206.

*Valenzuela-Fernández, A., Cabrero, J. R., Serrador, J. M., & Sánchez-Madrid, F. (2008). HDAC6: a key regulator of cytoskeleton, cell migration and cell–cell interactions. Trends in Cell Biology, 18(6), 291–297. https://doi.org/10.1016/J.TCB.2008.04.003

*Vázquez, Javier *et al*. (Oct. 2020). "Merging Ligand-Based and Structure-Based Methods in Drug Discovery: An Overview of Combined Virtual Screening Approaches". In: *Molecules* 25.20, p. 4723. ISSN: 14203049. DOI: 10 . 3390 / MOLECULES25204723.

*Vogl, Dan T *et al*. (2017). "Ricolinostat, the first selective histone deacetylase 6 inhibitor, in combination with bortezomib and dexamethasone for relapsed or refractory multiple myeloma". In: *Clinical Cancer Research* 23.13, pp. 3307-3315.

*Wang, Yunfei *et al*. (Feb. 2015). "Identification of histone deacetylase inhibitors with benzoylhydrazide scaffold that selectively inhibit class i histone deacetylases". In: *Chemistry and Biology* 22.2, pp. 273–284. ISSN: 10745521. DOI: 10.1016/j.chembiol.2014.12.015.

*Winkler, G. C., Barle, E. L., Galati, G., & Kluwe, W. M. (2014). Functional differentiation of cytotoxic cancer drugs and targeted cancer therapeutics. Regulatory Toxicology and Pharmacology, 70(1), 46–53. https://doi.org/10.1016/J.YRTPH.2014.06.012

*Xu, Y., Tang, H., Xu, Y., Guo, J., Zhao, X., Meng, Q., & Xiao, J. (2022). Design, Synthesis, Bioactivity Evaluation, Crystal Structures, and In Silico Studies of New α-Amino Amide Derivatives as Potential Histone Deacetylase 6 Inhibitors. Molecules, 27(10), 3335. https://doi.org/10.3390/MOLECULES27103335/S1

*Yamaguchi, Teppei *et al*. (Mar. 2010). "Histone deacetylases 1 and 2 act in concert to promote the G1-to-S progression". In: *Genes & Development* 24.5, pp. 455. ISSN: 08909369. DOI: 10.1101/GAD.552310.

*Yang, X-J and EHAT Seto (2007). "HATs and HDACs: from structure, function and regulation to novel strategies for therapy and prevention". In: *Oncogene* 26.37, pp. 5310-5310.

* Yang LP. Romidepsin: in the treatment of T-cell lymphoma. Drugs. 2011 Jul 30;71(11):1469-80. doi: 10.2165/11207170-000000000-00000. PMID: 21812508.

*Yoo, Y. G., Kong, G., & Lee, M. O. (2006). Metastasis-associated protein 1 enhances stability of hypoxia-inducible factor-1α protein by recruiting histone deacetylase 1. The EMBO Journal, 25(6), 1231.

https://doi.org/10.1038/SJ.EMBOJ.7601025
*Yu, Qingwen *et al*. (2023). “The role of histone deacetylases in cardiac energy metabolism in heart diseases”. In: *Metabolism* 142, pp. 155532.
*Zhang, Lei *et al*. (Jan. 2018). “Zinc binding groups for histone deacetylase inhibitors”. In: *Journal of Enzyme Inhibition and Medicinal Chemistry* 33.1, p. 714. ISSN: 14756374. DOI: 10.1080/14756366.2017.1417274.
*Zhang, Qing *et al*. (2019). “Histone deacetylases (HDACs) guided novel therapies for T-cell lymphomas”. In: *International journal of medical sciences* 16.3, pp. 424.
*Zhang, Li-Ying *et al*. (2024). “Role of histone deacetylases and their inhibitors in neurological diseases”. In: *Pharmacological Research* 208, pp. 107410.
*Zhang, L., Zhang, J., Jiang, Q., Zhang, L., & Song, W. (2018). Zinc binding groups for histone deacetylase inhibitors. Journal of Enzyme Inhibition and Medicinal Chemistry, 33(1), 714. https://doi.org/10.1080/14756366.2017.1417274
*Zhang, Ying *et al*. (2025). “Mechanisms of HDACs in cancer development”. In: *Frontiers in Immunology* 16, pp. 1529239.
*Zhao, Ting C, Zhengke Wang, and Tina Y Zhao (2020). “The important role of histone deacetylases in modulating vascular physiology and arteriosclerosis”. In: *Atherosclerosis* 303, pp. 36-42.
*Zheng, Wenyue *et al*. (Nov. 2022). “Small molecule angiotensin converting enzyme inhibitors: A medicinal chemistry perspective”. In: *Frontiers in pharmacology* 13. ISSN: 1663-9812. DOI: 10.3389/FPHAR.2022.968104.
*Zhou, Jingwei *et al*. (Mar. 2015). “Computational Design of a Time-Dependent Histone Deacetylase 2 Selective Inhibitor”. In: *ACS Chemical Biology* 10.3, pp. 687-692. ISSN: 15548937. DOI: 10.1021/CB500767C.
* Zuliani, V., Carmi, C., Rivara, M., Fantini, M., Lodola, A., Vacondio, F., Bordi, F., Plazzi, P. V., Cavazzoni, A., Galetti, M., Alfieri, R. R., Petronini, P. G., & Mor, M. (2009). 5-Benzylidene-hydantoins: Synthesis and antiproliferative activity on A549 lung cancer cell line. European Journal of Medicinal Chemistry, 44(9), 3471–3479. https://doi.org/10.1016/j.ejmech.2009.01.035.

Personal Background

Name: Ashly Mohan

Degree: Doctor of Philosophy (PhD) in Chemistry

Specialization: Chemistry

Institution: Universidad Autónoma de Nuevo León (UANL)

Department: Facultad de Ciencia Químicas

City, Country: San Nicolás de los Garza, México

Email: ashly.mohanpvx@uanl.edu.mx

Phone: 8135920499

ORCID: 0000-0001-5950-2599

LinkedIn: Ashly Mohan

Nationality: Indian

Languages: English (Fluent), Spanish (Basic)